About Drying of Hierarchically Structured Electrodes for High Energy Li-Ion Battery Applications

Zur Erlangung des akademischen Grades einer

DOKTORIN DER INGENIEURWISSENSCHAFTEN (DR.-ING.)

von der KIT-Fakultät für Chemieingenieurwesen und Verfahrenstechnik des Karlsruher Instituts für Technologie (KIT)
genehmigte

DISSERTATION

von

Jana Kumberg, M. Sc.
aus Malsch

Tag der mündlichen Prüfung: 21.07.2022

Erstgutachter: Prof. Dr. Wilhelm Schabel
Zweitgutachterin: Prof. Dr. Ulrike Krewer

I dedicate this dissertation to my father.
I very much wished that he could share this with me.

Preface

This dissertation originates from my research conducted as PhD student between June 2016 and July 2021 at the Thin Film Technology (TFT) group at Karlsruhe Institute of Technology (KIT). During this time, many people have significantly contributed to the success of this dissertation, and I would like to express my sincere gratitude to every single one of them.

First of all I would like to thank Prof. Dr.-Ing. Dr. h. c. Wilhelm Schabel and Dr.-Ing. Philip Scharfer, who employed me and supervised my work at the TFT group, for their support, the fruitful scientific discussions, and for the freedom they granted me during my research, which resulted in this dissertation. I am also grateful for the opportunity to present my results at numerous national and international conferences, due to their support. I would like to thank them and Margit Morvay especially for their support, understanding and consideration at a time when personal circumstances made the time-consuming work on a dissertation difficult for me. This was not a matter of course.

Futhermore, I would like to thank Prof. Dr.-Ing. Ulrike Krewer for providing the second review of this dissertation.

I am greatly indebted to Margit Morvay, who was always there to help me with all administrative issues related with the work at TFT/KIT. But furthermore she always supported and encouraged me during all of these past 5 years. The former and current members of the Insitute of Thermal Process Engineering (TVT)'s mechanical and electrical workshop, as well as lab staff, I would like to thank for their input on my design drawings, fabrication of various prototypes, and for conducting measurements. Among these are Michael Wachter, Andreas Roth, Stephan Fink, Steffen Haury, Max Renaud, Stefan Böttle, Sabrina Herberger, and Anette Schucker. My thanks also go to Prof. Dr.-Ing. Matthias Kind, Prof. Dr.-Ing. Thomas Wetzel, Dr.-Ing. Benjamin Dietrich, Sebastian Schwarz, Nicole Feger, and Vanessa Gamer for supervising and administrating my teaching obligations at the Institute of Thermal Process Engineering (TVT).

I am very grateful for the great and positive atmosphere at TVT and TFT, which is largely due to my former colleagues. They have contributed greatly to making the daily work routine enjoyable. I am grateful to them for making the meetings on research projects and scientific conferences unforgettable. For the pleasant collaboration and for all the scientific discussions along the way. But most of all, I am happy for all the time we spent together as friends, without talking about work during coffee breaks, lunch breaks, private activities and festivities.

I am deeply grateful for numerous fruitful scientific discussions I had with Werner Bauer, Marcus Müller and Yijing Zhen and the friendly and open collaboration with them and Wilhelm Pfleging, Margarete Offermann and Amalia Wagner that hugely contributed to this work. Without their valuable insights, their support by offering new characterization methods like mercury intrusion porosemitry, scanning electron microscopy, energy dispersive X-ray spectroscopy, laser-induced breakdown spectroscopy, cell assembly, calendering and much more, this work would not be what it is today.

Along that line I also have to express my deepest appreciation to Joyce Schmatz and the MaP team. Her deep knowledge concerning cryogenic broad ion beam scanning electron microscopy was invaluable and contributed a very important aspect to this work. I am very grateful for the many late hours, the friendly atmosphere and all the time she invested.

I also want to deeply thank Prof. Dr.-Ing. Nirschl and the Institute of Mechanical Process Engineering and Mechanics (MVM) with the research group Process Machines (VM) at the KIT for giving me the possibility to use the Inoue-Trimix mixer. I especially want to thank Julian Ungerer for this possibility and for the opportunity to use their Zetasizer.

This work would be nothing without all the students that assisted me and contributed substantially to my research during their bachelor, master's or diploma theses, or worked under my supervision as student assistants during my time at TFT: Simone Knaus, Sandro Spiegel, Jaroslav Knack, Christian Wachsmann, Christopher Dörrer, Andreas Altvater, Cedric Großelindemann, Kilian Adams, Oliver Dobler, Sarah Stolz, Florian Karg, Andreas Albrecht, Jella Kramer, David Burger, Johannes Fladerer, Narigul Khamzaeva, Thomas Renaldy, Sabine Mizera, Luisa Eymann, Ulf Garbe, Alimohammad Eghbalpoor and Victor Zaghini Francesconi.

I want to acknowledge the financial support during my early years of research from the Federal Ministry of Education and Research (Bundesministerium für Bildung und Forschung, BMBF) project HighEnergy (grant number 03XP0073B), HiStructures (grant number 03XP0243C), and the German Research Foundation (Deutsche Forschungsgemeinschaft, DFG, grant number 1266/9-3). This work also contributes to the research performed at the Center for Electrochemical Energy Storage Ulm-Karlsruhe (CELEST). My thanks also goes to the KIT-Publication Fund of the Karlsruhe Institute of Technology (KIT) for the partial funding of several of my scientific publications.

Finally, I want to thank all my friends and family members for supporting me with and distracting me from all work-related issues during all ups and downs accompanying my five years of PhD work. I especially want to thank Nils for being there for me with unwavering faith and unconditional support. Thank you.

Karlsruhe, August 2022

Jana Kumberg

Kurzfassung

Die Eigenschaften von Batterieelektroden werden durch die beim Trocknen eingestellten Prozessparameter beeinflusst. Diese wirken sich nicht nur auf die mechanischen Eigenschaften der Elektroden aus, sondern auch auf ihre Leistung in der gesamten Zelle. Dies liegt an der Mikrostruktur der Elektrode, die sich beim Trocknen bildet. Binder und andere Zusätze wie Leitruss werden durch den Kapillartransport des Lösungsmittels an die Oberfläche der Elektrode transportiert. Die Menge des Binder, die sich dort ansammelt, hängt von den Trocknungsbedingungen ab.

Die Trocknung dickerer Elektroden und ihr Zusammenhang mit dem Bindertransport wurde bisher nicht untersucht. Daher wurde in dieser Arbeit eine detaillierte Untersuchung der Auswirkungen der Trocknung auf die Eigenschaften von Batterieelektroden verschiedener Dicken durchgeführt. Es wurde gezeigt, dass die Bindermigration während der Trocknung bei Elektroden mit hoher Kapazität stärker ausgeprägt ist als bei Elektroden nach dem Stand der Technik, wobei beide von einer Erhöhung der Trocknungsrate betroffen sind. Bessere Haftungseigenschaften können bei gleicher Trocknungsgeschwindigkeit durch eine erhöhte Temperatur anstelle eines erhöhten Wärmeübergangskoeffizienten erreicht werden, doch bleibt der Einfluss begrenzt. Laser-induced breakdown spectroscopy konnte die Akkumulation des CMC-Binders an der Elektrodenoberfläche bei erhöhter Trocknungsrate nachweisen. In Zelltests mit dünnen und dicken Elektroden wurden für die langsamer getrockneten Elektroden höhere Entladekapazitäten, insbesondere im Vergleich bei höheren C-Raten von bis zu 3C, erreicht.

Zur Herstellung optimierter Elektroden ist es daher notwendig, den Trocknungsprozess im Detail zu verstehen, um dann Prozessalternativen vorschlagen zu können. In dieser Arbeit wird daher der Trocknungsprozess von Anoden für Lithium-Ionen-Batterien experimentell untersucht und mit Trocknungssimulationen verglichen. Sowohl der zeitliche Verlauf der Lösemittelbeladung als auch der Filmtemperatur wurden für unterschiedliche Elektrodendicken untersucht. Der Versuchsaufbau besteht aus einem stationären Konvektionstrockner (dem

sogenannten Comb Nozzle Trockner) und einer Einheit zur Messung gravimetrischer Trocknungsverlaufskurven.

Die Validierung der Trocknungssimulation wurde zunächst für dünne Elektroden durchgeführt. Das Simulationsmodell basiert auf Massen- und Energiebilanzen um den gesamten Elektrodenfilm und berücksichtigt auch die Kinetik des Massen- und Wärmeübergangs. Eine Abschätzung der Transportgrößen innerhalb und außerhalb des Films rechtfertigte die Annahme einer rein gasdominierten Trocknung im Modell bei der Berechnung des Trocknungsprozesses von dünnen Elektroden. Anhand von in-situ Temperaturmessungen der gesamten Folie mit einer Infrarotkamera wurde die Notwendigkeit der Berücksichtigung lokaler Wärmeübergangskoeffizienten nachgewiesen. Diese führen zu lateral messbaren Temperaturgradienten innerhalb der Folie aufgrund lokal unterschiedlicher Trocknungsraten im Film. Entsprechend wurde eine Simulation einer konstanten Trocknungsrate während der Trocknung um den lokalen Wärmeübergangskoeffizienten zu einem Modell unter Berücksichtigung lateraler Effekte erweitert. Sowohl die Simulation bei konstanter Trocknungsrate als auch diejenige mit lateraler Verteilung zeigten eine sehr gute Übereinstimmung zwischen Experiment und Simulation für dünne Elektrodenfilme. Die Simulation mit lateraler Verteilung des Wärmeübergangskoeffizienten konnte dabei eine bessere Vorhersage des Temperaturprofils liefern.

Eine Abschätzung der Transportgrößen deutete insbesondere für dickere Elektroden auf einen erhöhten Einfluss eines Widerstandes innerhalb des Films hin. Die experimentelle Beobachtung der Elektrodenunterseite während der Trocknung zeigte, dass sowohl bei dünnen als auch bei dickeren Elektroden ein signifikanter Kapillartransport des Lösungsmittels vorliegt. Es wurde ein kapillarer Durchbruch zur Elektrodenunterseite beobachtet, der bereits vor dem Ende der Filmschrumpfung stattfand. Bei dickeren Elektroden fand im Gegensatz zu den dünnen Elektrodenschichten allerdings eine deutlich unregelmäßige Porenentleerung statt. Mit zunehmender Schichtdicke fanden sich auf der Elektrodenunterseite zunehmend Cluster aus trockenen und lösungsmittelgefüllten Poren nebeneinander. Diese Beobachtung zeigt deutlich, dass ein Teil des Lösungsmittels durch kapillare Feuchtigkeitsleitung zur Oberseite der Elektrode transportiert wird. Ein anderer Teil wird vom Kapillarnetz getrennt und im Porenraum der Elektrode verdunsten und durch die Porenstruktur der Elektrode diffundieren und sich in einer Verlangsamung der Trocknungsrate niederschlagen.

Experimentell aufgezeichnete gravimetrische Trocknungskurven hin zu dickeren Elektroden bestätigten, dass eine Verringerung der Trocknungsrate ab dem Ende der Filmschrumpfung auftritt. Im Simulationsmodell wird dies mit dem Modell des wandernden Trockenspiegels berücksichtigt, welches einen Grenzfall ohne kapillare Feuchteleitung darstellt. Die experimentellen und simulierten Daten zeigen dennoch eine gute Übereinstimmung. Damit wurde ein hinreichend genaues Modell etabliert, das auch eine Übertragung auf die industrielle Trocknung von Batterieelektroden erlaubt.

Die Trocknungsrate bei der Elektrodentrocknung könnte durch ein verbessertes Prozessverständnis und eine verbesserte Prozesssteuerung erhöht werden, wäre aber durch die bereits bei geringen bis moderaten Trocknungsraten stattfindende Bindermigration noch immer begrenzt. Aus diesem Grund wurde nach zusätzlichen Konzepten geforscht, um der Bindermigration entgegenzuwirken.

Die Wechselwirkung zwischen Elektrodenpaste und Trocknung und die daraus resultierende Mikrostruktur wurde näher untersucht. Ziel war es, einerseits ein Verständnis für die grundlegenden Zusammenhänge aufzubauen und andererseits optimierte Pasten mit tendenziell geringerer Bindermigration abzuleiten.

Eine Variation der bisher verwendeten Referenzpaste wurde durchgeführt. Dabei wurden der Wirkstoff, das Mischverfahren und die Additivanteile innerhalb der Pasten variiert. Anhand von Kryo-BIB-REM-Aufnahmen wurde der Einfluss der verschiedenen Prozessparameter auf das gebildete Netzwerk innerhalb der feuchten Paste aufgezeigt. Diese zeigten, dass sich das intrinsische Netzwerk zwischen aktiven Partikeln und Bindern in den vier untersuchten Pasten stark unterscheidet. Das gebildete Netzwerk konnte wiederum mit der Haftkraft der Elektroden an der Ableiterfolie und der Neigung zur Bindermigration korreliert werden. So konnten auch bei hohen Trocknungsgeschwindigkeiten Elektroden mit erhöhter Haftkraft hergestellt werden. Bei den Zellen, die aus den Elektroden mit verbesserter Haftkraft hergestellt wurden, wurde jedoch keine konstante oder gar verbesserte Zellleistung erzielt. Die beste Leistung wurde bei den Elektroden mit stark reduziertem Bindemittelgehalt aber entsprechend geringer Haftkraft festgestellt.

Da eine ausreichende Haftkraft für die industrielle Handhabung von Elektroden notwendig ist, eine Reduzierung des Bindemittels aber zu einer verbesserten Zellleistung führt, stellen hierarchisch strukturierte Multilagen einen

Kompromiss zwischen diesen gegensätzlichen Anforderungen dar: Die Kombination einer haftungsoptimierten unteren Lage mit einer bindemittelreduzierten oberen Lage als mögliche Lösung für diesen Konflikt war Ausgangspunkt der Hypothese. Multilagen, die auf diesem Konzept basieren, zeigten im Vergleich zu einschichtigen Elektroden vielversprechende mechanische und elektrochemische Eigenschaften. Eine ausgewählte Kombination von zwei Pasten in einer Mehrschichtelektrode zeigte auch bei ca. zehnfach höherer Trocknungsrate sehr gute mechanische und elektrochemische Eigenschaften in der Vollzelle.

Mit diesem neuen Konzept zeigen auch hochkapazitive Elektroden zeigten verbesserte Entladekapazitäten gegenüber einlagig beschichteten Elektroden. Die Limitierung der Lithium-Diffusion ab C-Raten von ca. C/2 überlagert dabei allerdings den positiven Einfluss, der durch das Multilagen-Konzept erreicht wird. Insbesondere für die Herstellung hochkapazitiver Elektroden sind daher zusätzliche Konzepte notwendig.

Abstract

The properties of battery electrodes are influenced by the process parameters set during drying. These affect not only the mechanical properties of the electrodes, but also their performance in the entire cell. This is due to the microstructure of the electrode that is formed during drying. Binder and other additives such as conductive carbon black are transported to the surface of the electrode by the capillary transport of the solvent. The amount of binder that accumulates there depends on the drying conditions.

The drying of thicker electrodes and its relation to binder transport has not been studied so far. Therefore, in this work, a detailed study of the effects of drying on the properties of battery electrodes of different thicknesses was carried out. It was shown that binder migration during drying is more pronounced for high-capacity electrodes than for state-of-the-art electrodes, with both affected by an increase in drying rate. Better adhesion properties can be achieved at the same drying rate by increasing the temperature instead of increasing the heat transfer coefficient, but the effect remains limited. Laser-induced breakdown spectroscopy could demonstrate the accumulation of the binder CMC on the electrode surface at increased drying rate. In cell tests with thin and thick electrodes, higher discharge capacities were obtained for the slower dried electrodes, especially in comparison at higher C rates of up to 3C.

To produce optimized electrodes, it is therefore necessary to understand the drying process in detail in order to then propose process alternatives. In this work, the drying process of anodes for lithium-ion batteries is therefore investigated experimentally and compared with drying simulations. Both the time course of the solvent loading and the film temperature were investigated for different electrode thicknesses. The experimental setup consists of a stationary convection dryer (the so-called Comb Nozzle dryer) and a unit for measuring gravimetric drying curves.

The validation of the drying simulation was first performed for thin electrodes. The simulation model is based on mass and energy balances around the entire electrode film and also considers the kinetics of mass and heat transfer. An

estimation of the transport quantities inside and outside the film justified the assumption of a purely gas-dominated drying in the model when calculating the drying process of thin electrodes. Using in-situ temperature measurements of the entire film with an infrared camera, the need to consider local heat transfer coefficients was demonstrated. These lead to laterally measurable temperature gradients within the film due to locally different drying rates in the film. Accordingly, a simulation of a constant drying rate during drying was extended by the local heat transfer coefficient to a model considering lateral effects. Both the simulation with constant drying rate and the one with lateral distribution showed very good agreement between experiment and simulation for thin electrode films. The simulation with lateral distribution of the heat transfer coefficient could provide a better prediction of the temperature profile.

An estimation of the transport variables indicated an increased influence of a resistance within the film, especially for thicker electrodes. Experimental observation of the underside of the electrode during drying showed that there was significant capillary transport of the solvent for both thin and thicker electrodes. Capillary breakthrough to the underside of the electrode was observed to occur prior to the end of film shrinkage. However, for thicker electrodes, in contrast to the thin electrode films, a distinctly irregular pore emptying occurred. With increasing film thickness, clusters of dry and solvent-filled pores were increasingly found side by side on the underside of the electrode. This observation clearly shows that part of the solvent is transported to the top of the electrode by capillary moisture conduction. Another part is separated from the capillary network and evaporates in the pore space of the electrode and diffuses through the pore structure of the electrode and is reflected in a slowdown of the drying rate.

Experimentally recorded gravimetric drying curves towards thicker electrodes confirmed that a reduction in drying rate occurs from the end of film shrinkage. In the simulation model, this is accounted for with the moving drying front model, which represents a limiting case without capillary moisture conduction. Nevertheless, the experimental and simulated data show good agreement. Thus, a sufficiently accurate model has been established, which also allows transfer to industrial drying of battery electrodes.

The drying rate in electrode drying could be increased by improved process understanding and control, but would still be limited by the binder migration that

already occurs at low to moderate drying rates. For this reason, additional concepts were researched to counteract binder migration.

The interaction between electrode slurry and drying and the resulting microstructure was investigated in more detail. The aim was, on the one hand, to build up an understanding of the fundamental relationships and, on the other hand, to derive optimized slurries with a tendency towards lower binder migration.

A variation of the previously used reference slurry was carried out. The active material, the mixing process and the additive proportions within the slurries were varied. Cryo-BIB SEM images were used to show the influence of the different process parameters on the network formed within the wet slurry. These showed that the intrinsic network between active particles and binders differed greatly in the four slurries studied. The network formed could in turn be correlated with the adhesive force of the electrodes to the current collector and the tendency to binder migration. Thus, electrodes with increased adhesive force could be produced even at high drying rates. However, cells prepared from the electrodes with improved adhesion force did not show consistent or even improved cell performance. The best performance was found for the electrodes with greatly reduced binder content but correspondingly low adhesion force.

Since sufficient adhesive force is necessary for industrial handling of electrodes, but a reduction in binder leads to improved cell performance, hierarchically structured multilayers represent a compromise between these conflicting requirements: The combination of an adhesion-optimized bottom layer with a binder-reduced top layer as a possible solution to this conflict was the starting point of the hypothesis. Multilayers based on this concept showed promising mechanical and electrochemical properties compared to single-layer electrodes. A selected combination of two pastes in a multilayer electrode showed very good mechanical and electrochemical properties in the full cell even at about ten times higher drying rate.

With this new concept, even high-capacity electrodes showed improved discharge capacities compared to single layer coated electrodes. However, the limitation of lithium diffusion from C-rates of about C/2 overrides the positive influence achieved by the multilayer concept. Additional concepts are therefore necessary, especially for the production of high-capacity electrodes.

Table of Contents

Preface ..... **iv**

Kurzfassung ..... **vii**

Abstract ..... **xi**

Table of Contents ..... **xiv**

Symbols & Abbreviations ..... **xviii**

1. Introduction **1**
- 1.1 Motivation 1
- 1.2 Electrode Fabrication and State of the Art 2
- 1.3 Electrode Drying 6
- 1.4 Aim of this Work 12

2. Material and Methods **17**
- 2.1 Materials and Composition 17
- 2.2 Electrode Processing 19
  - 2.2.1 Mixing Process 19
  - 2.2.2 Coating Process 21
  - 2.2.3 Drying Process 21
- 2.3 Analytics 27
  - 2.3.1 Structural Properties of the Slurry 27
  - 2.3.2 Rheological Properties of the Slurry 28
  - 2.3.3 Mechanical Properties of the Dry Electrodes 33
  - 2.3.4 Structural Properties of the Dry Electrodes 34
  - 2.3.5 Electrical Properties of the Dry Electrodes 36
  - 2.3.6 Electrochemical Properties of the Cells 37

3. Drying of Thicker Electrodes **39**
- 3.1 Motivation and State of the Art 39
- 3.2 Experimental Setup 40
- 3.3 Results and Discussion 41
  - 3.3.1 Binder Migration 42
  - 3.3.2 Electrochemical Properties 55

4. Drying Behavior of Thicker Electrodes 59
4.1 Motivation and State of the Art 59
4.2 Experimental Setup 62
4.2.1 Gravimetric Setup 63
4.2.2 Infrared Camera (IR) Measurements 67
4.2.3 Digital Microscope Measurements 68
4.3 Simulation of Drying Curves 69
4.3.1 Constant Rate Model Simulation for Electrode Drying 69
4.3.2 Lateral Simulation Model for Electrode Drying 80
4.3.3 Moving Drying Front Model for Electrode Drying 83
4.4 Results and Discussion 85
4.4.1 Experimental Drying of Thinner Electrodes 86
4.4.2 Simulated Drying of Thinner Electrodes 92
4.4.3 Experimental Drying of Thicker Electrodes 99
4.4.4 Simulated Drying of Thicker Electrodes 109
4.4.5 Simulated Electrode Drying with a 3-Zone Dryer Concept 114

5. Influence of Slurry Properties 117
5.1 Motivation and State of the Art 117
5.2 Experimental Setup 118
5.3 Results and Discussion 122
5.3.1 Properties of the Wet Slurry 122
5.3.2 Properties of the Dry Electrode 128
5.3.3 Electrochemical Performance 135

6. Simultaneously Coated and Hierarchically Structured Multilayers 142
6.1 Motivation and State of the Art 142
6.2 Experimental Setup 144
6.3 Results and Discussion 145
6.3.1 Properties of the Dry Multilayer Electrodes 146
6.3.2 Electrochemical Performance of the Multilayer Electrodes 150
6.3.3 Extreme Drying Rates during Drying of Hierarchically Structured Electrodes 153

7. Summary and Outlook 158
7.1 Drying of Thicker Electrodes 159
7.2 Drying Behavior of Thicker Electrodes 160
7.3 Influence of Slurry Properties 162

7.4 Simultaneously Coated and Hierarchically Structured Multilayers 164
7.5 Outlook ... 166

References ... 169

List of Figures ... 179

List of Tables ... 201

Appendix ... 205
A Further Detailed Results of the Mixing Process ... 205
A.1 Dissolver ... 205
A.2 Kneader ... 206
B Further Detailed Results of Slurry Properties ... 208
B.1 Dynamic viscosity under CMC variation ... 208
B.2 Sedimentation under CMC variation ... 211
A.1 Dynamic viscosity of slurry (R), (S), (K) and (A) ... 212
B.3 SBR particle distribution ... 213
B.4 Further Cryo-BIB-SEM micrographs ... 214
C Further Detailed Results of Electrode Drying ... 219
C.1 Isothermal vs. non-isothermal drying ... 219
C.2 Estimation of the Biot Number and Capillary Drying ... 222
C.3 Drying Patterns at the Comb Nozzle Dryer ... 224
C.4 Dew Point Measurement ... 226
C.5 Simulation Model Optimization ... 227
C.6 Further Methods to Determine Drying Curves ... 231
D Further Detailed Results of Single Layer Electrodes ... 234
D.1 Comparison of Different Substrate Foils ... 235
D.2 Porosity of dry electrode layers ... 236
D.3 Cracking of the Reference Electrode during Drying ... 240
D.4 Cracking of slurry (R), (S), (K) and (A) in comparison ... 246
D.5 Variation of heat transfer coefficient during drying of slurry (K) ... 248
D.6 Binder migration of slurry (K) ... 249
D.7 90° Peeltest of a flat and an inclined layer ... 252
D.8 Setup for pull-off test ... 252
D.9 Electrical conductivity ... 254
D.10 Properties for electrochemical tests ... 255
D.11 Comparison of pouch and coin cells ... 256

E Further Detailed Results of Multilayer Electrodes 258
E.1 Simultaneous Coating of Multilayers 258
E.2 Drying of Simultaneous Multilayers 260

Symbols & Abbreviations

Latin Letters

Symbol	Unit	
A_{film}	m²	Film area
$\bar{A}$	-	Relative surface fraction
a_s	-	Solvent activity
$B(T_{m,b})$	K^{-1}	Thermal expansion coefficient
c_A	mAh cm^{-2}	Area capacity
c_p	J kg^{-1} K^{-1}	Heat capacity
C_{12}	W m^{-2} K^{-4}	Radiation exchange number
c_i	-	Concentration of component i
d_{50}	µm	Particle diameter at 50 % in the cumulative distribution
d	m	Diameter
F	N	Force
G^*	Pa	Complex shear modulus
G'	Pa	Storage modulus
G''	Pa	Loss modulus
g	m s^{-2}	Gravitational acceleration
h	m	Height
h_{el}	m	Electrode height
H_{film}	J	Enthalpy of the film
Δh_v	J kg^{-1}	Enthalpy of evaporation
$\dot{H}_S$	J s^{-1}	Enthalpy flux of solvent
K_c	-	Consolidation factor
K_A	-	Ackermann correction factor

Symbol	Unit	
K_{St}	-	Stefan correction factor
k	-	Fit parameter for BET model
l_c	m	Characteristic length
$\dot{M}_s$	kg s^{-1}	Mass flux of solvent
$\widetilde{M}_s$	kg mol^{-1}	Molar mass
$\dot{m}$	g m^{-2} s^{-1}	Specific drying rate
$\dot{M}$	kg s^{-1}	Mass flux
M	kg	Mass
m	g m^{-2}	Area weight
n_{mix}	rpm	Rotation speed during mixing
Na	-	Sodium
p_i^*	bar	Vapor pressure component i
p_i	Bar	Partial pressure component i
p	bar	Pressure
p_c	bar	Capillary pressure
$\dot{Q}_{dryer}$	W	Heat flux from the dryer to the film
$\dot{q}$	W m^{-2}	Specific heat flux
$\dot{Q}_{top}$	W	Heat flux at the top of the film
q_3	nm^{-1}	Density distribution
Q_3	-	Cumulative density distribution
R	Ω	Resistance
r	m	Radius
s	m	Deflection
$s(t)$	m	Distance from surface of moving drying front to surface of the electrode
t	s	Time
T	°C	Temperature
t_{mix}	min	Mixing time

Symbol	Unit	
T_{dryer}	°C	Dryer temperature
T_{film}	°C	Film temperature
t_{EOF}	s	Time of theoretical end of film shrinkage
$t_{first\ pore}$	s	Time of first observed pore at the electrode bottom
U_R	V	Current
U_{23}	V	Voltage between 2 and 3
u_{diff}	m s^{-1}	Diffusion velocity
u_{evap}	m s^{-1}	Evaporation rate
u_{sed}	m s^{-1}	Sedimentation speed
v	m s^{-1}	Velocity
w	W m^{-2} K^{-1}	Width parameter gauss curve
X	g g^{-1}	Solvent loading
$X_{S,EOF}$	g g^{-1}	Solvent loading (End Of Film shrinkage)
X_m	g g^{-1}	Fit parameter for BET model
x_c	W m^{-2} K^{-1}	Peak parameter gauss curve
y	m	Position in y direction
$\tilde{y}_{s,ph}$	-	Molar fraction of solvent at the phase boundary
$\tilde{y}_{s,g}$	-	Molar fraction of solvent in the gas phase
y_0	(W m^{-2} K^{-1})$^{-1}$	Offset of the gauss distribution
z	-	Fit parameter for BET model

Greek Letters

Symbol	Unit	
α_{bottom}	W m^{-2} K^{-1}	Heat transfer coefficient at the bottom of the film
α_{top}	W m^{-2} K^{-1}	Heat transfer coefficient at the top of the film
α_{TLC}	W m^{-2} K^{-1}	Heat transfer coefficient derived from the TLC measurement
α_{linreg}	W m^{-2} K^{-1}	Heat transfer coefficient derived from linear regression
$\beta_{s,air}$	m s^{-1}	Mass transfer coefficient at film surface
γ_A	%	Deformation amplitude
$\dot{\gamma}$	s^{-1}	Shear rate
δ	°	Phase shift angle
$\delta_{s,j}$	m² s^{-1}	Diffusion coefficient of solvent in medium j
ε	-	Porosity
ϵ	-	Emission coefficient
η	Pa s	Dynamic viscosity
η_0	Pa s	Zero-shear viscosity
θ	°	Contact angle
κ	m² s^{-1}	Thermal diffusivity
λ	W m^{-1} K^{-1}	Heat conductivity
ν	m² s^{-1}	Kinematic viscosity
$\tilde{\rho}$	mol m^{-3}	Molar density
ρ_i	kg m^{-3}	Density of component i
σ	W m^{-2} K^{-4}	Stefan Boltzmann constant
σ_s	mN m^{-1}	Surface tension of solvent
σ	S m^{-1}	Electrical conductivity
τ	K	Dew point

Symbol	Unit	
τ	Pa	Shear stress
φ	°	Angle
φ_i	-	Volume fraction component i
ω	s^{-1}	Angular frequency

Subscripts

0	Reference conditions or time at the beginning of drying
air	Air property
$Bottom$	From the bottom
c	Convection
dry	Property of dry film or time at the end of drying
$dryer$	Property at the dryer
el	Dry electrode
Eff	Effective property
EOF	Time or solvent loading at the end of film shrinkage
Exp	Experimental value
Fc	Free convection
$film$	Film (dry electrode and solvent) property
g	Property in the gas phase
i	Property of component i
m	Medium value between phase boundary and gas phase
max	Maximum value
min	Minimum value
$Overall$	Radiation and convection
ph	Property at the phase boundary
r	Radiation
rcp	Random closest packing
S	Solvent

$Theo$	Theoretical value
Top	From the top

Dimensionless Numbers

Bi	Biot number of heat transfer
Bi’	Biot number of mass transfer
Le_i	Lewis number of component i
Nu	Nusselt number
Pr	Prandtl number
Ra	Rayleigh number
Sc_i	Schmidt number of component i

Abbreviations

A	Additive-reduced
BC	Batch Coater
BET	Brunauer-Emmett-Teller model
C	Carbon
CMC	Carboxymethyl cellulose
CN	Comb Nozzle
Cryo-BIB-SEM	Cryogenic broad ion beam scanning electron microscopy
Cu	Copper
DS	Substitution degree
DSBB	Disodium 4,4‘-bis(2-sulfonatostyryl)-biphenyl
EC	Ethylene carbonate
EDS	Energy-dispersive X-ray spectroscopy
EMC	Ethyl methyl carbonate
EOF	End of Film shrinkage
f1	Copper foil 1

f2	Copper foil 2
f3	Copper foil 3
HDR	Higher Drying Rate
HE	High Energy
IAM-AWP	Institut für Angewandte Materialien - Angewandte Werkstoffphysik
IMRS	Inverse Micro Raman Spectroscopy
IR	Infrared
K	Kneader
KIT	Karlsruhe Institute of Technology
LCO	$LiCoO_2$: lithium cobalt oxide
LDR	Low Drying Rate
LFP	Lithium iron phosphate
LIB	Lithium-ion battery
LIBS	Laser-Induced Breakdown Spectroscopy
LiPF6	Lithium hexafluorophosphate
LMS, LMO	$LiMn_2O_4$: lithium manganese oxide spinel
LVE	Linear viscoelastic range
Na	Sodium
NG	Natural graphite
NMC, NCM	$Li(NiCoMn)O_2$: lithium-nickel-cobalt-manganese
NMP	N-Methyl-2-pyrrolidone
O	Oxygen
PET	Polyethylene terephthalate
PO	Polyolefins
PVDF	Polyvinylidene difluoride
R	Reference
S	Spherical
SBR	Styrene-butadiene rubber

SEI	Solid electrolyte interphase
SG	Synthetic graphite
SoA	State of the art
TGA	Thermogravimetric analysis
TLC	Thermochromic liquid crystal
TOF-SIMS	Time of Flight - Secondary Ion Mass Spectrometry
VC	Vinylene carbonate

1. Introduction

1.1 Motivation

With the “Paris Agreement” in 2015, the European Commission decided on reducing global emissions to prevent the global average temperature from increasing above a value of 1.5 °C compared to pre-industrial levels.[1] The „European Green Deal“ followed in 2019 and introduced an action plan with numerous measures to reach the goal of a greenhouse gas neutrality in the European Union until 2050.[2] As a consequence, the Federal Government of Germany passed the climate protection act in 2019 with the ambitious goal to reduce greenhouse gas emission by at least 55 % compared to 1990 until 2030.[3]

One part of the strategy to reach that goal is the promotion of electric vehicles, thus renewing the transport sector that accounts for about 20 % of Germany’s total emission and replacing internal combustion engines with seven to ten million new electric vehicles.[4] Another aspect the German government targets are investments into renewable energies as to enable a share of 65 % of renewable energies of the total consumption up to 2030.[3] Both strategies highly depend on efficient energy storage systems. The energy sector requires solutions for energy storage due to the fluctuations in available wind and solar energy, the transport sector due to consumers who expect long driving ranges, fast charging rates and high peak powers.

The battery system which meets all these requirements best until today are lithium-ion batteries. They unite high energy with high power density. Their adaption in the mass market though is still limited by the costs of electric vehicles, with 35 % of the total EV costs being incurred by the battery pack.[5] 75 % of the battery costs are manufacturing costs with about 40 % of these being related to the material.[6,7] An efficient utilization of these materials is mandatory to improve battery performance and to reduce prices. One approach to reduce the manufacturing costs is increasing the energy density of the electrodes and improving cell production in terms of improved yield rates and faster processing times.[5,6,8]

Increasing the electrodes thickness can lead to a gain in the volumetric energy density of up to 17% by increasing the ratio between active to inactive components and saving current collector materials such as copper and aluminum.. The active material percentage in an electrode stack can be improved from about 78 % to 95 % by increasing the electrodes thickness by a factor of three. This can reduce cell costs by about 12 % making the processing of electrodes of increased thickness very attractive.[9] With an increase of the electrode thickness, the fabrication steps need to be reevaluated though, since new challenges might evolve.

The process chain for lithium-ion battery manufacturing consists of a chain of consecutive process steps. It starts with the slurry mixing, followed by coating and drying of the electrodes and their further processing to build the final cell. Critical processing steps where the electrode thickness starts to play a role start with the coating, followed by the drying step.

Drying was shown to be a critical step aleady for thin electrodes. Higher drying rates were shown to be the cause of a deterioration of the cell performance.[10] This can be attributed to inhomogeneously distributed additives like binder or conductive agents within the electrodes microstructure, which forms during drying.[10–13] The electrode manufacturing process, in terms of the coating and drying step, thus directly affects the cell performance. This brings new challenges to electrode manufacturing, which is especially true when processing thicker electrodes.[14] To gain electrodes with a more homogenous distribution of the additives, the drying step and its influences have to be studied and understood in detail.

1.2 Electrode Fabrication and State of the Art

Lithium-Ion Batteries (LIB) are rechargeable electrochemical storage systems. Their working principle is based on lithium ions which intercalate between the active materials on the negative and positive electrode during charging and discharging of the battery. The schematic of a lithium-ion battery with a liquid electrolyte is shown in Figure 1.1. A separator is located between the electrodes, electrically isolating them while allowing lithium ions to pass through in both directions. An ion-conducting liquid electrolyte containing a lithium conducting salt surrounds the active material particles. To enable an electric pathway, the

active material particles are positioned as a film on metal foil current collectors. Typically for the cathode, aluminum foil with a thickness between 12 - 20 µm and on the anode side two times thinner copper foil with about 6 - 10 µm thickness is used in industry and this study.[6,15]

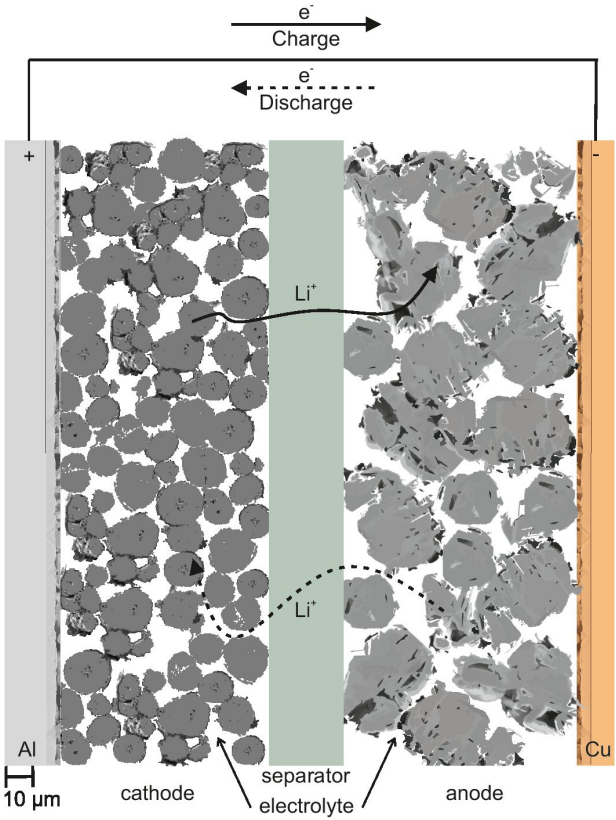

Figure 1.1: Schematic picture of a typical liquid-electrolyte-based lithium-ion battery. During discharge, the lithium ions diffuse in the electrolyte from anode to cathode, inducing an external electron flow. For charging, the process is reversed.

During discharge, the lithium ions diffuse in the electrolyte from anode to cathode, inducing an external electron flow. The ions intercalate into the active material of the cathode. For charging, the process is reversed. The microstructure of both electrodes, e.g. porosity and tortuosity is important for the diffusion and

intercalation of lithium ions through that structure and the microstructure with its electrical and mechanical properties impacts the performance of the cell. The structure must have a sufficient interconnection between particles and conductive agents as a path for electrons as well as a sufficient pore volume for diffusion of lithium ions in the electrolyte.[15]

The positive electrode, the cathode, typically consists of metal oxides with the four most common active materials being: lithium cobalt oxide (LCO or $LiCoO_2$ as chemical formula), lithium manganese oxide spinel (LMS, LMO or $LiMn_2O_4$ as chemical formula), lithium-nickel-manganese-cobalt (NMC or $Li(NiCoMn)O_2$ as chemical formula) and lithium iron phosphate (LFP or $LiFePO_4$ as chemical formula). NMC cathodes so far represent the most successful compromise of a high specific energy density, cycle life and costs. NMC cathode materials, with the original ratio of nickel, cobalt and manganese being identical, are referred to as NMC 1:1:1. Research nowadays focuses on nickel rich versions of NMC with the ratios of 5:3:1, 6:2:2 and 8:1:1, where NMC 6:2:2 is already being used in industrial production.[15–17]

The anode material is typically carbon-based with the range going from natural graphite (NG) to synthetic graphite (SG) and hard and soft carbons. To improve anode capacities silicon is added in next generation anodes, due to its very high theoretical capacity of 4200 mAh g^{-1} compared to that of carbon with 372 mAh g^{-1}. A high volume change of silicon during (de-)lithiation is still challenging though regarding mechanical electrode stability.[15–17]

A typical liquid electrolyte contains dissolved LiPF6 (lithium hexafluorophosphate) in a mixture of two or more organic carbonate solvents such as EC (ethylene carbonate) mixed in a mass ratio of 1:1 with EMC (ethyl methyl carbonate). Typically a small amount of VC (vinylene carbonate) of about 2 wt-% is added. Main properties of a good liquid electrolyte are: a good wetting behavior resulting in the formation of a homogenous solid electrolyte interphase (SEI) as a protective layer between the graphite particles and the electrolyte, a high lithium ion conductivity, thermal stability in a wide temperature operation range and an overcharge protection. A good separator has a high ion permeability, a low thickness and sufficient mechanical stability combined with a high thermal stability. These separators are often microporous membranes of non-woven mats or ceramic-

coated separators with the most common type being single- or multilayer separators of polyolefins (PO). Typical thicknesses are in the range of 6 – 20 µm.[16]

The microstructure of the electrodes is determined during the different processing steps. The process chain for coin cell fabrication which was also used throughout this work is depicted in Figure 1.2. It starts with a dry mixing step, followed by wet mixing, coating and drying of the slurry and calendering of the dry electrode. Electrodes are then cut, post dried and assembled to a coin cell. For large scale battery production and pouch cell fabrication, additional process steps are necessary: before formation winding or stacking of the electrode, contacting of the current collectors, insertion and sealing of the battery pack, electrolyte filling, sealing of the pack , press rolling and degassing might be done.[6]

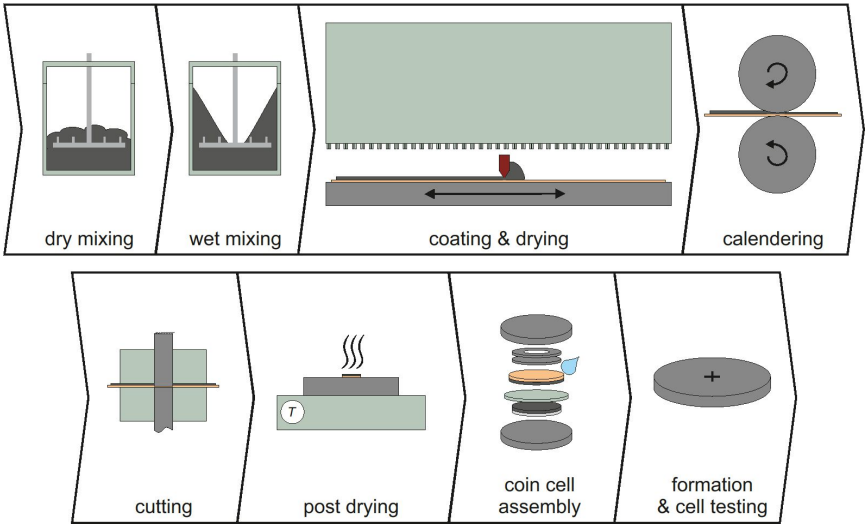

Figure 1.2: Process chain for coin cell fabrication starting with a dry mixing step, followed by wet mixing, coating and drying of the slurry and calendering of the dry electrode. Electrodes are then cut, post dried and assembled to a coin cell together with casing, separator, electrolyte, spring and spacer. The final step consists of formation and cell testing.

The first step in the process chain shown here is the dry mixing of graphite and carbon black to homogenize both materials. It is followed by the wet mixing of the active material, inactive additives like binder and carbon black with the solvent. For the anode, water is commonly used as solvent along with the binder system carboxymethyl cellulose (CMC), which is used as thickening agent, in

combination with styrene-butadiene rubber (SBR) to enhance the adhesion. For the cathode, N-Methyl-2-pyrrolidone (NMP) is the typical solvent with polyvinylidene difluoride (PVDF) as binder. In both electrodes carbon black is used to improve the electrical conductivity.[6] After mixing, the wet slurry is typically coated onto the current collector foil. In industrial scale, the wet electrode film is coated onto the substrate with a slot die. The film continues into the dryer, where the solvent is removed and the microstructure solidifies. The final microstructure is formed when the dry electrode is calendered and the particles are compressed to build a denser network with increased energy density. The electrodes are then cut into the format in dependency of the casing. For cell manufacturing, the electrode is subjected to a second intense drying step to remove remaining sorbed solvent. After post drying of both electrodes they are assembled to the final coin cell together with casing, separator, electrolyte, spring and spacer after which formation and final cell testing is conducted.

Mixing, coating and drying govern the developing microstructure of the dry electrode which influences cell performance.[10,18,19] This work focuses on the influence of drying on the microstructure of thin and thick electrodes. There are still many challenges that remain in relation to electrode drying which will be discussed in the following along with the state of the art of electrode drying.

1.3 Electrode Drying

Due to the possibilities of improving cell performance and reducing cell costs, a lot of research focuses on understanding and describing the drying behavior of electrodes for lithium-ion batteries. The enhancement of drying time offers the possibility of greatly reducing cell costs by increasing the throughput and saving investments for dryer lengths.[8] The coating process itself has been proven to allow for web speeds of 50 m min^{-1} for intermittent coating[20], with the possibility for even higher coating speeds, which was investigated within the research group.[21] Currently, the limiting factor for the production speed is the drying time.

The current status in drying rates in combination with resulting dryer length and drying times of today is calculated and shown in Figure 1.3 under the assumption of industrially relevant process parameters. The calculation is based on an

electrode with a dry area weight of 74 g m^{-2} (2.5 mAh cm^{-2}) with an initial wet film solid content of 43 wt.-% and a wet film thickness of approximately 130 µm with a dry film thickness of about 90 µm. For the estimations and initial calculation, a constant drying rate model was assumed, with an exemplary web speed of 50 m min^{-1}. It shows and anticipates that an increase of the drying rate from the documented current state of the art at approximately 0.75 g m^{-2} s^{-1} after Kwade et al. (2018) marked in red, to the orange marked area is quite promising to reduce dryer length.[6]

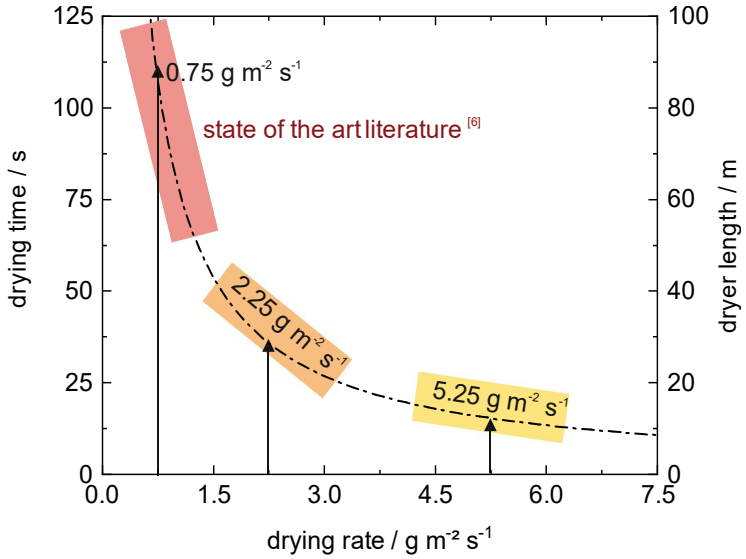

Figure 1.3: Drying time (left) and dryer length (right) in dependency of the drying rate at a typical web speed of 50 m min^{-1}. Both values are calculated for a typical electrode of dry area weight of 74 g m^{-2} (2.5 mAh cm^{-2}) with an initial solid content of 43 %. The red area marks the published state of the art with 1-2 min drying time after Kwade et al. (2018) and therefore the reference drying rate of this work.[6] The orange and yellow areas mark 3 to 7 times higher drying rate ranges, which are aimed to reach in this work and which form an upper limit of drying rates applied in industry in electrode drying. The influence of up to 7 times higher drying rates than the documented state of the art on electrode properties will therefore be investigated.

The aim of this work is to investigate drying rates up to the orange and yellow range which includes the drying rate of 5.25 g m^{-2} s^{-1} which is up to a factor 7 times higher than the published state of the art. From unconfirmed sources it is known that drying rates of even up to 4 g m^{-2} s^{-1} are applied in Asian companies

for industrial electrode drying. Since no published sources are available, the state-of-the-art drying rate after Kwade et al. (2018) is used as reference and as a lower limit for the drying rate in this work.[6] The goal of this research is to clarify the open questions on how higher drying rates can be achieved, what are the limitations and what is the impact on electrode properties as well as what strategies can be followed towards an optimized microstructure. This will be explained in the following. This knowledge gain is to be transferred and applied to drying of thick electrodes.

During electrode drying, the binder and the carbon black, which are present within the wet slurry, have been shown to migrate away from the particle-substrate interface.[10,11,13,18] This results in a loss of adhesion force of the electrode, thus deteriorating the mechanical properties and possibly leading to delamination of the electrode from the current collector and a loss of electrical contact during cell cycling. Correlated with the binder migration a loss in cell performance has been shown.[10,18,22]

To illuminate the dependency between drying rate, adhesion and binder migration in more detail Figure 1.4 by Jaiser et al. (2016), a predecessor in the authors working group at KIT-TFT, is given.[10] In the depicted graph Jaiser et al. (2016) used a NMP-based anode slurry that allowed for the detection of the characteristic fluor-atom of the PVDF binder. [10] The adhesion force was measured for electrodes which were first dried at a high drying rate (HDR) of 1.2 g m^{-2} s^{-1} and after the transition time further dried at a low drying rate (LDR) of 0.5 g m^{-2} s^{-1}. The adhesion force decreased in dependency of the point of transition, whereas a time interval in the beginning was not affected by the high drying rate. This point of time was called first critical point of time ($t_{c,1}$). The adhesion dependency on the transition time was related to the fluor content at the bottom of the electrode, shown on the right y-axis in Figure 1.4. Adhesion and fluor-binder concentration showed good agreement.[10] It was concluded that the adhesion force and the binder migration are closely related and that the adhesion force is thus a measure for the homogeneity of the microstructure in terms of the additive distribution. This is also an assumption in this work. Since only water-based formulations were investigated in this work, which do not possess comparable traceable atoms, a similar experiment could not be repeated.

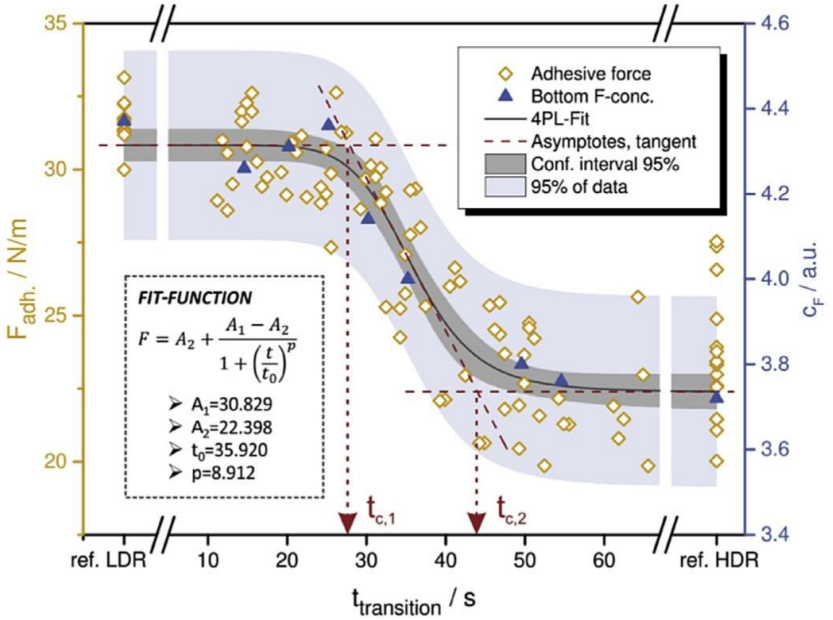

Figure 1.4: Adhesion force in dependency of the drying rate and the transition time chosen to change between the drying rates. The adhesion force is correlated with the fluor content at the electrode bottom and thus the binder content. (Reproduced from Jaiser et al. (2016), predecessor in the authors working group at KIT-TFT, with permission from Elsevier.)[10]

Two insights can be derived from Figure 1.4: First, the microstructure depends on the drying rate and second, the microstructure depends on the point of time at which a high or low drying rate is applied. An explanation as to why the electrode microstructure depends on the drying rate and furthermore on the time a certain drying rate is applied can be given to some extent, when the exact drying mechanism is considered.

In Figure 1.5 a model of how a particulate electrode film dries is given. When the film is coated, the solvent content is so high that the drying can initially be compared to that of pure water. The solvent evaporates at the surface of the wet film (Figure 1.5a) and the film shrinks. At one point and in the ideal case, the particles have reached their most dense network with the End of Film shrinkage (EOF). In an ideal case the solvent further saturates the capillary network (Figure 1.5b).

If the interconnection of the capillary network filled by solvent is sufficient, and a network with a pore radii distribution is present, further drying takes place by capillary transport. The smallest pores remain filled and suck water from larger pores to the surface. Depending on the drying conditions and material system, capillary pore emptying may even start before the end of film shrinkage.[23] Additives within the solvent like the binders and carbon black are dragged along with the solvent through the capillaries to the electrodes surface. In the partly filled network (Figure 1.5c), evaporation still takes place at the surface of the electrode at the menisci of the solvent-filled capillaries. Only if some liquid clusters remain within the electrode without connection to the rest of the network (Figure 1.5d) solvent will evaporate within the microstructure and diffuse to the surface of the electrode. At last, the dry electrode film (Figure 1.5e) with the particle network and a distribution of the additives results.

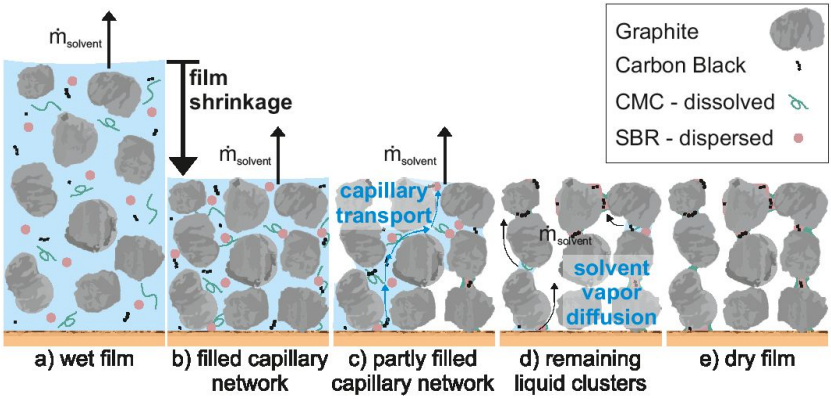

Figure 1.5: Model presentation of the drying behavior of an electrode for lithium-ion batteries. The solvent of the wet film (a) evaporates at the film surface until the EOF, where all capillaries are filled within the network (b). Capillary transport moves the solvent to the electrode surface where it evaporates (c). If remaining liquid clusters exist, solvent evaporates within the particle network and diffuses to the surface (d). The dry electrode film results (e). Figure taken from Kumberg et al., 2019.[24]

A limiting case where no capillary transport would take place, could theoretically be possible: A water front, homogeneously receding into the film. To be able to describe the case when no capillary transport takes place and the water front homogeneously retreats into the porous film the moving drying front model was proposed by Krischer (1956), which considers transport resistances for gaseous solvent within a porous film.[25]

Capillary transport though, being in fact a mechanism during drying of thin electrodes and transporting binder to the electrode surface was shown by cryogenic broad ion beam scanning electron microscope (Cryo-BIB-SEM): Electrode drying was interrupted, and films directly frozen in a nitrogen slush. Cross sections of these films were investigated and capillary pore emptying as well as a developing binder gradient were shown.[26] This capillary transport leads to a prevailing constant drying rate even after the end of film shrinkage, which was shown in an experiment determining a drying curve by taking samples and measuring their residual moisture.[10]

The reason why the drying rate itself influences the binder distribution can be assumed to be caused by different mechanisms. One influence might lie in the drying mechanism and the starting point of capillary pore emptying itself, another might be different drag forces resulting from different drying rates. Binders and carbon black might partly be adsorbed on the active material particles and dragged off by the solvent. The higher the drying rate, the faster the volume flow of water to the surface and thus the drag force the additives are exposed to. Some research has also reasoned with back diffusion of the additives during drying: At a lower drying rate, the time for additives accumulated at the electrodes surface to diffuse back is higher.[10,27] This will be further discussed in this work.

To answer the question why a certain time interval of a high drying rate can be applied without a deterioration of the microstructure, the drying model must be considered. Since capillary transport is thought to be the main mechanism to lead to an inhomogeneous binder distribution, a connection between the first critical time ($t_{c,1}$) and the beginning of pore emptying can be assumed. The end of film shrinkage and the beginning of pore emptying were shown to coincide by Jaiser et al. (2017) for a polyhedral graphite which was also used in the experiment shown in Figure 1.4. The beginning of pore emptying was detected in an experiment using a fluorescent marker to visualize the solvent-filled surface area and the end of film shrinkage was measured by a laser. It was shown that for this material system during the initial drying time when the film shrinks and no capillary pore emptying takes place, no binder migration takes place and high drying rates can be applied. For another spherical graphite and for the higher drying rate of 1.2 g m^{-2} s^{-1}, the start of capillary pore emptying was observed even before the end of film shrinkage.[23] It was therefore concluded, that the beginning of pore emptying is the relevant point of time during electrode drying which is

associated with binder migration. The beginning of pore emptying, and the end of film shrinkage typically coincide but do not have to.

So far, mainly literature has been summarized, on which this work strongly builds and which is the basis of all investigations in the following sections. Of course, there is a great deal of other literature on electrode drying with specific foci. These are addressed at the beginning of each main section with their respective focus.

1.4 Aim of this Work

Based on current literature as summarized in section 1.3 (Electrode Drying), it can be concluded that if the exact drying curve of an electrode can be predicted, an optimized drying profile can be applied in an industrial dryer and a more homogenous binder distribution can be gained. This is challenging and becomes even more so regarding thicker electrodes. In Figure 1.6 a state-of-the-art electrode with a thickness of 75 µm and an area weight of 65 g m^{-2} (2.2 mAh cm^{-2}) is compared to a thick electrode of 300 µm and 275 g m^{-2} (9.3 mAh cm^{-2}). It can be deduced that capillary transport gets more complex when the thickness is increased. It is known from literature that thicker electrodes are more prone to exhibit undesirable binder migration.[11]

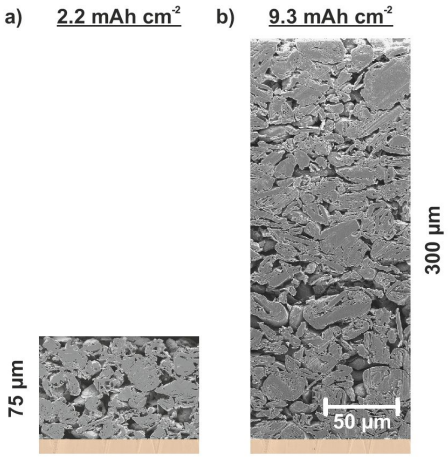

Figure 1.6: SEM micrographs showing the comparison of the cross sections of a thinner state-of-the-art electrode (a, left) and a thicker electrode (b, right). Figure taken from Kumberg et al., 2019.[24]

The goal of this work is to validate or falsify four hypotheses which will be presented in the following. To do so, the effect of binder migration in relation with thinner and thicker electrodes will be investigated in detail and related to the drying process. The *first hypothesis* in this work which will be addressed in section 3 (Drying of Thicker Electrodes) states that, when electrode thickness is increased compared to the state of the art, new challenges arise in relation to drying rate, microstructure formation and binder migration. A more comprehensive discussion of current literature on the subject can be found at the beginning of section 3. Drying-induced binder migration is discussed there in detail. It is assumed that thicker electrodes suffer more severely from binder migration than thinner electrodes. Therefore, process limitations regarding the drying rate are sought to be determined in this section.

The increased film thickness also leads to more complexity concerning the drying mechanism. While it can be assumed that thinner electrodes dry mainly at lower Biot numbers and controlled by the mass transport resistance in the gas phase, thicker electrodes might be subject to solvent transport resistances in the film due to the growing complexity of their microstructure.[10] Different simulation efforts exist on the matter of modelling the drying process of particulate systems. These reach from the consideration of heat and mass transfer to complex

pore-network modelling.[25,28–35] In terms of modelling the drying of battery electrodes only very few works in literature can be found. A detailed discussion on the current status of research follows in the beginning of section 4.[36–38] As far as the author is aware, no attempt has yet been made to model the drying process of thicker electrodes in combination with experimental validation by drying curves.

To develop optimized drying profiles for industrial dryers and for electrodes with an adaptable film thickness, a model with a manageable complexity which considers the boundary conditions would be needed. A drying model considering drying being controlled solely by the gas phase would be less complex than one considering film transport within the porous structure. Pore network modelling in a 3-phase-system would be most complex. In this work a model is developed which is able to describe the drying curve of electrodes of different thicknesses in dependency of different drying conditions. The *second hypothesis* in this work which is the content of section 4 (Drying Behavior of Thicker Electrodes), aims to validate or falsify the question if the drying process of thinner electrodes is governed mainly by the gas phase and if, when thicker electrodes are dried, how the influence of film resistances increases. With drying being assumed to become more challenging for thicker electrodes, the drying process itself will be illuminated to investigate hypothesis (2). A model is sought to be established that allows for simulation of the drying of thin and thick electrodes. With the hypothesis being that while drying of thin electrodes can be described by constant drying kinetics, this does not apply for thicker electrodes due to the increasing complexity of their microstructure. An extended model is used to account for a growing resistance within the film towards solvent transport. The simulation is validated by experiments using a stationary (comb nozzle) dryer, which was modified in this work and which allows for industrially relevant drying rates. The model is exemplarily used to predict the drying course of an electrode in a virtual 3-zone dryer.

Multi-zone drying allows for a faster drying process, while maintaining the properties of the electrodes at the level of an overall slower process. It relies on low drying rates during much of the drying process though. Therefore, there will always be a limit for reducing the drying time. One limiting factor for increasing the drying rate was found to be binder migration, which deteriorates the adhesion force between the current collector and particles as well as the electrochemical

performance.[10] One could consider though whether binder migration could be reduced by changing process parameters other than those from the drying process. One factor could be the interaction between active material particles and the binder as well as the network formed and stabilizing the whole system.

The physicochemical properties of the slurry or materials contained in the slurry, such as particle size (distribution), surface properties, or binder content, could influence the effects of the drying process on the resulting electrode. A lot of studies were dedicated to the binders and their influence on the rheological behavior of the slurry as well as their effect on the electrochemical cell performance.[39–42] The current literature will be addressed in the beginning of section 5. A consideration that has been insufficiently addressed so far to the author's knowledge is the interlink between rheological properties, their impact during drying and on the electrochemical cell performance.

These interrelationships will be investigated in section 5 (Influence of Slurry Properties). The *third hypothesis* of this work, which is reviewed in section 5, is as follows: Drying has different effects on the developing electrode microstructure in dependency of the physicochemical properties of the slurry and the interaction between binder and active material and the formed network. The correlation between material, mixing and drying will be illuminated to investigate hypothesis (3). It is examined whether the physicochemical properties of the slurry impact binder migration. Regarding the slurry, a variation of mixing device, active material and slurry composition is compared with the reference recipe from section 3. Cryo-BIB-SEM pictures of all slurries are correlated with adhesion measurements and cell tests.

Another possibility to enhance electrode properties by homogenizing the binder distribution, would be to apply coating concepts like multilayer electrodes with individual properties in each layer, with the available literature on simultaneous multilayer coatings being discussed in the beginning of section 6.[43–45] This could open up the possibility of drastically increasing the drying rate without degrading the properties of the electrodes. Studies exist in literature addressing the coating process of simultaneous multilayers in detail, but not the drying process. Section 6 (Simultaneously Coated and Hierarchically Structured Multilayers) aims to falsify or validate the *fourth hypothesis* that by multilayer coating and drying and a targeted combination of two layers, optimized electrodes can

be produced at significantly higher drying rates than the current state of the art (SoA). Insights on binder migration and cell performance of multilayers derived from combining slurries from section 5 are used to find an optimum pairing.

To investigate all four hypotheses, different slurries were coated and dried as thinner and thicker electrodes as single or multilayers under defined boundary conditions. Suitable characterization methods need to be found to characterize material, slurry, electrode, and cell. The experimental methods which are used to answer all four hypotheses will be presented in section 2 (Material and Methods). Special experimental or simulative details will be given in the corresponding sections. This applies especially to hypothesis (2), where an experimental setup to measure drying curves of electrodes has to be built which will be presented in section 4.2. Experimental results are supplemented by a simulation model describing the drying process of thin and thick electrodes which is presented in section 4.3 (Simulation of Drying Curves).

The overall goal is a knowledge-based improvement of the drying process of lithium-ion battery anodes, with an emphasis on thick electrodes. The goal is to enable fast drying times while keeping good cell performance to advance battery research and production. A drying time of 1-2 min for state-of-the-art electrodes is used as reference for comparison based on current literature[6].

2. Material and Methods

In this section, the experimental approaches of this work are presented. This includes the process chain from mixing over coating and drying to coin cell fabrication. Analytical methods to evaluate slurry, dry electrode and coin cells are also described.

2.1 Materials and Composition

A reference slurry is used throughout this work with a recipe aimed at processing thick electrodes due to its high content of binders. Deviations from this recipe only appear in section 5 (Influence of Slurry Properties) and section 6 (Simultaneously Coated and Hierarchically Structured Multilayers) dealing with different slurries and multilayers. The respective recipes will be presented in the corresponding section. The reference recipe is comprised of a non-spherical graphite (SMGA, Hitachi Chemical Co. Ltd., Japan) with 93 wt.-% in the dry electrode, a median diameter of $d_{50} = 18.4\,\mu m$ and a theoretical discharge capacity of 360 mAh g^{-1}. The additives used are 1.4 wt.-% carbon black (Super C65, Timcal, Switzerland), 1.87 wt.-% CMC (Sunrose MAC500LC, Nippon Paper industries, Japan) and 3.73 wt.-% SBR (Zeon Europe GmbH, Japan), as listed in Table 2.1. Carbon black is used to improve the electrical conductivity and to improve the rheological properties of the slurry. Is has a median particle diameter (d_{50}) of 32 nm, but forms aggregates with diameters between 100 – 300 nm. These aggregates form agglomerates due to Van-der-Waals forces in the size of a few microns.[46,47] The agglomerates need to be broken down and homogeneously dispersed during the mixing step.[48] CMC is mainly used to enhance slurry properties like viscosity and sedimentation stability. CMC with a substitution degree of 0.67 and a molecular weight of 349 kg mol^{-1} was used in this work. SBR was provided as a dispersion of SBR in water. SBR is used to enhance the cohesion between the particles and the adhesion between particles and current collector. All ingredients summed up to a solid content in the slurry of 43 wt.-%. Throughout this work, three different copper foils were used as substrate. These copper foils have in common that they all had a thickness of approximately 10 µm and

the identical width of 200 mm. Following copper foils were used: The first one is a shiny copper foil (Nippon Foil Mfg. C., Japan) and will be addressed as foil 1 (f1). The second foil will be called (f2) in the following. It is a matte, dendritically deposited foil (Schlenk Metallfolien Gmbh & Co. Kg). The third foil (f3) is a shiny, electrodeposited foil (Civen Metal, China). Since the surface texture impacts the adhesion between the foil and the graphite particles, the foil itself influences the adhesion force. The impact of a change in process conditions like drying rate or electrode area weight on the adhesion force is there, independent of the substrate. Consequently, all results in this work are comparable independently of the copper foil used, as will be further discussed in section 3.

When electrodes which were coated onto two different substrates are being compared, the adhesion force is normalized on the following drying conditions and electrode area weight: For normalization, the adhesion force of the electrode on the substrate was used which was dried at a drying rate of 0.75 g m^{-2} s^{-1} and at a heat transfer coefficient of 35 W m^{-2} K^{-1} and at an area weight of around 60 g m^{-2}. Absolute values and a comparison of the adhesion force of the three substrates can be found in the Appendix in Figure A. 7-22.

Table 2.1: Overview of the composition of the slurry and the dry electrode of the **reference** recipe consisting of graphite (SMGA), carbon black, the binders CMC and SBR and distilled water in case of the wet slurry.

Material	Wet slurry wt.-%	Dry electrode wt.-%
graphite SMGA	40	93
carbon black	0.6	1.4
CMC (binder)	0.8	1.87
SBR (binder)	1.6	3.73
Distilled water	57	-

2.2 Electrode Processing

The devices used in this work for slurry mixing, coating, and drying are presented in this section.

2.2.1 Mixing Process

The main task of mixing is the dispersion of all ingredients with the goal to manufacture a homogenous, stable slurry that can be homogenously coated onto a substrate. The proper dispersion of carbon black agglomerates in terms of size distribution has been shown to be an important property of cathode slurries.[19,49]

Two different mixers used in this work are introduced – dissolver and kneader. The dissolver is used for the reference recipe in section 3 (Drying of Thicker Electrodes) and section 4 (Drying Behavior) with a nominal volume of up to 0.8 l.[50] The second mixer is a kneader with a nominal volume of up to 15 l and was used for the slurry variation at larger scales (section 5) for investigating concepts for improved electrodes by studying the Influence of Slurry Properties.[51]

Dissolver

To mix slurries in laboratory scale, a dissolver (Dispermat CN10, VMA Getzmann, Germany) was used. The vessel with a diameter of 100 mm has a double jacket for cooling and a connection to a vacuum pump. The custom-built toothed dissolver disc which is pictured in Figure 2.1b was designed to enhance vertical transport. It has a diameter of 70 mm and is designed for the small batch volume of 0.5 l. The dissolver disc for the 0.8 l vessel has a diameter of 160 mm. The mixing principle of the dissolver is based on the so-called “doughnut”-effect, which is pictured in Figure 2.1a. A vortex forms, which leads to a high energy input and efficient mixing, since agglomerates are continuously transported to the rotating dissolver disc. Different mechanisms lead to dispersing and grinding of agglomerates. Upstream of the disc’s teeth a pressure builds up. This leads to a negative pressure at the backside and an alternating stress between pressure and suction for the agglomerates. Another factor is the impact effect between dissolver disc and agglomerates, as well as the shear flow caused by the fast-rotating disc.[50] The exact mixing procedure used in this work is explained in the appendix, Figure A. 7-1.

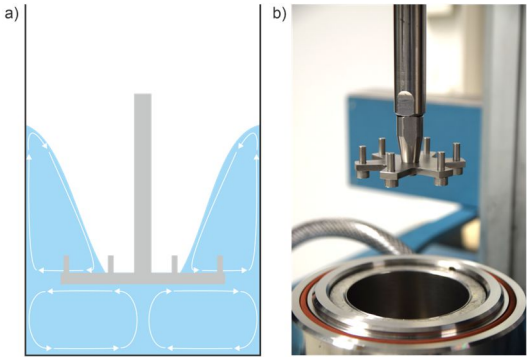

Figure 2.1: Schematic of the flow fields of a dissolver a) and picture of the dissolver disc b) after VMA Getzmann GmbH.[50]

Kneader

To investigate the influence of another mixing device on electrode performance, the kneader Inoue TX-15 (Inoue MFG., Inc., Japan) was used. In this planetary gear mixer three tools rotate around a main axis in the middle (see Figure 2.2).

Figure 2.2: Mixing tool of the kneader Inoue Trimix TX-15 (MVT-VM, KIT).

Furthermore, all three kneading hooks rotate around their own axis. High shear forces are induced between the mixing tools and the vessel.[51] The mixing procedure in the kneader used in this work is described in the appendix, Figure A. 7-2.

2.2.2 Coating Process

In industrial coating typically a slot die coating device is used as a state-of-the-art option for continuous processing.[6] Since electrode films in this work were produced batch-wise with the focus on the influence of drying conditions, in many of the studies in this work the electrode films were fabricated using less complex knife coating. Single layered electrodes for later characterization and cell coin fabrication were processed in the so called "Batch Coater" and the "Comb Nozzle" dryer (see section 2.2.3). Films were batch-wise produced and coated with a film applicator (UA2000.60 or UA2000.100 Proceq, former Zehntner, Switzerland) with a width of 60 mm or 100 mm. A reservoir of the slurry was dosed in front of the coating knife with a syringe and the film was formed either by movement of the knife with a fixed substrate or the other way around with a velocity of 6 m min^{-1}. The film thickness was adjusted by adjusting the gap of the coating knife. To investigate the difference to the industrial coating method "slot die", especially for simultaneously coated multilayers, exemplary films were coated using a slot die to compare results and determine the applicability of the investigated multilayer films for industrial scale. Detailed information and results about this topic can be found in the appendix, Figure A. 7-40 and in current works by Diehm et al.(2020)[43].

2.2.3 Drying Process

For the drying of electrode films two different dryers were used. The first one is the so called "Batch Coater" (BC) with impinging slot air nozzles and the second one the so called "Comb Nozzle" dryer (CN) with a honey-combed nozzle structure and integrated suction of air.

Batch Coater (BC)

The BC consists of a drying and coating unit, with a dryer hood with an array of 20 slot nozzles with adjustable boundary conditions and drying rates similar to industrial dryers. They can be adjusted in a range of the averaged heat transfer coefficient between 35 W m^{-2} K^{-1} and 80 W m^{-2} K^{-1}. More details about the construction are given in former works by Baunach and Jaiser et al.[10,52–54] In this lab scale dryer, a periodic movement of the film enables homogenous drying conditions under the nozzle array. The film is coated on the substrate, which is

fixed on a heating plate by a vacuum groove as is shown in Figure 2.3. The vacuum ensures a smooth substrate and enables a uniform heat flux into the film, since a direct contact between the heating plate, the copper substrate and the film is provided. The heating plate is mounted on top of a linear guide with a stepper motor, controlled by a LabView program. Therefore, an automated drying sequence can be conducted with the drying time or the time of the periodic movement within the dryer chamber adjustable to the wet film thickness. A saturation of the dryer air within the chamber is evaded by spherical-shaped suction nozzles for exhaust air removal, which are positioned at both sides in between all nozzles.

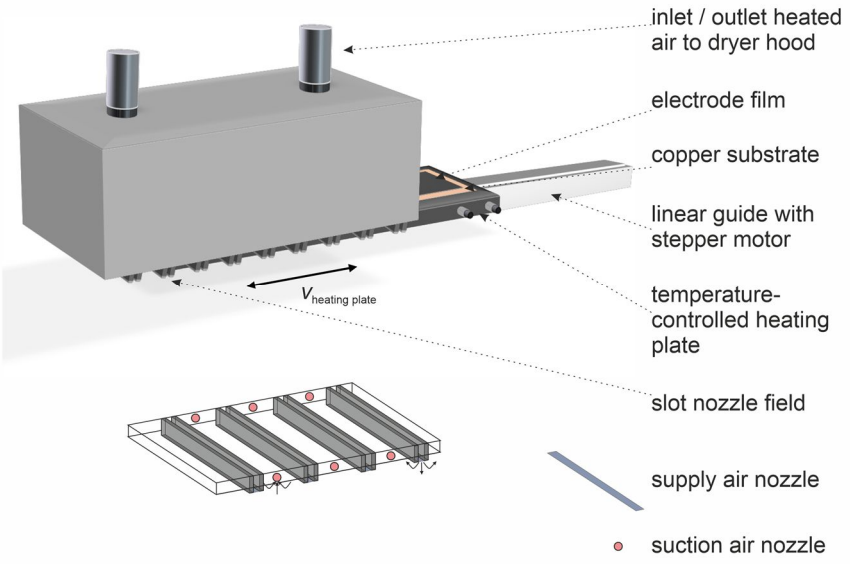

Figure 2.3: Picture of the Batch Coater (BC) used for defined drying of electrode films. The dryer hood has an array of 20 slot nozzles where heat transfer coefficients between 35 W m^{-2} K^{-1} and 80 W m^{-2} K^{-1} can be adjusted. A periodic movement of the film which is fixed on a heating plate enables homogenous drying conditions under the nozzle array. Spherical-shaped suction nozzles for exhaust air removal are positioned at both sides in between the supply air slot nozzles.

In the BC, drying is realized under isothermal drying conditions. A specific drying rate can be adjusted. In the experiments presented in this work, the temperature of the heating plate and dryer in the BC are adjusted to the temperature a film would take as adiabatic wet bulb temperature when dried in a convective roll-2-roll dryer under a predefined drying rate. Due to the high heat flux by

contact, the temperature of the heating plate defines the isothermal drying conditions.

The mass flux of solvent $\dot{M}_s$ during drying in the Batch Coater is mainly dependent on the values shown in equation (2.1).

$$\dot{M}_s = f(T_{wet\ bulb}, \alpha_{top}, \tilde{y}_{s,g}) \tag{2.1}$$

The isothermal drying temperature $T_{wet\ bulb}$ is adjusted and equals the temperature of the dryer and the temperature of the heating plate. The molar fraction of solvent in the gas phase $\tilde{y}_{s,g}$ is measured and the heat transfer coefficient is also adjusted by the air flow in the dryer. The latter is dependent on the combination of the volume flow of air in the nozzles and the form, arrangement, and size of the nozzles. Correlations can be found in the VDI Wärmeatlas 2013, section G10 (Martin/Schabel) Prallströmungen.[55] The dependency between drying rate as adjusted in the Batch Coater at a concrete temperature ($T_{wet\ bulb}$), heat transfer coefficient and molar fraction of solvent in the gas phase (which correlates to a certain dew point) and the dryer temperature T_{dryer} under non-isothermal conditions is depicted in Figure 2.4.

The drying rate and the wet bulb temperature are calculated in dependency of the theoretical dryer temperature under non-isothermal conditions. Here, an air flow from the top and the bottom to the substrate is assumed with the identical values of the heat transfer coefficient and dryer temperature. An example is marked for a dryer temperature of 59 °C, a heat transfer coefficient of 35 W m^{-2} K^{-1} and a dew point of 15 °C. These settings result in a drying rate of 0.75 g m^{-2} s^{-1} and a wet bulb temperature of 32 °C.

These drying conditions with a drying rate of 0.75 g m^{-2} s^{-1} and a heat transfer coefficient of 35 W m^{-2} K^{-1} serve as the reference drying conditions throughout this work. Since the dew point temperature cannot be regulated, it was measured instead and the wet bulb temperature was set to a value that resulted in the targeted drying rate 0.75 g m^{-2} s^{-1}. The drying temperature was therefore regulated in a range of about 1-2 °C in dependency of the on the humidity prevailing during the respective day. More details on the calculation are given in section 4.3 (Simulation of Drying Curves).

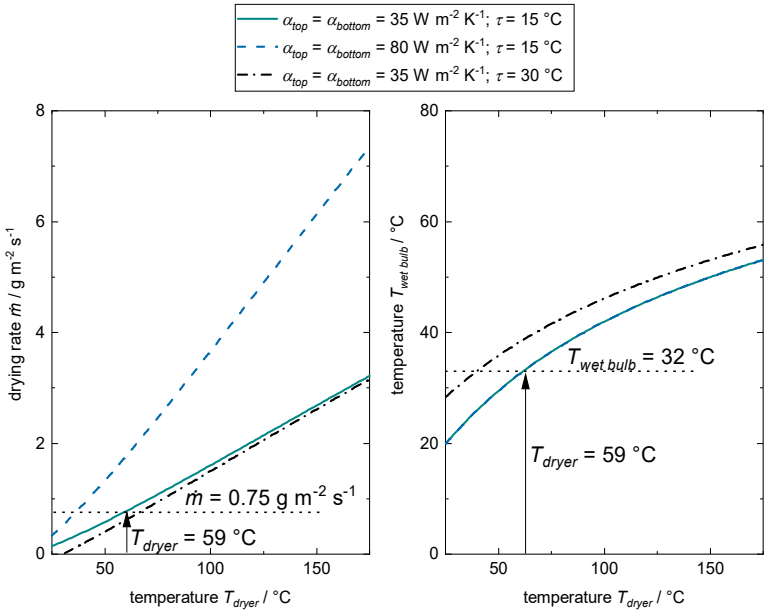

Figure 2.4: Interdependency between the drying conditions of an industrial convection dryer and its temperature T_{dryer} and the drying conditions in the Batch Coater at wet bulb temperature $T_{steady\ state}$ (derived from the relative humidity of air), as well as the resulting drying rate. The drying rate was 0.75 g m^{-2} s^{-1}, the heat transfer coefficient varied between 80 and 35 W m^{-2} K^{-1} and the dew point temperature of the drying air between 15 and 30 °C. For the industrial dryer an identical air flow from the top and the bottom was assumed. Figure taken from Kumberg et al., 2019. [24]

Experimental drying rates were determined in the batch coater by residual moisture measurements and compared to theoretically set ones. These are given in Figure 2.5. Two different theoretical drying rates of 0.75 g m^{-2} s^{-1} and 7 g m^{-2} s^{-1} were adjusted at a heat transfer coefficient of 35 W m^{-2} K^{-1}. The drying time was measured, and the solvent loading was determined by weighing each sample in the wet and again in the dry state. The procedure was repeated until a drying curve developed. At the high drying rate, only few measurements were possible due to the experimental setup.

The experimental drying rate was determined by a linear fit of the experimental data. This results in the experimental drying rates of 0.5 g m^{-2} s^{-1} and 5 g m^{-2} s^{-1}. For both theoretically adjusted extreme drying rates of 0.75 g m^{-2} s^{-1} and

7 g m^{-2} s^{-1} the factors 1.5 and 1.4 were found respectively between the theoretical and the experimental values. It is therefore assumed that a correction factor of 1.45 can be applied to convert from theoretical to experimental drying rates if the same heat transfer coefficient of 35 W m^{-2} K^{-1} is applied and the converted drying rate lies in between the investigated theoretical boundaries of 0.75 g m^{-2} s^{-1} and 7 g m^{-2} s^{-1}. Throughout this work the drying rates in regard to the batch coater will therefore be either addressed as "theoretical" values, meaning the uncorrected values, or as "experimental" or "corrected" values. The latter especially applies for section 6 (Simultaneously Coated and Hierarchically Structured Multilayers), where high speed drying is in the focus for improving electrode manufacturing and actual drying rates are of relevance. This is exemplarily shown for the theoretical drying rate of 3.2 g m^{-2} s^{-1} used in this section, which was corrected to the drying rate of 2.2 g m^{-2} s^{-1} as given in Figure 2.5.

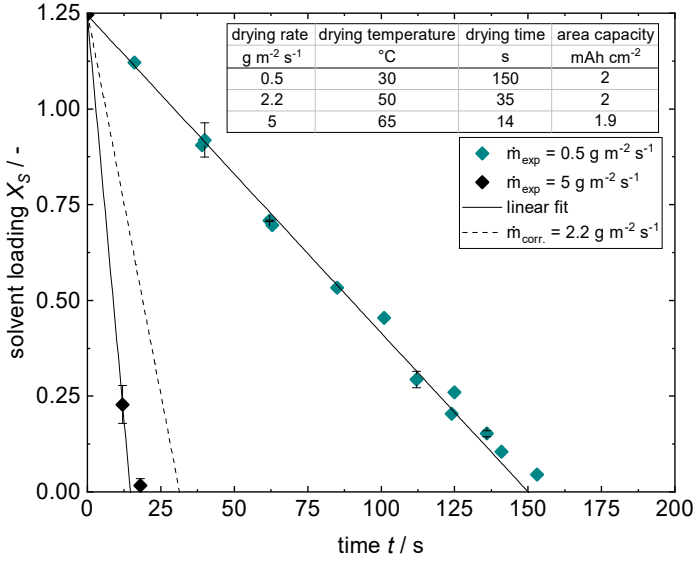

Figure 2.5: Experimental drying curves at different drying rates in the Batch Coater. The solvent loading as a function of drying time was determined by interrupting the experiment and measuring the residual moisture content of the electrodes. The heat transfer coefficient during all experiments was 35 W m^{-2} K^{-1} at a dew point of 10 °C. The reference slurry with the composition presented in Table 2.1 was used. Figure taken from Kumberg et al., 2021.[56]

Comb Nozzle (CN)

The Comb Nozzle dryer is a stationary dryer with a honeycomb-shaped impinging-jet nozzle field with alternating supply air and additional nozzles for exhaust air removal (see Figure 2.6), with the comb nozzle being patented by P. Cavadini, W. Schabel and P. Scharfer.

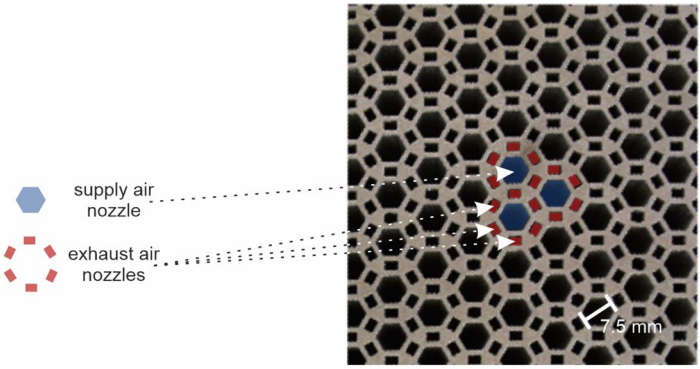

Figure 2.6: Comb Nozzle field with marked supply and exhaust air nozzles. Comb Nozzle field from CN Drying Technology.

The supply air nozzles are surrounded by suction nozzles. The nozzle shape and arrangement were optimized for allowing very homogenous drying conditions even though neither the dryer hood nor the substrate are moving.[57] The nozzle field thus allows to adjust heat transfer coefficients in the range of 20 W m^{-2} K^{-1} – 120 W m^{-2} K^{-1}. The heat transfer coefficient in dependency of the distance between dryer hood and substrate and most importantly the flow rate of air has been analyzed using thermochromic liquid crystals (TLCs) prior to this work, as explained by Cavadini et al. (2014).[57] The nozzle design was optimized for a narrow distribution of local heat transfer coefficients, yet a residual distribution width remains. The laterally averaged heat transfer coefficient will be referred to as α_{TLC} from this point on. The dryer can be operated in two modes: the first is similar to the Batch Coater under isothermal drying conditions, when films are coated on top of a heating plate beneath the dryer hood of the CN. The second option is a gravimetric setup, where films are fixed in a free hanging frame and are surrounded by air. This also enables a more detailed investigation of the drying process, since a transparent substrate can be used to observe pore emptying.

This will be explained in detail in section 4.4.1 (Experimental Drying of Thinner Electrodes).

2.3 Analytics

The characterization methods starting with the slurry up to coin cell analysis are presented in this section. Properties of the reference slurry used in this work are given.

2.3.1 Structural Properties of the Slurry

The structural properties of the slurries can be characterized and investigated by means of particle size distributions. These serve to evaluate the mixing process. E.g. the breaking down of carbon black agglomerates can be determined, which is crucial for battery performance.[19] Furthermore, the particle size distribution provides information about the particle size distribution of the graphite particles which will form into the microstructure of the dry electrode during drying. All information put together allows to understand the drying process in more detail based on the mixing process.

The particle size distribution was measured with a Mastersizer 3000 (MAL1086270, Malvern Panalytical, UK). Particle sizes between 0.1 µm - 3500 µm can be detected. During measurements, the device settings were “non-spherical particles”, the averaged refractive index of graphite with 2.0 for the particles, and of 1.33 for the dispersion medium water. The density of graphite was specified with 2200 kg m^{-3} and the absorption index was set to 1. A determination of the background noise was executed before the actual measurement. The laser shading was between 8 % and 12 % for all measurements. The mixer was set to 1500 rpm. Each sample was measured three times in a row by pumping the liquid in a circle and thereby continuously passing the measuring cell. For each slurry at least three samples were measured.

The particle size distributions of the reference slurry and the pure graphite powder are shown in Figure 2.7. The pure graphite powder was measured in distilled water without a mixing step in the dissolver. The reference recipe was mixed in the dissolver after th2e procedure given in the appendix A.1. The measured pure

graphite powder shows a monomodal distribution and a d_{50} of 17.1 µm compared to a d_{50} of 18.4 µm according to the manufacturer. The reference slurry has a d_{50} of 17.2 µm and shows a second peak at around 0.17 µm, which can be attributed to fractured carbon black aggregates introduced by the recipe. Compared to the pure graphite, the reference slurry also shows a shoulder in the particle range between 1 and 5 µm which most likely is attributed to carbon black aggregates mixed with sheared off graphite flakes.

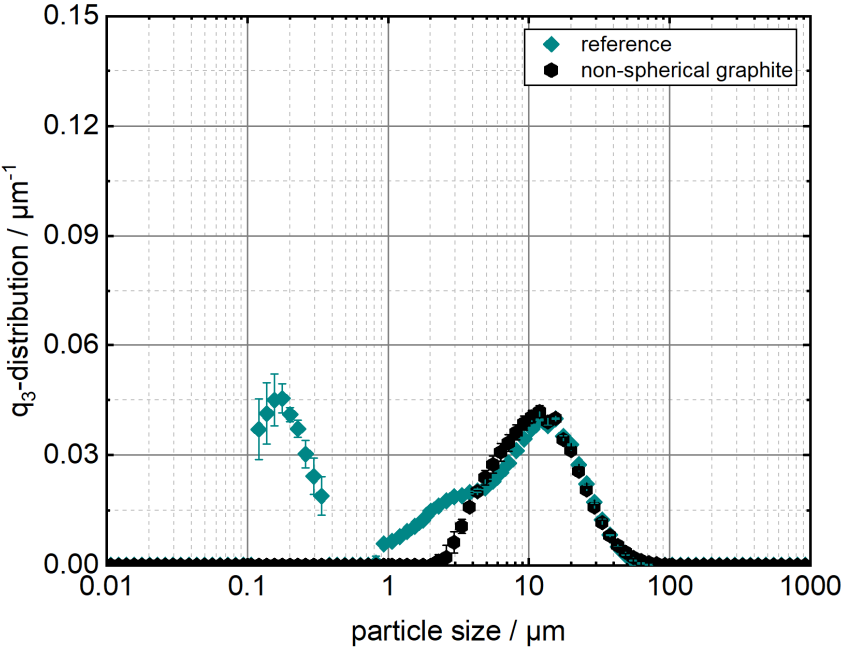

Figure 2.7: Density distribution as a function of the particle size of the reference slurry and the pure graphite powder in water. The pure graphite powder has a d_{50} of 17.1 µm. The reference slurry has a d_{50} of 17.2 µm and shows a second peak at around 0.17 µm, which can be attributed to fractured carbon black aggregates

2.3.2 Rheological Properties of the Slurry

The rheological behavior of the slurry provides information about the suitability for slot die coating and its influence on the drying process due to the stability of the dispersion and the interactions between particles among each other and

between the particles and polymer chains. Rotatory and oscillatory measurements were executed. For each slurry at least three measurements were performed.

Rotational viscosimetry

The dynamic viscosity η can be determined by Newton's law in equation (2.2) with the shear stress τ and the shear rate $\dot{\gamma}$.

$$\eta = \frac{\tau}{\dot{\gamma}} \tag{2.2}$$

The shear rate is defined by the two plates model shown in Figure 2.8 as the velocity difference dv at a certain height difference dy (equation (2.3)) when the top plate is moved at the velocity v and the bottom plate is fixed.

$$\dot{\gamma} = \frac{dv}{dy} \tag{2.3}$$

The shear stress τ thereby is the force F applied to the upper plate in relation to the plate area A (see equation (2.4)).

$$\tau = \frac{F}{A} \tag{2.4}$$

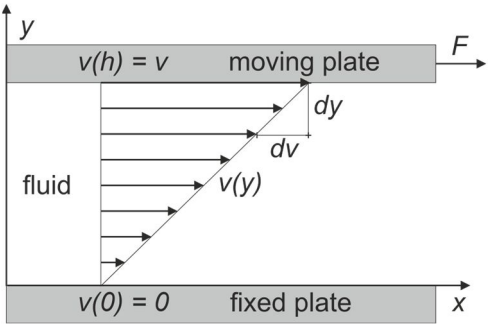

Figure 2.8: Newton's law of shear stress with a fixed plate at the bottom, a moving plate at the top and a linear velocity profile known as "Couette flow".

A rheometer physica MCR101 (Anton Paar, Austria) with a plate to plate measurement system of the type PP25-SN 30563 with a diameter of 25 mm was used. The temperature was set to 25 °C and the distance of the plates to 500 µm during

all measurements with a solvent trap to reduce evaporation placed on top of the measurement plate. The measurement protocol was an upward ramp of the shear rate from 0.01 s^{-1} to 1000 s^{-1}, a stop at 1000 s^{-1} for 10 s and a downward ramp to the shear rate of 0.01 s^{-1} with 10 measurements per decade.

The dynamic viscosity of the reference slurry in dependency of the shear rate is shown in Figure 2.9. A shear thinning behavior of the battery slurry becomes obvious. Particles and in particular the carbon black form agglomerates when exposed to no or only low shear rates and bind and immobilize a part of the solvent. Under shear, particles are oriented along the shear direction and agglomerates are broken down, thereby releasing solvent. This leads to a decrease of the viscosity.[58,59] The hysteresis indicates thixotropic behavior due to agglomerates which form again over time.

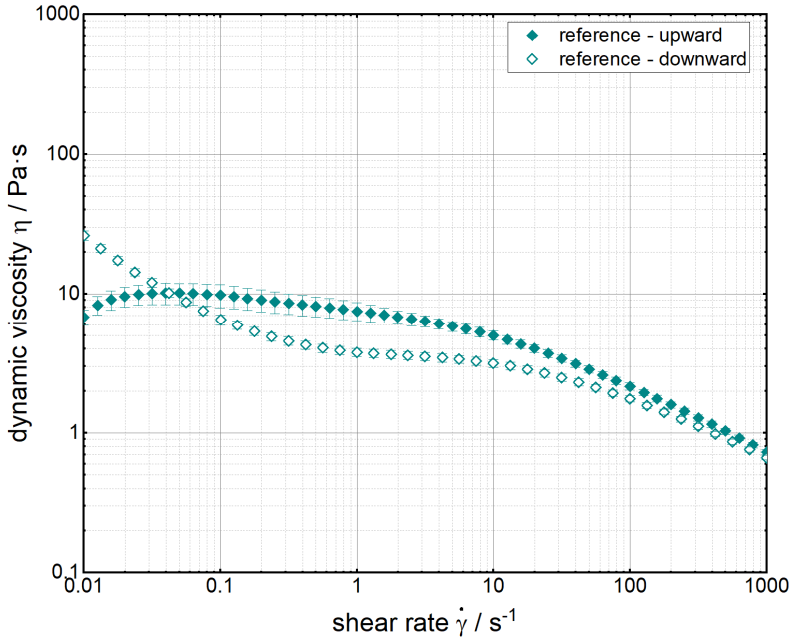

Figure 2.9: Dynamic viscosity of the reference slurry as a function of increasing (upward) and decreasing (downward) shear rate with the composition given in Table 2.1.

Oscillatoric viscosimetry

To further illuminate the stability and strength of the network of particles and polymer in the slurry by its viscoelastic properties, oscillatory measurements were done in addition to the rotational ones. Therefore, as a first step an amplitude test was done, under variation of the shear strain γ caused by the deflection or deformation s to a certain angle in relation to the gap height h (see equation (2.5)).

$$\gamma = \frac{s}{h} = \tan \varphi \tag{2.5}$$

If a time-dependent shear strain $\gamma(t)$ is given, it can be described by the sinus function in equation (2.6) with the strain amplitude γ_A and the angular frequency ω.

$$\gamma(t) = \gamma_A \sin[\omega\, t] \tag{2.6}$$

The system response to the shear stress $\tau(t)$ is a sinus function as well, with the amplitude τ_A. While in the ideally elastic case no delay between shear strain and the response is present, there is a time delay in the viscoelastic case with the phase shift angle δ (equation (2.7)). For an ideally viscous fluid $\delta = 90°$.

$$\tau(t) = \gamma_A \sin[\omega\, t + \delta] \tag{2.7}$$

The complex shear modulus G^* can be described under knowledge of $\gamma(t)$ and $\tau(t)$ (equation (2.8)).

$$G^* = \frac{\tau(t)}{\gamma(t)} \tag{2.8}$$

The tangens of the phase shift angle is the ratio between the viscous and the elastic part of the viscoelastic shear strain after equation (2.9).

$$\tan \delta = \frac{G''}{G'} \tag{2.9}$$

Herein, G'' is the loss modulus, describing the deformation energy which is irreversibly lost during shearing which is caused by changes in the structure of the sample and as such being the viscous behavior. The storage modulus G' is the reversibly stored deformation energy in the sample and represents the elastic behavior of the sample. As a result, fluids with a phase shift angle between 45°-90°

are closer to ideally viscous behavior and are referred to as liquid-like, while fluids with a phase shift angle between 0°- 45° are referred to as gel-like.[59]

The test procedure for the slurries investigated in this work was as follows: In an amplitude test at the angular frequency of 1 s^{-1}, the shear strain was logarithmically increased from 0.005 % to 100 %. The linear viscoelastic (LVE) range was determined at a shear strain of 1 % for the frequency sweep. In the LVE range, no irreversible changes in the fluids structure are caused by the shear strain during the test. The frequency was increased from 0.1 s^{-1} to 150 s^{-1}.

From amplitude and frequency sweep the storage and loss modulus were derived, and the phase shift angle in dependency of the angular frequency determined. This is depicted in Figure 2.10 for the reference slurry.

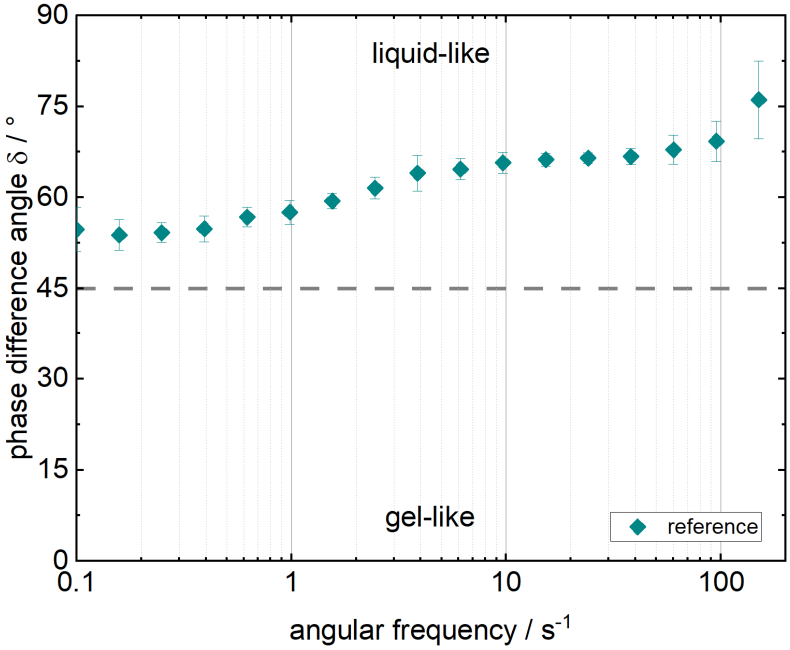

Figure 2.10: Phase difference angle of the reference slurry in dependency of the angular frequency with the composition of the slurry given in Table 2.1.

The phase shift angle lies well in the liquid-like domain in the whole range of the angular frequency. This means that no strong network between particles and polymer is present which encompasses the whole structure.

2.3.3 Mechanical Properties of the Dry Electrodes

To determine the mechanical properties of the dry electrode films, adhesion force measurements were conducted using a universal testing machine (LS1, Ametek, USA) with a 90 peel test device and a 10 N load cell. The electrode coatings were fixed onto a metal plate by double-sided adhesive tape. The adhesive tape was used to fixate the electrode coating to the metal plate while the force was measured to delaminate the coating from the copper foil substrate of the electrode. The prerequisite for this is that the double-sided tape adheres better to the metal plate and to the electrode coating than the electrode coating to the copper substrate, which was the case in all tests. Each coating was pressed onto the tape with a metal roller weighing 10 kg. The copper foil was fastened into a clamp and the substrate was peeled from the coating under a permanent angle of 90°, which was ensured by the substrate automatically moving forward under the same velocity of 100 mm min^{-1} as the clamp moving upward (see Figure 2.11). The peel-off force was measured, and the adhesion force determined in relation to the sample width in form of a line force. The samples had a width of 30 mm and at least three measurements were conducted per coating.

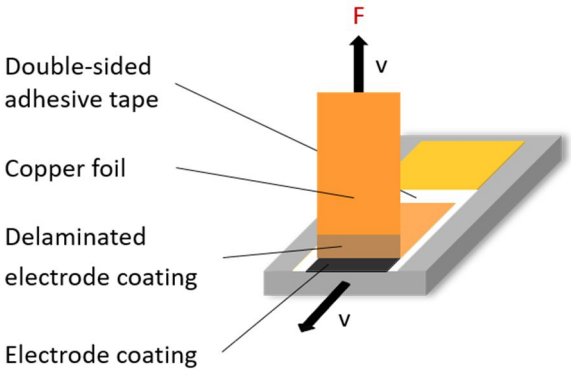

Figure 2.11: 90° peel test to measure the adhesion force of the dry electrode coatings on a substrate.

2.3.4 Structural Properties of the Dry Electrodes

How structural properties of the dry electrodes like area weight, porosity, and pore size distribution were determined is explained in the following section.

Area weight and porosity

The area weight of the dry electrode m_{el} was calculated from the mass of the electrode M_{el} in relation to its area A_{el}. The as-processed electrode weight was measured with an analytical scale (MSE225P-000DU, Sartorius) and the area weight of the substrate subtracted. The total porosity can be derived from the electrode area weight m_{el}, its thickness h_{el} and the average density of the dry electrode composite materials and mixture ρ_{el} according to equation (2.10) and (2.11).

$$\varepsilon = 1 - \frac{m_{el}}{\rho_{el}\, h_{el}} \tag{2.10}$$

The density of the dry electrode depends on the mass fractions of all components x_i with their respective densities ρ_i and was calculated according to the mass fractions of the recipe as shown in equation (2.11).

$$\rho_{el} = \frac{1}{\frac{x_{graphite}}{\rho_{graphite}} + \frac{x_{carbon\ black}}{\rho_{carbon\ black}} + \frac{x_{CMC}}{\rho_{CMC}} + \frac{x_{SBR}}{\rho_{SBR}}} \tag{2.11}$$

The electrode thickness was measured with a digital measuring probe (ID-H0530, Mitutoyo) and a flat measuring head.

The solvent loading at the point where the saturation is 1 and all pores are theoretically solvent-filled and the film stops to shrink, is considered with the theoretical end of film shrinkage X_{EOF}. It can be determined from the porosity and the density of the used solvent $\rho_{solvent}$ according to equation (2.12).

$$X_{EOF} = \frac{\rho_{solvent}\, \varepsilon\, h_{el}}{m_{el}} \tag{2.12}$$

Pore Size Distribution

Pore size distributions were measured for the dry electrodes, determined by mercury intrusion porosimetry (Pascal 140/440 EVO, Thermo Scientific). The pore

size distribution of the reference electrode is depicted in Figure 2.12. It shows the main peak at a pore diameter of around 5 µm and the second smaller peak at 12 µm. Since the particle size itself is at around 18.4 µm and based on the SEM micrographs given in Figure 1.6 and Figure 2.13 it is assumed that pores found at higher pore diameters are due to surface pores at the electrode and can be neglected. Thus, two small peaks in the pore size distribution at 36 µm and 64 µm are neglected.

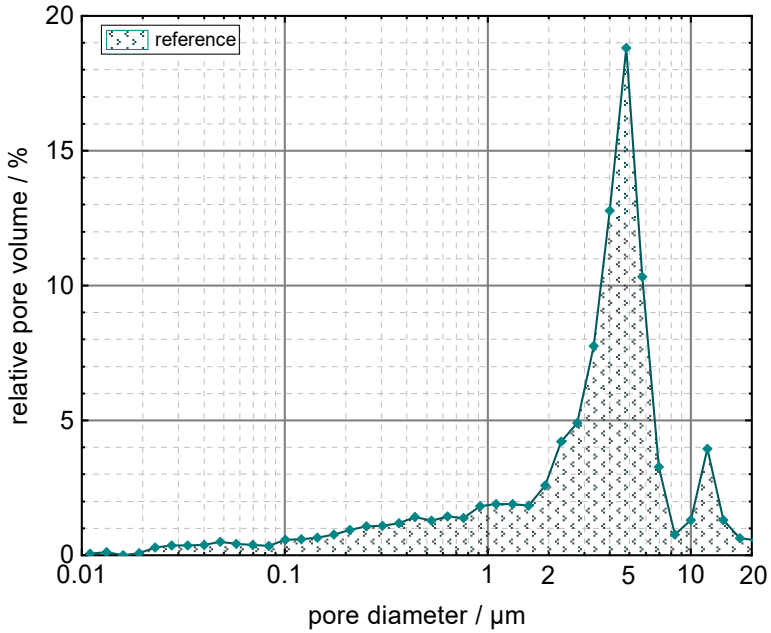

Figure 2.12: Pore size distribution of the dry reference electrode with the composition given in Table 2.1. It shows the main peak at a pore diameter of around 5 µm and the second smaller peak at 12 µm.

A SEM cross section (Zeiss Merlin SEM) of an electrode with the aforementioned pore size distribution (Figure 2.12) is shown in Figure 2.13. The cross section was prepared by means of Broad Ion Beam Slope-Cutting (Leica Mikrosysteme GmbH, Germany). The graphite particles and the pores are clearly visible. Contact between graphite particles and the substrate at the bottom can also be observed.

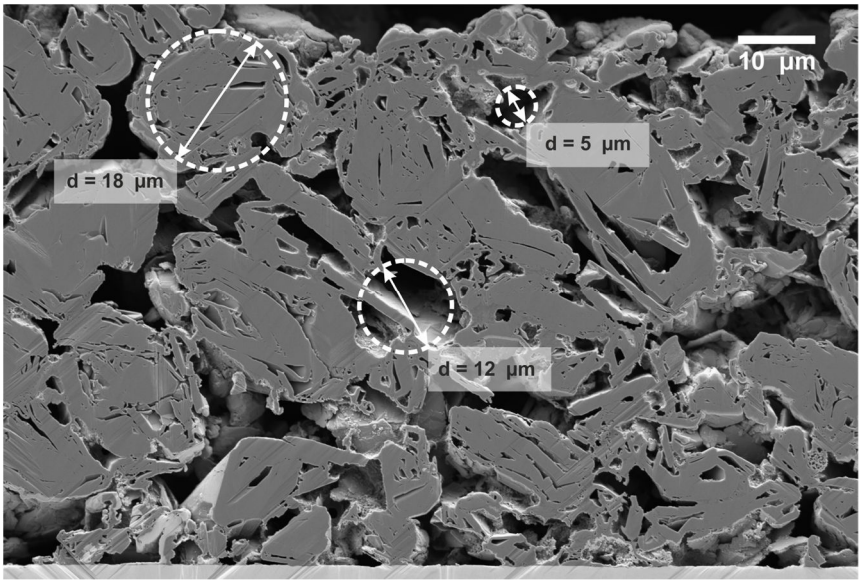

Figure 2.13: SEM micrograph of the dry reference electrode with the composition given in Table 2.1 showing its microstructure and pore size distribution. The d_{50} of the particle size distribution is 18.4 µm (Figure 2.7). The pore size distribution has a main peak at ~5 µm and a smaller peak at ~12 µm (Figure 2.12). Based on this SEM micrograph, pore sizes above 20 µm and especially two more small peaks in the pore size distribution at 36 µm and 64 µm are neglected since it is assumed that surface pores appeared in the measurement.

2.3.5 Electrical Properties of the Dry Electrodes

The electrical conductivity σ was measured with the electrodes positioned between two copper cylinders with a diameter of 40 mm and an area of $A_{cylinder}$= 12.6 cm², as pictured in Figure 2.14. A current was applied by an E3633A power supply (Agilent Technologies) and the voltage difference U_R was measured with a multimeter (2700, Keyence) using a four-wire setup. The electrical conductivity was derived from the voltage drop U_{23} between the two cylinders, with the intrinsic resistance R of the setup being 11 kΩ, and calculated after equation (2.13).

$$\sigma = \frac{U_R h_{el}}{U_{23} R A_{cylinder}} \tag{2.13}$$

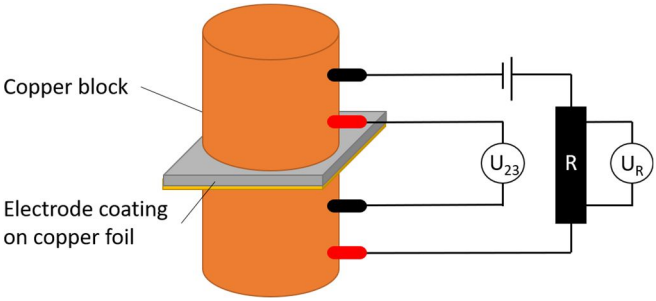

Figure 2.14: Measurement setup for the electrical conductivity. A current was applied by an E3633A power supply (Agilent Technologies) and the voltage difference U_R measured with a multimeter (2700, Keyence) using a four-wire setup. The electrical conductivity was derived from the voltage drop U_{23} between the two cylinders with a diameter of 40 mm and an area of $A_{cylinder}$= 12.6 cm², with the intrinsic resistance R of the setup being 11 kΩ.

It has to be kept in mind, that not a single homogenous material is measured in this setup, but the entire electrode, with the copper foil and the porous structure consisting of active material, carbon black and binder materials. Hence the measured average specific conductivity contains multiple components. If changes in the specific conductivity of the electrode are observed, these have to be linked to changes of the internal resistance network, since the specific conductivity of each pure material is a constant. Whether these changes are due to the resistivity of the microstructure or whether contact resistances at the electrode surface or even both change cannot be conclusively determined.

The sample size was a square of 45 x 45 mm. The copper cylinders were weighted on top with 1.8 kg of mass during all measurement to ensure a homogenous pressure and contact between the coating and the top cylinder.

2.3.6 Electrochemical Properties of the Cells

To determine the influence of different processing steps on the electrochemical properties of the electrodes fabricated in this work, coin or pouch cells were

produced and tested. Pouch cells were thereby produced and tested in cooperation with the IAM-ESS institute and the working group of Werner Bauer at KIT. To produce coin cells, equipment was purchased and put into operation in the frame of this work, so coin cells could be produced at small scale at the TFT laboratory. A procedure and setup were established so all steps within the process chain from slitting to coin cell assembly could be executed in a glovebox under argon atmosphere (see Figure 1.2). Cell testing was performed in the air-conditioned facilities of IAM-ESS, where a "TFT cell tester" was set up.

Before coin cell manufacturing, anodes were calendered by a Hot Rolling Press (GN MR 100 H from Gelon, China). For state-of-the-art coin cell manufacturing, cathodes with an area loading of 12.2 mg cm^{-2} and a theoretical capacity of 2.0 mAh cm^{-2} with NMC622 (BASF, Germany) were used for the respective thin anodes. For high energy coin cell manufacturing, cathodes with an area loading of 40.9 mg cm^{-2} and a theoretical capacity of 6.8 mAh cm^{-2} were combined with thick anodes. A polypropylene fleece (Adfiltec GmbH, Germany) was used as separator and the electrolyte was a mixture of EC:EMC 3:7 with 1M $LiPF_6$ and 2 % VC (Gelon, China). The diameter of the anode was 16 mm and that of the cathode 13 mm. The separator had a diameter of 17 mm. Prior to cell assembly, the separator and the electrodes were heated to 100 °C for 20 min to remove remaining residual solvent. For the cell test, identical charging and discharging rates were applied, consisting of a formation cycle at C/20, two cycles at C/10 and two cycles at C/5, followed by each 5 cycles at C/2, 1C, 2C, and 3C, followed by 5 cycles at C/2.

3. Drying of Thicker Electrodes

The following section will address the question how drying influences the binder distribution, especially when the electrode thickness is increased.[1]

3.1 Motivation and State of the Art

To reduce the costs for battery packs, an increase of the area weight of the electrodes is targeted. This leads to material savings in the form of separator and current collector and increases the volume density of active materials, since the inactive components currently take up about 20 % of the total volume. It was shown though that increasing the area weight above 3-4 times that of a state-of-the-art electrode results in a serious loss of cell performance at C rates above C/5.[60,61] This is mainly attributed to limited mass transport of lithium ions in the electrolyte phase.[62,63] To improve cell performance of high energy electrodes at high C rates, new pathways for lithium ions are introduced in the electrode by post-processing with a laser or other approaches.[64–67] The coating and drying processes thereby hugely impact the electrode performance as well, as was explained earlier. Accumulated binder at the surface of thin anodes caused by drying under high drying rates is thought to hinder lithium ion transport and deteriorate cell performance.[11,68] This was shown to also happen at the cathode side.[69] Since the drying mechanism itself depends on the thickness of the electrode, the question arises how electrode thickness, drying rate and binder distribution are connected to one another. The drying rate and the related loss of adhesion and its impact on cell performance will be investigated in the following.

---

[1] Results presented in this section are part of the following publication by the author:[24]
Kumberg, J.; Müller, M.; Diehm, R.; Spiegel, S.; Wachsmann, C.; Bauer, W.; Scharfer, P.; Schabel, W. (2019): Drying of Lithium-Ion Battery Anodes for Use in High-Energy Cells. Influence of Electrode Thickness on Drying Time, Adhesion, and Crack Formation. In: Energy Technol. 3, S. 1900722. DOI: 10.1002/ente.201900722.

3.2 Experimental Setup

Mixing, Coating & Drying: All electrodes in the following section have been mixed in the dissolver (section 2.2.1 Mixing Process), coated by knife coating (section 2.2.2 Coating Process) and dried in the batch coater, which was presented in section 2.2.3 Drying Process.

Annealing: An annealing experiment was conducted with a state-of-the-art electrode which was dried at a theoretical drying rate of 0.75 g m^{-2} s^{-1} and a heat transfer coefficient of 35 Wm^{-2} K^{-1}. The aim was to distinguish between the influence of the drying rate itself and an associated increase of the drying temperature. Samples of the dry electrode were positioned between two metal plates to avoid bending and to ensure a homogeneous heat input. The plates with the samples were transferred to a vacuum furnace which was preheated to the respective temperature and left there for 10 min at 10 mbar. The experiment was repeated for different temperatures.

Laser-induced breakdown spectroscopy (LIBS)

Laser induced breakdown spectroscopy (LIBS) was used to study the CMC binder distribution over the film height by means of detecting the specific sodium (Na) atom contained in the CMC binder. The measurements were executed by Y. Zheng and W. Pfleging from IAM-AWP, KIT.[64,65,70] The method was shown to be able to analyze the lithium distribution in cycled anodes.[71] It was also used to measure the CMC distribution in cathodes.[72] Therefore, this method is also capable of investigating CMC binder distributions in anodes.

Laser pulses are used to ablate material from thick, calendered electrodes layer by layer. A spectrometer meanwhile detects the composition of the sublimated area of a size of 5x5 mm by means of an element analysis. As a result, a 3D mapping of sodium, comprised of stacked layer images, is obtained. These layers can be analyzed one by one for their average sodium content. Electrodes with a theoretical capacity of 12 mAh cm^{-2} (356 g m^{-2}) and 13.5 mAh cm^{-2} (401 g m^{-2}) were calendered to a thickness of about 260 µm. The exact properties are listed in Table 3.1. The electrodes were dried at a theoretical drying rate of 0.75 g m^{-2} s^{-1} and 3 g m^{-2} s^{-1} with a heat transfer coefficient of 35 W m^{-2} K^{-1}. The wavelength of the laser was 1030 nm, the pulse frequency 100 Hz at a pulse

duration of 1.5 ns and a pulse energy of 3 mJ. The horizontal resolution was 100 µm. From the investigated 5x5 mm only a section of 4 x 4 mm is evaluated to exclude edge effects. In total, 58 or 66 layers were measured for each electrode, with every fourth layer being analyzed. Starting from the top, every fourth layer was analyzed until copper was detected in the last 4 or 8 layers, resulting in 55 or 52 relevant layers. The number of layers consequently was assumed to correspond to the dry film thickness, which results in an ablated layer thickness of 4.8 µm and 5.1 µm respectively. A summary is given in Table 3.1.

Table 3.1: Properties of the electrodes analyzed by LIBS. Electrodes with a theoretical capacity of 12 mAh cm^{-2} (356 g m^{-2}) and 13.5 mAh cm^{-2} (401 g m^{-2}) were calendered to a thickness of about 260 µm and a porosity of 0.36 and 0.39 respectively. In each step 4.8 µm or 5.1 µm were ablated and analyzed by LIBS.

Drying rate	Area capacity	Electrode thickness	Porosity	Analyzed layers	Ablated Layer thickness
g m^{-2} s^{-1}	mAh cm^{-2}	µm	-	-	µm
0.75	13.5	265	0.36	55	4.8
3	12.0	263	0.39	52	5.1

Adhesion Measurements and Cell Test: Adhesion measurements were conducted as described in section 2.3.3 (Mechanical Properties of the Dry Electrode). Cell tests were performed according to section 2.3.6 (Electrochemical Properties of the Cells).

3.3 Results and Discussion

In this section, the results of the influence of the drying rate on binder migration, and cell performance will be presented.

3.3.1 Binder Migration

Binder migration in dependency of electrode thickness and drying rate will be discussed in the following section.

Adhesion and electrode thickness

The impact of an increase of the electrode thickness in form of an enhanced area weight and a higher theoretical capacity, on the adhesion force is shown in Figure 3.1.

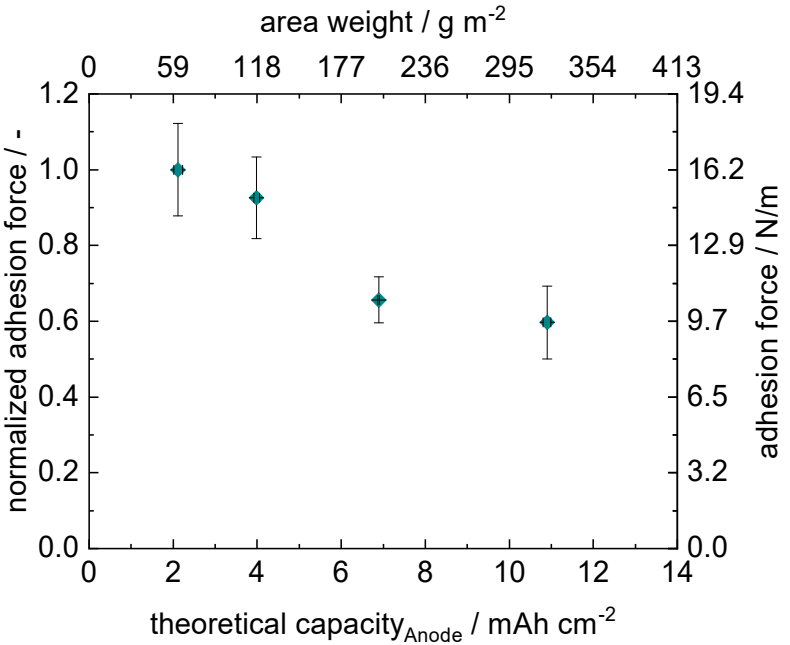

Figure 3.1: Normalized adhesion force of electrodes of differing theoretical capacities dried with a theoretical drying rate of 0.75 g m^{-2} s^{-1} and a heat transfer coefficient of 35 W m^{-2} K^{-1}. The area weight corresponding to a theoretical capacity is given as top x-axis. The absolute adhesion force is given as right y-axis. Normalization is conducted to guarantee comparability throughout this work, since absolute values depend on the copper foil used. The adhesion force of the reference electrode dried at a drying rate of 0.75 g m^{-2} s^{-1} and a heat transfer coefficient of 35 W m^{-2} K^{-1} at a capacity of 2.5 mAh cm^{-2} is used for normalization. Figure taken from Kumberg et al., 2019.[24]

The adhesion force was normalized on the adhesion force of a state-of-the-art electrode dried with a theoretical drying rate of 0.75 g m^{-2} s^{-1} and a heat transfer coefficient of 35 W m^{-2} K^{-1}. This corresponds to an absolute adhesion force of 16.2 N m^{-1} for copper foil (f1) and the electrode with a theoretical capacity of 2.1 mAh cm^{-2}. When increasing the area weight by a factor of about 5 to an area capacity of 10.9 mAh cm^{-2}, 40 % of the adhesion force are lost. This corresponds to a value of 9.7 N m^{-1}. In literature a lower adhesion force limit of about 6 N m^{-1} is mentioned for cell production in pouch cells and thin electrodes.[21] For electrode fabrication this limit has to been kept in mind. Another important aspect though is, that a loss in adhesion might implicitly stand for a binder accumulation at the electrodes surface, which might negatively affect cell performance, regardless of the adhesion limit for manufacturing: One possible reason for the decreasing adhesion force was addressed in section 1.3 (Electrode Drying) for thin electrodes and will be further investigated in section 4.4.3 (Experimental Drying of Thicker Electrodes) in relation to thicker electrodes: Capillary transport, which appears to be the driving mechanism behind solvent transport within thin and thick electrodes during drying. Additives like the binder dissolved or dispersed within the slurry are dragged along with the solvent away from the electrode and accumulate at the surface. If capillary pore emptying behaves differently for thick electrodes than for thin electrodes will be investigated in section 4 (Drying Behavior of Thicker Electrodes). In a first approximation it is assumed that the decreased adhesion force of thick electrodes can be related to disappearance of binder from the substrate-electrode interface.

One factor different for thicker than for thinner electrodes could be longer pathways for back-diffusion of binder within still solvent filled capillaries. With capillary transport enriching the wet electrode surface with binder, a concentration gradient evolves within the electrode. This could lead to back diffusion of binder. However, the distance would be significantly higher for thick electrodes. To estimate whether back-diffusion is likely to occur, an evaluation of the different physical mechanisms acting on a single SBR sphere can be done:

A consolidation factor K_C was calculated according to equation (3.1) after Baunach et al. (2015).[52] It is the ratio between the sedimentation speed u_{sed} and the diffusion velocity u_{diff} directed to the bottom in relation to the evaporation speed u_{evap} directed to the surface. If $K_C = 1$ evaporation, diffusion and

sedimentation are in the same range. If $K_C \ll 1$ diffusion and sedimentation are neglectable compared to evaporation.

$$K_C = \frac{u_{diff} + u_{sed}}{u_{evap}} \tag{3.1}$$

The sedimentation speed, diffusion velocity and evaporation rate were calculated for the SBR binder, according to equation (3.2) to (3.6).

The sedimentation speed can be determined after Stokes, in equation (3.2) under knowledge of the SBR particle diameter $r_{p,SBR}$ and the respective densities of the SBR particle $\rho_{p,SBR}$ and the solvent ρ_s as well as the viscosity of the solvent between the particles η. The mean particle diameter of the SBR is 153 nm (see Appendix, Figure A. 7-7) and its density 1750 kg m^{-3}. The solvent was assumed to be pure water and the temperature to be 30°C.

$$u_{sed} = \frac{2r_{p,SBR}^2 g\left[\rho_{p,SBR} - \rho_s\right]}{9\,\eta} \tag{3.2}$$

The diffusion velocity was calculated after Fick's law according to equation (3.3). An upper boundary for the back diffusion can be obtained by assuming a SBR concentration of zero at the substrate ($c_{SBR,bottom}$) and a maximum concentration at the top ($c_{SBR,top}$).

$$u_{diff,SBR} = -\delta_{eff,SBR,water} \frac{\left[c_{SBR,bottom} - c_{SBR,top}\right]}{h_{el}} \tag{3.3}$$

The diffusion coefficient of SBR in water $\delta_{SBR,water}$ can be approximated with Stokes-Einstein assuming a single particle in a liquid medium (see (3.4)). T hereby is the absolute temperature in Kelvin and k_B the Boltzmann constant.

$$\delta_{SBR,water} = \frac{k_B\,T}{6\pi\,\eta\,r_p} \tag{3.4}$$

The effective diffusion coefficient of the SBR in the liquid phase of the porous electrode structure was derived after Zehner, Bauer and Schlünder under the assumption that diffusion takes place only in the liquid phase of the porous electrode structure according to equation (3.4).[55] For all estimations the solvent was

assumed to be water and the film porosity ε was derived from experiments (see Table 4.2).

$$\delta_{eff,SBR,water} = \delta_{SBR,water}\left[1 - \sqrt{1-\varepsilon}\right] \tag{3.5}$$

To calculate the evaporation rate u_{evap}, the drying rate $\dot{m}_s$ and the solution density ρ_s need to be known, as can be seen in equation (3.6). For the drying rate, the theoretical drying rate of 0.75 g m^{-2} s^{-1} was used.

$$u_{evap} = \frac{\dot{m}_s}{\rho_s} \tag{3.6}$$

Table 3.2: Summary of the different driving forces the SBR binder is exposed to during drying in dependency of the electrode thickness h_{el} and its effect on the consolidation factor K_c which sets diffusion, sedimentation and evaporation into relation, after Baunach et al. (2015).[52]

h_{el}	$u_{diff,SBR}$	u_{sed}	u_{evap}	K_C
µm	µm s^{-1}	µm s^{-1}	µm s^{-1}	-
75	$5.2 \cdot 10^{-4}$	0.012	0.754	0.016
150	$2.5 \cdot 10^{-4}$	0.012	0.754	0.016
225	$1.7 \cdot 10^{-4}$	0.012	0.754	0.016
300	$1.2 \cdot 10^{-4}$	0.012	0.754	0.016

The consolidation factor for the SBR, $K_C \ll 1$ (~ 0.02) shows a clear tendency for the SBR accumulating at the surface, because the evaporation rate strongly superimposes the influence of diffusion and sedimentation, as is shown in Table 3.2. A higher electrode thickness has no relevant influence on K_C. This means that a back diffusion is highly unlikely to make a realistic difference, regardless of the electrode's thickness. With the diffusion velocity being about 1500 times slower than the evaporation rate, rather an impact of sedimentation would be possible, though sedimentation speed is also 63 times slower than evaporation. However, it must be kept in mind that such a simplified estimation does not

necessarily account for the real electrode and gradients might still be balanced over shorter distances.

Adhesion and drying rate

Since the drying rate is known to impact the binder distribution in NMP-based electrodes, experiments have been conducted to verify this behavior in the water-based system using CMC and SBR as binders.[10,11] The drying rate was adjusted by either regulating the isothermal drying temperature or by varying the air flow rate and the resulting heat transfer coefficient. Two different heat transfer coefficients of 35 W m^{-2} K^{-1} and 80 W m^{-2} K^{-1} were investigated to distinguish between the influence of temperature and heat/mass transfer coefficient as was proposed by Baunach et al. (2015).[73] The results are given in Figure 3.2a and Figure 3.2b for electrodes with the two extreme theoretical capacities of 2.5 mAh cm^{-2} (m = 74 g m^{-2}) and 12.5 mAh cm^{-2} (m = 371 g m^{-2}) respectively.

The normalized adhesion force is presented in dependency of the drying rate. Two drying rates of 1.5 g m^{-2} s^{-1} and 2.5 g m^{-2} s^{-1} have been adjusted either by temperature or heat/mass transfer coefficient variation. The different settings are marked with the numbers (1) to (4) and are also listed in Table 3.3. Since the normalization was conducted for an electrode dried with a drying rate of 0.75 g m^{-2} s^{-1}, which achieves higher adhesion forces than the electrodes examined, a value of one is not reached here. Within these experiments, the electrode dried with the lower drying rate of 1.5 g m^{-2} s^{-1} and the lower heat transfer coefficient of 35 W m^{-2} K^{-1} achieves the highest adhesion force. This is true for both the thin and thick electrodes.

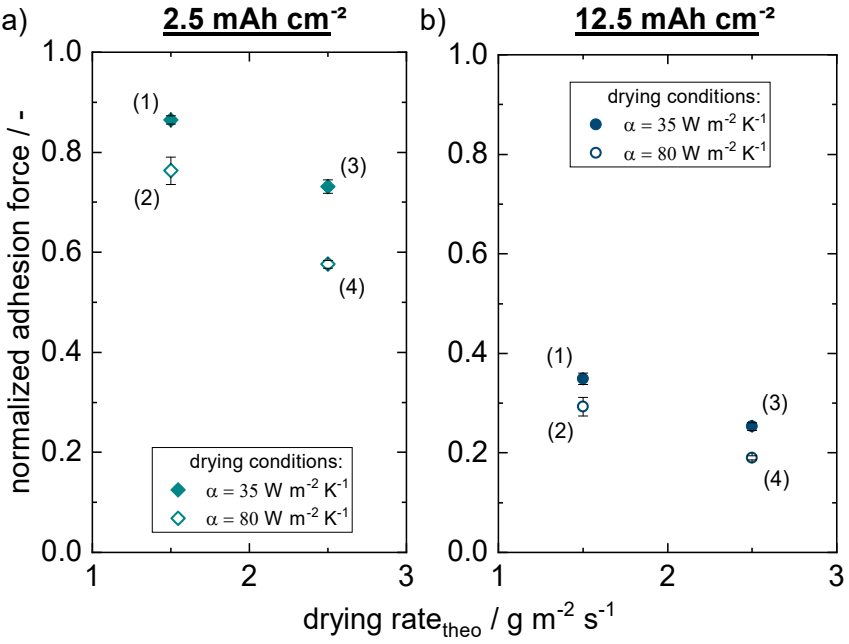

Figure 3.2: Normalized adhesion force of electrodes with two different theoretical capacities of 2.5 mAh cm^{-2} (m = 74 g m^{-2}) and 12.5 mAh cm^{-2} (m = 371 g m^{-2}) which were dried under variation of the drying rate, according to an experiment after Baunach et al.[73] The drying rate was adjusted either by variation of the temperature or the heat transfer coefficient, corresponding to the settings (1) to (4), also summarized in Table 3.3. The adhesion force of the reference electrode dried at a drying rate of 0.75 g m^{-2} s^{-1} and a heat transfer coefficient of 35 W m^{-2} K^{-1} at a capacity of 2.5 mAh cm^{-2} is used for normalization. Figure taken from Kumberg et al., 2019. [24]

Overall, the thick electrodes only reach adhesion values of around 50 % of the thin electrodes. Apparently, an increase of the drying rate leads to a loss in adhesion in both cases. Interestingly, the resulting adhesion force at setting point (3) (high drying rate and high drying temperature) is identical to the one at setting point (2) (low drying rate and low temperature). This means that a high drying temperature is favorable compared to a high heat transfer coefficient for adjusting a certain drying rate.

Table 3.3: Settings (1) to (4) of the heat transfer coefficient and the corresponding isothermal drying temperature to adjust a certain drying rate corresponding to those in Figure 3.2.

Setting	Drying $rate_{theo}$	Heat transfer coefficient	Isothermal drying temperature
	g m^{-2} s^{-1}	W m^{-2} K^{-1}	°C
(1)	1.5	35	41
(2)	1.5	80	31
(3)	2.5	35	49
(4)	2.5	80	41

The reason for the positive effect of the higher isothermal temperature could be an annealing of the binder. To evaluate an impact of annealing, samples of the reference electrode (drying rate 0.75 g m^{-2} s^{-1}, heat transfer coefficient 35 W m^{-2} K^{-1} and 2.5 mAh cm^{-2}) were first dried under identical conditions and then annealed at different temperatures. The adhesion force of these samples was measured and is shown in Figure 3.3 in dependency of the respective annealing temperature.

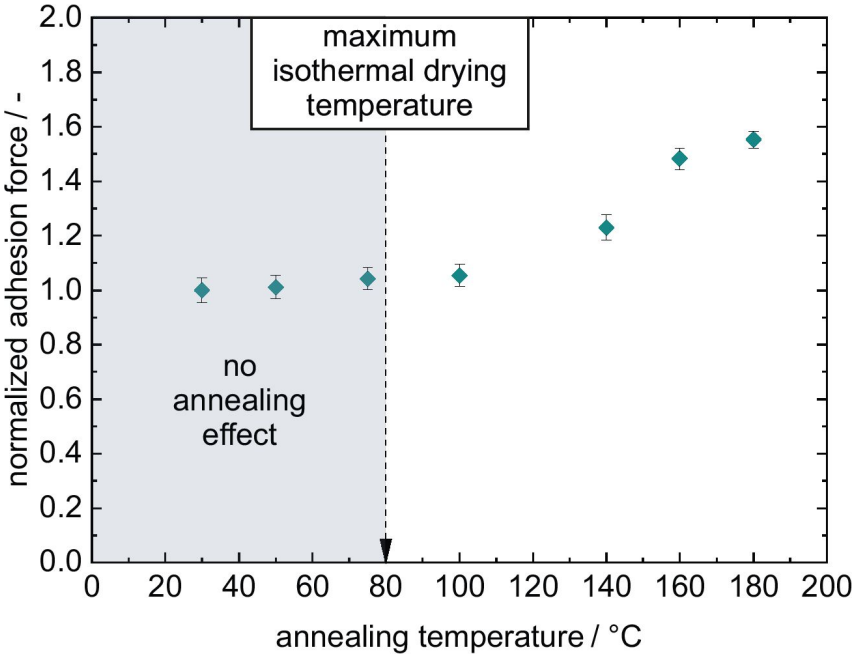

Figure 3.3: Influence of an annealing temperature on the adhesion force of the reference electrode. The electrode was dried prior to annealing at a drying rate 0.75 g m^{-2} s^{-1} a heat transfer coefficient of 35 W m^{-2} K^{-1} and an isothermal drying temperature of 31 °C and had an area capacity of 2.5 mAh cm^{-2}. The definite impact of annealing starts well after relevant isothermal drying temperatures used for drying in this work (see appendix Table A. 2), thereby allowing to separate the effect annealing has on adhesion from the one of drying temperature. The adhesion force of the reference electrode dried at a drying rate of 0.75 g m^{-2} s^{-1} and a heat transfer coefficient of 35 W m^{-2} K^{-1} at a capacity of 2.5 mAh cm^{-2} is used for normalization. Figure taken from Kumberg et al., 2019.[24]

An increase of the adhesion force by 60 % is evident compared to samples without annealing. The maximal isothermal drying temperature used throughout this work was 80 °C and is marked as well. The clear impact of an annealing step becomes noticeable only for temperatures higher than 100 °C. Therefore, the observed positive influence of elevated temperatures at identical drying rates on the adhesion force cannot originate from annealing of the binders. The observed effects are much more distinct than the annealing experiment shows for temperatures below 100 °C.

To expand the range of validity of the finding that a higher drying temperature leads to better adhesion force at an identical drying rate, a wider range of drying

rates was investigated. The exact settings of the heat transfer coefficient and the corresponding isothermal drying temperature to achieve a certain drying rate are listed in the appendix, Table A. 2. The normalized adhesion force in dependency of the drying rate up to a value of 16 g m^{-2} s^{-1} is presented in Figure 3.4. Again, the two theoretical capacities of 2.5 mAh cm^{-2} (m = 74 g m^{-2}) and 12.5 mAh cm^{-2} (m = 371 g m^{-2}) are compared while the heat transfer coefficients are varied between 35 W m^{-2} K^{-1} and 80 W m^{-2} K^{-1}. Normalization was conducted with the adhesion force of the reference electrode (drying rate 0.75 g m^{-2} s^{-1}, heat transfer coefficient 35 W m^{-2} K^{-1} and 2.5 mAh cm^{-2}). Note that varying copper substrates have been used in the experiments. Accordingly, the normalization is based on two different absolute values of the adhesion force. The data points are labeled accordingly. The adhesion force of the reference electrode on (f1) was 18.2 N m^{-1} and on (f2) 9.7 N m^{-1}. Even though the absolute values of the adhesion force deviate strongly, its dependency on the drying rate is reflected independently of the substrate. In Figure 3.4, a clear decrease of the adhesion force along with an increasing drying rate is visible. Again, the adhesion level of the thick electrode lies well beneath that of the thin electrode. The course of the curve appears to be shifted downwards linearly. All electrodes which were dried with the higher heat transfer coefficient and a lower temperature show lower adhesion forces than those dried with lower heat transfer coefficients and higher temperatures. These curves also seem to be shifted parallel, at least up to a drying rate of about 6 g m^{-2} s^{-1}. The adhesion force at higher drying rates appears to converge towards a value between 20 % and 30 % of the reference electrode (drying rate 0.75 g m^{-2} s^{-1}, heat transfer coefficient 35 W m^{-2} K^{-1} and 2.5 mAh cm^{-2}). A similar plateau is reached by the thick electrode for high drying rates. The values of the adhesive force at this point correspond to those measured when the electrodes were dried without any SBR binder.

Two conclusions can be drawn from this: First, the SBR binder appears to be mainly responsible for the adhesion force, since without SBR only 20 % to 40 % of the reference adhesion force is achieved. Second and more important, high drying rates result in similar values as found for electrodes not containing SBR at all. This confirms the absence of SBR at the substrate-electrode interface and hence the proposed mechanism of binder migration at high drying rates.

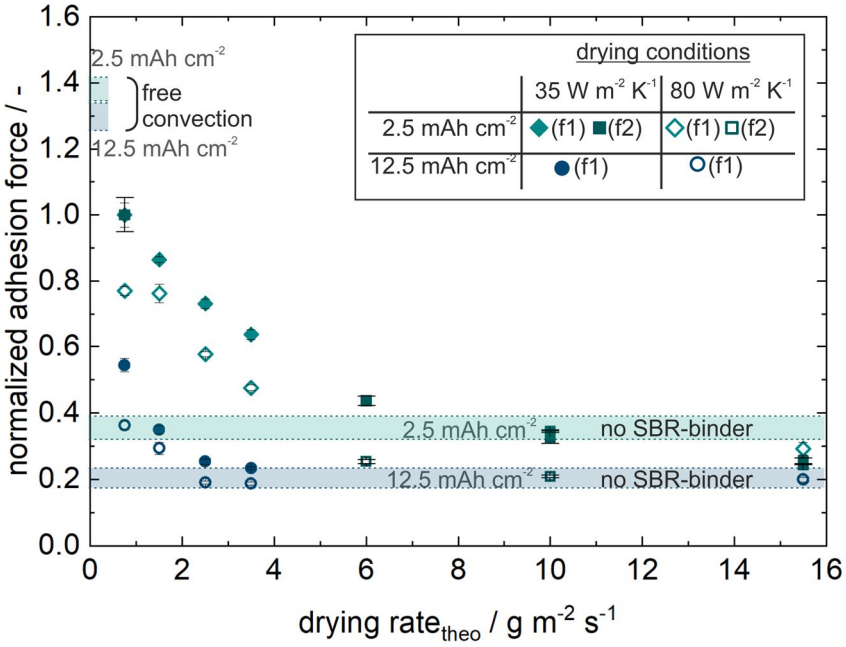

Figure 3.4: Normalized adhesion force in dependency of the drying rate for two different area capacities of 2.5 mAh cm^{-2} (m = 74 g m^{-2}) and 12.5 mAh cm^{-2} (m = 371 g m^{-2}). The heat transfer coefficient was varied between 35 W m^{-2} K^{-1} and 80 W m^{-2} K^{-1} to distinguish between the influence of increasing the heat transfer coefficient and the isothermal drying temperature to increase the drying rate. An upper boundary for the adhesion force is found for electrodes dried under free convection and a lower boundary when electrode are dried without any SBR binder. Two different substrates (f1) and (f2) were used. The adhesion force of the reference electrode dried at a drying rate of 0.75 g m^{-2} s^{-1} and a heat transfer coefficient of 35 W m^{-2} K^{-1} at a capacity of 2.5 mAh cm^{-2} is used for normalization. Figure taken from Kumberg et al., 2019. [24]

In accordance with the lower limit of the adhesive force, an upper limit was found as well. This limit originates from measurements which were made after drying electrodes under ambient conditions, thus a drying under free convection. An increase in adhesion force by a factor of 1.4 for thin electrodes and by 2.3 for thick electrodes is observed. However, the drying rate was estimated to be around 0.01 g m^{-2} s^{-1} for a dew point of 15 °C and a heat transfer coefficient of 2.2 W m^{-2} K^{-1} which is too small to be feasible in industry. Here, diffusion and sedimentation are likely to occur and lead to the high adhesion force.

Altogether, a higher drying rate and an increase of the electrode thickness seem to negatively affect the adhesion force. To a small extent, this can be counteracted by using higher drying temperatures and lower heat transfer coefficients. One reason which might cause this could be increased drag forces when drying at higher drying rates. These could be able to remove partly adsorbed binder from graphite particle surfaces. Since diffusional processes are unlikely to occur, another explanation as to why a higher temperature positively influences the adhesion force will be discussed in section 5.

Binder distribution and drying rate

To validate the adhesion force measurements, an experiment was conducted to measure the CMC amount at the top and bottom of electrodes which were dried at two different drying rates. The dry electrodes were peeled off from the substrate and their top and bottom were analyzed by energy-dispersive X-ray spectroscopy (EDS) to detect sodium (Na) contained in the CMC binder. The results are summarized in Table 3.4. The sodium content at top and bottom is almost identical for the electrode which was dried at the lower drying rate of 0.75 g m^{-2} s^{-1}. For the electrode dried at a higher drying rate of 6 g m^{-2} s^{-1}, almost twice the amount of sodium detected at the bottom was found at the top.

Table 3.4: Comparison of the CMC-binder content at the top and the bottom of two electrodes dried at a low state of the art drying rate[6] of 0.75 g m^{-2} s^{-1} and a higher drying rate of 6 g m^{-2} s^{-1} by measuring the sodium content, which is only present in the (Na-)CMC-binder. The content is given in atomic percent (at.-%).

Drying $rate_{theo}$	Sodium content (CMC) bottom		Sodium content (CMC) top	Na content top/bottom
g m^{-2} s^{-1}	at.-%		at.-%	-
0.75	0.29	≈	0.26	0.9
6	0.19	<<	0.39	2.1

The experimental setup does not allow a quantification of binder migration but is able to prove the assumption that the observed loss of adhesion and binder depletion at the bottom of the electrode are connected. Although this method

detects CMC and not SBR binder, it can be assumed that CMC depletion at the electrode's bottom correlates with SBR depletion, as will be discussed in section 5 (Influence of Slurry Properties).

To make a more quantitative statement about binder migration, another characterization method was applied: Laser-Induced Breakdown Spectroscopy (LIBS). Quantitative determination of the CMC binder distribution was conducted by LIBS for thick electrodes dried at two different drying rates in cooperation with Y. Zheng and W. Pfleging from IAM-AWP, KIT.[64,65,70–72] The CMC binder distribution of thick electrodes which were dried at two different drying rates was investigated. The results are given in Figure 3.5.

The electrode with the mapping shown on the left was dried at a low drying rate of 0.75 g m^{-2} s^{-1} and the one on the right at 3 g m^{-2} s^{-1} with the respective values of their thickness, porosity and area capacity summarized in Table 3.1. The colored scalebar specifies a low Na-content as blue and a high content as red and is given as the percentage of the sodium content at the respective layer and position in relation to the total sodium content which was measured over the whole electrode. In Figure 3.5 left, the color code indicates an accumulation of sodium and hence CMC binder at the surface of the slowly dried electrode. However, this trend is much more distinct in case of the electrode dried at a higher rate. Overall, the color code indicates less sodium at the substrate-electrode interface and more sodium at the electrode surface compared to the slower dried electrode. This also results in a steeper gradient in the Na or CMC concentration respectively over the height of the electrode.

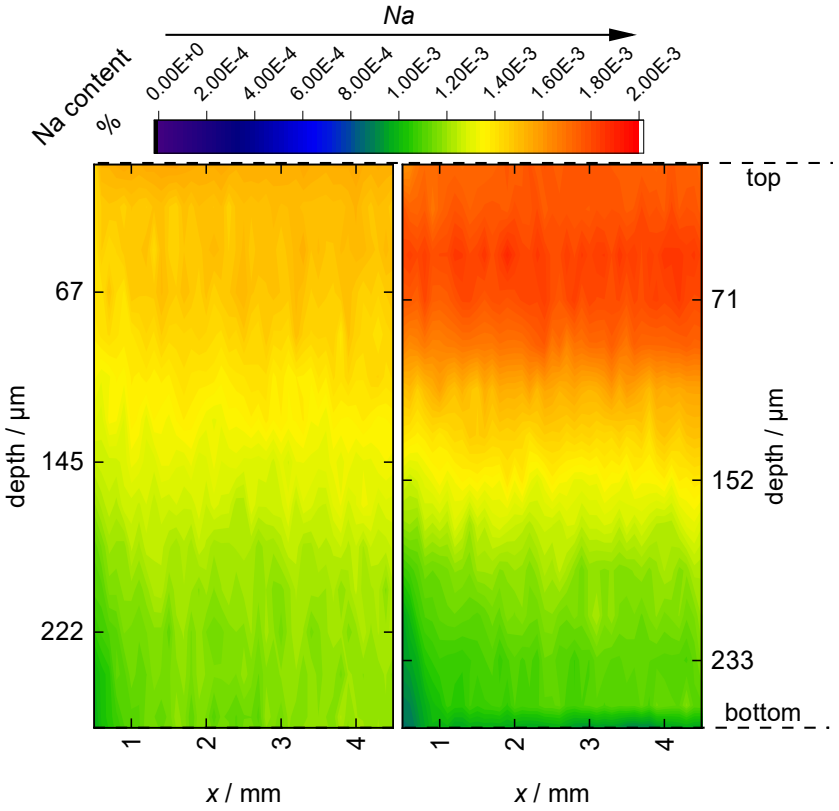

Figure 3.5: LIBS measurements which were made by Y. Zheng and W. Pfleging at IAM-AWP, KIT. The Na-CMC distribution of two thick electrodes of an area capacity of 12 mAh cm^{-2} (356 g m^{-2}), left and 13.5 mAh cm^{-2} (401 g m^{-2}), right is given from the top of the electrode into the depth of the electrode reaching to the bottom. The measurement was conducted over an area of 5 x 5 mm. On the x-axis a width of 4 mm is shown to avoid edge effects with the averaged Na-content for the respective position. The electrodes were dried at a low drying rate of 0.75 g m^{-2} s^{-1} (left) and a four times higher drying rate of 3 g m^{-2} s^{-1} (right), with the respective values of their thickness, porosity and area capacity summarized in Table 3.1. The CMC-binder distribution over their height is compared.

In summary, electrode thickness and drying rate both influence the binder distribution, which was shown by adhesion force measurements, EDX and LIBS. Enhanced properties can be gained by choosing higher temperatures rather than high heat transfer coefficients during drying. An additional aspect when drying

thicker electrodes is crack formation during drying. This is addressed in the appendix in section D.3 and D.4, since it exceeds the scope of this work at this point.

3.3.2 Electrochemical Properties

To extend the previous investigations on the influence of drying parameters on the mechanical properties of the electrodes by the impact drying has on the electrochemical properties, thin electrodes were assembled into coin cells. Their area capacities and porosities are summarized in Table 3.5. All variations in drying rate are restricted to the anode, cathodes were not modified. To establish whether an increase of the drying rate negatively affects the cell performance of water-based anodes, cell tests were conducted. The results are given in Figure 3.6. Since the advantage of an elevated temperature compared to an increased heat transfer coefficient on adhesion and binder migration was shown, all drying rates were adjusted with a heat transfer coefficient of 35 W m^{-2} K^{-1}. Experimentally validated drying rates were 0.5 g m^{-2} s^{-1}, 2.2 g m^{-2} s^{-1} and 5 g m^{-2} s^{-1} (*cf.* Figure 2.5). This resulted in drying times of 134 s, 35 s and 14 s, respectively.

Table 3.5: Area weight and porosity for different thinner and thicker electrodes dried at 2 and 3 different drying rates which were built into coin cells.

Drying rate variation	Experimental drying rate	Area capacity	Porosity
-	g m^{-2} s^{-1}	mAh cm^{-2}	-
1	0.5	2.1	0.5
2	2.2	2.2	0.54
3	5	2.1	0.54
1	0.5	8.8	0.43
2	2.2	8.5	0.47

The specific discharge capacity is given for different C rates. In the cycle test, the difference is most pronounced for the C rate of 3 C. While the cells derived from the electrodes dried at 0.5 g m^{-2} s^{-1} and 2.2 g m^{-2} s^{-1} show identical discharge capacities, the cell with the electrode dried at 5 g m^{-2} s^{-1} performs about 25 % worse. This is in accordance with results from Jaiser et al. (2016) for the NMP-PVDF anode system.[10] An effect of the porosity can be excluded at this point since the porosity of the fast dried electrode is with 0.54 identical to the one of the electrode dried at 2.2 g m^{-2} s^{-1}. An explanation therefore can be given with the binder: The binder is thought to preferentially accumulate on electrochemically active sites. A higher amount of binder at the electrodes surface would be caused by the high drying rate and therefore lead to an increased hindrance of the phase transfer, which is particularly important at higher currents.[39]

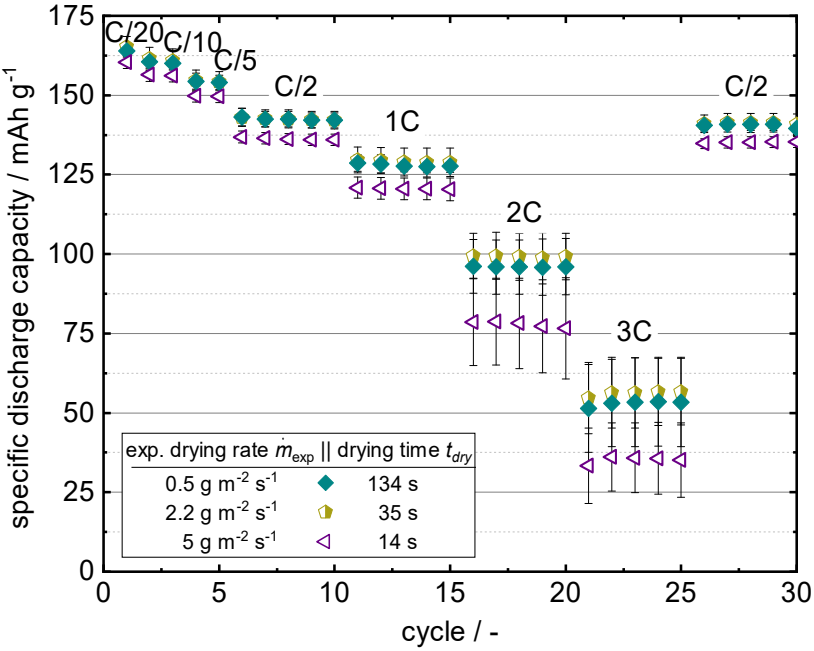

Figure 3.6: Influence of different drying rates on cell performance of thin electrodes with an area capacity between 2.1 mAh cm^{-2} and 2.2 mAh cm^{-2} built into coin cells (see respective area capacities in Table 3.5). Drying was conducted at three different experimentally validated drying rates and at a heat transfer coefficient of 35 W m^{-2} K^{-1}.

The experimental finding that the electrodes perform identical at a drying rate of 0.5 g m^{-2} s^{-1} and 2.2 g m^{-2} s^{-1} was not expected, based on literature. Jaiser et al. (2016) varied the drying rate between 0.5 g m^{-2} s^{-1} and 1.2 g m^{-2} s^{-1} and detected a significant loss in cell performance for the faster dried electrode. However, Jaiser et al. (2016) did not vary the temperature but the heat transfer coefficient. This differs from the experiments conducted here, since the temperature was varied instead of the heat transfer coefficient. In accordance with the lower adhesion loss at increased temperatures (see Figure 3.2) the electrochemical performance does not deteriorate. This will be discussed in more detail in section 5 (Influence of Slurry Properties). Jaiser et al. (2016) furthermore investigated a NMP-PVDF solvent-binder system instead of a water-based system with dissolved CMC binder in combination with dispersed SBR binder used in this work.[10]

To examine the influence of the coating thickness and the drying rate on the electrode performance, electrodes with high area capacity of 8.5 mAh cm^{-2} and 8.8 mAh cm^{-2} were built into coin cells. The applied drying rates were 0.5 g m^{-2} s^{-1} and 2.2 g m^{-2} s^{-1}. The results are presented in Figure 3.7 as the discharge capacity over the cycle number at different C rates. Data of area capacity, drying rate and porosity is summarized in Table 3.5. A difference between the electrode dried at a drying rate of 0.5 g m^{-2} s^{-1} and the one dried at 2.2 g m^{-2} s^{-1} becomes apparent from the beginning. The specific discharge capacity of the electrode dried at 0.5 g m^{-2} s^{-1} exceeds that of the faster dried electrode at all C rates. Since this difference is present from the beginning and the area capacities are not completely identical it cannot be clearly assigned to a drying influence though.

Both electrodes experience a severe loss in discharge capacity at C rates exceeding C/5, which is in accordance with findings from Singh et al. (2016) reported for thick electrodes.[60] A slower drying rate only marginally influences the cell performance at higher C rates, compared to the performance loss caused by increasing the area weight when comparing Figure 3.6 and Figure 3.7 in total.

In summary, it can be concluded that an increase of the drying rate leads to an adhesion loss at the current collector, and a loss in the specific discharge capacity for both thin and thick electrodes, with the restriction that this applies to the capacity of thin electrodes only for the electrodes dried at 5 g m^{-2} s^{-1}. Since drying

evidently impacts electrode properties, the drying process with the special focus on thick electrodes will be illuminated in the following section.

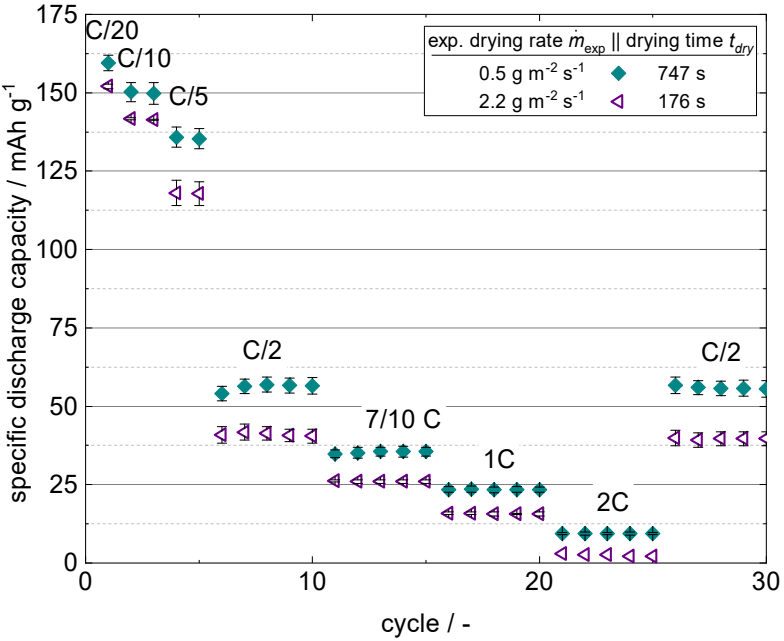

Figure 3.7: Influence of different drying rates on cell performance of thick electrodes with an area capacity of 8.5 mAh cm^{-2} and 8.8 mAh cm^{-2} built into coin cells (see respective area capacities in Table 3.5). Drying was conducted at two different experimentally validated drying rates and at a heat transfer coefficient of 35 W m^{-2} K^{-1}.

4. Drying Behavior of Thicker Electrodes

In this section an experimental and simulative approach is proposed to describe the drying behavior of thin and thick battery electrodes in terms of solvent removal. A simulation model to calculate the solvent loading and film temperature over the drying time is presented and experimentally validated. The experimental setup is comprised of a stationary convection dryer with a measurement setup to record gravimetric drying curves. To investigate the drying process in more detail, two supplementary experiments were conducted: In the first one in situ temperature changes in the film were measured using an infrared camera to validate the simulated temperature curve. In the second one the start of capillary pore emptying was observed using a digital microscope. Based on the findings about the onset of capillary pore emptying, the linear simulation model was extended to consider transport limitations within the porous electrode film in the form of a moving drying front model.[1]

4.1 Motivation and State of the Art

The electrode microstructure forms during the solidification and drying process. As was shown in previous works, the drying process itself impacts the cell performance.[10,11,13] The description and improved understanding of the drying process is therefore important on the way to manufacture improved electrodes and

[1] Results presented in this section are based on two publications by the author:[74,75]
Kumberg, J.; Baunach, M.; Eser, J. C.; Altvater, A.; Scharfer, P.; Schabel, W. (2020): Investigation of Drying Curves of Lithium-Ion Battery Electrodes with a New Gravimetrical Double-Side Batch Dryer Concept Including Setup Characterization and Model Simulations. In: Energy Technol. 3, S. 2000889. DOI: 10.1002/ente.202000889.
Kumberg, J.; Baunach, M.; Eser, J. C.; Altvater, A.; Scharfer, P.; Schabel, W. (2021): Influence of Layer Thickness on the Drying of Lithium-Ion Battery Electrodes—Simulation and Experimental Validation. In: Energy Technol., S. 2100013. DOI: 10.1002/ente.202100013.

reduce battery costs. Since a high drying rate affects the electrode properties especially after the beginning of pore emptying has been reached, drying profiles can be applied in industrial dryers to reduce the drying time and meanwhile maintain or improve electrode properties.[10,23,38,68] A goal is to implement drying profiles in industrial multizone dryers. Therefore, the drying behavior has to be understood and critical points during electrode drying need to be known and predictable. If the beginning of pore emptying is known, a drying profile with a high drying rate in the beginning and before pore emptying starts, a moderate drying rate during pore emptying, followed again by a high drying rate, could be applied. Since exact knowledge on drying mechanisms, especially when drying thick electrodes, is scarce, a trial-and-error setting of parameters is usually used, which is work and cost-intensive. Especially with the aim of increasing the area weight of electrode films and considering the optimal case of a flexible product line with customized area weights, being able to predict the area-weight-dependent course of drying is an imperative.

In previous studies drying curves of state-of-the-art anodes and cathodes have been measured by means of measuring the residual moisture at different drying times.[10,38] These hinted on linear drying kinetics for the thin electrodes investigated there.[10,38] To further illuminate electrode drying, with a focus on solvent transport in the microstructure, Cryo-BIB-SEM experiments were performed, which showed that capillary pore emptying likely occurred during electrode drying.[26] In another experiment, cathodes were dried by means of an oven and the drying behavior studied using thermogravimetric analysis (TGA) measurements during drying. A dependency between drying temperature and cell performance was shown with an optimum at a drying temperature of 80 °C. However, drying times between 50 min – 300 min were used in this study which does not correspond to industrially relevant drying times of 2 min and below.[76] The drying behavior of liquid coatings was investigated by Yamamura et al. (2009) using a gravimetric setup to measure the complete film during drying, and compared to a heat flux measurement, showing good agreement. The drying conditions were not entirely defined, since drying was realized by a heating plate in those experiments.[34]

In addition to experimentally obtained drying curves, simulations can be found in literature which describe the transient solvent evaporation in battery electrodes. Wood et al. (2017) used simulations to compare the costs for solvent

removal of NMP-based and water-based electrodes and calculated the necessary energy input for drying based on mass and energy balances.[36] Susarla et al. (2018) used a continuum modeling approach with a volume-averaging model to calculate drying curves. A 1-D-model is applied and capillary transport was not taken into account in these studies.[37] Recent simulation efforts were based on assumptions valid for thin electrode coatings, taking solely gas phase resistances into account. Drying gets more complex with an increase in film thickness due to the increasing impact of the pore structure in the two or three-phase-system a drying electrode represents. The pore interconnectivity and pore size distribution of micro and nanopores gets relevant for solvent diffusion in the gas phase as well as for solvent transport through the capillaries.

First scientific findings of capillary transport playing an important role during drying of porous media were reported by Comings and Sherwood (1934).[33] They described capillary transport to be caused by small pores with small surface menisci leading to different capillary pressure. Liquid is sucked from larger pores and into the smaller pores, which remain solvent-filled, while the larger pores are emptied. Consequently, a high drying rate remains after the end of film shrinkage since water is continuously transported by capillary transport to the surface where it evaporates depending on the surrounding air conditions. A decreasing drying rate would only be expected if surface menisci retreat into the film and the liquid within the film evaporates with a diffusional resistance dependent on the distance between the menisci and the surface of the porous film. Schlünder (1988) hereby showed that a constant drying rate could prevail up to a wet surface area of up to 1 % if evenly and finely distributed capillaries were present and the ratio of the capillary pore radius to the flow and concentration-dependent viscous boundary layer thickness was small.[35] To account for the resistance of the film when all menisci have retreated into the film and no capillary transport takes place, a moving drying front model was proposed by Krischer (1956).[25] Schlünder introduced a moisture conductivity coefficient κ with two limiting cases. The first limit is $\kappa \to \infty$ which describes an infinite solvent conductivity in the porous structure where film resistances are irrelevant. The second limit is $\kappa \to 0$ where a solvent front is present as is the case in the moving drying front model. In between both limits solvent profiles within the porous structure are present and κ is a function of solvent properties like viscosity and surface tension as well as properties of the microstructure like tortuosity and porosity in addition to the dependency on the solvent loading.

To describe the drying of a more complex microstructure, consisting of a network of interconnected pores with a pore size distribution, pore network modelling, 2D simulations and percolation models have been used and reported in literature.[28–32] A lot of work has been done on model systems, requiring extensive computational efforts. In this work a simulation is presented which is based on a drying kinetics model without resolving the pore network in two or three dimensions, thus predicting drying curves of electrodes with little computational effort. The mass transfer resistance in the film is investigated and included to be able to describe experimental drying curves, which are obtained for the first time for this kind of porous materials.

Such a validation of a simulation with experimental drying curves has not been presented in literature so far to the author's knowledge. The major challenge for such a system is to obtain experimentally defined drying conditions and measure continuously and in-situ the mass of the electrode film at the low mass changes present during drying, while not interfering with the drying process itself. In the following a simulative approach is introduced that calculates and describes the drying curves of electrode films at different boundary conditions and with different electrode thicknesses. The simulated drying curves are compared with experiments at such defined drying conditions. In-situ measurement of solvent mass loss and temperature over drying time can be compared with simulation results.

4.2 Experimental Setup

The drying behavior of battery electrodes was investigated experimentally by three different experimental configurations introduced in this section. All setups use convective drying air with the Comb Nozzle dryer introduced in section 2.2.3. The reference coating slurry used was presented in section 2 and 3 as opposed to a slurry variation introduced in section 5 (Influence of Slurry Properties). The three setups used and modified within this section differ in the measurement equipment that was installed below the film and in the substrate material, required for the individual measurement. In the first setup (see Figure 4.1), gravimetric drying curves were recorded using a balance, and the film temperature was recorded at a single point. In the second configuration using the same dryer, IR measurements were performed to visualize the temperature

distribution of the film during drying (see Figure 4.3). The third variation was the coating on a transparent substrate and the observation of air-filled capillaries breaking through to the film's bottom using a digital microscope (see Figure 4.4). The three setups are explained in detail in the following sections.

4.2.1 Gravimetric Setup

To record gravimetric drying curves of films with different thicknesses, the experimental setup shown in Figure 4.1 was used.

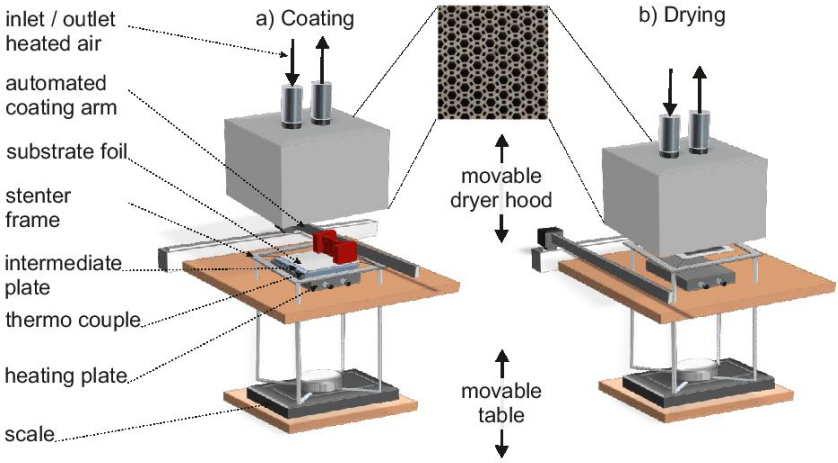

Figure 4.1: Experimental procedure of coating (a, left) and drying (b, right) in the Comb Nozzle dryer. The substrate is fixed in a stenter frame which stands on a precision balance, separated from the setup by spaces through a tabletop. During coating in a), the coating knife is placed on the substrate and moved by an automated coating arm to coat a precise film. A PET-foil with a rectangular cut-out was used as mask during coating and removed directly afterwards. For the drying step in b), the scale along with the tensioned frame and the substrate are moved upwards and the dryer hood downwards. The intermediate plate is removed, resulting in a free hanging copper foil substrate with the electrode slurry film. Figure taken from Kumberg et al., 2020.[74]

For the coating step (Figure 4.1a), the substrate was positioned on an intermediate plate as additional support for the substrate during knife coating, which was itself positioned on top of a heating plate. The substrate was fixed in a stenter frame which stood on a precision balance (Sartorius MC1LC12005), separated

from the setup by spacers through a tabletop. For the coating step, the coating knife was placed on the substrate and moved by an automated coating arm at a velocity of 6 m min^{-1} to coat a precise film. A defined coating area along with a homogenous film thickness is mandatory for the interpretation of the drying curve. Therefore, a polyethylene terephthalate (PET) foil with a rectangular cut-out of 9x9 cm was used as mask during coating and removed directly afterwards, thus defining the size of the coating A_{el}. The coating procedure is schematically shown in Figure 4.2. The knife-coating width and length were broader than the cut-out. Thus, elevated edges were removed along with the PET-mask before drying.

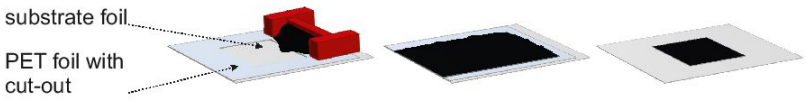

Figure 4.2: Coating procedure. For the coating step, the coating knife was placed on the substrate and moved by an automated coating arm at a velocity of 6 m min^{-1} to coat a precise film. Since a defined coating area along with a homogenous film thickness is mandatory for the interpretation of the drying curve, a polyethylene terephthalate (PET) foil with a rectangular cut-out of 9x9 cm was used as mask during coating and removed directly afterwards, thus defining the size of the coating A_{el}. Figure taken from Kumberg et al., 2020 [74]

For the drying step (Figure 4.1b), the scale along with the stenter frame and the substrate were moved upwards by a pneumatic cylinder within 1 s and the dryer hood was moved downwards. Subsequently, the intermediate plate was removed, resulting in a free hanging copper foil substrate with electrode slurry coating. The distance between the dryer hood and the substrate was set to 2 cm with a resulting heat transfer coefficient α_{TLC} of 35 W m^{-2} K^{-1}. The distance between the heating plate at the bottom and the substrate was 3.6 cm to enable free convection in the air gap. These conditions were chosen not only for experimental reproducibility but also with regards to defined boundary conditions for subsequent drying simulations.

The temperature of the heating plate $T_{heating\ plate}$ was set to 50 °C in all experiments that are shown here. The temperature of the air T_{dryer} was around 80 °C and was adjusted for each experiment according to the dew point and the drying rate. The substrate was copper foil (f3) (electrodeposited, CIVEN Metal, China) of 19 x 19 cm with a thickness of 10 µm. The temperatures of the heating plate,

the drying air and the film were measured with a thermocouple (type T) during each experiment. The parameters used for the drying experiments conducted in this work are summarized in Table 4.1.

Table 4.1: Parameters for the three different experimental setups combined with the comb nozzle dryer to investigate the drying behavior of battery electrodes. The setups consisted of (1) a gravimetric installation, (2) an IR camera inserted beneath the dryer and (3) a digital microscope used to investigate capillary pore emptying. The specific settings used in each setup during drying are summarized. All three setups were developed and built within this work, whereas the comb nozzle dryer itself was built prior to this work.[57]

Drying setup	T_{dryer}	$T_{heating\ plate}$	α_{TLC}	A_{el}	Substrate
	°C	°C	W m^{-2} K^{-1}	cm^2	-
1: Gravimetric	80	50	35	9 x 9	Copper foil (f3)
2: IR camera	48	-	35	10 x 14	PET foil
3: Microscope	86	-	35	9 x 9	Glass plate

Four different film thicknesses (or area weights (m_1-m_4)) were investigated. Their experimentally obtained dry area weight m, film thickness h_{el} as well as the derived values of the theoretical capacity c_A, porosity ε and solvent loading at the end of film shrinkage $X_{s,EOF}$ are listed in Table 4.2. The solvent loading of the film can be derived from the total mass of the wet film under knowledge of the dry mass of the film. The dry mass was measured for each film after the drying experiment. Since the dry mass was measured in the laboratory environment, the respective sorbed water amount was calculated using data of a colleague in the group who focused on the topic of water absorption in the same electrode materials. The sorbed amount of water was subtracted from the measured dry film weight after Eser, Kumberg et al. (2019).[77] It was between 0.3 and 1.3 g m^{-2} which corresponds to about 0.5 % to 1.8 % of the dry area weight. For each experimental drying curve investigated in this work, at least three experiments were conducted. This results in the error bars given in Table 4.2 for h_{el}[a)]. The standard deviation within a single electrode film is given under standard

deviation[b]. It grows with increasing averaged film thickness and lies between 6 % to 8 % of the total film thickness.

The porosity slightly decreases with growing film thickness. This behavior can be assumed to be caused by the higher film thickness or area weight needing more time to dry and offering more space for the particles to align themselves, resulting in a lower porosity. For the simulation, the thickness-dependent porosity must be taken into account. In this work, a linear empirical fit of the form $\varepsilon_i = -1.081 \cdot 10^{-4} \frac{m_i}{g\, m^{-2}} + 0.592$ was used, with m_i in $g\, m^{-2}$, which is shown in detail in Figure A. 7-23 in the Appendix. The solvent loading at the end of film shrinkage was determined according to equation (2.12).

Table 4.2: Overview of the film properties of the gravimetric experiments for the four electrodes, sorted by their dry area weight m. The measured dry area weight m, film thickness h_{el} and theoretical capacity c_A, porosity ε and solvent loading at the end of film shrinkage $X_{s,EOF}$ are given. The solvent loading of the film can be derived from the total mass of the wet film under knowledge of the dry mass of the film. The dry mass was measured for each film after the drying experiment. The standard deviation within a single electrode film is given under standard deviation[b]. It grows with increasing averaged film thickness and lies between 6 % to 8 % of the total film thickness.

m	c_A	h_{el}[a]	Standard deviation[b]	ε	$X_{S,EOF}$
g m^{-2}	mAh cm^{-2}	µm	µm	-	g g^{-1}
m_1 = 72 ± 5	2.4 ± 0.2	83 ± 5	± 5	0.584	0.658
m_2 = 160 ± 12	5.4 ± 0.4	176 ± 13	± 13	0.575	0.632
m_3 = 201 ± 1	6.8 ± 0.0	220 ± 1	± 18	0.570	0.621
m_4 = 278 ± 10	9.4 ± 0.3	299 ± 16	± 24	0.562	0.600

[a] The indicated errors refer to the repetition of the experiment.

[b] The indicated errors refer to the standard deviation of a single film.

4.2.2 Infrared Camera (IR) Measurements

To determine the temperature of the electrode film during drying, a new experimental setup was constructed within this work using an infrared (IR) camera (FLIR T530) instead of gravimetric measurements. The experimental setup below the film was changed and the heating plate at the bottom of the film as well as the balance were removed, so that the IR camera could be placed underneath the substrate. As substrate PET foil was used. This prevented IR-reflections of e.g. a metal copper foil. The drying air temperature was set to 48°C due to the close proximity of the camera body to the substrate. The experimental conditions were adapted in order to avoid overheating of the camera body. The heat transfer coefficient was set to 35 W m^{-2} K^{-1}. Coating was done manually with the film being fixed in the stenter frame which was then transferred to its final drying position (see Figure 4.3).

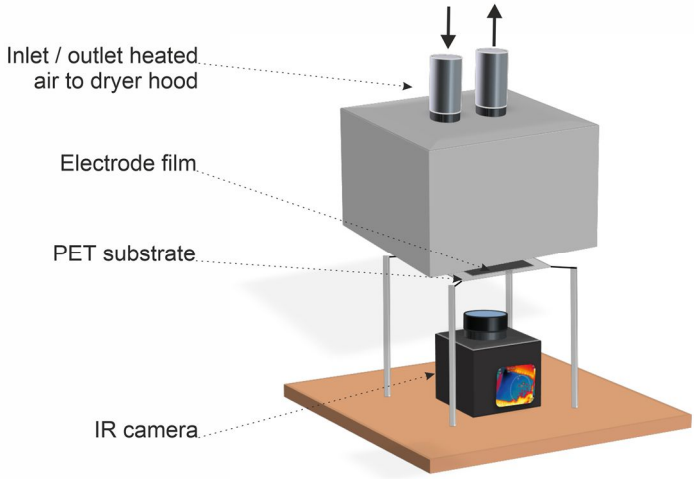

Figure 4.3: Experimental setup to investigate drying patterns using an infrared (IR) camera during electrode drying with the comb nozzle dryer. The electrode film is coated on top of a transparent PET substrate. The choice of substrate allows the investigation of the film temperature without interferences due to reflections.

The chamber around the film was covered with black non-reflecting cloth in order to minimize the impact of exterior IR-radiation. The film temperature was recorded by the IR camera and in parallel measured by a thermocouple type T.

Since no gravimetric measurement was done, no mask for coating area conditioning had to be used during knife coating.

4.2.3 Digital Microscope Measurements

To illuminate the capillary transport within the electrode microstructure and accurately detect the point of time at which the first empty pores break through to the bottom of the film, the experimental setup depicted in Figure 4.4 was designed and constructed within this work.

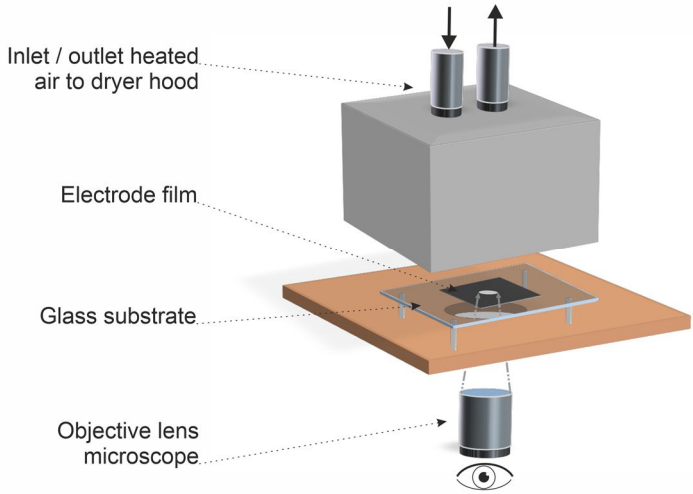

Figure 4.4: Experimental setup to investigate the pore emptying behavior during drying with the comb nozzle dryer. The electrode film is coated by the automated coating arm on top of a transparent glass substrate. The choice of substrate allows the visualization of pore emptying and is also necessary to prevent the movement of the substrate in and out of focus. Figure taken from Kumberg et al., 2021.[75]

A heat transfer coefficient of α_{TLC} = 35 W m^{-2} K^{-1} and a film temperature of 80 °C were used during the experiments. To observe the pore emptying, a digital microscope (Keyence, VHX-6000) was installed with the objective lens positioned underneath the substrate and recording the films bottom during drying through a round cut-out. The electrode film was coated by the automated coating arm on top of a transparent glass substrate. The choice of substrate allowed the visualization of pore emptying and was also necessary to prevent the movement

of the substrate in and out of focus, which would be the case with a more flexible substrate such as the PET foil used during IR experiments (section 4.2.2).

4.3 Simulation of Drying Curves

The simulation model will be presented in the following sections. In the first step, film drying is considered to be mainly dependent on the surrounding air conditions, without accounting for heat or mass transfer resistances within the film. This one-dimensional model, which assumes a homogenous coating and drying area, will be extended to a lateral model in the gas phase, which takes different local drying conditions due to the lateral distribution of impinging heat transfer coefficients in the experimental setup into account (see section 4.3.2 Lateral Simulation Model for Electrode Drying). As a last approach, a film resistance for mass transport in the porous electrode structure is considered and implemented using a moving drying front model as one limiting case described by Schlünder.[35] Its utilization to describe the drying of electrodes of differing thicknesses is critically reviewed in this work.

4.3.1 Constant Rate Model Simulation for Electrode Drying

Drying of a wet film is the removal of a solvent from a solid material by an input of energy and solvent evaporation. This energy can be introduced into the film by IR or laser radiation, by physical contact with a hot surface due to heat conduction, or by a hot gas utilizing convective heat transport. A gas flow is needed in all cases, since not only the energy for solvent evaporation, but also the removal of the solvent-enriched gas phase is necessary. As long as the film surface is saturated with solvent, the drying rate depends on the gradient of the solvent content in the drying gas compared to that at the film gas phase interface. The solvent fraction in the gas phase depends on the air temperature and relative humidity, while the solvent fraction at the interface is determined by the thermodynamic phase equilibrium and the solvent loading of the film. The kinetics of drying are further controlled by the heat transport through the boundary layer into the film, described with the heat transfer coefficient α and the mass transport of evaporated solvent away from the film, described with the mass transport

coefficient $\beta_{i,\infty}$. If no resistance within the film exists to hinder solvent from getting to the surface, an equilibrium is established between incoming heat flux and outgoing enthalpy flux due to evaporation. Consequently, the film temperature remains at a constant equilibrium temperature, which is called the wet-bulb temperature. Only if transport limitations within the film start to play a role, the drying rate will start to decrease and the film temperature increases. From that point on, the solvent content of the film might not only be time-dependent, but also dependent on the position within the film. This is for example the case in polymer film drying.[78] When drying porous or particulate films though, capillary transport of the solvent to the film surface plays an important role.[26] The solvent loading would not be dependent on the position of the film if capillaries transport solvent from the interior of the pore-network to the film surface. Apart from mass transport, heat transfer also influences the drying kinetics. If a film possesses a poor thermal conductivity, a temperature gradient over the film height might result.

Assumptions for Balancing

To evaluate whether a resistance of heat or mass transfer contributes, the Biot number of heat (Bi) and mass transfer (Bi') can be used according to equation (4.1) and equation (4.2) respectively. It is calculated by the resistance outside the film (α_{air} or $\beta_{s,air}$) in relation to the resistance within the film ($\frac{\lambda_{dry}}{h_{el}}$ or $\frac{\delta_{s,eff}}{h_{el}}$).

$$Bi = \frac{\alpha_{air}\, h_{el}}{\lambda_{dry}} \tag{4.1}$$

$$Bi' = \frac{\beta_{s,air}\, h_{el}}{\delta_{s,eff}} \tag{4.2}$$

The diffusion coefficient δ_i, which has to be calculated to determine $\delta_{s,eff}$ (see equation (4.42)), is calculated after the Fuller-equation and is dependent on the temperature and the pressure.[79] The experimental conditions during the gravimetric experiment were used for estimation, with the wet-bulb temperature of the film being approximately 31 °C and the pressure being the ambient pressure of 1.013 bar. The effective diffusion coefficient $\delta_{s,eff}$ was calculated after Zehner, Bauer and Schlünder, under the assumption that diffusion of the solvent takes place only in the gaseous phase and not within the active material.[55] The thermal conductivity λ_{dry} of the electrode was considered with a value of 2.46 W m^{-1} K^{-1}

for a dry electrode.[80] This would be the worst case, since the thermal conductivity of a wet electrode can be expected to be higher than that of a dry one with air in its pores ($\lambda \approx 0.03$ W m^{-1} K^{-1}) instead of water ($\lambda \approx 0.6$ W m^{-1} K^{-1}). For the heat transfer coefficient α_{air}, the value of 35 W m^{-2} K^{-1} was assumed (see Table 4.1), resulting in a mass transfer coefficient of 0.037 m s^{-1}, with the relation between heat and mass transfer defined by Lewis' law.[55] Since the Biot number is dependent on the film thickness, the Biot numbers for heat and mass transfer were calculated for different film thicknesses, which are summarized in Table 4.3.

Table 4.3: Calculated Biot numbers of heat (Bi) and mass transfer (Bi')and the effective diffusion coefficient $\delta_{s,eff}$ within the porous electrode at different electrode thicknesses.

	$\delta_{s,eff}$	Bi	Bi'
	m^2 s^{-1}	-	-
h_{el} = 83 µm	9.4 10^{-6}	0.001	0.304
h_{el} = 176 µm	8.6 10^{-6}	0.003	0.644
h_{el} = 220 µm	8.3 10^{-6}	0.003	0.805
h_{el} = 299 µm	7.7 10^{-6}	0.004	1.094

Since the film porosity is a function of the film thickness and decreases with increasing film thickness (see Table 4.2), the effective diffusion coefficient is also a function of the film thickness (compare Appendix, Figure A. 7-24). At the smallest thickness of 83 µm the Biot number of heat transfer ($Bi \approx 0.001$) as well as the Biot number of mass transfer ($Bi' \approx 0.3$) are well below 1, and the drying therefore governed by the kinetics outside the film. This is true for the heat transfer even at the highest film thickness of 299 µm, with $Bi \approx 0.004$. Hence, temperature gradients over the film height can be neglected. The values for the mass transfer though get close to 1 and even above for the highest film thickness ($Bi' \approx 1.1$), meaning that the inner mass transfer resistance grows. A more detailed calculation at which electrode thickness the Biot number for mass transport takes on values above 1 can be found in the Appendix (section C.2). This is

supplemented by an estimation if capillary pressure, approximated for a bundle of identical single capillaries, is sufficient to transport solvent to the electrode surface even at high thicknesses. Capillary transport is a very important aspect during drying of porous coatings and the Biot number above 1 needs only to be taken into account if no or reduced capillary solvent transport takes place.

The models which are introduced in the following build on each other with the simulations written and programmed in python script. In the first step only thin electrode films are considered. Based on the Biot numbers, no spatially resolved simulation was used under the assumption that heat and mass transfer resistances within the film are neglectable. This can be reasoned with capillary transport moving the solvent to the surface on the one hand, and the fact that even if capillaries break and liquid clusters remain within the microstructure, no significant influence would be expected based on the value of $Bi' << 1$ for thin electrodes. Sorption behavior of the solvent in the battery electrode, consisting mainly of the polymer fraction of 5.6 wt-% and 93 wt-% of the active material, were considered using sorption data of Eser et al. (2019) for battery electrodes.[77] With the thermal conductivity of the active material being sufficiently high, a uniform temperature over the film height would be expected.

With increasing thickness of the electrode though, mass transport limitations within the porous structure start to dominate when considering values of the Biot number of mass transfer. This could influence the drying process in total starting at the point when liquid clusters remain in the microstructure without connection to the capillary network. An increasing amount of these clusters is expected with increasing thickness, since the probability of disturbed transport ways increases as well. Therefore, the model will be extended to account for transport resistances within the microstructure (section 4.3.3 Moving Drying Front Model).

Schematic Model

For balancing, the whole electrode film was considered as depicted in Figure 4.5. This includes the copper foil, with the thermal conductivity of the copper foil being $\lambda_{substrate}$= 395 W m^{-1} K^{-1} and thus being 160 times higher than that of the electrode film and its resistance therefore being neglectable. Solvent evaporation was assumed to take only place at the surface of the film. The main heat input is realized by the dryer from the top with a convective and radiative heat flux. The

heat flux from the bottom is considerably smaller and is composed of free convection and radiation.

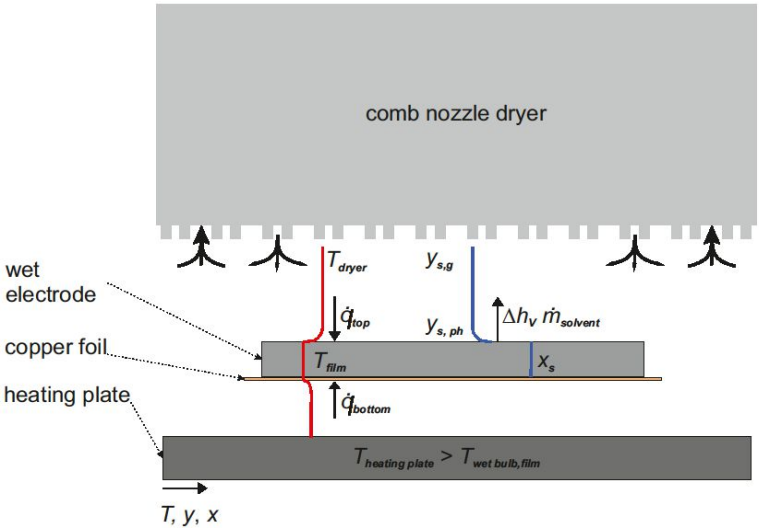

Figure 4.5: Schematic of relevant in- and outgoing heat flows and mass fluxes during electrode drying in the comb nozzle dryer. An ingoing heat flux from the dryer at the top as well as an ingoing heat flux from the heating plate at the bottom can be seen. There is no contact between heating plate and electrode film. An outgoing enthalpy flux into the surrounding at the top of the film is caused by solvent evaporation. Figure taken from Kumberg et al., 2020.[74]

Simulation Model: Instationary Energy Balance and Heating Phase

The transient enthalpy balance of the film consists of the ingoing heat fluxes from the top $\dot{Q}_{top}$ and the bottom $\dot{Q}_{bottom}$ and the evaporation enthalpy flux of the solvent $\dot{H}_S$ leaving the film, according to equation (4.3). The time-dependent enthalpy of the film dH_{film}/dt depends on the film mass M_{film}, the heat capacity $c_{p,film}$ and the difference between the film temperature T_{film} and the reference temperature T_0 with a value of 0 °C.

$$\frac{dH_{film}}{dt} = \frac{d\left(M_{film}\, c_{p,film}\left[T_{film} - T_0\right]\right)}{dt} = \dot{Q}_{top} + \dot{Q}_{bottom} - \dot{H}_S \qquad (4.3)$$

The enthalpy flux of the solvent depends on the evaporating mass flux of solvent $\dot{M}_S$, the temperature-dependent heat capacity of the solvent $c_{p,S}$ and the temperature-dependent evaporation enthalpy Δh_v after equation (4.4).

$$\dot{H}_S = \dot{M}_S\left[c_{p,S}\left[T_{film} - T_0\right] + \Delta h_v\left(T_{film}\right)\right] \tag{4.4}$$

The film temperature changes during drying as soon as solvent evaporation decreases. The film is comprised of the contribution of the dry electrode ($M_{el}\ c_{p,el}$), the copper foil or substrate ($M_{Cu}\ c_{p,Cu}$) and the solvent ($M_S\ c_{p,S}$). The mass of the electrode and the copper foil were constant, in contrast to the mass of the solvent. The change of the heat capacities of all components within the time discretization during simulation was assumed to be very small. Thus, an averaged value for the heat capacity during each time step at the averaged film temperature was calculated. Equation (4.5) results:

$$\begin{aligned}\frac{\left[M_{el}\ c_{p,el} + M_{Cu}\ c_{p,Cu} + \ M_S\, c_{p,S}\right]dT_{film} + c_{p,S}\left[\ T_{film} - T_0\right]\, dM_S}{dt} \\ = \ \dot{Q}_{top} + \dot{Q}_{bottom} - \ \dot{M}_S\left[c_{p,S}\left[\ T_{film} - T_0\right] + \Delta h_v\left(T_{film}\right)\right]\end{aligned} \tag{4.5}$$

To calculate the heat capacity of the dry electrode at different temperatures, the correlation in equation (4.6) after Loges et al. (2016) was used, which was determined in a temperature range of 0 °C to 50 °C.[81]

$$\frac{c_{p,el}\left(T_{film}\ in\ °C\right)}{J\ g^{-1}\ K} = \ 6.841 \cdot 10^{-1} + 2.996 \cdot 10^{-3}\frac{T_{film}}{°C} \tag{4.6}$$

The temperature-dependent heat capacity of the copper foil was calculated according to the "Chemical Properties Handbook".[82] To calculate the temperature $T_{film,2}$ after a time step Δt, equations (4.7) and (4.8) are solved.

$$\frac{dT_{film}}{dt} = \frac{\dot{Q}_{top} + \dot{Q}_{bottom} - \dot{M}_S\ \Delta h_v\left(T_{film}\right)}{M_{el}\ c_{p,el}\left(T_{film}\right) + M_{Cu}\ c_{p,Cu}\left(T_{film}\right) + \ M_S\ c_{p,S}\left(T_{film}\right)} \tag{4.7}$$

$$T_{film,2} = T_{film,1} + \frac{dT_{film}}{dt}\Delta t \tag{4.8}$$

For each time step, the solvent loading X and the mass of the remaining solvent M_S are solved as well (equation (4.9) and (4.10)).

$$X_{n+1} = X_n - \frac{\dot{M}_S}{M_{el}} \Delta t \tag{4.9}$$

$$M_S = X_{n+1}\, M_{el} \tag{4.10}$$

Evaporating Mass Flux

By solving the kinetic equation (4.11), the evaporating mass flux $\dot{M}_s$ can be determined.

$$\dot{M}_s = K_{St}\, \widetilde{M}_s\, \beta_{s,air}\, \tilde{\rho}_{air}(T_{m,t})\; A_{film}\left[\tilde{y}_{s,ph} - \tilde{y}_{s,g}\right] \tag{4.11}$$

It depends on the gradient of the molar fraction of solvent at the interface $\tilde{y}_{s,ph}$ and in the gas phase $\tilde{y}_{s,g}$. It is further determined by the temperature-dependent molar density of the air $\tilde{\rho}_{air}(T_{m,t})$ under the assumption of an ideal gas, the molar mass of the solvent $\widetilde{M}_s$ and the evaporation area A_{film}. $T_{m,t}$ hereby is the averaged temperature between the dryer and the film surface. The Stefan correction factor K_{St} considers additional mass transport caused by interactions between evaporating solvent molecules and resulting drag flows and is calculated after equation (4.12).

$$K_{St} = \frac{\ln\left[\dfrac{1-\tilde{y}_{s,g}}{1-\tilde{y}_{s,ph}}\right]}{\tilde{y}_{s,ph} - \tilde{y}_{s,g}} \tag{4.12}$$

The molar fraction of the solvent in the gas phase can be calculated after equation (4.13) as ratio of the saturation vapor pressure at the dew point temperature $p^*(\tau_g)$ by an Antoine equation in relation to the ambient pressure p.[55]

$$\tilde{y}_{s,g} = \frac{p^*(\tau_g)}{p} \tag{4.13}$$

For the molar fraction of solvent at the interface, the vapor pressure at film temperature and the activity a_s are divided by the ambient pressure (see equation (4.14)).

$$\tilde{y}_{s,ph} = \frac{p^*(T_{film})\, a_s}{p} \tag{4.14}$$

The activity is 1 for a pure solvent and remains at a value of $a_s = 1$ at higher solvent loadings. Only if the solvent loading reaches lower values, the activity

starts to drop. It can be calculated using the Brunauer-Emmett-Teller model given in equation (4.15).

$$X = \frac{X_m k\, a_s\, z}{[1 - a_s\, z][1 + [k - 1] a_s\, z]} \tag{4.15}$$

To integrate the model into the simulation it was converted to the activity in dependence of the solvent loading and the fit parameters k, X_m and z (see equation (4.16)). These values were experimentally determined for an uncalendered anode by Eser et al. (2019), from the TFT working group. The values X_m = 2366.9 ppm, k = 12.9 and z = 1.0 were used.[77]

$$a_{s,1/2} = -\frac{2X - kX + X_m k}{2X(k-1)} \pm \left[\left[\frac{2X - kX + X_m k}{2X(k-1)}\right]^2 + \frac{1}{z^2(k-1)}\right]^{\frac{1}{2}} \tag{4.16}$$

The mass transfer coefficient $\beta_{s,air}$ is determined via the Lewis analogy in equation (4.17), which correlates the heat to the mass transfer coefficient.

$$\beta_{s,air} = \frac{\alpha_{top}}{Le_{s,air}^{1-n}\, \tilde{\rho}_{air}(T_{m,t}) \left[\tilde{c}_{p,air}(T_{m,t})[1 - \tilde{y}_{s,g}] + \tilde{c}_{p,s,gaseous}(T_{m,t})\tilde{y}_{s,g}\right]} \tag{4.17}$$

The Lewis number $Le_{s,air}$ is the ratio between mass transport (Schmidt number Sc) and heat transport (Prandtl number Pr). The Lewis number therefore depends on the thermal conductivity of air λ_{air} in relation to the molar density and the heat capacity of air ($\tilde{\rho}_{air}$, $\tilde{c}_{p,air}$) which are determined after VDI Wärmeatlas (see equation (4.18).[55] It is further related to the diffusion coefficient of the solvent in air $\delta_{s,air}$, derived from the Fuller equation.[79] The exponent n of the Lewis number reflects the air conditions during drying and is assumed to be n = 0.42 for turbulent flows.

$$Le_{s,air} = \frac{Sc_{s,air}}{Pr_{s,air}} = \frac{\lambda_{air}}{\tilde{\rho}_{air}\, \tilde{c}_{p,air}\, \delta_{s,air}} \tag{4.18}$$

Heat Input from the Top

The heat input from the top $\dot{Q}_{top}$ is comprised of the Ackermann correction factor K_A, the heat transfer coefficient at the top $\alpha_{top,overall}$, the film area A_{film} and the temperature difference between film and dryer according to equation (4.19).

$$\dot{Q}_{top} = K_A \, \alpha_{top,overall} \, A_{film} \left[T_{dryer} - T_{film} \right] \tag{4.19}$$

The Ackermann correction accounts for the mass transfer in terms of an enthalpy flux, influencing the heat transfer. It is defined after equation (4.20).

$$K_A = \frac{\ln \left[1 + \frac{c_{p,s}(T_{m,t}) \left[T_{dryer} - T_{film} \right]}{\Delta h_v(T_{film})} \right]}{\frac{c_{p,s}(T_{m,t}) \left[T_{dryer} - T_{film} \right]}{\Delta h_v(T_{film})}} \tag{4.20}$$

The temperature-dependent material-specific properties are calculated after the VDI Wärmeatlas.[55]

The total heat transfer coefficient $\alpha_{top,overall}$ from the top can be derived by addition of the contributions of convection $\alpha_{top,convection}$ and radiation $\alpha_{top,radiation}$ after equation (4.21). The linearized and modified Stefan-Boltzmann equation is used, which assumes an additive composition of the heat transfer coefficients. This is an engineering approach after the VDI Wärmeatlas, applicable if the share of radiative heat transfer is well below the convective and for low to moderate temperatures.[55]

$$\alpha_{top,overall} = \alpha_{top,convection} + \alpha_{top,radiation} \tag{4.21}$$

Convective Heat Transfer Coefficient $\alpha_{top,convection}$

The convective heat transfer coefficient $\alpha_{top,convection}$ of the comb nozzle dryer was determined using thermochromic liquid crystals prior to this work (α_{TLC}).[57] A change of the air flow rate or the distance between the dryer hood and the substrate leads to a different heat transfer coefficient (distribution). This will be explained in more detail in section 4.4.1 (Experimental Drying of Thinner Electrodes). Due to the complex experimental procedure which requires an exact adjustment of the distance between film and dryer hood within mm-range, another method was used to determine the heat transfer coefficient for each experiment: By analyzing the experimental slope of the solvent loading over time during the constant rate period, the drying rate can be derived ($\dot{m}_{s,exp} = \Delta X / \Delta t \cdot M_{el} / A_{el}$) as shown in Figure 2.5. The heat transfer coefficient can be determined via the Lewis analogy after equation (4.22).

$$\alpha_{top,linreg} = \frac{\dot{m}_{s,exp}\, Le_{s,air}^{1-n}\, \tilde{c}_{p,air}}{K_{St}\, \tilde{M}_s \left[\tilde{y}_{s,ph} - \tilde{y}_{s,g}\right]} \tag{4.22}$$

Radiative Heat Transfer Coefficient $\alpha_{top,r}$

The radiative heat transfer coefficient from the top was calculated using the linearized and modified Stefan-Boltzmann equation (4.23).

$$\alpha_{top,radiation} = \frac{C_{12,\mathrm{top}} \left[T_{dryer}^4 - T_{film}^4\right]}{\left[T_{dryer} - T_{film}\right]} \tag{4.23}$$

Among the dryer and the film temperature T_{dryer} and T_{film}, respectively, it depends on the radiation exchange number $C_{12,top}$. Since the nozzle field and the film are parallel to each other, equation (4.24) can be used.[55] For the nozzle field, an emission coefficient for oxidized aluminum of $\epsilon_{nozzle\ field} = 0.2$ and for the film the emission of graphite with $\epsilon_{film} = 0.76$ was estimated. The Stefan-Boltzmann constant is $\sigma = 5.67 \cdot 10^{-8}\ Wm^{-2}\ K^{-4}$.

$$C_{12,top} = \frac{\sigma}{\frac{1}{\epsilon_{nozzle\ field}} + \frac{1}{\epsilon_{film}} - 1} \tag{4.24}$$

Heat Input from the Bottom

Since no evaporation takes place at the bottom of the film, the heat flux $\dot{Q}_{bottom}$ can be described by equation (4.25).

$$\dot{Q}_{bottom} = \alpha_{bottom,overall}\, A_{film} \left[T_{heating\ plate} - T_{film}\right] \tag{4.25}$$

The heat transfer coefficient at the bottom $\alpha_{bottom,overall}$ is composed of a contribution due to free convection $\alpha_{bottom,free\ convection}$ and radiation $\alpha_{bottom,radiation}$ after equation (4.26).

$$\alpha_{bottom,overall} = \alpha_{bottom,free\ convection} + \alpha_{bottom,radiation} \tag{4.26}$$

In the following, the determination of $\alpha_{bottom,free\ convection}$ and $\alpha_{bottom,radiation}$ is addressed.

Heat Transfer by Free Convection from the bottom

To evaluate whether heat transfer by free convection takes place and if so, calculate the exact value, the Rayleigh number (Ra) defined after equation (4.27) is important. Since the driving mechanism behind free convection are density fluctuations caused by temperature differences, it depends on the temperatures of two surfaces, here $T_{heating\ plate}$ and T_{film}, in close vicinity to each other, with their distance l_c. Ra further depends on the isobaric thermal expansion coefficient $B(T_{m,b})$ which can be approximated with $B(T_{m,b}) = 1/\ T_{m,b}$ under the assumption of an ideal gas. $T_{m,b}$ hereby is the average temperature of heating plate and film. The acceleration of gravity g, the kinematic viscosity of air ν_{air} and the thermal diffusivity κ_{air} are needed as well.

$$Ra = \frac{\mathrm{B}(T_{m,b})\ g\ [T_{heating\ plate} - T_{film}] {l_c}^3}{\nu_{air}(T_{m,b})\ \kappa_{air}(T_{m,b})} \tag{4.27}$$

For two extended parallel plates with their margins not influencing free convections, the Nusselt number (Nu) in dependency of the flow conditions, which are assessed by the value of the Rayleigh number, can be determined. Equation (4.28) and (4.29) are based on section F3 in the VDI Wärmeatlas.[55] The lower limit is a value of $Ra\ =\ 1707$, where the Nusselt number becomes 1 ($Nu\ =\ 1$) and the heat transport is solely conductive.

For values of $1707 < Ra < 2.2 \cdot 10^4$, a laminar flow is present, and

$$Nu = 0.208\ Ra^{0.25} \tag{4.28}$$

For values of $Ra > 2.2 \cdot 10^4$ a turbulent flow is present, and

$$Nu = 0.092\ Ra^{0.33} \tag{4.29}$$

The heat transfer coefficient can be calculated in dependency of the Nusselt number, the thermal conductivity of air λ_{air} and the distance between heating plate and substrate after equation (4.30).

$$\alpha_{bottom,free\ convection} = \frac{\mathrm{Nu}\ \lambda_{air}(T_{m,b})}{l_c} \tag{4.30}$$

Due to the experimental setup, the temperature and therefore the density stratification will change during drying: At the beginning, the film temperature is at the

wet-bulb temperature and therefore lower than the temperature of the heating plate. At the end of the constant rate period, the film will start to warm up, until its temperature exceeds that of the heating plate. From that point on, a stable stratification and solely conductive heat transport can be expected.

Heat Flux by Radiation from the Bottom

The contribution of radiation from the bottom is determined after equation (4.31) in accordance with the top, with the difference of the contributing temperatures, here T_{film} and $T_{heating\ plate}$ and a different radiation exchange number at the bottom $C_{12,bottom}$.

$$\alpha_{bottom,radiation} = \frac{C_{12,bottom}\left[T_{film}^4 - T_{heating\ plate}^4\right]}{\left[T_{film} - T_{heating\ plate}\right]} \tag{4.31}$$

For the two parallel plates, meaning the heating plate and the substrate, the radiation exchange number can be determined after equation (4.32). The emission coefficient of the heating plate was considered with that of oxidized aluminum $\epsilon_{heating\ plate} = 0.2$ and the substrates with polished copper $\epsilon_{substrate} = 0.03$.

$$C_{12,bottom} = \frac{\sigma}{\frac{1}{\epsilon_{heating\ plate}} + \frac{1}{\epsilon_{substrate}} - 1} \tag{4.32}$$

4.3.2 Lateral Simulation Model for Electrode Drying

As an extension to the constant rate model, where a laterally uniform drying over the whole area is assumed, the extended model accounts for different local drying conditions over the area and a lateral distribution of the heat transfer coefficient in the gas phase. By this approach the distribution of heat transfer coefficients, which is relevant when drying with the comb nozzle dryer, is considered. For drying simulation this was realized by combining an array of drying curves from the constant rate simulation model, weighted according to the frequency of occurrence of each heat transfer coefficient, to one drying curve. As a result, different local drying rates are considered, while a lateral solvent transport is not accounted for. In Figure 4.6 the distributions of the heat transfer coefficient for five different values of a median value for the heat transfer coefficient (α-median) are given. To each value of a heat transfer coefficient its relative surface

fraction $\bar{A} = A(\alpha)/A_{film}$ is assigned. The shown distribution was determined by TLC measurements prior to this work, at a distance of 20 mm between substrate and dryer hood at five different air flow rates which resulted in the given values of the heat transfer coefficient.[57]

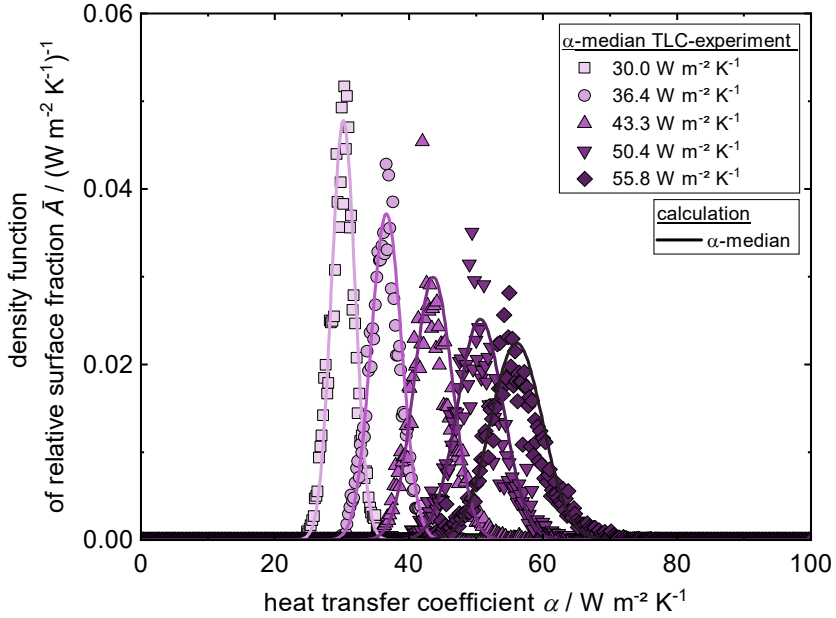

Figure 4.6: Heat transfer distribution for different values of a median heat transfer coefficient and the respective relative surface area. The distributions of the heat transfer coefficient for five different values of a median value for the heat transfer coefficient (α-median) are given. To each value of a heat transfer coefficient its relative surface fraction $\bar{A} = A(\alpha)/A_{film}$ is assigned. The shown distribution was determined by TLC measurements prior to this work. Figure taken from Kumberg et al., 2020.[74]

To implement the distribution into the simulation, a gaussian fit was used to describe the experimental data, which is given in equation (4.33). The parameters of the fit curve were the offset y_0, which was approximated with zero for all data, the curve width w, the peak position x_c, the heat transfer coefficient (distribution) and the area A. The step size of the heat transfer coefficient was 0.2 W m^{-2} K^{-1}. The area A was normalized to $A = 1$, meaning that the sum of the relative fractions always adds up to be one.

$$\bar{A} = y_0 + \frac{A}{w\sqrt{\frac{\pi}{2}}}\, e^{-2\left[\frac{\alpha - x_c}{w}\right]^2} \tag{4.33}$$

The parameters w and x_c in dependency of the experimental value of the median heat transfer coefficient are given in Figure 4.7.

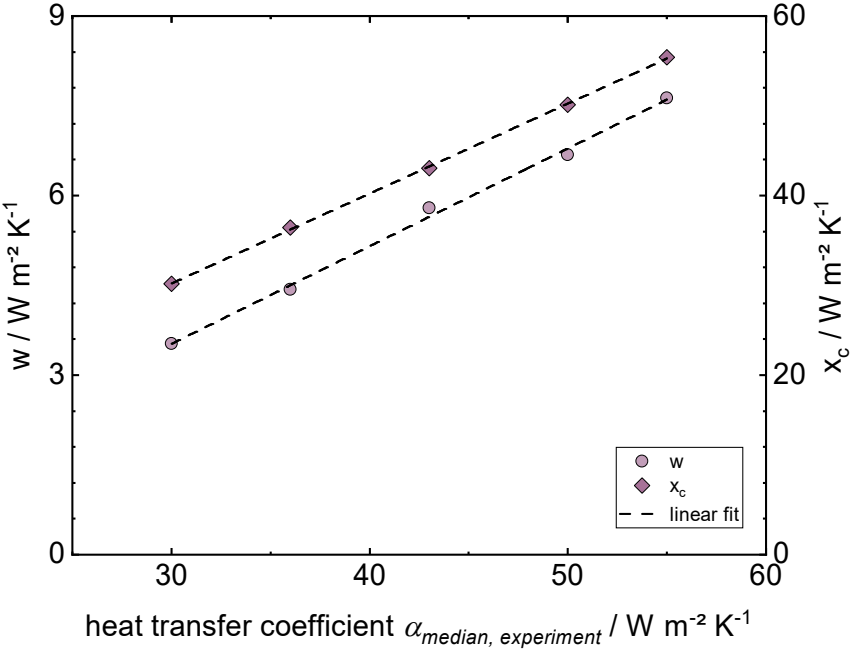

Figure 4.7: Parameters w and x_c of the gaussian fit function in dependency of the experimentally determined heat transfer coefficients α-median. They clearly show a linear relation. Based on this, the linear fit functions in equation (4.34) and (4.35) can be used to describe their dependency on the heat transfer coefficient. Figure taken from Kumberg et al., 2021.[74]

They clearly show a linear relation. Based on this, the linear fit functions in equation (4.34) and (4.35) can be used to describe their dependency on the heat transfer coefficient.

$$w = 0.16328\ \alpha_{median} - 1.37641\ W\ m^{-2}\ K^{-1} \tag{4.34}$$

$$x_c = 1.00223\ \alpha_{median} + 0.13585\ W\ m^{-2}\ K^{-1} \tag{4.35}$$

The impact of the distribution of the heat transfer coefficient on the heat flux as well as on the resulting evaporating mass flow are shown in equation (4.36) to (4.37). The time-dependent temperature and solvent loading are calculated for each heat transfer coefficient, resulting in a set of temperature and solvent loading curves with their respective area fraction. To derive the temperature and solvent loading of the film in total, the single curves are merged into one, after equation (4.38) and (4.39).

$$\dot{Q}_{top,i} = K_A\left[\alpha_{top,c,i} + \alpha_{top,r}\right] A_{film}\left[T_{dryer} - T_{film}\right] \tag{4.36}$$

$$\dot{M}_{s,i} = K_{St}\,\tilde{M}_s\,\frac{\alpha_{top,c,i}}{Le^{1-n}\,\tilde{\rho}_{air}\;\tilde{c}_{p,air}}\,\tilde{\rho}_{air}\,A_{film}\left[\tilde{y}_{s,ph} - \tilde{y}_{s,g}\right] \tag{4.37}$$

$$T_{film}(t) = \sum_{i=1}^{n} T_{film,i}(t)\,\bar{A}_i \tag{4.38}$$

$$X_s(t) = \sum_{i=1}^{n} X_{s,i}(t)\bar{A}_i \tag{4.39}$$

4.3.3 Moving Drying Front Model for Electrode Drying

Heretofore, the proposed model assumes that capillary transport provides a solvent-saturated electrode surface throughout drying. Consequently, no transport resistances within the film are of any importance and were considered in the simulation. This is reasonable for thin electrode films, as was justified by evaluating the Biot numbers of heat and mass transfer and based on literature.[10] However, the validity of this assumption for thick electrode films has not been investigated yet and can reasonably been questioned due to the high complexity of the electrodes microstructure. As was shown by the estimation of the Biot numbers of heat and mass transfer, a heat transfer resistance within the film is only marginally affected by the film thickness (section 4.3.1 Constant Rate Model). This is, however, not true for mass transfer resistances within the film. With a growing film thickness, the significance of mass transfer resistances within the film increases, until it even exceeds the resistance in the gas phase. Therefore, a film resistance must be considered in the model for the case that capillaries break, and liquid clusters remain within the microstructure which are then subject to mass transfer resistances during solvent vapor diffusion. To correctly implement

transport phenomena, the interdependency between capillary pore emptying as a function of pore radii distribution and pore network, as well as solvent evaporation and transport within the microstructure would have to be considered. As explained earlier, complex pore network modelling would be the instrument of choice, under the assumption that the intricate, real microstructures were accessible by experiments. Even then, high computational efforts would be involved.

Consequently, to establish a feasible model with minimal computational expense, which is able to accurately describe the drying process, even though it does not account for capillary transport phenomena, the moving drying front model as proposed by Krischer and expanded by Schlünder was implemented.[25,35] It assumes that the solvent retreats into the porous film as a homogenous drying front and that transport resistances grow in dependency of the distance of the retreating solvent front to the porous surface, as shown in Figure 4.8. The onset of the retreating solvent front and the film resistance starting to play a role was assumed to correspond to the end of film shrinkage, which can be determined after equation (2.12).

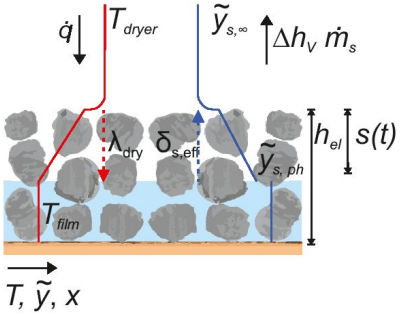

Figure 4.8: Model of the moving drying front after Krischer and Schlünder.[25],[75] It assumes that the solvent retreats into the porous film as a homogenous drying front and that transport resistances grow in dependency of the distance of the retreating solvent front to the porous surface. Figure taken from Kumberg et al., 2021.

For the heat flux, equation (4.19) was transformed to equation (4.40), with the series connection of heat transfer resistances α_{top} in the gas phase and $\lambda_{dry} / s(t)$ in the film. λ_{dry} is the thermal conductivity of the dry electrode and $s(t)$ the time-dependent distance between the assumed drying front and the electrode surface. It was calculated anew in each time-step of the simulation.

$$\dot{q}_{top} = K_A \frac{1}{\frac{1}{\alpha_{top}} + \frac{s(t)}{\lambda_{dry}}} \left[T_{dryer} - T_{film}\right] \tag{4.40}$$

The mass transport resistance is implemented accordingly. Equation (4.11) was extended to equation (4.41), by replacing the resistance in the gas phase $\beta_{s,air}$ by the series connection of mass transfer resistances of film and gas phase.

$$\dot{m}_s = K_S \widetilde{M}_s \frac{1}{\frac{1}{\beta_{s,air}} + \frac{s(t)}{\delta_{s,eff}}} \tilde{\rho}_{air}(T_{m,t}) \left[\tilde{y}_{s,Ph} - \tilde{y}_{s,\infty}\right] \tag{4.41}$$

The diffusion coefficient within the porous film $\delta_{s,eff}$ was calculated after Zehner, Bauer and Schlünder (equation (4.42)) with the diffusion coefficient of the solvent in air $\delta_{s,air}$ and the film porosity ε.

$$\delta_{s,eff} = \delta_{s,air}\left[1 - \sqrt{1-\varepsilon}\right] \tag{4.42}$$

4.4 Results and Discussion

The results of experimentally gained as well as simulation-based insights into drying of battery electrodes of different thicknesses will be presented in this section which is structured as follows:

In the beginning, experimental drying curves of thin electrodes based on the reference slurry (section 3 Drying of Thicker Electrodes) will be discussed with an emphasis on the influence of the heat transfer coefficient distribution introduced by the Comb Nozzle dryer, recorded by an IR camera, which is an important basis for the simulation using the lateral model. The experimental investigation of the drying behavior of thin electrode films is further supplemented by the detection of the onset of capillary pore emptying using a digital microscope, which is necessary to evaluate the moving drying front model. In the next step, a comparison of the experimentally determined drying curves with the simulation using the constant rate and the lateral model is undertaken.

These findings are then transferred to the drying of thick electrodes with the presentation of the experimental results. These are again compared to the

simulation including the model of the moving drying front. In the last step, all models are compared and their applicability in dependency of the film thickness is evaluated.

4.4.1 Experimental Drying of Thinner Electrodes

To illuminate the drying mechanism of thin electrode films, different experimental methods were applied, as detailed in section 4.2.

Experimental Drying Curves Using the Gravimetric Setup

Experimentally obtained drying curves of thin electrodes, recorded with the setup presented in section 4.2.1 (Gravimetric Setup) are discussed here. In the experiment, the course of the total film mass over time as well as the film temperature at the position of the thermocouple are measured. The dryer temperature was set to 80 °C and the heat transfer coefficient α_{TLC} to 35 W m^{-2} K^{-1} (for more details see Table 4.1). A drying curve of an electrode film with an area weight of 72 g m^{-2}, with its further properties listed in Table 4.2, is depicted in Figure 4.9. The solvent loading linearly decreases until it reaches a constant value around zero. This is illuminated by a linear regression of the gravimetric data. The constant drying rate prevails well after the end of film shrinkage, which is marked by a dashed line at a solvent loading of 0.658 $g_{solvent}$ $g_{dry\ mass}^{-1}$.

The temperature starts at an initial value of 26.2 °C, according to the ambient conditions in the lab. With the onset of drying, the film temperature assumes the wet bulb temperature which is the equilibrium temperature caused by the incoming energy from the top and the bottom as opposed to the outgoing enthalpy of evaporation. This temperature prevails almost until the end of the constantly decreasing solvent loading. At this point, the film temperature increases since solvent evaporation decreases or even stops, when the film is dry. During heating up of the film, the energy flow at the bottom of the film changes from ingoing to outgoing. Therefore, the film takes on a constant temperature in the end, resulting from the equilibrium of the input heat energy from the dryer on top and the outgoing heat flux at the bottom.

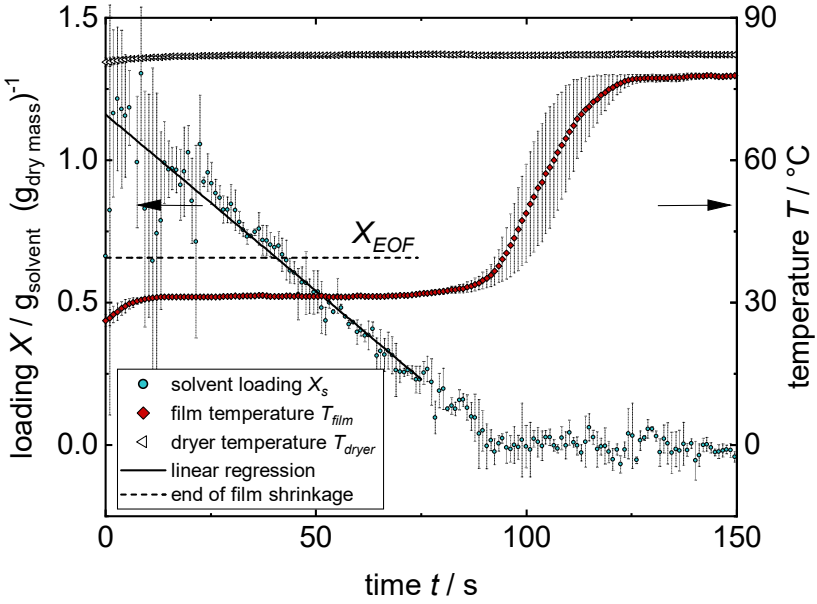

Figure 4.9: Experimentally obtained drying curve of a thin electrode film, with the solvent loading and the film temperature over time. The area weight was 72 g m^{-2}, with further properties listed in Table 4.2. The solvent loading linearly decreases until it reaches a constant value around zero. This is illuminated by a linear regression of the gravimetric data. The constant drying rate prevails well after the end of film shrinkage at a solvent loading of 0.658 $g_{solvent}$ $g_{dry\ mass}^{-1}$ which is marked by a dashed line. Figure taken from Kumberg et al., 2020.[74]

Since for each experimental drying curve shown in this work at least three experiments were conducted, error bars are given for the solvent loading, the dryer, and the film temperature. The larger error bars in the beginning are caused by the sample movement and accompanying table vibrations due to the pneumatic movement from coating position to measurement position, as described in section 4.2.1 (Gravimetric Setup). They are less pronounced at increasing film thicknesses due to the larger total mass and later in drying after the sample has reached its measurement position. The error bars of the film temperature indicate a deviating course of the individual measurements during the heating up phase of the film. This behavior will be further illuminated in the following.

Temperature Distribution Using an IR camera

To evaluate the influence of the distribution of the heat transfer coefficient (see Comb Nozzle characteristics in section 2.2.3) on film drying, experiments as described in section 4.2.2 were conducted using an IR camera. A thin electrode film was coated onto a transparent PET foil and its temperature evolvement recorded. Drying parameters were set similar to the gravimetric setup (see Table 4.1) with the identical heat transfer coefficient of α_{TLC} = 35 W m^{-2} K^{-1}. The dryer temperature was set to 48 °C to protect the IR camera. Recordings of the IR camera at four different times during film drying are shown in Figure 4.10.

The first image (Figure 4.10a) shows the wet bottom of the electrode film after 0 s of drying, appearing in a blue color correlating with a temperature around 20 °C and the expected wet bulb temperature at the chosen drying conditions. In the background, the comb nozzle field can be detected in a yellow to white coloring and a temperature of about 44 °C. Within the film, a white circle marks the film area that was analyzed for its average film temperature during drying. It includes two exemplary measurement points “Sp1” and “Sp2” which show a similar film temperature around 22.5 °C at this point of drying. After 136 s of drying time have passed (compare Figure 4.10b), the film has partially left the wet bulb temperature. In the marked area, red spots have appeared with an elevated temperature of 35.7 °C (Figure 4.10b, Sp1). Meanwhile, Sp2 still remains at a lower temperature of 22.2 °C. This trend continues, since after 145 s of drying, Sp1 is at 39.8 °C and Sp2 still at 22.3 °C (see Figure 4.10c). From both pictures (Figure 4.10b and Figure 4.10c), an elevated film temperature can be detected at the lower right corner, while the rest of the film seems to dry homogenously apart from the hot spots. At this corner the distance to the dryer hood was slightly reduced and therefore explains the faster drying in this region. After a drying time of 250 s both measurement points Sp1 and Sp2 take on similar values around 44 °C, as can be seen in Figure 4.10d. The film within the marked area now appears in a homogenous yellowish to white color. Blue coloring can only be detected at the left-hand side of the film and outside the relevant area, where an elevated film thickness caused by residual slurry is present due to the coating procedure. Besides the spatially resolved investigation of drying, this set-up was used for comparison of IR-measured temperature to a thermocouple fixed to the rear side of the sample (marked in Figure 4.10d).

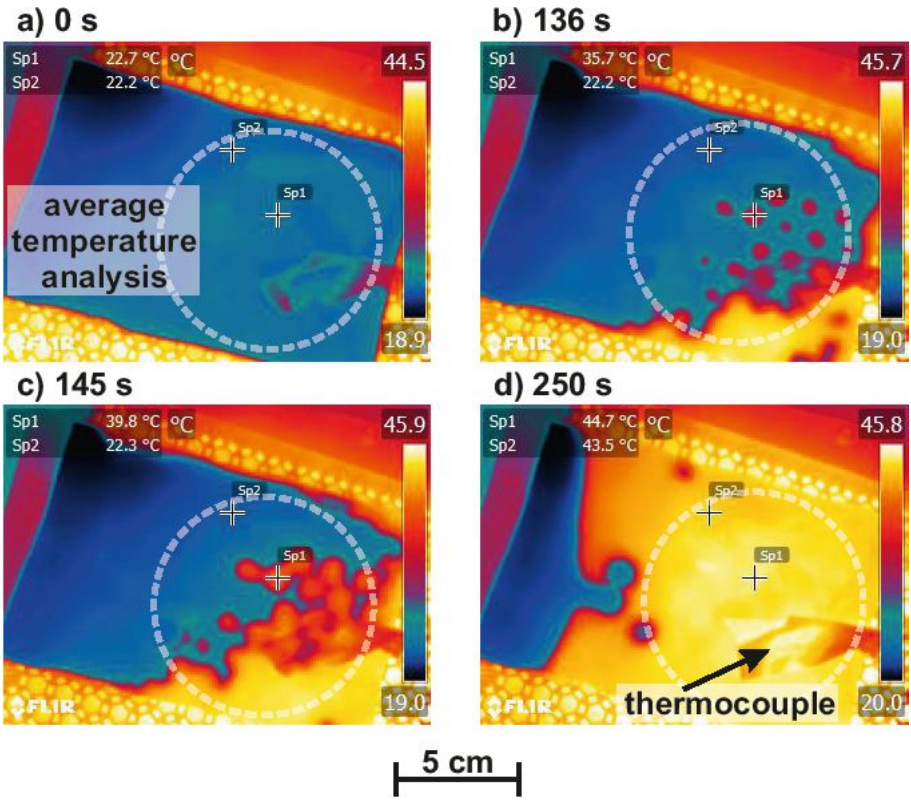

Figure 4.10: IR images which were derived from a recording of the film temperature of an electrode during drying using an IR camera recording from below through a PET substrate. Different times during electrode drying are shown with a) showing the film after 0 s and therefore at the beginning of drying. In b) the same film is shown after a drying time of 136 s and in c) after 145 s. In d) the film is dry within the marked area after a drying time of 250 s. The white circle marks the area which was used for averaging. The obtained values are plotted in Figure 4.11 against the drying time. Figure taken from Kumberg et al., 2020.[74]

One important finding is that the assumption of a homogenous drying over the film area seems not to be accurate. The hot spots in Figure 4.10b and Figure 4.10c match the supply air nozzles of the comb nozzle dryer in size and patterning, which can be found in the background of each picture. The elevated temperature hints that these parts of the film are already dry and no evaporative cooling takes place anymore. This could be caused by the higher heat transfer coefficient directly at the impingement jet stagnation point beneath the supply air nozzle. This

is also confirmed by patterns in the electrode films when drying at extremely high drying rates (see Appendix, Figure A. 7-15 and Figure A. 7-16). For the simulation it is assumed that no significant lateral solvent transport is present contrary to the evident vertical solvent transport caused by capillary transport. This is reasoned with the differences in length scale which is in the range of 10 mm for a nozzle width (see Figure 2.6) in lateral direction and only about 0.1 mm in the vertical direction for the electrode thickness, hence a difference of about two orders of magnitude.

The averaged film temperature inside the marked area in Figure 4.10, recorded by the IR camera, compared to the film temperature logged by the thermocouple is shown in Figure 4.11. The course of the temperature is identical within the first 100 s of drying for both methods. During the transient phase, the temperature value evaluated from the IR image is higher at first and then below the thermocouple. However, both converge towards the same value at the high stationary temperature. The different course during heating can be explained by the local measurement of the thermocouple. As became evident in Figure 4.10, inhomogeneous heating during drying takes place. Therefore, the locally measured temperature from the thermocouple deviates from the average temperature derived from the IR measurement. Since in the gravimetric set-up the temperature is measured by a thermocouple, inhomogeneous drying and heating explains the large deviation of the film temperature for three repetitions of the same experiment.

In summary, results in this section suggest, that the distribution of the heat transfer coefficient is indeed an important factor during drying and should be considered in the simulation.

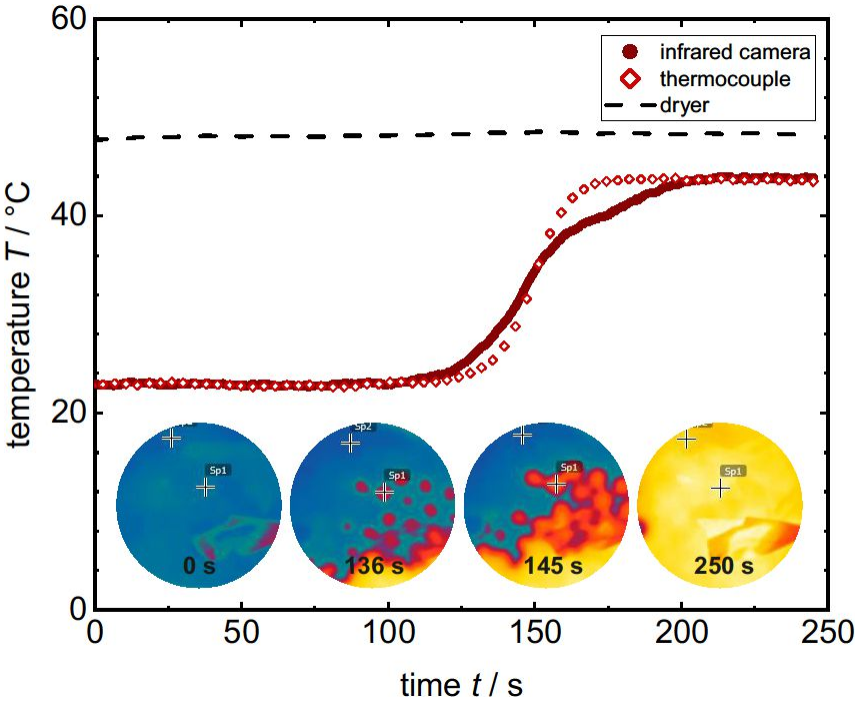

Figure 4.11: Temperature curve of the electrode film recorded with the IR camera. The averaged film temperature taken with the IR camera is compared to that logged by the thermocouple. The course of the temperature is identical within the first 100 s and both converge towards the same value at the stationary temperature. Figure after Kumberg et al., 2021. [74]

Pore-Emptying Behavior Using a Digital Microscope

To investigate whether capillary pore emptying plays a role during electrode drying and at what point empty pores appear, electrodes were examined from below by digital microscopy during drying. The electrode was therefore coated onto a transparent glass substrate (section 4.2.3). Drying conditions were set to those of the gravimetric experiment with a heat transfer coefficient α_{TLC} of 35 W m^{-2} K^{-1} and a dryer temperature of 80 °C. For more information refer to Table 4.1. Pictures of the electrode bottom at different drying times are shown in Figure 4.12.

At the beginning of drying (0 s, Figure 4.12a), the film appears homogeneous. After drying for 45 s, the first empty pore appears. It is circled in Figure 4.12b. More empty pores follow and only after eight more seconds (Figure 4.12c and a

total drying time of 53 s), empty pores are visible homogeneously distributed all over the film. Their density grows in the images showing the film after 60 s and 70 s of total drying time (Figure 4.12d and Figure 4.12e respectively), until no changes can be detected any more after 120 s in Figure 4.12f. The images clearly show that capillary pore emptying is an important mechanism during drying, and that it contributes during the larger part of the total drying time. A comparative investigation will be presented along with results regarding thick electrodes in section 4.4.3 (Experimental Drying of Thicker Electrodes).

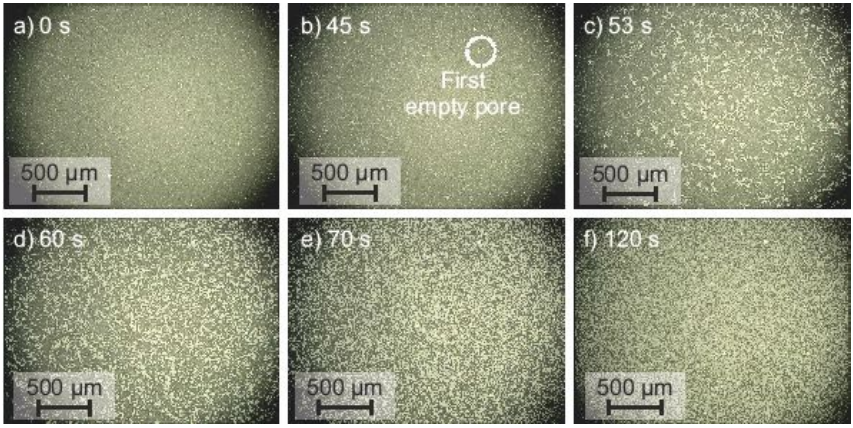

Figure 4.12: Bottom view of an electrode filmed during drying with a digital microscope through a glass substrate. a) shows the wet film at 0 s, the beginning of drying. In b) the first empty pore can be observed after 45 s. c) shows the film after 54 s, d) after 60 s and e) after 70 s with the propagation of empty pores. The film changes no more in f) after 120 s of drying time. The drying course in terms of solvent loading and film temperature will be discussed along with Figure 4.19. Figure taken from Kumberg et al., 2021.[75]

4.4.2 Simulated Drying of Thinner Electrodes

In this section, the application of the constant rate and the lateral model on the drying course of thin electrodes is discussed and compared to experimental data.

Simulation using the Constant Rate Model

The experimental drying curve, comprised of the solvent loading and temperature over time, is compared to the constant rate simulation in Figure 4.13. For the constant rate model only the median value of the heat transfer coefficient is used

to calculate the course of solvent loading and temperature over time. As was explained in section 4.3.1 (Constant Rate Model), the heat transfer coefficient was on the one hand determined according to set drying parameters based on prior dryer characterization using TLCs, resulting in α-median$_{TLC}$. This was on the other hand compared to the heat transfer coefficient derived from a linear regression of the experimentally obtained solvent loading data (*cf.* Figure 4.9), therefore called α-media$_{linreg}$. The dew point for the simulation was derived from a separate dew point measurement during electrode drying (see Appendix, Figure A. 7-17). Both approaches are compared in Figure 4.13. The calculated course of the solvent loading linearly decreases in both cases but follows the experimental solvent loading only in the case of the simulation using the heat transfer coefficient derived from the linear regression.

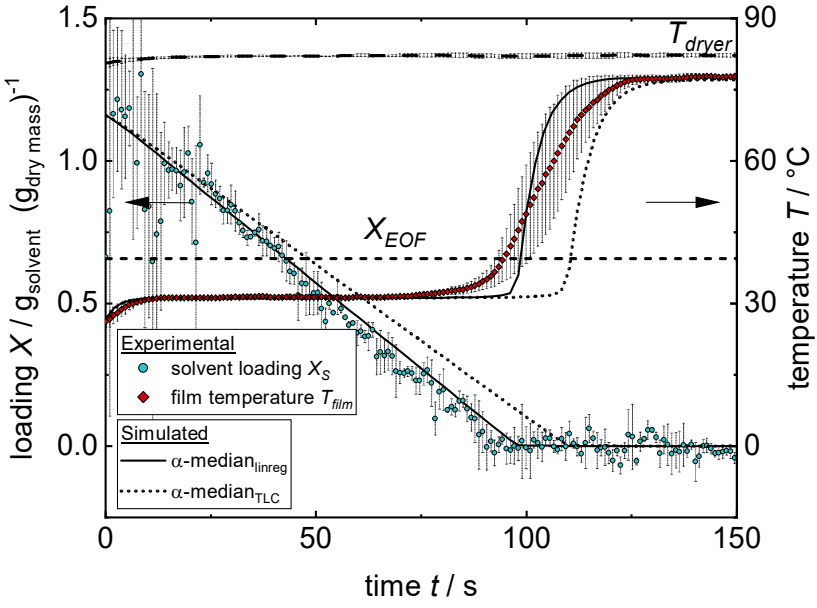

Figure 4.13: Simulated drying curve of a thin electrode film using the constant rate model. The simulation using the heat transfer coefficient derived from TLC measurements (α-median$_{TLC}$) is compared to that based on the determination of the heat transfer coefficient by linear regression (α-median$_{linreg}$). Figure taken from Kumberg et al., 2020.[74]

The slope of the solvent loading calculated with α-median$_{TLC}$ is less steep than the experimental data. The dryer was first characterized with TLCs to set the drying boundary conditions. An exact determination of the real boundary conditions during each experiment must then be made from the slope of the drying curve due to the sensitivity regarding the manually adjusted distance between substrate and dryer hood. As a consequence, α-median$_{linreg}$ with 39.3 W m^{-2} K^{-1} is the actual heat transfer coefficient during the experiment and higher than the calculated 35 W m^{-2} K^{-1} of α-median$_{TLC}$. The drying rate is close to constant during the entire drying process. The sorption equilibrium becomes only relevant at around 100 s, where the curve shows an almost undetectable curvature right before the film is dry. The simulated solvent loading therefore does not reach zero, but the equilibrium solvent loading at the given conditions regarding the phase equilibrium.

The simulated temperature curve follows the experimentally determined initial heating-up phase of the film to the wet bulb temperature during the constant-rate period and the resulting temperature level quite well for both heat transfer coefficients. The second heating-up phase, which starts with the reduced evaporative cooling at the end of the constant rate period, is not correctly simulated in both cases. The reason for this can be assumed to be the spatial distribution of the heat transfer coefficient in combination with the local measurement of the temperature by a thermocouple (see Figure 4.10). The usage of a homogeneous median value obviously is not capable to reproduce the experimental data. It results in an identical drying rate at every lateral position of the film. Consequently, the simulated temperature will only start to rise if the film is dry or has reached the sorption equilibrium. As was shown in section 4.4.1 (Experimental Drying of Thinner Electrodes), the distribution of the heat transfer coefficient leads to non-uniform drying of the film, which will be considered in the following to simulate the temperature drying curve.

Simulation using the Lateral Model

The distribution of the heat transfer coefficient depends on its median value set during drying, according to equation (4.33). Therefore, α-median has to be determined in a first step, to derive the distribution with its respective relative surface area. The calculated heat transfer coefficient distribution is shown in Figure 4.14 for the value of α-median$_{linreg}$ = 39.3 W m^{-2} K^{-1} which was set in the experiments presented in the previous section 4.4.1. The peak of the Gaussian curve

reflects the heat transfer coefficient with the highest relative surface fraction, which is α-median$_{linreg}$ = 39.3 W m^{-2} K^{-1}. The values extend in both directions and entail a range from 33 W m^{-2} K^{-1} to 46 W m^{-2} K^{-1}. A turquoise legend is contained in the graph with a darker shade for the higher surface fractions and going to almost white as the relative surface fraction decreases to zero. This coloring corresponds to the shaded areas in similar color which are included in Figure 4.15 for the solvent loading course.

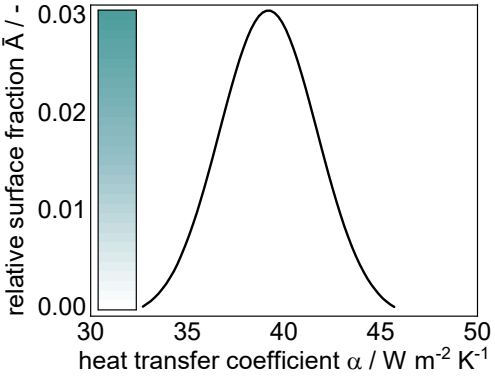

Figure 4.14: Calculated distribution of the heat transfer coefficient derived for α-median$_{linreg}$ = 39.3 W m^{-2} K^{-1}. The turquoise legend assigns a grade of shading to the relative surface fraction of a respective heat transfer coefficient within the distribution. Figure taken from Kumberg et al., 2020.[74]

The drying curves simulated by the lateral model, which accounts for the distribution of the heat transfer coefficient, are shown in Figure 4.15. They are compared to the course derived from the constant rate model. Both calculations are based on α-median$_{linreg}$ = 39.3 W m^{-2} K^{-1} and the course of solvent loading and temperature is shown. Since the lateral model simulates an array of area-weighted drying curves for each heat transfer coefficient, the contributing curves are depicted in Figure 4.15 as well. The intensity of the shading reflects the relative surface area of the respective heat transfer coefficient. The array of curves of solvent loading and temperature add up to the curve of the accumulated α-distribution under consideration of their respective relative surface fractions. This accumulated curve is given as well and is compared to the one derived from α-median:

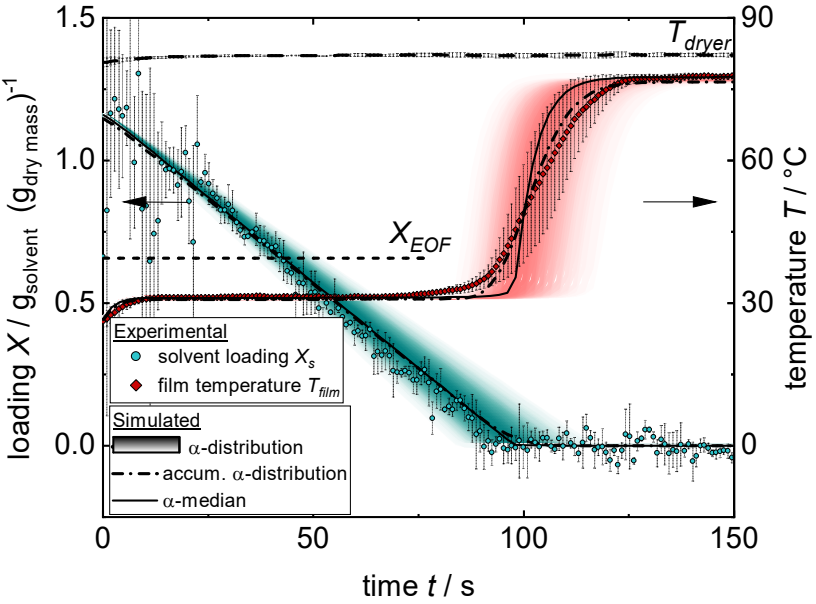

Figure 4.15: Experimental and simulated drying curve of thin electrode. The constant rate model (α-median) is compared to the lateral model (accum. α-distribution). Both calculations are based on α-median$_{linreg}$ = 39.3 W m^{-2} K^{-1}. The courses of solvent loading and temperature are shown. Since the lateral model simulates an array of area-weighted drying curves for each heat transfer coefficient, the contributing curves are depicted as well. The intensity of the shading reflects the relative surface area of the respective heat transfer coefficient (see Figure 4.14). The array of curves of solvent loading and temperature add up to the curve of the accumulated α-distribution under consideration of their respective relative surface fractions. Figure taken from Kumberg et al., 2020.[74]

The course of the solvent loading is almost identical for both simulation approaches, except for a slightly prolonged drying time of the accumulated drying curve at the end of drying. The more pronounced difference appears in the temperature curve. The accumulated curve follows the experimental course almost perfectly, while the one derived from α-median shows a very steep heating up phase which first lags behind the experimental data and then overtakes them. The reason is the consideration of different lateral states of drying with the accumulated α-distribution. Dry areas which are subjected to the highest heat transfer coefficients dry out earlier and start to heat up. These appear to slightly heat up the film in total due to the good thermal conductivity of the film, since heating

up started early in all repetitions of the experiments. This can be deducted from the small standard deviation of the temperature in the beginning. Since the end of the constant rate period and the start and end level of the temperature are accurately determined by the constant rate model, it seems to be sufficient to predict the drying course of a thin electrode film.

The solvent loading is significantly more important for the process design than the exact course of the temperature during the second heat-up phase. Under knowledge of the solvent loading during each time step, the dryer zones could be set to meet certain requirements (see section 4.4.5) and improve electrode properties. The temperature course though gives important insights regarding the end of the constant rate period. Other than the solvent loading, the film temperature can be measured in industrial dryers.

Evaluation of Model Parameters

To examine the simulation model and its input parameters in more detail, the contributions of radiation, convection and free convection at the top and bottom as well as the necessity of the Stefan and Ackermann correction are analyzed. The course of the heat flux densities during drying for the respective contributions as well as their total sum are shown in Figure 4.16.

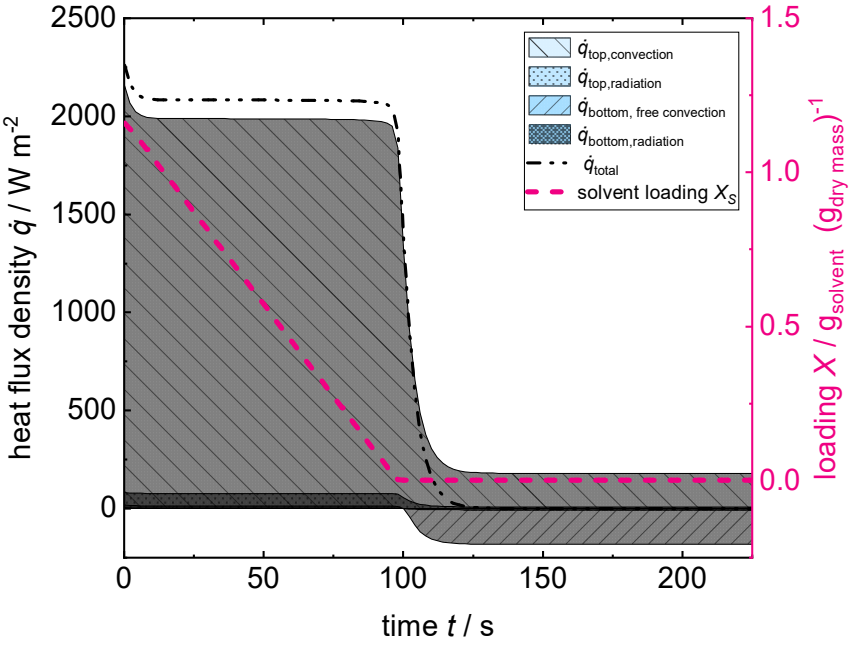

Figure 4.16: Heat flux densities of radiation at the top and bottom, convection and free convection as well as the sum of all contributions during drying of a thin electrode are given, left y-axis. The corresponding course of the solvent loading is given on the right y-axis. After roughly 100 s once the film temperature rises above the temperature of the heating plate, the heat flux caused by free convection changes from ingoing to outgoing. Averaged values of the heat flux densities during the steady-state phase and at the end of drying are summarized in Table 4.4. Figure after Kumberg et al., 2021.[74]

The highest total heat flux is evident within the first seconds of drying since the temperature gradient is at its highest until the film has heated up and reached the wet bulb temperature. The heat fluxes then remain constant until the first regions of the film are dry and the film temperature again increases. The huge impact of the convective heat transfer from the comb nozzle dryer is evident in the first 100 s of drying. At this point, the radiation from the top contributes with 3.7 % to the total heat flux density, while radiation at the bottom is negligibly small with 0.2 % (see Table 4.4).

Table 4.4: Parameters for the three different experimental setups used to investigate the drying behavior of battery electrodes.

	$\dot{q}_{bottom,r}$	$\dot{q}_{bottom,fc}$	$\dot{q}_{top,r}$	$\dot{q}_{top,c}$	K_{St}	K_A
	Wm^{-2}	Wm^{-2}	Wm^{-2}	Wm^{-2}	-	-
$T_{film} = T_{steady\ state} = 30.8°C$	3.5	14.1	77.1	1981.1	1.031	0.989
Contribution in %	0.17	0.68	3.71	95.44	/	/
$T_{film,end} = 77.9\ °C$	-6.4	-182.0	8.5	180.0	1	1

Free convection contributes with only 0.7 % to the total heat flux density during the steady-state phase. This leaves 95.4 % of the heat flux density to be caused by convection from the dryer (absolute numbers are given in Table 4.4). This impact changes when the film is dry. Once the film temperature rises above the temperature of the heating plate, the heat flux caused by free convection changes from ingoing to outgoing. The equilibrium temperature of the dry electrode now results from the ingoing heat fluxes of convection and radiation at the top and the outgoing heat fluxes of radiation and free convection at the bottom of the film. This is reflected in the sum of the heat flux densities which equals zero at the end of the second heating phase at roughly 125s.

Averaged values of the heat flux densities during the steady-state phase and at the end of drying are summarized in Table 4.4. The Stefan and Ackermann correction factors are listed as well. As long as solvent evaporates, both K_{St} and K_A have values other than one. Still, both values are very close to unity and could be neglected for simplification.

4.4.3 Experimental Drying of Thicker Electrodes

The experimental investigation of the drying behavior of thick electrodes will be presented in the following.

Gravimetric Drying Curves of Electrodes with Differing Area Weights

The course of the solvent loading and the film temperature of electrodes of four different area weights m_1-m_4 is shown in Figure 4.17, bottom. Detailed information on the exact area weights and film thicknesses is summarized in Table 4.2. For better interpretation, the experimental data is also shown in form of the (wet) area weight of the drying electrode over time (Figure 4.17, top). The data for the lowest area weight m_1 is thereby identical to the one discussed in sections 4.4.1 and 4.4.2 for thin electrodes. For better visualization, data points have been reduced to only every fourth data point in all curves and curves have been shortened in the graph of the solvent loading to avoid overlapping.

In the graph showing the (wet) area weight over time, the different dry area weights are visible as constant plateaus at the end of drying. The slope of all four curves is close to parallel at the beginning of drying, which means roughly within the first 100 s. This means that drying conditions in form of the drying rate were close to identical. In the course of the solvent loading over time, the linear curve of the electrode with the lowest area weight (m_1) stands in contrast to the drying curves of all electrodes with higher area weights. All of the latter show a deviation from the linear course after more or less the first half of the respective drying time. Since the porosity depends on the area weight of the electrode, the solvent loading at the end of film shrinkage is slightly different for all area weights. Consequently, it is represented by a grey shaded area with its lower limit corresponding to the electrode with the highest area weight and vice versa. The temperature curves are similar for all films in the beginning. The increased area weight therefore seems not to significantly influence the duration of the initial heating-up phase to the wet bulb temperature. A prolonged second heating-up phase after the constant rate period appears to be present with increasing area weight. The experimental data m_2-m_4 clearly show that the constant rate simulation, on which both, the constant rate and the lateral model are based on, does not suffice to describe the drying behavior of thick electrodes. Both models cannot account for the long non-linear course of the solvent loading during the second half of drying. This will be further investigated in the following.

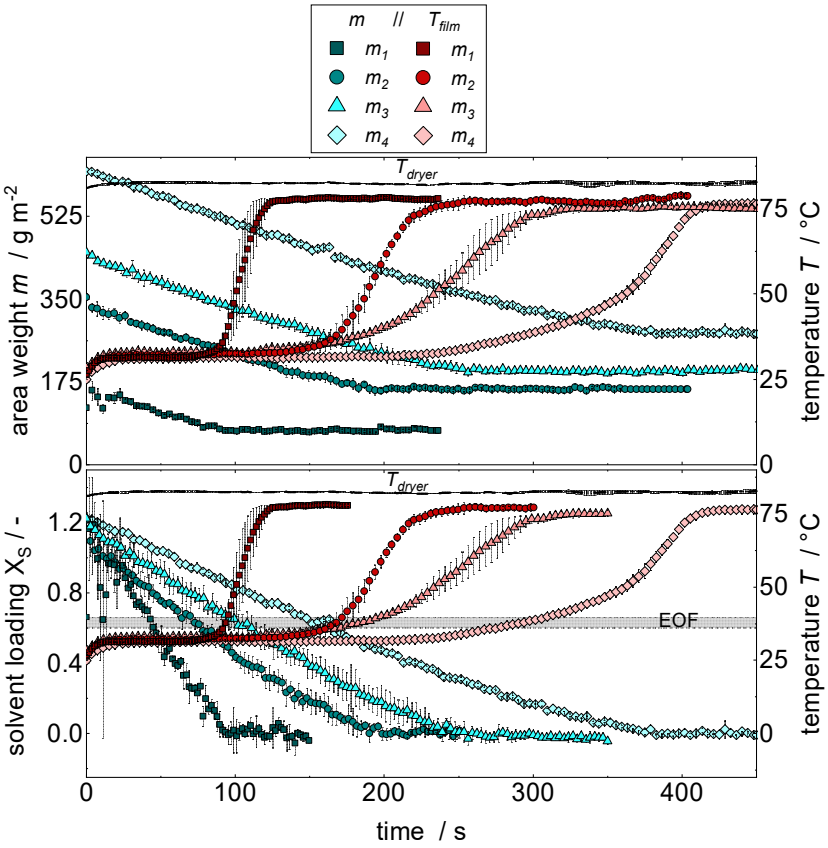

Figure 4.17: Experimental drying curves of thick electrodes with different area weights m_1-m_4, listed in Table 4.2. At the top, the (wet) area weight of the four electrodes over drying time is given. At the bottom, the solvent loading over drying time is plotted. Figure taken from Kumberg et al., 2021.[75]

Pore Emptying Behavior of Electrodes with Differing Area Weights

In an experiment to further illuminate capillary transport in drying of thick electrodes, the digital microscope was used to observe pores breaking through to the bottom of the electrodes. The experimental details are given in section 4.2.3 (Digital Microscope). Different times during drying for the four different area weights which have been investigated are shown in Figure 4.18. The lowest area

weight m_1 corresponds to the one already discussed in section 4.4.2 (Simulated Drying of Thinner Electrodes).

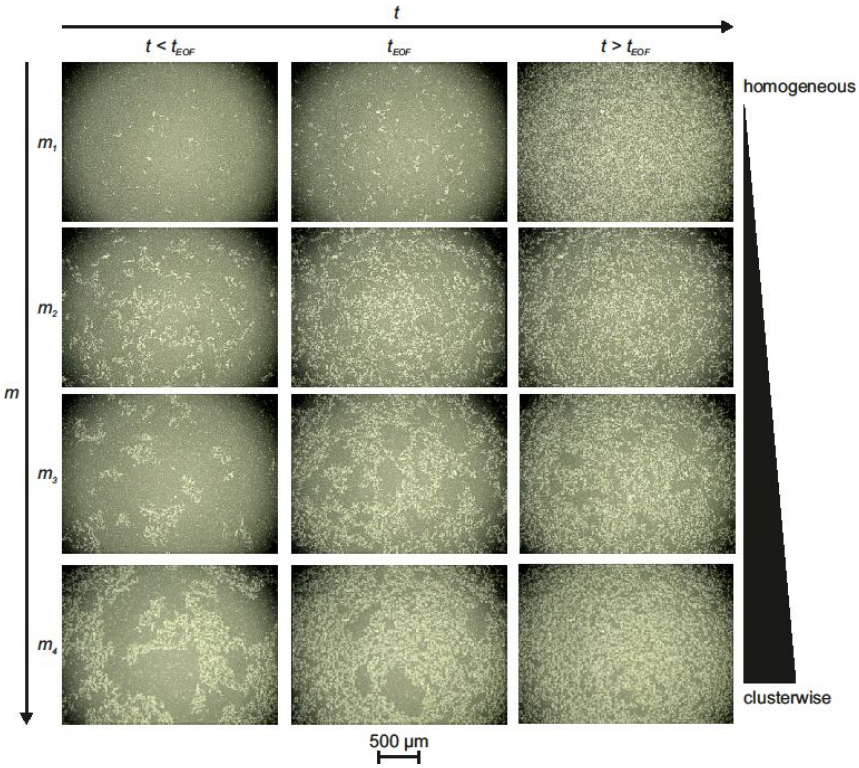

Figure 4.18: Drying patterns of electrodes of different area weights at three different times during drying. In an experiment to further illuminate capillary transport in drying of thick electrodes, the digital microscope was used to observe pores breaking through to the bottom of the electrodes. An increased clusterwise drying with an increasing area weight can be observed. Figure taken from Kumberg et al., 2021.[75]

A homogeneous development of empty pores during drying is present for the lowest area weight electrode m_1. Some empty pores seem to break through to the bottom of the electrode before the end of film shrinkage ($t < t_{EOF}$). The state of empty pores at the bottom at the calculated time of the end of film shrinkage t_{EOF} is shown for all four area weights. The number of empty pores at the bottom at this point increases with the area weight. Another observation is an increased clusterwise drying with an increasing area weight. This points towards the

existence of regions which are not accessible for capillary transport, while other regions show a very early onset of capillary drying. At last a point of time after the end of film shrinkage ($t > t_{EOF}$) is shown for all four area weights. These images show that after some time, the liquid clusters disappear and all pores are starting to empty at one point of drying. Since the end of film shrinkage could not be measured directly due to the dryer hood above and the microscope below the film, an indirect method to determine different times during the experiment was used, which is explained in the following.

Experimental Pore Breakthrough and the End of Film Shrinkage

During the experiment with the digital microscope, a thermocouple was used to record the film temperature. As was shown in section 4.4.2 (Simulated Drying of Thinner Electrodes), the experimentally obtained temperature curve can be described by a simulation if the heat transfer coefficient is known. Therefore, in the case of the experiment with the digital microscope, the median heat transfer coefficient of the simulated temperature curve was fitted using the lateral model, until the experimental and the simulated temperature curves match. The heat transfer coefficient was found to be 36 W m^{-2} K^{-1}. This is shown in Figure 4.19.

With a known median value of the heat transfer coefficient, the solvent loading can be simulated as well, and thus the end of film shrinkage was determined. To simulate both temperature and solvent loading, the model had to be adapted to the glass substrate, with a heat capacity of 720 J kg^{-1} K^{-1} and a weight of 58.7 g as well as the missing heating plate at the bottom. This explains the slow initial heating phase, since the glass substrate which is heated up contributes a large part to the total weight. For better comparison, the times during electrode drying of the thin electrode shown in Figure 4.12b-f are marked. The times determined in the video, especially for the electrode to reach its dry state, coincide well with the simulated solvent loading (Figure 4.19f and Figure 4.12f). The time of the simulated EOF, calculated after (2.12), lies between c) und d), which is in accordance with the most pronounced increase in pore breakthroughs observed with the microscope (see Figure 4.12). This procedure to determine the end of film shrinkage was repeated for the thicker electrodes. In all simulations the same heat transfer coefficient of 36 W m^{-2} K^{-1} was assumed since all experiments were performed directly after one another without changing the dryer setup.

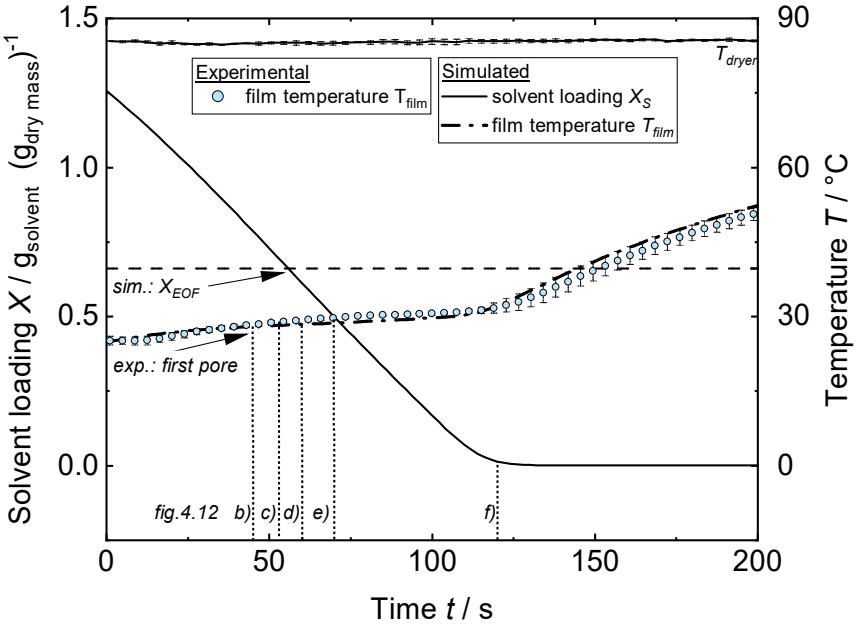

Figure 4.19: Simulation of the solvent loading curve of the experiment with the digital microscope, based on the heat transfer coefficient found by fitting experimental and simulated temperature curves to one another. The heat transfer coefficient was 36 W m^{-2} K^{-1}. The slow temperature increase is caused by the use of the glass substrate in the experiment compared to copper or PET foil in the other two experiments. The glass plate contributes a large amount of additional weight which has to be warmed up, which was also considered in the simulation. Different times of the experimental procedure to observe capillary pore emptying as shown in Figure 4.12b-f are marked.

To compare simulation and experiment, the theoretically obtained times of the end of film shrinkage $t_{EOF,theo}$ are compared to the experimentally observed times $t_{first\ pore,exp}$ in Figure 4.20, when first pores at the bottom of the electrode film become visible.

The actual time is compared to the normalized time, defined as the quotient of $t_{first\ pore,exp}$ to $t_{EOF,theo}$. In absolute values, the time deviation between first pore and EOF seems to be almost neglectable with a value of 6 s for the electrode with the lowest area weight of 67 g m^{-2}. With increasing area weight, the difference between both times increases until it reaches an absolute value of about 60 s for the electrode with the highest area weight of 276 g m^{-2}. The growing

deviation for thicker electrodes is emphasized and also found in the normalized time, which also further deviates from 1 with increasing area weights.

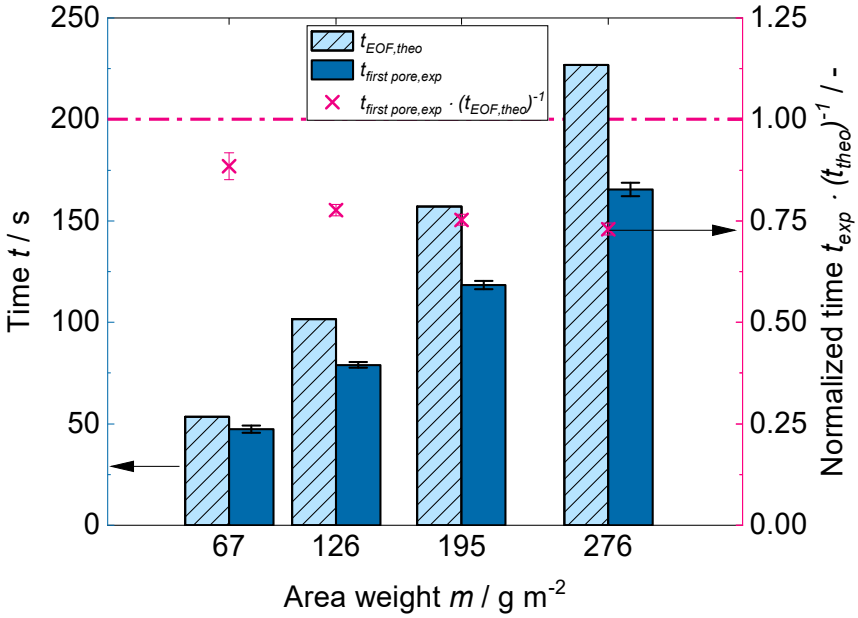

Figure 4.20: Comparison between experimentally determined time when first pores are visible $t_{first\ pore,exp}$ using the setup with the digital microscope and theoretically determined end of film shrinkage $t_{EOF,theo}$ for electrodes with four different area weights. The absolute times are given on the left y-axis and compared to the appearance of the first pore appearing in relation to the theoretical end of film shrinkage shown on the right y-axis. Figure taken from Kumberg et al., 2021.[75]

In summary, it is necessary to distinguish the drying mechanism of thin electrodes with the lowest area weight studied in this work in comparison with electrodes with a higher area weight: While capillary transport was more uniform for the thinnest investigated electrode, this was not the case for all thicker electrodes. Liquid clusters were observed when thicker electrodes of higher area weight were dried. Another important observed difference is the start of capillary pore emptying. For thinner electrodes, a coincidence of the time of the calculated end of film shrinkage with the experimental beginning of pore emptying was observed. For thicker electrodes though, a growing deviation between the end of film shrinkage and the first empty pore is found. For the thickest electrode the

first empty pores occur at a maximum of 27 % before the end of film shrinkage. An earlier onset of capillary pore emptying might hereby influence the time of the end of film shrinkage and shift it to a later drying time.

Different distributions of the particles within the solvent during drying are discussed in literature. One approach for estimating the particle movement during drying was suggested by Cardinal et al. (2010).[84] In dependency of the drying conditions particles take on different positions over the film height. They either dry evenly distributed over the film height in the diffusion regime, accumulated at the surface in the evaporation regime, or mainly positioned at the films bottom in the sedimentation regime. This was also investigated in the TFT working group by Baesch and Gracia et al.[84–86] Evaporation, sedimentation and diffusion are related to one another. This approach is relevant for low solid fractions, was applied in literature though in a similar method. An estimation of the driving forces a graphite particle in a battery slurry experiences during drying is presented by Baunach et al. (2015) in earlier work of the TFT working group. The formation of a consolidation layer, similar to particle drying in the evaporation regime is critically discussed there and found to be probable for welt electrode films.[52] This will be transferred to the drying of thick electrodes in the following.

To evaluate, whether a consolidation layer is likely, the consolidation factor K_C was calculated according to equation (3.1) after Baunach et al. (2015)[52] for graphite particles in a CMC-solution. It is calculated as presented in section 3.3.1 (Binder Migration) and equation (3.1) to (3.6). The mean graphite particle radius was assumed to be r_P = 9.2 µm (see Figure 2.7). The density of the particle was considered with 2260 kg m^{-3} and the density of the CMC-solution with 1002 kg m^{-3}. The dynamic viscosity of the CMC solution at zero shear was derived from experimental curves using the cross-model. This resulted in a zero shear viscosity of 21.7 Pa s.

The diffusion velocity slightly changes with the electrodes area weight, due to the dependency on the volume fraction difference between the start of drying $\varphi_{p,0}$ and the end of film shrinkage $\varphi_{p,EOF}$ (see equation (4.43)), since the porosity changes with the area weight (see Figure A. 7-24).

$$u_{diff} = -\delta_{p,CMC-solution} \frac{\left[\varphi_{p,0} - \varphi_{p,EOF}\right]}{2\, r_p} \tag{4.43}$$

To calculate the evaporation rate u_{evap}, the drying rate $\dot{m}_s$ and the solution density ρ_s need to be known. For the drying rate, experimentally obtained values, which will be presented in the following (see also Table 4.6), were used which take on a value of around 1 g m^{-2} s^{-1}. They slightly differ due to the experimental setup, resulting in different values for u_{evap}.

The resulting value of the consolidation factor is well below one, as can be seen in Table 4.5. Thus, according to Baunach et al. (2015), the influence of the evaporation clearly exceeds the one of sedimentation and diffusion and a consolidation layer could be expected.[52] This is also evident from the absolute values of diffusion, sedimentation and evaporation.

An evaluation of the corresponding drying regime after Cardinal et al. (2010) can also be done.[84] The Peclet number Pe_c and the Sedimentation number N_S.[84–86] Despite the high solid fraction in battery slurries, Peclet number and sedimentation number can be estimated, resulting in a value for $\log(N_S)$ of -1.8 and $\log(Pe_c)$ of 5.8. From this also a clear drying in the evaporation regime and the tendency for particles consolidating at the films surface would be expected.

What needs to be considered at this point though, is the influence of the high volume fraction of the graphite particles, which lies at $\varphi_{p,0}$ = 0.59 at the beginning of drying and at $\varphi_{p,EOF}$ = 0.73 at the end of film shrinkage. The maximal path length a particle would be able to move is shown by relating the distance between maximal and minimal film thickness $h_0 - h_{EOF}$ to the diameter of one particle d_p. For the thinnest electrode this is only two times the diameter of one particle. For the thickest electrode it is nine times its diameter. This leaves not much room for particle movement. So far, no formation of a consolidation layer during drying of thin electrodes was reported even though the drying was observed.[26] Still, an accumulation of particles at the top of the film, moving closer together and thereby building a consolidation layer, could happen for drying of thicker electrode films. This might be one explanation for an earlier onset of capillary transport as was observed for thicker electrodes: The proximity of the particles to one another could lead to the formation of a small meniscus at the

top. Capillary pressure could increase and transport solvent to the surface from within the electrode film.

Table 4.5: Summary of the different driving forces a graphite particle is exposed to during drying in dependency of the area weight m and its effect on the consolidation factor K_c which sets diffusion, sedimentation and evaporation into relation, after Baunach et al. (2015).[52]

m	u_{diff}	u_{sed}	u_{evap}	K_C	$\frac{h_0 - h_{EOF}}{d_p}$
g m^{-2}	µm s^{-1}	µm s^{-1}	µm s^{-1}	-	-
m_1 = 72 ± 5	7.5·10^{-9}	0.011	0.894	0.0120	2.2
m_2 = 160 ± 12	8.0·10^{-9}	0.011	1.055	0.0101	5.1
m_3 = 201 ± 1	8.1·10^{-9}	0.011	1.125	0.0095	6.6
m_4 = 278 ± 10	8.5·10^{-9}	0.011	1.145	0.0093	9.4

Capillary transport depends on the capillary pressure $p_c = 2\gamma \cos\theta / r_c$, which mainly depends on the radius r_c of a capillary, the interfacial tension γ and the wetting angle θ. The smaller r_c is, the higher the pressure. For thin electrodes, the critical pore radius is assumed to be reached close to the end of film shrinkage, when the particles have moved to their closest packing. A meniscus forms at the surface and small capillaries reach to the bottom of the electrode. Capillary transport begins. The fact that for thicker electrodes capillary transport begins even before the particles have reached their theoretical point of densest packing is surprising. One explanation could be the formation of a consolidation layer, which is a locally densest particle packing at the top of the wet film.

Based on the images recorded by the digital camera, capillaries breaking through to the films bottom does not seem to be a uniform phenomenon over the whole surface area. Inaccessible liquid clusters seem to remain within the structure. These will be considered in the simulation, which will be addressed in the following section.

4.4.4 Simulated Drying of Thicker Electrodes

The simulation of the drying behavior in terms of temperature and solvent loading of electrodes with higher area weights is presented. It is a combination of the moving drying front model (MDF) (section 4.3.3) with the constant rate model, as opposed to solely linear drying kinetics without the MDF model applied to thin electrodes in section 4.4.2. As input parameter the heat transfer coefficients were determined by linear regression of the experimental data for drying electrodes of different area weights. These are summarized in Table 4.6.

Table 4.6: Overview of the experimentally determined drying conditions of the electrodes with the four area weights m_1 - m_4. The heat transfer coefficients were determined by linear regression of the experimental data.

m	$T_{wet\ bulb}$	$\dot{m}_s$	$\alpha_{top,linreg}$
g m^{-2}	°C	g m^{-2} s^{-1}	W m^{-2} K^{-1}
m_1 = 72 ± 5	31.5	0.89	39.3
m_2 = 160 ± 12	31.7	1.04	46.1
m_3 = 201 ± 1	32.3	1.12	52.2
m_4 = 278 ± 10	31.4	1.14	51.1

The simulation results and experimental drying curves of the electrodes with four different film thicknesses or area weights (m_1-m_4) are shown in Figure 4.21 with a single graph for each film. The electrode with m_1 was discussed in the previous sections 4.4.1 and 4.4.2. The courses of solvent loading and temperature over time are shown. Experimental data and simulation are compared. Complete drying at a constant drying rate is depicted in each solvent loading curve as a reference. The constant rate model using accumulated α-median and the lateral simulation using the accumulated α-distribution are given.

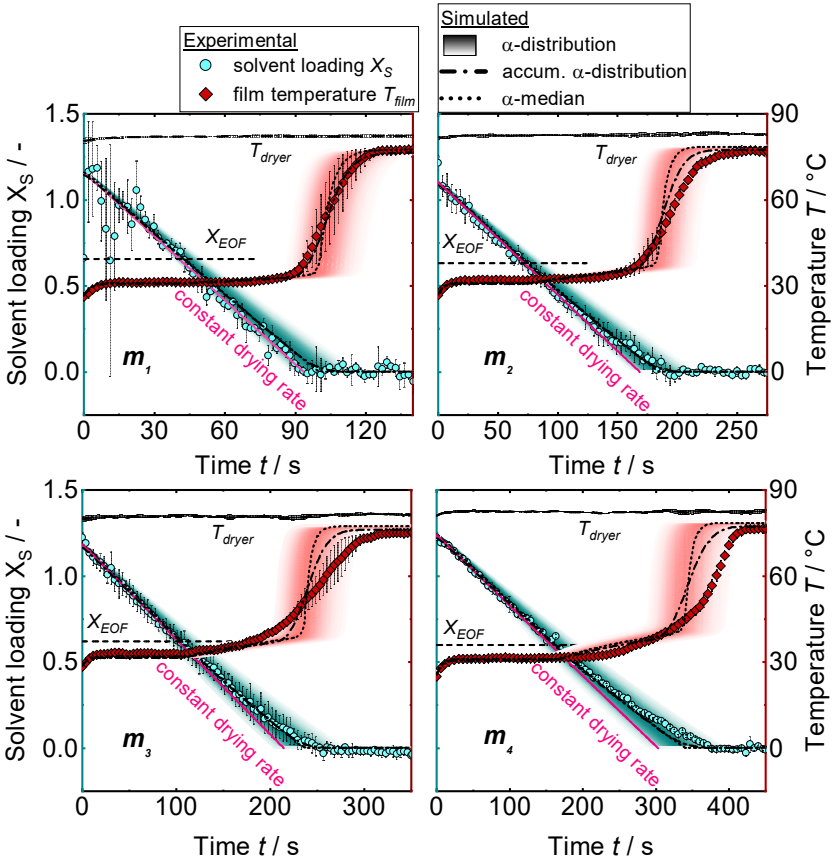

Figure 4.21: Experimental and simulated gravimetric drying curves and film temperatures for four different area weights $m_1 - m_4$.with a single graph for each film. The constant rate model (α-median) is compared to the lateral model (accum. α-distribution). Both calculations are based on the values of α-median$_{linreg}$ given in Table 4.6. The courses of solvent loading and temperature are shown. Since the lateral model simulates an array of area-weighted drying curves for each heat transfer coefficient, the contributing curves are depicted as well. The intensity of the shading reflects the relative surface area of the respective heat transfer coefficient (see Figure 4.14). The array of curves of solvent loading and temperature add up to the curve of the accumulated α-distribution under consideration of their respective relative surface fractions. Figure taken from Kumberg et al., 2021.[75]

Since the lateral model simulates an array of area-weighted drying curves for each heat transfer coefficient, the contributing curves are depicted as well as shaded area. The intensity of the shading reflects the relative surface area of the respective heat transfer coefficient (see Figure 4.14). The array of curves of

solvent loading and temperature add up to the curve of the accumulated α-distribution under consideration of their respective relative surface fractions.

In all cases (m_1-m_4) a constant drying rate appears to be applicable in the beginning. However, besides m_1, all other electrodes at some point during drying show distinct deviations from the linear course. This deviation increases both in magnitude and timespan covered along with the electrode area weight. In case of m_4 the deviation already starts close to the EOF. The temperature curves deviate even more from the experimental data. The choice of the heat transfer coefficient is reflected in the simulation, with the accumulated α-distribution being closer to the experiment. Differences still occur due to the measurement setup, which only measures the temperature at a single spot, compared to the simulation which accounts for the whole film.

The assumption that the end of film shrinkage (EOF) is the starting point of the moving drying front (MDF)-model contributing to drying seems to be justified. This can be reasoned with film drying before the EOF being mainly governed by film shrinkage and a solvent-rich surface of the film. This though, stands in contrast with the findings that capillary pore emptying appears to actually start before the EOF for thicker electrodes. An explanation as to why the MDF-model is still able to predict the solvent loading quite well could be the superposition of two mechanisms in the real drying mechanism.

It was shown that capillary transport takes place during drying which would lead to a constant drying rate throughout drying. It was also shown though, that capillary transport is not uniformly present over the whole area, especially for thicker electrodes (see Figure 4.18). If whole clusters within the microstructure were cut off from capillary transport, they would have to dry by solvent evaporation through the pores, which can be described by the MDF model. Consequently, the MDF model reflects the actual drying course in an averaged form: at the beginning supposedly only few liquid clusters exist, which agrees well with the small contribution of the film resistance at this time. As drying proceeds, more liquid clusters form, which can be close to the surface or deeper within the microstructure. Meanwhile capillary pore emptying continues. The simulated resistance grows, and therefore matches the average of capillary transport in combination with longer and shorter ways for solvent vapor diffusion. The simulation overestimates the actual drying time only in the case of the highest area weight m_4,

where higher amounts of clusters have been found (cf. Figure 4.18) and the highest time difference between first pore and EOF. This might lead to the necessity of an earlier onset of the MDF model in the simulation.

A comparative analysis of the three simulations (MDF with accum. α-distribution, MDF with α-median, and constant rate drying) is given in Figure 4.22 in dependency of the area weight of the electrodes.

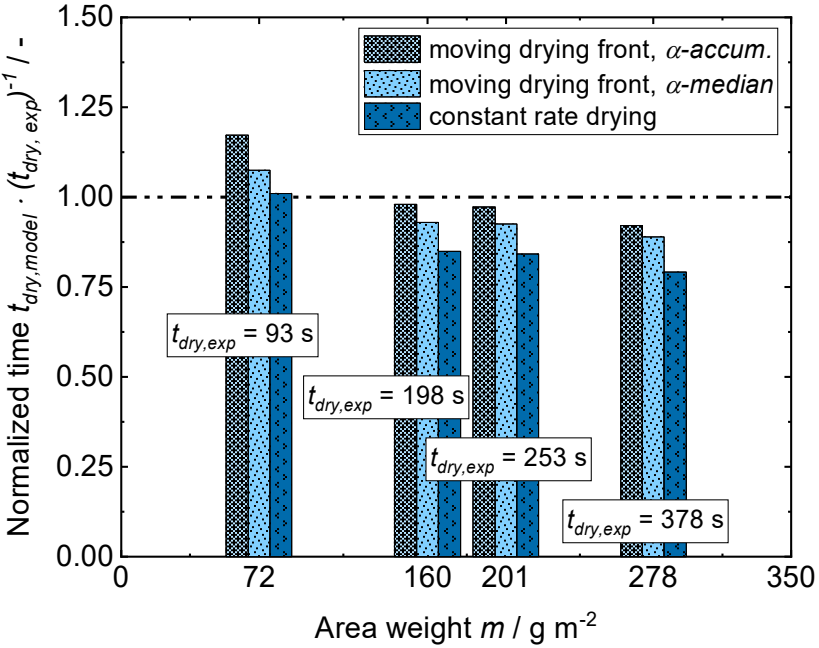

Figure 4.22: Comparison of the drying models MDF with accum. α-distribution, MDF with α-median, and constant rate drying in dependency of the area weight. The simulated drying times are compared with the experimental data at the time the solvent loading reaches 1 % in relation to the equilibrium solvent loading. Absolute times are given in Table 4.7. Figure taken from Kumberg et al., 2021.[75]

The experimental drying time is compared to the one predicted by each simulation type. Since the sorption equilibrium is included in the simulation, this value is the lower limit of the solvent loading in the electrode. The electrode mass is here defined as “dry” when 99 % of the solvent has been removed in relation to the equilibrium solvent amount ($X_{hygroscopic}$).

For the electrode with the lowest area weight, the linear kinetics describe the drying best. Both simulations using the MDF model predict a drying time of up to 10 s longer. This is in line with expectations since homogenous capillary transport was observed and no evidence of delayed drying due to liquid clusters became evident. It is different though for all higher area weights, which is reflected in the comparison between experiment and simulation. In all three cases, linear drying kinetics overestimate the drying speed up to a relative error of 20 % and an absolute error of 87 s at the highest area weight.

When comparing the MDF simulation based on the constant rate model (α-median) and the lateral model (α-distribution), the lateral model exceeds the constant rate model in precision for all area weights. The exact time values are summarized in Table 4.7. The MDF model can predict the solvent loading curve for drying of electrodes with elevated area weights. This is true even though it was shown that the actual drying process is more complex than the model considers. Properties of the dry electrodes derived from the comb nozzle dryer as well as a comparison of drying under non-isothermal and isothermal conditions are given in the appendix C.1 and C.3.

Table 4.7: Comparison of the drying models in dependency of the area weight. The simulated drying times are compared with the experimental data at the time the solvent loading reaches 1 % in relation to the equilibrium solvent loading.

m	$t_{dry,exp}$ exp.	$t_{dry,MDF,\alpha-accum.}$ sim.	$t_{dry,MDF,\alpha-median}$ sim.	$t_{dry,linear}$ sim.
g m^{-2}	s	s	s	s
$m_1 = 72 \pm 5$	94	108	102	94
$m_2 = 160 \pm 12$	203	210	198	168
$m_3 = 201 \pm 1$	257	275	260	214
$m_4 = 278 \pm 10$	389	400	378	302

A model optimization based on the python script to obtain a more realistic representation of the drying process was performed and can be found in the

Appendix (section C.5). In the optimization the simulated solvent loading was fitted to the experimental solvent loading in each time step by variating the proportion of the area which dries with the MDF model, while the other area fraction was assumed to dry without film resistances.

4.4.5 Simulated Electrode Drying with a 3-Zone Dryer Concept

The solvent evaporation of electrodes with differing area weights as well as binder migration as a function of the drying rate were discussed so far. The question arises, which conclusions can be drawn from these findings for industrial-scale electrode drying. One important gain is the combination of findings in this work with results from Jaiser et al. (2016) about critical times during electrode drying (see section 1.3 Electrode Drying).[68] In that study a three (or multi)-zone drying profile is proposed, allowing for moderate drying conditions during the sensitive time intervals in the process: before the beginning of pore emptying until a point nearing the dry electrode. To implement this profile into an industrial dryer, either a lot of trial-and-error based experiments or an accurate knowledge of the relevant points of time would be necessary. The simulations presented in section 4 are capable of predicting the exact drying course of electrodes of differing area weight. Precise estimations of the sensitive intervals during drying can therefore be obtained. The simulation requires the dryer temperature and gas phase loading in each zone, the solvent loading when entering the dryer and the dry area weight of the film, as well as the volume flow dependent heat transfer coefficient of the dryer. To determine the heat transfer coefficient, either theoretical estimations based on the VDI Wärmeatlas or an experimental approach can be used.[55] The first stage of drying can be used to determine the heat transfer coefficient as was shown in section 4. Therefore, measurement techniques to access the drying curves could be included in the dryer. This could for example be realized by measuring the film shrinkage over time with a laser, by taking wet samples at varying positions along the dryer length and determine their residual solvent content, or under usage of a heat flux sensor (see Appendix, Figure A. 7-20 and Figure A. 7-21).

The simulation of a 3-zone-drying profile for a state-of-the-art electrode film with a web speed of v_{line} = 10 m min^{-1} at a dryer length of 9 m is shown in Figure 4.23.

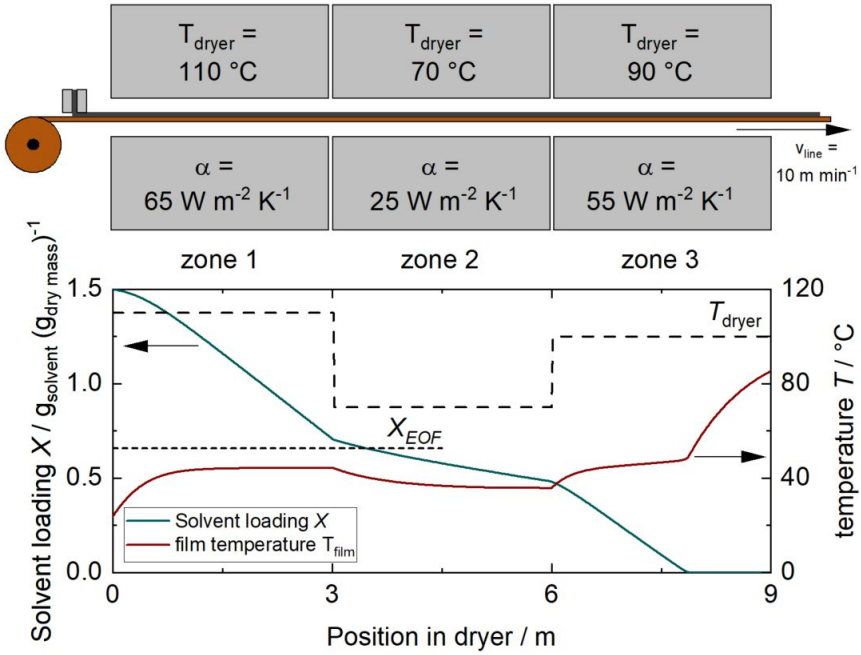

Figure 4.23: Exemplary drying curve of a state-of-the-art electrode in a three-zone dryer with an exemplary length of 9 m divided into zones of 3 m each. Web speed was assumed to be 10 m min^{-1}. The drying is assumed to be realized by an array of slot nozzles at the top and the bottom of the film with identical heat transfer coefficients, with their specific values as well as drying temperatures given in the top of the figure. One-sided coating and drying is assumed, though double-sided coating could easily be implemented. The end of film shrinkage is reached at the beginning of the second dryer zone. In zone three a higher dryer temperature and heat transfer coefficient are applied.

The drying is assumed to be realized by an array of slot nozzles at the top and the bottom of the film with identical heat transfer coefficients. Here the film is assumed to be coated only on the top of the substrate. A double-sided coating case could easily be implemented in the simulation as well. The dryer temperature and heat transfer coefficient are highest in the first zone. Accordingly, the steepest fall of the solvent loading takes place in the first zone. This is followed by a flatter slope of the solvent loading in the second zone with lower values for both heat transfer coefficient and dryer temperature. The film temperature takes

on the wet bulb temperature corresponding to the respective drying conditions in zone 1 and zone 2. Drying conditions were chosen as to reach the end of film shrinkage (EOF) within the beginning of the second dryer zone with moderate drying. In zone three a higher dryer temperature and heat transfer coefficient compared to zone two are applied. In zone 3 the film reaches its dry state and from this point on the film temperature starts to rise above the wet bulb temperature.

The model can be adapted as well for multizone dryers, different dryer lengths, electrode area weights as well as different solvents. It is a tool to simulate industrial drying of battery electrodes and towards a digital twin. Shorter drying times and improved cell performance can be gained from it.

5. Influence of Slurry Properties

Binder migration due to capillary transport during the drying step was proven to be a problem which severely affects cell performance. Different approaches to mitigate binder migration will be addressed in the following section. The impact of slurry mixing on the intrinsic structure of the wet slurry and the resulting dry microstructure will be discussed with the focus on advantageous slurry properties. With the aim to improve electrochemical performance and mechanical stability, various slurries are investigated in the following section. It was shown that a reduced binder content can improve cell performance, but at the same time diminishes the adhesion force of the electrode. This might affect industrial roll-to-roll processing as well as long-term stability in the form of cycle life.[21,39] Therefore, different slurries are examined with the goal of finding connections between their physicochemical properties and their tendency for binder migration during drying. [1]

5.1 Motivation and State of the Art

The binder system CMC and SBR has been subject in recent research. As shown in this work (section 3) and in literature, the adhesion force in the system of CMC and SBR is mainly attributed to the SBR binder, while CMC is necessary as a thickening agent.[39–42] The actual binding mechanism between active material, carbon black and both binders is quite complex though.[40,87,88] Adsorption of SBR on the active material was found to be related to the adsorption of CMC on the active material, which is ultimately connected with the surface properties of the active material, the molecular weight, and the substitution degree of

[1] Results presented in this section are based on the following publication by the author:[56]
Kumberg, Jana; Bauer, Werner; Schmatz, Joyce; Diehm, Ralf; Tönsmann, Max; Müller, Marcus; Ly, Kevin; Scharfer, Philip; Schabel, Wilhelm. (2021): Reduced Drying Time of Anodes for Lithium-Ion Batteries through Simultaneous Multilayer Coating. In: Energy Technol., S. 2100367. DOI: 10.1002/ente.202100367.

CMC.[89,90] CMC seems to preferably adsorb on graphite, leading to a hindrance of SBR adsorption on graphite if the CMC content in the slurry is too high.[40] Since the CMC molecule consists of a backbone and functional carboxyl groups, with their number depending on the substitution degree of the CMC, the CMC adsorption itself is dependent on the surface properties of the particle system.[90] While the CMC hydrocarbon backbone seems to preferably bond to more ordered surfaces by Van der Waals forces, the functional carboxyl groups are more prone to form stronger bonds to more disordered surfaces and protruding edges with OH groups on its surface.[87] It was further found that the bond between functional groups and disordered surface areas can build strong ester bonds during dehydration as was shown by FT-IR spectroscopy.[87] A Time of Flight - Secondary Ion Mass Spectrometry (TOF-SIMS) proved a direct correlation between the choice of graphite, CMC adsorption and the CMC distribution in the dry electrode, with a more homogenous distribution being achieved when the CMC formed ester bonds.[87]

It was shown that the rheological behavior of the slurry is largely influenced by the CMC. At low CMC and SBR concentrations, the slurry shows gel-like behavior due to hydrophobic attraction, if not enough CMC or SBR binder adsorbs on the particles surface to stabilize them. When increasing both binders, CMC preferably adsorbs and disperses the graphite. When increasing the CMC content even further, it forms a polymeric network resulting in a gel-like slurry.[40] CMC was found to form a network at levels of about 2 wt% in the dry composite.[91]

The specific adsorption behavior is used to tailor slurries in the following sections.

5.2 Experimental Setup

In this section, different slurries are investigated that differ by the choice of the active material, the mixing device used and the formulation. Experiments which are specific for this section are the Inverse Micro Raman Spectroscopy (IMRS)[92], which was used to analyze the active material powders. Unique are also the Cryo-BIB-SEM measurements, used to examine the slurries in their wet state.

Mixing: The four different slurries investigated in this section (see Table 5.1) with the composition of the respective dry electrodes are summarized in Table 5.2. The first slurry is the reference (R), which was used in the previous sections 3 and 4 and which is based on a mixing process in a dissolver. For a variation of the active material, a spherical-shaped graphite was used, resulting in slurry (S), with identical process conditions as used for the reference except for the change of the active material. As another variation, the mixing process was changed to a kneader, resulting in slurry (K). To preserve comparability with the reference system, the non-spherical graphite with a content of 93 wt-% is used in the recipe. The last slurry is based on an additive-reduced recipe, thus being named slurry (A). The formulation of the additive-reduced slurry (A) is based on a bachelor's thesis by U. Garbe, where an extensive variation of all additives SBR, CMC and carbon black was conducted, with slurry (A) showing the best electrochemical performance when built into a coin cell among the investigated compositions.[93] More information about the influence of the CMC content on slurry properties can be found in the appendix B. An active material content of 95.4 wt-% in the dry electrode is used.

Table 5.1: Overview of the denotation and differentiation of the slurries which are investigated in this section. The first slurry is the reference (R), for slurry (S) a spherical-shaped graphite was used. A change of the mixing process to a kneader, resulted in slurry (K) and an additive-reduced recipe in slurry (A). Exact recipes are given in Table 5.2.

	Reference (R)	Spherical (S)	Kneader (K)	Additive-reduced (A)
Graphite	non-spherical	spherical	non-spherical	non-spherical
Mixing device	dissolver	dissolver	kneader	dissolver
Active material content wt-%	93	93	93	95.4

For slurry (R), (K) and (A) the non-spherical graphite with a d_{50} of 18.4 µm and for slurry (S) a spherical graphite powder with a d_{50} of 10.3 µm (both from Hitachi Chemical Co. Ltd., Japan) was used. The BET surface area of both

graphites was measured by mercury intrusion porosimetry to be 3.7 $m^2 g^{-1}$ for the spherical graphite and 2.7 $m^2 g^{-1}$ for the non-spherical graphite.

Table 5.2: Overview of the composition of the dry electrodes derived from the four different slurries as presented in Table 5.1. The recipes are given for the dry electrode in wt-% for the respective material. Each wet slurry had a dry mass fraction of 43 wt-%.

Material	Reference (R)	Spherical (S)	Kneader (K)	Additive-reduced (A)
graphite SMGA / wt-%	93	93	93	95.43
carbon black / wt-%	1.4	1.4	1.4	1.00
CMC / wt-%	1.87	1.87	1.87	1.45
SBR / wt-%	3.73	3.73	3.73	2.12

Coating, Drying & Cell Manufacturing: All electrodes in the following section have been coated by knife-coating (section 2.2.2 Coating) and were dried in the batch coater (section 2.2.3 Drying). The cells were manufactured according to section 2.3.6 (Electrochemical Properties).

Inverse Micro Raman Spectroscopy

Spectra of pure graphite powders were measured by Inverse micro-Raman spectroscopy (IMRS). The system consists of a confocal Raman system (Labram, Jobin Yvon) and an inverted microscope (Olympus), as described in more detail elsewhere.[92] The spot size of each measurement was between 2 and 3 µm. For examination of the inner surface of graphite particles, which is relevant to interpret the influence of the mixing process with the kneader, graphite powder was grinded with a mortar. At least three measurements per position and per powder were performed.

Cryogenic Broad Ion Beam Scanning Electron Microscopy (Cryo-BIB-SEM)

The sample preparation for Cryo-BIB-SEM and the measurement procedure are shown in Figure 5.1. The process was described in more detail by Jaiser et al. (2017).[26] Cryo-BIB-SEM measurements were done by J. Schmatz, from Microstructures and Pores (MaP) Aachen. The wet slurries were coated and immediately transferred into frozen nitrogen slush without any drying taking place and a transfer time of roughly 1-2 s.

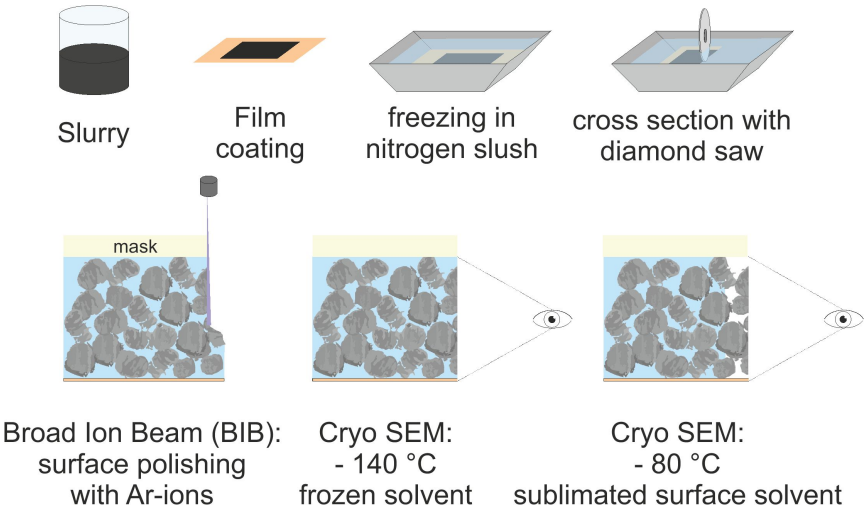

Figure 5.1: Cryo-BIB-SEM preparation and measuring protocol to obtain micrographs of anode slurries showing the internal pore volume after solvent sublimation. The wet slurries were coated and immediately frozen in nitrogen slush without any drying taking place. The cross sections were prepared in a first step by cutting the immersed film with a diamond saw before being transferred to the Cryo-Broad Ion Beam. The surface was ablated by three argon ion guns. First all capillaries of the cross section are filled by frozen water at a specified temperature of -140 °C. To sublimate the solvent and obtain a clear view into the internal pore volume, the chamber was heated to -80 °C. Figure taken from Kumberg et al., 2021.[56]

The nitrogen slush ensures instant freezing of the sample without interference due to the Leidenfrost effect. The cross sections were prepared in a first step by cutting the immersed film with a diamond saw before being transferred to the cryogenic Broad Ion Beam (Cryo-BIB, Leica TIC3X), where a smooth and damage-free surface was obtained. The surface was ablated by three argon ion guns at an accelerating voltage of 5 kV for a period of 3-4 hours. Thereby about 50 µm material in depth was removed. The samples than were transferred by a nitrogen-

cooled vacuum transfer (Leica VCT100) into the cryogenic SEM chamber. At this point, all capillaries of the cross section are filled by frozen water at a specified temperature of -140 °C. To sublimate the solvent and obtain a clear view into the internal pore volume, the chamber was heated to -80 °C.

5.3 Results and Discussion

In the following section a comparison of the properties of the four different slurries as well as the derived electrodes and cells will be presented. Interrelationships between wet film, dry electrode and cell performance will be discussed in detail for the different systems (R), (S), (K) and (A) with an emphasis on their stability towards high drying rates.

5.3.1 Properties of the Wet Slurry

The goal by varying process conditions was to establish a different adsorption and networking behavior of binders and graphite in the wet slurry, with the ultimate aim to tailor electrode properties. To assess the wet microstructure of the four electrode slurries, Cryo-BIB-SEM micrographs were examined. The images are shown in Figure 5.2. Each slurry is shown in an overview and a detailed image, except for the reference, where two detailed images are given. The graphite particles are visible while being surrounded by a network formed by the CMC binder. For better visualization, exemplary shapes formed by the CMC are highlighted by a red rectangle in each overview picture but the additive-reduced one.

Cryo-BIB-SEM of Slurry (R): Reference

Slurry (R) is shown in Figure 5.2a. The non-spherical graphite particles in the overview image (Figure 5.2a, middle) are surrounded by a network structure formed by the CMC binder, which seems to be composed of rectangular cells. In the first close-up (Figure 5.2a, left) the adsorption of the CMC on the graphite surface becomes visible. Part of the graphite surface as well as the CMC structure seems to be covered by spheres. This can be observed in more detail in the second close-up (Figure 5.2a, right). Especially the CMC binder seems to be covered with these spheres, which are most likely the SBR binder particles, which have not coalesced into a film yet due to the preparation process. With a d_{50} of

153 nm, the diameter of the detected spheres correlates with the diameter measured for the SBR binder in a Zetasizer used to measure the particle size (see Figure A. 7-7, Appendix).

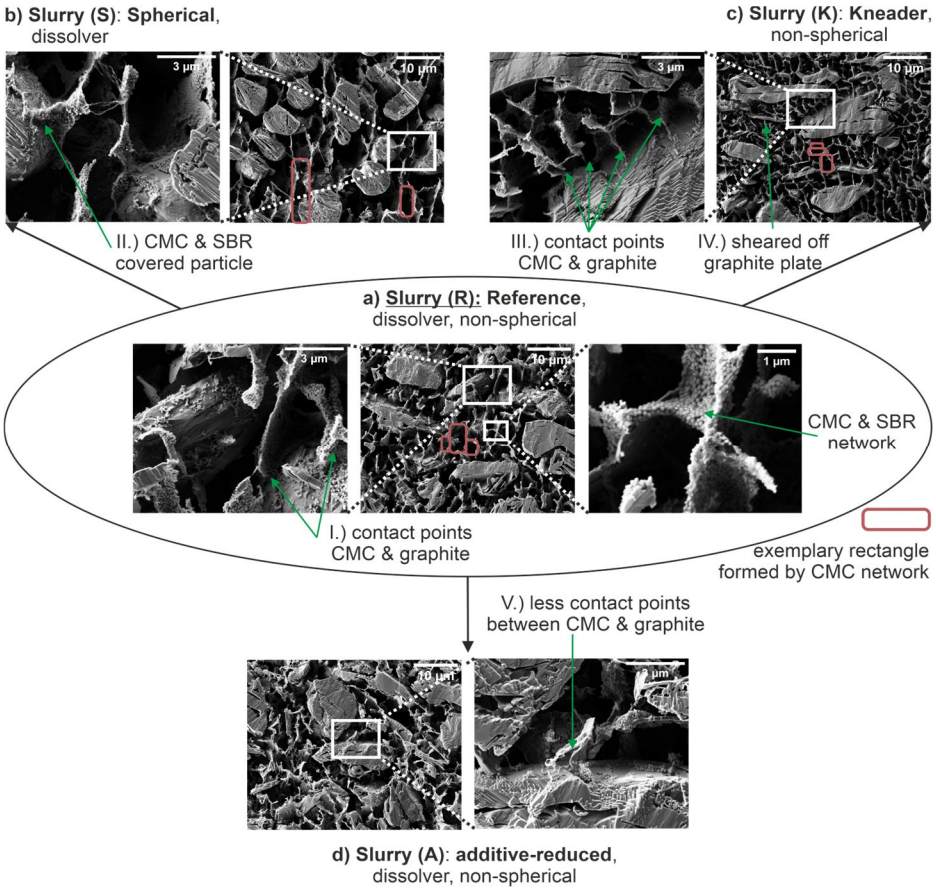

Figure 5.2: Cryo-BIB-SEM micrographs of the four wet slurries denoted in Table 5.1. In a) the reference (R) is shown in overview and with two detailed images. b) shows slurry (S) based on the spherical graphite in overview and detail, c) the kneader-based slurry (K) in overview and detail and d) the additive-reduced slurry (A). The graphite particles are visible while being surrounded by a network formed by the CMC binder. For better visualization, exemplary shapes formed by the CMC are highlighted by a red rectangle in each overview picture but the additive-reduced one. More SEM images are given in the Appendix. Cryo-BIB-SEM measurements were done by J. Schmatz, from Microstructures and Pores (MaP) Aachen. Figure taken from Kumberg et al., 2021.[56]

The carbon black can also be detected in both close-ups as smaller agglomerates either covering the graphite particle (Figure 5.2a, left) or mixed in with the CMC-SBR network (Figure 5.2a, right). More SEM images are given in the Appendix (see Figure A. 7-8 – Figure A. 7-11). The finding that CMC preferably adsorbs on the graphite while the SBR is found in a smaller fraction on the graphite especially at protruding edges agrees with literature, where the competing adsorption of CMC and SBR was described.[42]

Cryo-BIB-SEM of Slurry (S): Spherical

In the overview picture of slurry (S) (Figure 5.2b, right) the spherical-shaped graphite particles surrounded again by the CMC network can be seen. The shape of the binder network differs from the one in the reference though.

The polymer chains seem more elongated, and the rectangles formed by the network are larger. When looking at the close-up (Figure 5.2b, left), it appears as if the CMC covers the particles instead of only anchoring at their surface. The SBR binder appears to be attached to the CMC again. A possible explanation for the different adsorption behavior of the CMC on the non-spherical and the spherical graphite can be given by the Raman spectra shown in Figure 5.3, when relating it to current literature.[87]

The intensity normalized on the maximum intensity is given over the Raman shift for both graphite powders. The G-peak is identical for both graphites, while the D-peak deviates. In the case of the non-spherical graphite almost no D-peak is evident, while a pronounced D-peak is present in the spectrum of the spherical graphite. Since a disordered crystal structure is indicated by the prominent D-peak, it can be assumed that the surface of the spherical graphite is prone to provide OH-groups on its surface and is therefore likely to bond with the functional groups of the CMC as shown by Chang et al. (2019).[87] These bonds were also proven to establish strong ester bonds during dehydration, which would lead to a better fixation of the binder compared to the non-spherical graphite, where bonding forces mainly are governed by Van der Waals forces.[87] The significance of the Raman spectrum of the grinded graphite powder will be discussed in the following section.

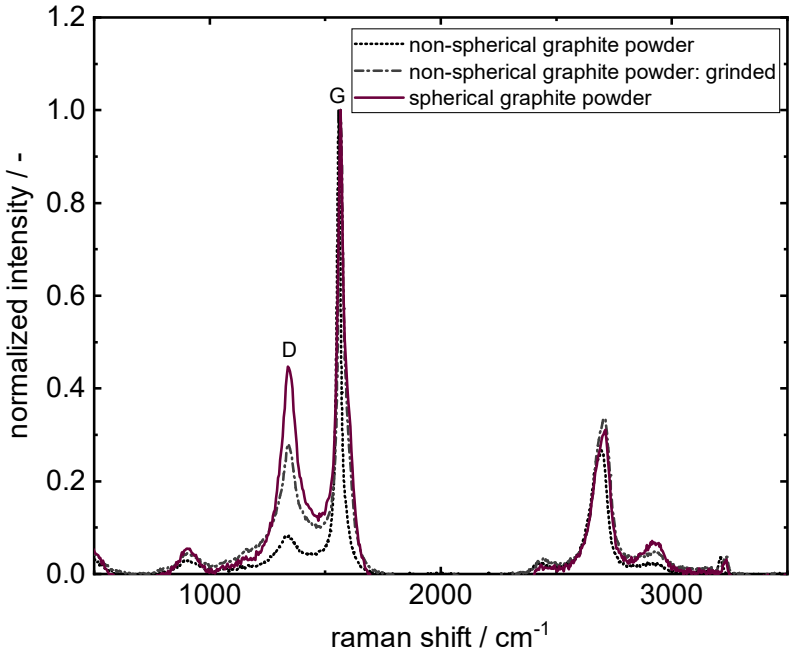

Figure 5.3: Raman spectrum of the pure graphite powders of the non-spherical and the spherical graphite as well as the grinded non-spherical graphite powder. All spectra are normalized on the maximum intensity of the respective spectrum. Figure taken from Kumberg et al., 2021.[56]

Cryo-BIB-SEM of Slurry (K): Kneader

Slurry (K), originating from the kneading process, is depicted in (Figure 5.2c). The non-spherical graphite particles are embedded within a CMC network as already found for slurries (R) and (S) (see overview image, Figure 5.2c, right). The CMC structure though is again different. It appears denser, more branched and smaller cells are formed by the binder network. Consequently, more contact points between the CMC and the graphite can be observed, as marked in Figure 5.2c, left. The SBR binder again seems to mainly adhere to the CMC. Two explanations for the different graphite-binder network might apply: The mixing in the kneader induces higher shear forces on the graphite particles due to the mixing process at higher solid contents in the beginning (cf. appendix, A). This results in a partial grinding of the larger graphite particles and graphite layers being sheared off. One of these sheared-off graphite plates is marked in Figure 5.2c, left. The higher shear forces therefore lead to a slightly smaller d_{50} of 15.4 µm

for slurry (K) compared to 17.24 µm for slurry (R) and 18.4 µm of the pristine non-spherical graphite powder. It also leads to a better deagglomeration of the carbon black, as is reflected in the particle size distribution given in Figure 5.4. A higher content of nano-sized fragments between 100 nm to 500 nm of diameter are found for slurry (K) compared to slurry (R). A superposition with sheared off particle fragments cannot entirely be excluded though. The smaller particle fragments impact binder bridging and thereby the rheological behavior of the slurry. The dynamic viscosity of slurry (K) is significantly higher than that of the other three slurries (see Appendix Figure A. 7-6).[94]

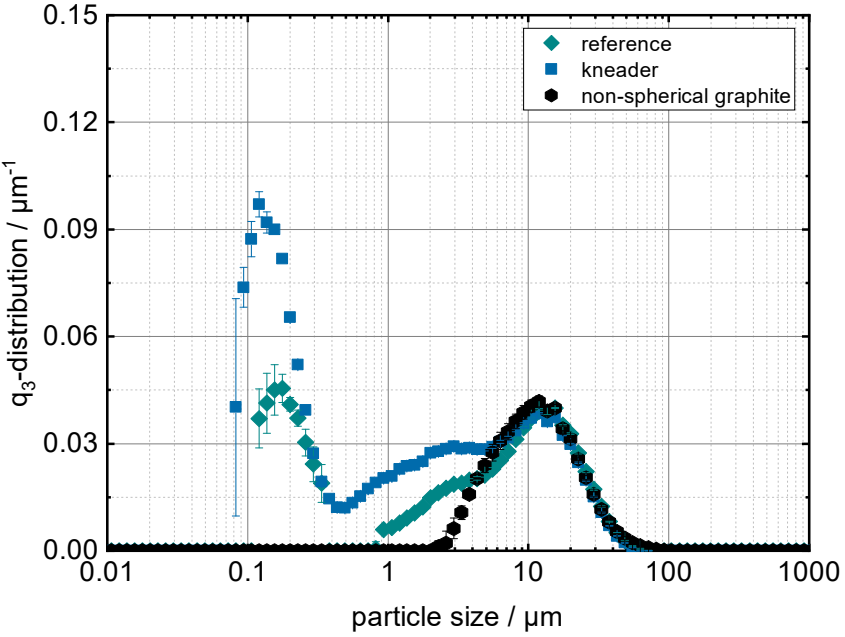

Figure 5.4: Density distribution as a function of the particle size of the reference slurry (R), slurry (K) and the pristine non-spherical graphite. Figure taken from Kumberg et al., 2021.[56]

For a more detailed analysis of the rheological properties, the phase shift angle δ as a function of the angular frequency ω was determined for all four slurries investigated in this section. It is shown in Figure 5.5. Slurry (R) and slurry (A) clearly show liquid-like behavior since their phase shift angle is above 45 ° (see section 2.3.2). This is also true for slurry (S), though it almost reaches the limit

to gel-like behavior. Slurry (K), on the other hand, shows a distinct gel-like behavior. From literature, this would either be expected due to binder depletion in the slurry and agglomeration of large graphite particles trapping solvent in their center, or by increasing the CMC binder content to levels where polymer networks form.[40] More details on the interrelationship between CMC and slurry are given in the appendix B. Since the recipe was not changed to a higher binder content, a binder depletion could be expected, especially since a higher surface is available due to the shearing off of graphite plates. Since the graphite particles seem to be stabilized in the slurry (Figure 5.2c, right) another explanation seems to apply.

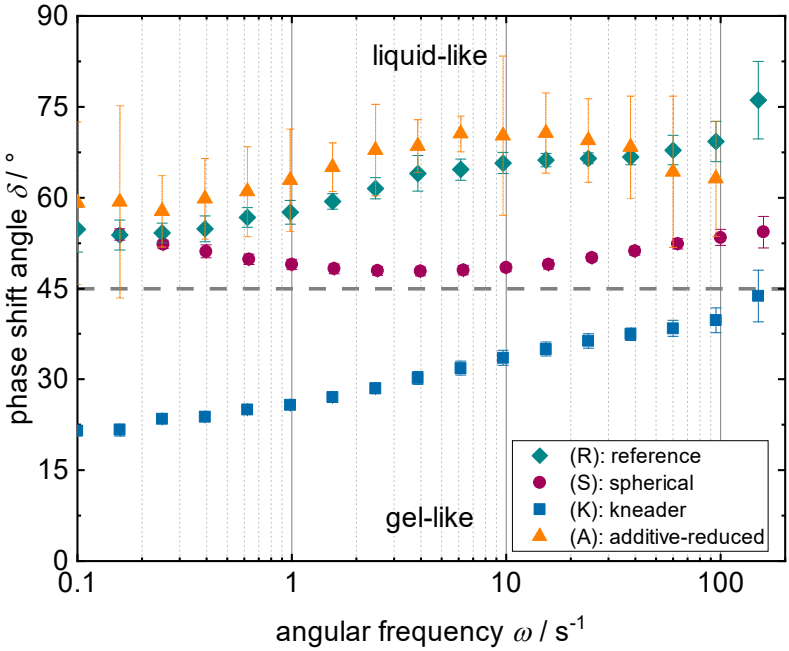

Figure 5.5: Phase shift angle as a function of the angular frequency ω for the four slurries (R), (S), (K) and (A)investigated in this section. (R) hereby stands for the slurry using the reference recipe, (S) for the spherical graphite, (K) for the kneading process and (A) for the additive-reduced recipe. Figure taken from Kumberg et al., 2021.[56]

The adsorption of the CMC on the graphite appears to be improved compared to slurry (R), since more contact points are present and a denser network is formed. This could be attributed to the properties of the inner surface area of the non-

spherical graphite powder, which was also analyzed for its Raman spectrum. A higher D-peak is present in Figure 5.3 for the grinded non-spherical graphite, compared to that of the pure graphite powder contained in slurry (R). Consequently, an improved adsorption of the functional CMC groups to the grinded graphite within slurry (K) could result, improving adhesion.

Cryo-BIB-SEM of Slurry (A): Additive-reduced

The additive-reduced slurry (A) is shown in Figure 5.2d. The CMC/SBR network between the graphite particles in the overview image (Figure 5.2d, right) seems to be not fully developed. Fewer contact points to the graphite appear to exist (Figure 5.2d, left) compared to slurry (R). This is in accordance with the rheological measurements, showing a clear liquid-like behavior of the slurry. The viscosity in dependency of the shear rate is also lower compared to that of all other three slurries (cf. Figure A. 7-6).

5.3.2 Properties of the Dry Electrode

The influence of the slurry's intrinsic structure on the dry electrode and its tendency to show binder migration in dependency of the drying rate is evaluated.

Adhesion force as a function of the area capacity

In a first step, the adhesion force of electrodes of different area capacities as shown in Figure 5.6 is measured. Each measurement point consists of at least three different samples which were measured, explaining the error bars of the adhesion force as well as of the area capacity. All investigated parameters, the active material, the mixing process and the additive content, led to a different absolute adhesion level, as can be seen in Figure 5.6. In this case, all electrodes were coated on copper foil f3 (cf. Table A. 3) and were dried with a theoretical drying rate of 0.75 g m^{-2} s^{-1} at a heat transfer coefficient of 35 W m^{-2} K^{-1}.

The adhesion force of the reference electrode lies approximately in the middle of the other three slurries and shows the already observed behavior of decreasing adhesion forces when the area capacity is increased. The percentage change in adhesion force between minimum and maximum area capacities (*cf.* Figure 5.6) is also summarized in Table 5.3. For (R) a value of 59.8 % is obtained. The adhesion force of electrode (S) lies well above the adhesion of electrode (R). This

could be due to the smaller particles and the lower porosity (see Appendix, Figure A. 7-25), leading to more contact points between substrate and particles.

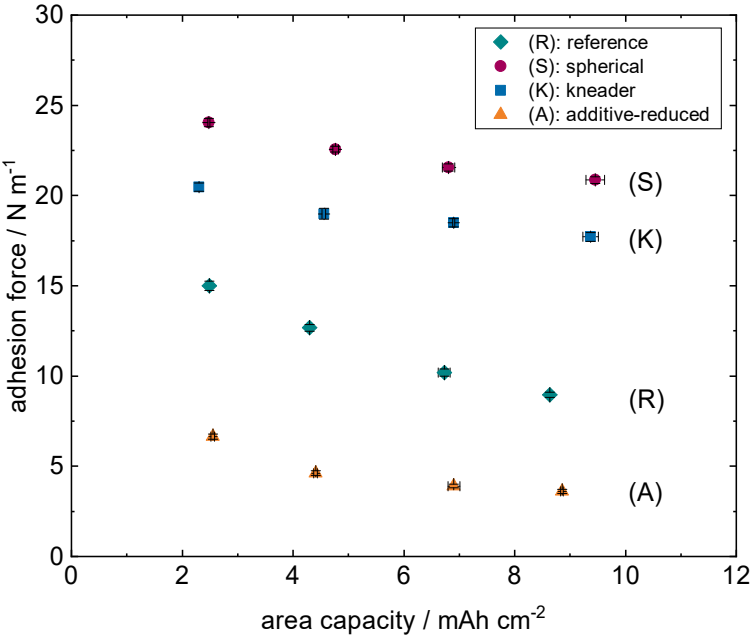

Figure 5.6: Adhesion force as a function of the area capacity of electrodes derived from the four slurries (R), (S), (K) and (A). (R) hereby stands for the electrode using the reference recipe, (S) for the spherical graphite, (K) for the kneading process and (A) for the additive-reduced recipe. The theoretical drying rate was 0.75 g m^{-2} s^{-1} ,the isothermal drying temperature about 30 °C and the heat transfer coefficient 35 W m^{-2} K^{-1}. All slurries were coated on substrate foil (f3).

The same could apply for electrode (K), which has an adhesive force below that of electrode (S) but well above electrode (R). Again, the particle size distribution and lower porosity with more smaller particle fractions appears to lead to more contact points and therefore a better adhesion. In both cases though, the adhesion force remains almost at one level ($\Delta F < 15\ \%_{abs}$), when the area capacity is increased. Furthermore, a calendering step to match the porosities of electrode (R) and (K) does not compensate for the difference of the initial adhesion forces (see Appendix, Figure A. 7-26). Calendering approximately doubles the adhesion force in both cases but does not increase the adhesion force to the same level. Therefore, it can be assumed that the binder distribution or more precisely the

bond between binder and particles always contributes to the adhesion force, independently of calendering.

As was explained in the last section, a better adsorption of the CMC binder on the spherical particles and the particles derived from the kneaded slurry would be expected compared to the reference slurry. It was also observed that the adhesion promoting SBR binder seems to preferentially adhere to the CMC. As a result, in that train of thought, more SBR-covered CMC remains at the particles of slurry (S) or (K) thereby increasing the adhesion force of the resulting electrodes (S) or (K) compared to that of electrode (R). A more immobilized and bound binder seems to also better withstand the capillary drag during drying of thicker electrodes. The very low adhesion force of electrode (A) also follows this reasoning. Less additives and therefore less binder was used in the formulation of slurry (A). Consequently, less binder can adsorb on the particle surface, forming a looser network compared to slurry (R), since less binder is available in the solvent. The absolute adhesion force of slurry (A) is even below the limit of 9 N m^{-1}, stated as lower limit for industrial processing in literature.[21] Apart from the overall lower absolute adhesion force, the relative losses in adhesion of electrode (A) are similar to the ones of electrode (R) with about -45 % from minimum to maximum area capacity.

Table 5.3: Percentage change in adhesive force when increasing the area capacity from the minimum (≈ 2.5 mAh cm^{-2}) to the maximum area capacity (≈ 9 mAh cm^{-2}) given in Figure 5.6 for the respective electrode. This is compared to the change of the adhesion force when increasing the drying rate from 0.75 g m^{-2} s^{-1} to 3 g m^{-2} s^{-1} as shown in Figure 5.7. (R) hereby stands for the electrode using the reference recipe, (S) for the spherical graphite, (K) for the kneading process and (A) for the additive-reduced recipe. Values above 100 % mean, that adhesion values of the electrodes dried at 3 g m^{-2} s^{-1} lie above the ones gained at the lower reference drying rate of 0.75 g m^{-2} s^{-1}.

	(R)	(S)	(K)	(A)
	%	%	%	%
$\frac{F_{@\ min\ cap.}}{F_{@\ max\ cap.}}$ / -	59.8	86.7	86.5	54.2
$\frac{F_{@\ 0.75\ g\ m^{-2}\ s^{-1}}}{F_{@\ 3\ g\ m^{-2}\ s^{-1}}}$ / -	68.4	114.8	100.4	68.8

Adhesion force of single layers as a function of the drying rate

An increase of the drying rate was accomplished by increasing the drying temperature. The effect on the adhesion force is shown in Figure 5.7, with the isothermal drying temperature to the respective drying rate given as the upper x-axis. The drying temperature was calculated at a dew point temperature of 15 °C and a heat transfer coefficient of 35 W m^{-2} K^{-1} and might deviate from the given values by ± 1 °C in dependency of the exact dew point temperature during the experiment.

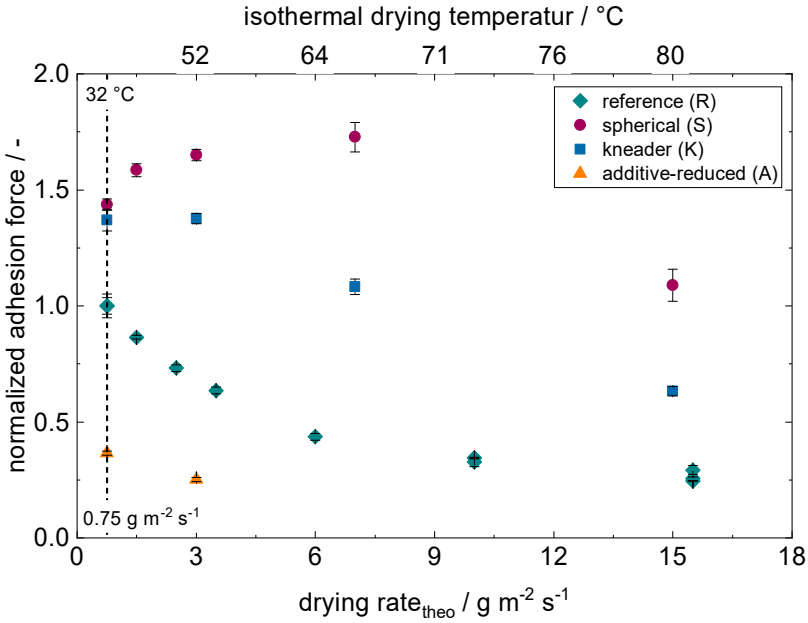

Figure 5.7: Normalized adhesion force as a function of the drying rate of electrodes derived from the four slurries (R), (S), (K) and (A). (R) hereby stands for the electrode using the reference recipe, (S) for the spherical graphite, (K) for the kneading process and (A) for the additive-reduced recipe. The heat transfer coefficient was 35 W m^{-2} K^{-1}. Slurry (R) was coated on substrate foil (f1) or (f2), as detailed in Figure 3.4. Slurry (K) was coated on foil (f1) and slurry (S) and (A) were coated on (f3). The absolute adhesion force in dependency of the substrate used for normalizing is given in Figure A. 7-22, Appendix. The adhesion force of the reference electrode dried at a drying rate of 0.75 g m^{-2} s^{-1} and a heat transfer coefficient of 35 W m^{-2} K^{-1} at a capacity of 2.5 mAh cm^{-2} is used for normalization.

Electrode (R) behaves as discussed in section 3 (Drying of Thicker Electrodes) with a decrease of the adhesion force at an increase of the drying rate. In contrast to the reference electrode (R), the adhesion force of electrode (S) increases with an increasing drying rate with an improvement of about 15 % of the adhesion force at a drying rate of 3 g m^{-2} s^{-1} compared to the one of the electrodes dried at 0.75 g m^{-2} s^{-1} (see Table 5.3). An increase in the adhesion force can be observed up to a theoretical drying rate of 7 g m^{-2} s^{-1}, where the adhesion force reaches a peak value. This finding is surprising based on section 3. It can be explained though with the results showing different adsorption behavior of the CMC and the graphite particles (c.f. Figure 5.2). It can be assumed that a stronger adsorption force of the CMC binder and the spherical graphite particles is present compared to the non-spherical graphite. This holds true especially under the assumption that ester reactions take place. Since the kinetics of the chemical reaction can be assumed to be temperature-dependent, a temperature rise would accelerate the reaction and therefore the number of strongly bonded sites. This would result in an improved adhesion force.

Since the increase of the drying rate was accomplished by increasing the temperature from about 32 °C at a theoretical drying rate of 0.75g m^{-2} s^{-1} to a temperature of about 66 °C at a theoretical drying rate of 7 g m^{-2} s^{-1}, the temperature was increase by about 30 °C, resulting in a potential increase of reaction kinetics. One could also assume that the reaction kinetics compete with the drying rate in the form of the speed at which solvent and binder are transported away from the reaction site. This would explain the collapse of the adhesion force at the highest drying rate of 15 g m^{-2} s^{-1}, since binder is transported away so fast that it cannot undergo any chemical reactions.

The impact of an increased drying rate on electrode (K) is slightly different than on electrode (S). The adhesion force is constant up to a theoretical drying rate of 3 g m^{-2} s^{-1} and then drops. Even though the adhesion force is not as high as the one of electrode (S), the adhesion level is still well above that of electrode (R). Less available sites for strong CMC-particle-bonds compared to slurry (S) might lead to the observed, reduced dependence on the drying temperature. Another relevant factor could be the presence of a higher number of small sheared-off particle fragments within electrode (K), which are covered by binder. Even though the binder distribution over the film height seems to be more homogenous than the one of electrode (R), a thin top layer with a high binder content can be

found in the LIBS measurements (see Appendix, Figure A. 7-34) and can also be found in SEM images taken from the top of the electrode (see Appendix, Figure A. 7-33). This means that binder migration still takes place, even though the binder is better bound to the particle surfaces.

The adhesion force of electrode (A) drops at about the same rate as electrode (R) at an increase of the drying rate from 0.75 to 3 g m^{-2} s^{-1}. About 30 % of the adhesion is lost due to the higher drying rate in both cases. This is attributed to binder migration and weaker bonds between CMC binder covered by SBR binder and the graphite particles, as is the case for electrode (R).

Electrical conductivity of single layers at two different drying rates

State-of-the-art (SoA, 2.2 mAh cm^{-2}) and high energy (HE, 6.6 mAh cm^{-2}) electrodes from all four investigated slurries were analyzed with respect to their electrical conductivity. The results are shown in Figure 5.8 for electrodes dried at two different experimentally validated drying rates of 0.5 and 2.2 g m^{-2} s^{-1}. The electrodes dried at the lower, experimentally validated drying rate $\dot{m}_{exp}$ of 0.5 g m^{-2} s^{-1} all possess a higher electrical conductivity than those dried at 2.2 g m^{-2} s^{-1}. Also, all state-of-the-art electrodes have a lower electrical conductivity than the high energy electrodes. This higher conductivity of the thicker electrodes cannot directly be explained, because the specific conductivity, being a material constant, should be independent of the electrode thickness. As mentioned earlier though, the measured specific conductivity is a superposition of the specific conductivities of the materials contained in the porous electrode and their network. Changes in its microstructure will therefore affect the resistance network of the electrode. One reason for a higher specific conductivity of the thicker electrodes could be a relatively smaller contribution of the presumably limiting contact resistance at the electrode surface to the overall resistance of the electrode related to its volume.

Since the trends in regards to the effect of different slurries are identical for thin and thick electrodes, these will be discussed together: The electrical conductivities of electrodes (R) and (S) are similar for both drying rates. The one of electrode (K) is slightly higher, while electrode (A) shows very low values.

A loss in the electrical conductivity at an increase of the drying rate can be assumed to be caused by the capillary pore emptying during which not only binder

but also small particles like carbon black are transported to the electrode surface. Carbon black was associated with the CMC-SBR-clusters based on the Cryo-BIB-SEM images. It seems to interact mainly by weaker van der Waals forces, based on literature.[46,95,96] Capillary drag forces during pore emptying could therefore move part of the carbon black, leading to a more inhomogeneous distribution at a higher drying rate. This might also be true for the SBR particles. Since the absolute amount of free graphite surface was not significantly changed when changing the formulation, based on the BET surfaces, it can be assumed that free CMC and SBR binder as well as carbon black are present within all slurries, except for the additive-reduced slurry (A), forming a mobile phase.

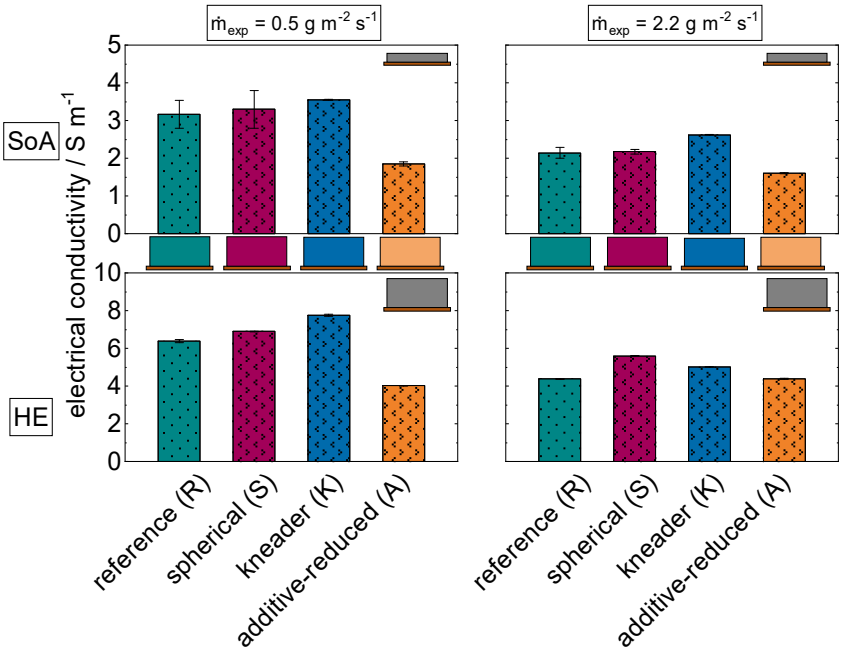

Figure 5.8: Top: Electrical conductivity of electrodes (R), (S), (K) and (A) of state-of-the-art area capacity of about 2.2 mAh cm^{-2} dried at the two different experimentally validated drying rates of 0.5 and 2.2 g m^{-2} s^{-1}. Bottom: The electrical conductivity of high energy electrodes with an averaged area capacity of 6.6 mAh cm^{-2} dried at the same two drying rates in comparison. (R) hereby stands for the electrode using the reference recipe, (S) for the spherical graphite, (K) for the kneading process and (A) for the additive-reduced recipe.

Another cause for the decreased conductivity at a higher drying rate could be the measurement itself, which could be sensitive to the contact resistance between the electrode surface and the copper block on top of it. This would be in line with the lower electrical conductivity of the thinner electrodes, as mentioned earlier. Isolating binder accumulations on the top of the electrode could increase the contact resistance further. The higher electrical conductivity of electrode (K) can be caused by the broader particle size distribution due to the sheared-off flaked graphite and the more deagglomerated carbon black, resulting in a lower porosity and more electrical pathways within the electrode structure. These are in part still prone to migration during drying though, as can be seen by the decreased conductivity at the higher drying rate.

Following the same logic, the low electrical conductivity of electrode (A) is caused by the lack of conductive pathways due to the binder and carbon black-reduced formulation. Since there is only a limited amount of available surface for adsorption on the graphite particles, the amount of free binder and carbon black would be less than is the case for slurry (R), which results in the less stable CMC network shown in the Cryo-BIB-SEM micrographs (Figure 5.2). Less CMC, which competitively adheres to the graphite surface, leaves more space for direct contact between carbon black and the graphite surface itself where it does not contribute to new pathways. This and the fact of the overall reduced amount of carbon black agrees well with the loss in conductivity of almost 45 % for the reference electrode (R) and only of about 15 % for the additive-reduced electrode (A) at an increase of the drying rate.

The electrical conductivity of all four slurries at four different area capacities shows a similar trend as the one described here and will therefore not be discussed further at this point (see Appendix, Figure A. 7-37).

5.3.3 Electrochemical Performance

To evaluate the electrochemical properties of the four different slurries, coin cells were built from the respective electrodes, dried at two different drying rates.

Electrochemical performance of single layers at two different drying rates

Coin cells were built from the four different anodes (R), (S), (K) and (A) for state-of-the-art area capacities dried at the experimentally validated drying rates

of 0.5 g m^{-2} s^{-1} and 2.2 g m^{-2} s^{-1}. Their exact area capacities and porosities are listed in Table A. 4 and Table A. 5. These coin cells were tested for their electrochemical performance which is shown in Figure 5.9. Their specific discharge is given for different C rates. A different performance of all cells becomes evident within the first cycles and further increases until it is most pronounced at 3C. Since all anodes were combined with the identical cathode, the different specific discharge capacities can be attributed to the different anodes. While cell (R) and (A) perform similar at low C rates, cell (K) and especially cell (S) have a significantly lower discharge capacity, which remains true even for higher C rates. This could be attributed to the slightly higher surface area of these both cells. Also different intrinsic capacities between the spherical and the non-spherical graphite cannot be completely excluded, though they should be identical referring to the manufacturer. Since the balancing was identical for all cells, the available surface area introduced by the graphite particles defines the irreversible lithium loss due to the formation of the SEI layer. While the spherical graphite has a BET surface area of 3.7 g m^{-2}, the non-spherical has a surface area of 2.7 g m^{-2}. A higher surface area in electrode (K) is caused by the fragmented particles.

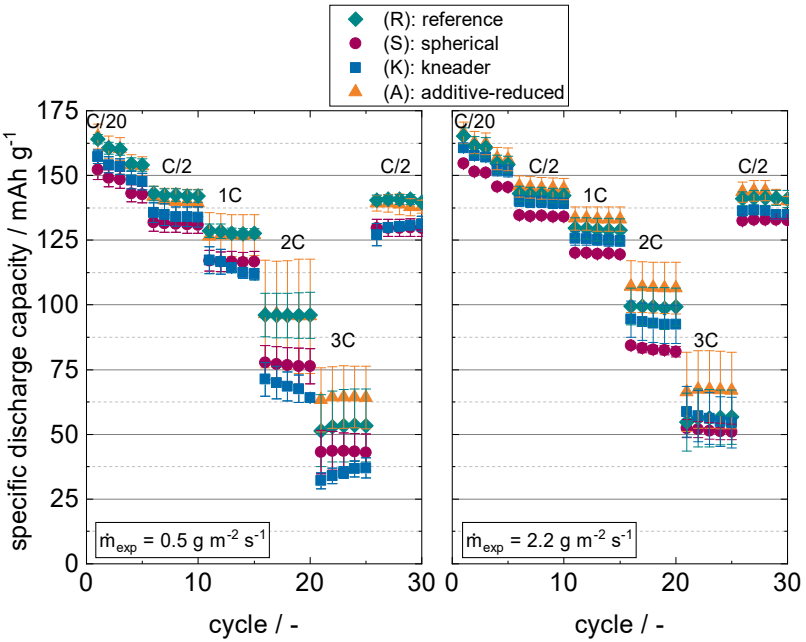

Figure 5.9: Coin cell test of cells (R), (S), (K) and (A), derived from the respective slurries. (R) hereby stands for the electrode using the reference recipe, (S) for the spherical graphite, (K) for the kneading process and (A) for the additive-reduced recipe. For anode manufacturing the experimental drying rates were 0.5 g m^{-2} s^{-1} and 2.2 g m^{-2} s^{-1}. State-of-the-art anodes were used with their exact area weights and porosities listed in Table A. 4 and Table A. 5 in the Appendix. Figure taken from Kumberg et al., 2021.[56]

Cell (A), derived from the additive-reduced slurry (A), shows the best performance over all C rates for the slowly dried electrode ($\dot{m}_{exp}$ = 0.5 g m^{-2} s^{-1}) as well as for the faster dried electrode ($\dot{m}_{exp}$ = 2.2 g m^{-2} s^{-1}). This is in accordance with literature and would be expected, due to the smaller effect of a binder layer hindering lithium ion transport.[21,39,68]

The effect of the drying rate is also almost neglectable for the reference cell (R), as was shown earlier (see section 3.3.2 Electrochemical Properties). This behavior could be explained along with that of the other cells: The discharge capacities of cell (S) and (K) are slightly improved by drying at a higher drying rate. This correlates with the constant or even improved adhesion force and could be an effect of the stronger ester bonds at the elevated drying temperature. These might

lead to a stronger fixation of binder throughout the microstructure which therefore does not accumulate at the electrode surface and leaves more active sites during cycling. The reference slurry (R) is based on the non-spherical graphite particles, which show even as non-grinded powder a small D-peak in the Raman spectrum (Figure 5.3). Thus, the formation of few ester bonds is possible and a positive effect of an increased drying temperature might outweigh the negative effect of an increased drying rate to some extent.

For each coin cell only thirty cycles were considered for the analysis of a broader spectrum of the parameters “slurry-type” and “drying rate”. To establish the validity of the obtained results for larger cycling numbers as well as their application in pouch cells, electrodes (R) and (K) were built into pouch cells and cycled for 100 cycles (see Appendix, Figure A. 7-38). Pouch cells in general show better discharge capacities especially at higher specific capacities[97]. The influences of the choice of slurry found for coin cells are also found for pouch cells[102]. Consequently, the coin cell tests are regarded as representative to evaluate the influence of different process parameters based on comparison with the reference.

In Figure 5.10, the coin cell test of the high capacity anodes (R), (S), (K) and (A) at an approximate area capacity of 8.8 mAh cm^{-2} dried at the two different drying rate of 0.5 g m^{-2} s^{-1} and 2.2 g m^{-2} s^{-1} is shown. The discharge capacity at different C rates is considered. Below C/5 the results are similar to the state-of-the-art cells: electrode (A) performs best and cells based on (S) and (K) perform worst. The advantage of (A) does not negate the severe capacity loss all four cells suffer at C rates of C/2 and higher, as was also reported by Singh et al. (2015, 2016).[60,61] Contrary to the state-of-the-art cells, the high capacity ones are also negatively affected by the increased drying rate. This could be attributed to the earlier onset of capillary pore emptying compared to the state-of-the-art electrodes, and a more severe binder migration. Especially for slurry (K), which performs even worse than the reference. Here, an additional contribution of a denser surface layer consisting of smaller particles and binder can be assumed (see Appendix, Figure A. 7-33 and Figure A. 7-34).

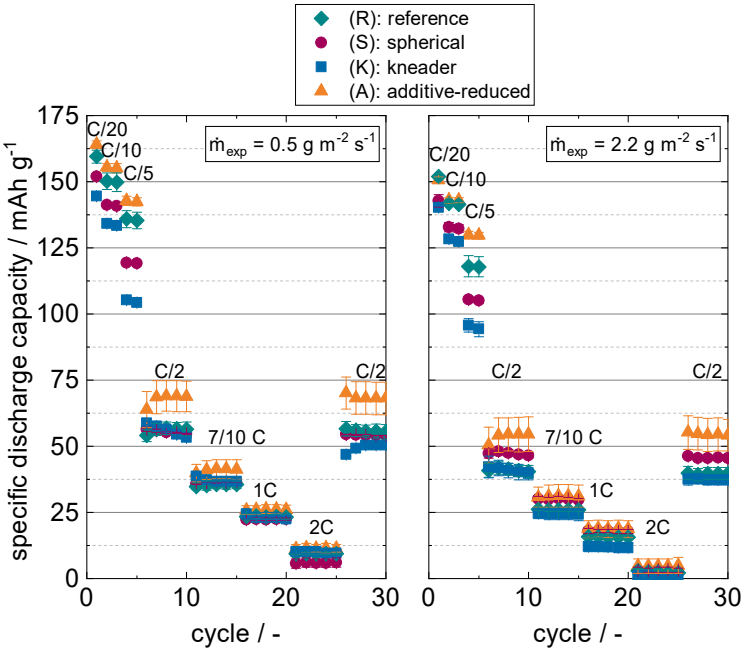

Figure 5.10: Coin cell test of cells (R), (S), (K) and (A), derived from the respective slurries. (R) hereby stands for the electrode using the reference recipe, (S) for the spherical graphite, (K) for the kneading process and (A) for the additive-reduced recipe. For anode manufacturing the experimental drying rates were 0.5 g m^{-2} s^{-1} and 2.2 g m^{-2} s^{-1}. High capacity anodes were used with their exact area weights and porosities listed in Table A. 6 and Table A. 7 in the appendix. Figure taken from Kumberg et al., 2021.[56]

In summary, it was shown in this section that electrochemically and mechanically beneficial electrode properties do not necessarily coincide. The best electrochemical performance was observed for the additive-reduced slurry (A) even at an increased drying rate. Its adhesion force though is the lowest of the slurries investigated here and lies even below the limit of 9 N m^{-1}, stated as lower limit for industrial processing in literature.[21] In contrast to this, the adhesion force of the spherical slurry (S) was the highest and was shown to increase even when the drying rate was 9 times increased. The electrochemical performance though was even below that of the reference for electrode area weights corresponding to the state-of-the-art. The alternative slurries showed no advantage in electrochemical performance of thick electrodes, as the discharge capacities reached very low values when applying C rates higher than C/5. The adhesion force though was

positively affected. The adhesion force loss was reduced to about 15 % for slurry (S) and (K) compared to a loss of about 45 % for slurry (R) and (A) when the area weight was increased by a factor of about 4.

Since by just tuning the slurry, no electrode with improved mechanical and electrochemical properties was found, the following addresses multilayer coatings of battery electrodes. This technique enables a targeted adjustment of electrode properties to enhance either mechanical or electrochemical properties. This is achieved by tuning the composition of the individual layers, combining them in a multilayer coating with improved properties. This allows for more flexibility regarding properties of the respective layers. A slurry with advantageous electrochemical properties at the top shall be combined with a slurry which is less prone to binder migration and can therefore be used as a bottom layer.

6. Simultaneously Coated and Hierarchically Structured Multilayers

It was shown in the last section that properties like the adhesion force or electrical conductivity of dry electrodes can be tuned by changing the properties of the slurry. Advantageous adhesion forces are mandatory for industrial scale handling of the electrodes, which are subjected to bending in the R2R process. Depending on the slurry, even increased drying rates can be applied while maintaining or even improving the adhesion force. Despite improved mechanical properties, cells derived from these electrodes do not necessarily show enhanced electrochemical characteristics. Apart from the active material itself, this can be attributed to binder which may block lithium-ion pathways in pores or on the active material and thereby reduces the cell performance. This was shown in this work by an additive-reduced formulation showing advantageous cell performance. The downside here is the handling of these electrodes, since very poor adhesion results from the additive reduction.

Hence, to combine the most advantageous mechanical and electrochemical properties in one electrode, simultaneously coated multilayers are the consequent step which will be investigated in the following. [1]

6.1 Motivation and State of the Art

Simultaneously coated cathode multilayers have shown to improve the performance of lithium-ion batteries in literature: In one case this was realized by varying the formulation of each layer with respect to the ratio between two

[1] Results presented in this section are based the following publication by the author:[56]
Kumberg, Jana; Bauer, Werner; Schmatz, Joyce; Diehm, Ralf; Tönsmann, Max; Müller, Marcus; Ly, Kevin; Scharfer, Philip; Schabel, Wilhelm. (2021): Reduced Drying Time of Anodes for Lithium-Ion Batteries through Simultaneous Multilayer Coating. In: Energy Technol., S. 2100367. DOI: 10.1002/ente.202100367.

conductive additives contained in the slurries, while maintaining the binder content constant in both layers.[44] In a follow-up work, the binder content was varied, with a higher binder content in the bottom layer, while maintaining the total binder content identical to the reference.[45] Both approaches improved discharge rates, capacity and battery life cycles of the cells containing the two-layered cathodes compared to the single-layered reference electrodes.

On the anode side, simultaneously coated multilayers with different binder contents in the two layers have also been proven to improve cell performance by Diehm, Kumberg et al. (2020)[43]. The focus was the coating process. Since CMC impacts the rheological properties and enables simultaneous coating of two layers on top of each other, only the SBR binder was varied in the two layers. This guaranteed a stable multilayer coating as was shown by determination of the coating window. Intermixing of both layers was only detected at coating speeds below 1 m min^{-1}. The layer thickness ratio was 1:1. The slurries presented in the work of Diehm et al. (2020) were all based on the kneading process also applied in this work and used the identical reference recipe as the one presented here. The results of the reference mentioned there are therefore comparable with the ones derived from slurry (K).[43]

Another possibility to tune the properties of an electrode is by the coating of sequential multilayers, which means two or more coating and drying steps after one another. This enables the fixation of certain properties within defined layers of the electrode without intermixing of the layers being a problem. One disadvantage is the necessity of more than one coating and drying step. Another problem which was described in literature is the formation of a boundary layer which might influence cell performance.[98] This approach was therefore not further investigated in this work.

A similar approach, which can be used to further enable the use of binder-reduced recipes, is the application of a thin primer layer before the actual coating takes place to promote adhesion. This was also shown to positively affect cell performance.[21] An additional coating and drying step is still needed for the primer layer though.

Consequently, the application of a primer layer will be compared to simultaneously coated multilayers in the following. The goal hereby is to combine slurries with good adhesion properties in the bottom layer with slurries with good

electrochemical performance in the top layer. The ultimate goal is to increase the drying rate and minimize drying times while maintaining good mechanical and electrochemical cell properties.

6.2 Experimental Setup

Mixing: The four different slurries (R), (S), (K) and (A) were mixed after the recipe shown in the previous section 5.2. The primer layer was processed without active material with a ratio between SBR, CMC and carbon black of 1:1:1 at a water content of 97.3 wt-%, according to Diehm et al. (2020).[21] Slurry (A) was combined with the spherical slurry (S), slurry (K) derived from the kneading process and the primer layer (primer) as bottom layer. This resulted in the multilayers (S || A), (K || A) and (primer || A). In an alternative variation slurry (S) as bottom layer was combined with the reference slurry (R) as top layer. This is the multilayer (S || R). In the connotation the first slurry always stands for the bottom layer: (bottom || top). The multilayers with the additive-reduced slurry (A) on top differ in their total composition from the multilayers without gradient and from the single layers. The exact compositions of all multilayers are given in Table 6.1.

Table 6.1: Overview of the composition of the dry multilayer electrodes derived from combination of the four different slurries in wt-%. The multilayers (S || A), (K || A), (primer || A) and (S || R) - (bottom || top) are shown. (R) hereby stands for the electrode using the reference recipe, (S) for the spherical graphite, (K) for the kneading process and (A) for the additive-reduced recipe.

Material	(S || A)	(K || A)	(primer || A)	(S || R)
graphite SMGA	94.62	94.62	95.43	93
carbon black	1.13	1.13	1.00	1.4
CMC	1.59	1.59	1.45	1.87
SBR	2.66	2.66	2.12	3.73

Coating: For coating of multilayers, the coating stability was investigated via a multilayer slot die (see Appendix, Figure A. 7-40). The electrodes which were used for later characterization and coin cell fabrication were coated by two coating knifes in a row (for more information see Appendix E.1).

The layer thickness ratio between bottom and top layer was adjusted by the gap width of the coating knifes and was 1/3 bottom layer and 2/3 top layer for all simultaneously coated multilayers. This results in two separate layers which do not intermix and approximately possess the layer ratio 1:3. This can be seen in Figure 6.1 with the example of slurry (S) in the bottom layer and slurry (R) in the top layer.

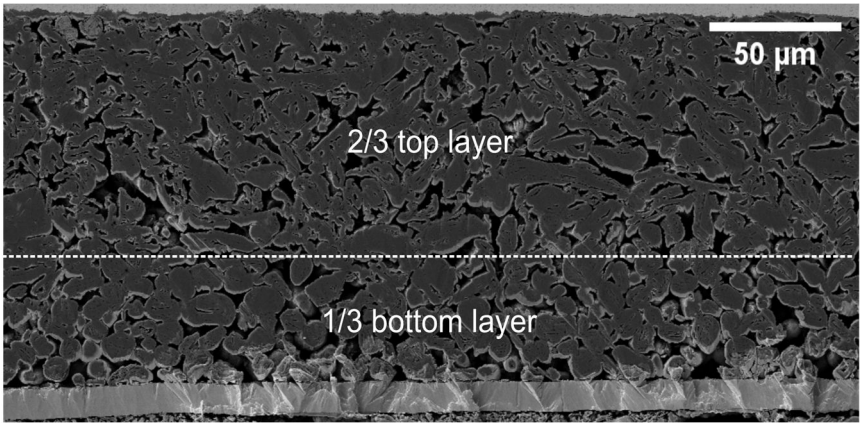

Figure 6.1: SEM cross section of a dry multilayer with the spherical slurry (S) at the bottom and the reference slurry (R) at the top. The layer thickness ratio is 1/3 bottom layer and 2/3 top layer. Figure taken from Kumberg et al., 2021.[56]

Drying & Cell Manufacturing: All electrodes in the following section have been dried in the batch coater (see section 2.2.3 Drying). The cells were manufactured according to section 2.3.6 (Electrochemical Properties).

6.3 Results and Discussion

As was done for the single layered electrodes derived from the four slurries, the adhesion force, electrical conductivity, and electrochemical performance of

multilayer electrodes was measured. State-of-the-art and high energy electrodes are compared as well as electrodes dried at the experimental drying rate of 0.5 g m^{-2} s^{-1} and 2.2 g m^{-2} s^{-1}.

6.3.1 Properties of the Dry Multilayer Electrodes

Adhesion force and electrical conductivity were measured for the multilayer electrodes. The following configurations were investigated in the following: The simultaneously coated multilayer consisting of the spherical slurry (S) at the bottom and the additive-reduced slurry (A) at the top, resulting in the multilayer (S || A). The slurry derived from the kneader (K) at the bottom and slurry (A) on the top, addressed as the multilayer (K || A). The layer thickness ratio was 1/3 bottom to 2/3 top layer. And as the last setup the primer layer as a thin, dry precoating and adhesion promoting layer at the bottom combined with slurry (A) on top, thus being the multilayer (primer || A).

Adhesion force of multilayers as a function of the drying rate

In Figure 6.2, the adhesion force of the multilayers is shown at two different drying rates. The multilayer electrodes are compared to the single layer electrodes derived from the reference slurry (R) in turquoise squares, and slurry (A) as orange line. The orange line visualizes the lowest adhesion level which was found throughout this work. It also corresponds to the adhesion force of the top layer (A) used in the multilayer setup. The adhesion force of the additive-reduced slurry (A) as single layer lies below the limit of 9 N m^{-1}, which is an orientation for industrial processing.[21] Details on drying conditions for all electrodes presented, like isothermal drying temperature and heat transfer coefficient, are given in Figure 2.5. For all area capacities and both drying rates, especially the simultaneously coated multilayers improve the adhesion force of the whole electrode when regarding the difference to the adhesion force of the top layer (A) as a single layer. The adhesion force of the multilayers (S || A) and (K || A) lies above that of the single layer reference electrode (R) for all area capacities. It is lower though than the respective bottom layers (S) and (K) coated as single layers (c.f. Figure 5.6). One reason for this could be that the multilayers contain an overall lower binder content of 4.25 wt-% in the dry electrode, compared to 5.6 wt-% of the single layers (c.f. Table 6.1).

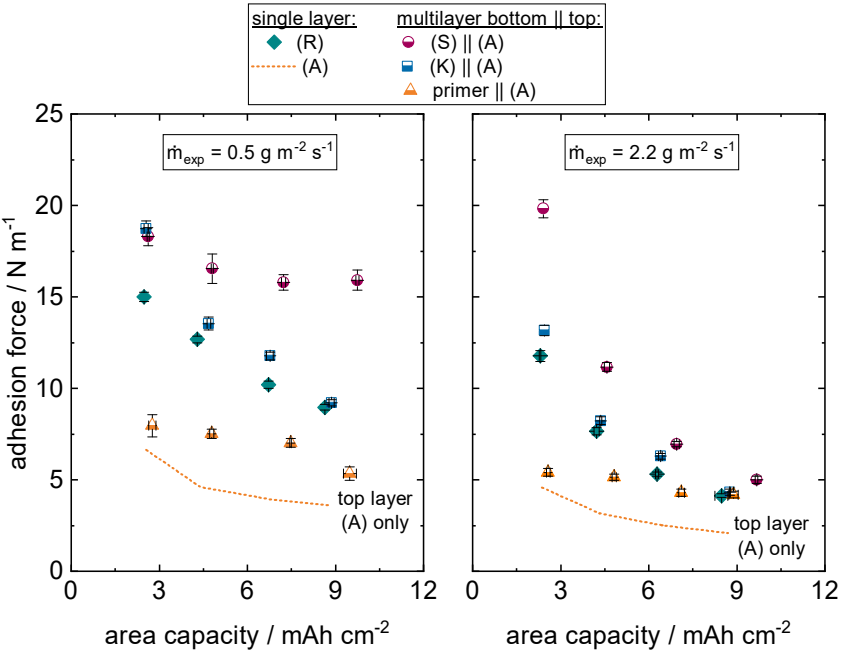

Figure 6.2: Adhesion force of multilayered electrodes as a function of the area capacity compared to the single layered reference (R) and electrode (A) as a line, which was used as top layer. The single layered electrode reference (R) is compared with the multilayers (S || A), (K || A), and (primer || A) - (bottom || top). (S) hereby stands for the electrode using the spherical graphite, (K) for the kneading process and (A) for the additive-reduced recipe. The adhesion force of the electrodes dried at the two experimental drying rates 0.5 g m^{-2} s^{-1} and 2.2 g m^{-2} s^{-1} is compared. For all electrodes substrate (f3) was used. Detailed experimentally validated drying conditions are given in Figure 2.5.

The adhesion force of the slowly dried multilayer (S || A) is almost constant over all area capacities. This is not true for the same multilayer dried at the high drying rate: The adhesion force decreases at an increase of the area capacity until the level of the single top layer (R) is almost reached at the highest area capacity.

A similar behavior can by observed for the simultaneously coated multilayer (K || A), with the difference that the adhesion loss at higher area capacities is present at both drying rates. As such the adhesion force is similar to the one of the reference electrodes (R) for the highest area capacity. Since the overall binder content is still lower than that of the reference electrode, a positive effect of the multilayer is still present. Only the electrode setup with the primer layer

(primer || A) does not suffer from significant influences of the electrode area weight or the drying rate. Since the primer layer was coated and dried before the actual electrode consisting of slurry (S) was applied, this meets the expectations. A small effect of the drying rate can be observed which could be explained by the thickness of the primer layer which is only in the range of a few microns.[21] Its overall adhesion is increased by the primer layer, which because clear from the comparison with the single layer (A). The absolute adhesion force though is still below the reference and the limit of 9 N m^{-1}, contrary to observations in literature, where a higher impact was reported.[21]

However, the results altogether imply that the assumption of a stable bottom layer which is not influenced during drying is not true. The hypothesis was that ester bond formation during drying fixes the bond between the active material and the CMC binder and also keeps the SBR binder at position. The drying rate though did influence the adhesion force of the multilayer electrodes. An explanation for this behavior could be the multilayer setup influencing the drying mechanisms by itself. Besides a concentration gradient of the two binders in the respective layers, which might increase the unwanted binder migration at the multilayer setup, the mechanism of capillary pore emptying could also have an impact: capillaries might transport liquid from the electrode bottom to the surface earlier than is the case for single layers with the pore size distribution of only one graphite type. More details especially regarding pore size distributions of the two different electrodes originating from the two graphites along with first insights into drying of multilayers will be presented in the appendix E.

The focus of this work lies, besides drying of (thick) single layer electrodes, on gaining first insights on (dis-) advantages of simultaneously coated multilayers, and the possibility to improve electrochemical performance combined with drying at high drying rates. A follow-up work could focus on investigating the drying process of multilayer electrodes itself with an emphasis on clearly separated pore size distributions of two or more materials in the respective layers and its influence on the drying mechanism.

Electrical conductivity of multilayers as a function of the drying rate

The electrical conductivity of the multilayers was measured and is compared to that of the reference (R) and the single top layer (A) in Figure 6.3. State-of-the-art area weight electrodes ($c_A \approx 2.6$ mAh cm^{-2}) and high energy electrodes ($c_A \approx 7.0$ mAh cm^{-2}), dried at the two different drying rates are shown.

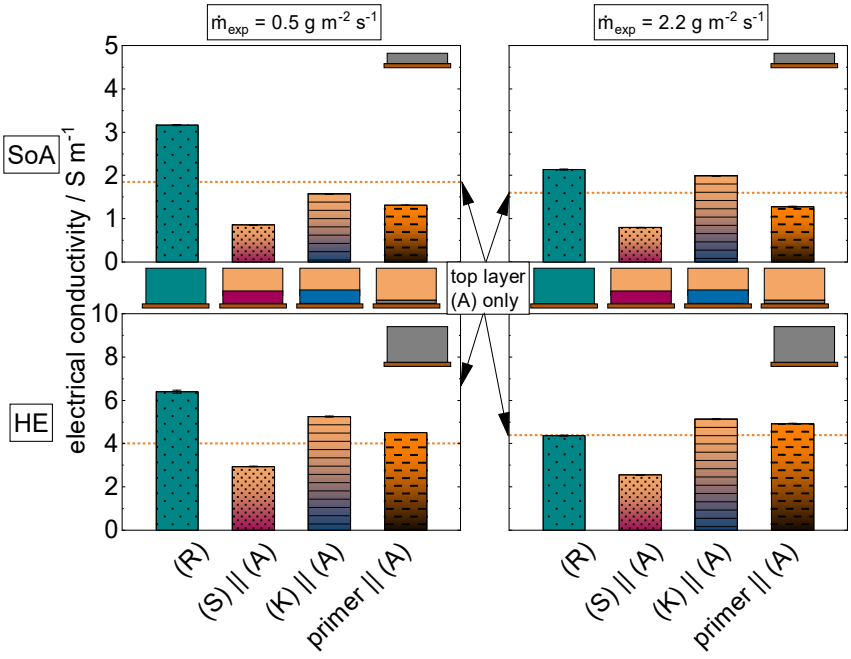

Figure 6.3: Top: Electrical conductivity of multilayer electrodes of state-of-the-art (SoA) area capacity of about 2.6 mAh cm^{-2} dried at the two different experimentally validated drying rates of 0.5 and 2.2 g m^{-2} s^{-1}. Bottom: The electrical conductivity of high energy (HE) electrodes with an averaged area capacity of 7.0 mAh cm^{-2} dried at the same two drying rates in comparison. Electrical conductivity of the three multilayer setups compared to the single layered reference (R) and electrode (A) as a line which was used as top layer. The single layered electrode reference (R) is compared with the multilayers (S || A), (K || A), and (primer || A) - (bottom || top). (S) hereby stands for the electrode using the spherical graphite, (K) for the kneading process and (A) for the additive-reduced recipe. The conductivity of the electrodes dried at the two experimental drying rates 0.5 g m^{-2} s^{-1} and 2.2 g m^{-2} s^{-1} (left and right column) as well as the electrical conductivity of state-of-the-art (c_A = 2.6 mAh cm^{-2}) and high energy (c_A = 7.0 mAh cm^{-2}) electrodes is compared.

The electrical conductivity as a function of all four investigated area weights is shown in Figure A. 7-48, in the Appendix. For both area weights and both drying

rates, the electrical conductivity of the reference electrode (R) is the highest, according to its highest content of the conductive agent carbon black. The electrical conductivity of the multilayer configurations (K || A) and (primer || A) are similar to the one of the single-layered electrode (A), which is depicted as yellow-dotted line.

Only the conductivity of the multilayer (S || A) lies well below that of the others. These trends are similar for both drying rates and both area weights. The electrical conductivity in general is higher at the higher area weights as was the case for the single-layered electrodes, due to the dependency on the electrode thickness. The drying rate on the other hand does not influence the electrical conductivity of the multilayers to such an extent as was true for the single layers. This could be attributed to the different properties of the two layers. The electrical conductivity is governed by the conductivity of the less conductive layer, which is the additive-reduced electrode (A) as was shown before. In the case of multilayer (S || A) the clear separation of both layers without a smooth transition from the spherical to the non-spherical graphite layer could cause the low conductivity (*cf* Figure 6.3). A non-observable impact of the higher drying rate at the state-of-the-art area weight could hint on fixed additives within the bottom layer of slurry (S). The multilayer (K || A) shows a slight increase in conductivity at the higher drying rate which could be caused by additives being dragged from the bottom layer into the less-conductive top layer consisting of slurry (A). Since the multilayer with the primer (primer || A) mainly consists of slurry (A), its conductivity is quite similar to that of electrode (A). The slightly reduced conductivity at the state-of-the-art area weight electrode might result from the primer layer which consists of only 33 % conductive carbon black and of 66 % of both binders SBR and CMC. A slight insulating effect could therefore manifest itself especially in combination with thin electrodes.

6.3.2 Electrochemical Performance of the Multilayer Electrodes

Thin and thick multilayer anodes were built into coin cells and tested for their electrochemical performance. A cycle test was conducted with the state-of-the-art multilayer electrodes which were dried at the experimentally validated drying

rates of 0.5 g m^{-2} s^{-1} and 2.2 g m^{-2} s^{-1}. Their specific discharge capacities under variation of the C rate as a function of the cycle are shown in Figure 6.4.

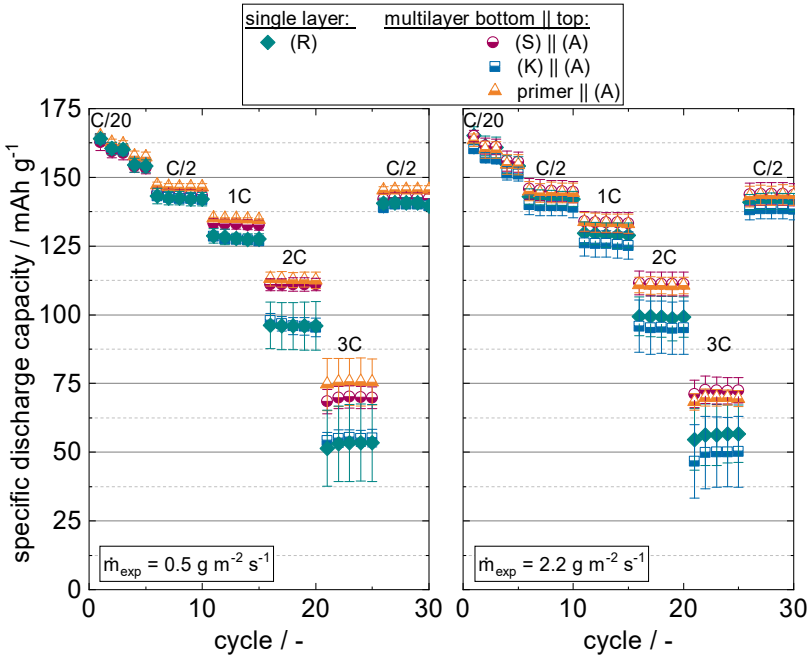

Figure 6.4: Coin cell test of simultaneously coated multilayer anodes against single layer cathodes, compared with the single-layered reference. The single layered electrode reference (R) is compared with the multilayers (S || A), (K || A), and (primer || A) - (bottom || top). (S) hereby stands for the electrode using the spherical graphite, (K) for the kneading process and (A) for the additive-reduced recipe. For anode manufacturing the experimental drying rates were 0.5 g m^{-2} s^{-1} and 2.2 g m^{-2} s^{-1}. State-of-the-art anodes were used with their exact area weights and porosities listed in Table A. 8 and Table A. 9 in the Appendix. Figure taken from Kumberg et al., 2021.[56]

In the case of the slower dried electrodes, contrary to the single layers, the discharge capacities at the lowest C rate of C/20 match for the multilayers, which might be attributed to the lesser influence of the bottom layers consisting of slurry (S) and (K), which only contribute 1/3 to the total electrode. As the C rate is increased, a deviation between the discharge capacities of the respective cells becomes evident. This is again most pronounced at the C rate of 3C. While the multilayer (K || A) performs identical to the reference, both multilayer (S || A)

and (primer || A) outperform them by almost 30 % at 3C. This trend remains true at the higher drying rate.

The electrochemical performance of the electrode with the primer layer exceeding that of the others is not surprising, since it mainly consists of slurry (A), which outperformed the other single layers already due to the low binder content. One disadvantage of the primer layer is the necessity of two individual coating and drying steps, first for the primer layer and second for the actual electrode. The other drawback is the adhesion force, still below the limit of 9 N m^{-1} for industrial processing.[21] The multilayer (S || A) consisting of the spherical slurry (S) as bottom layer and the additive-reduced slurry (A) on top, shows competitive electrochemical performance, while its adhesion force is twice that of the primer-based multilayer and can be processed in only one coating and drying step. On top of that, the drying rate for the state-of-the-art electrode can be significantly increased without loss of adhesion or electrochemical performance.

The identical multilayer configurations were also investigated as high energy cells and the results are presented in Figure 6.5. As was true for the high energy single layer cells, the discharge capacity of all cells deteriorates significantly for C rates of C/2 or higher. While all single layers (cf. Figure 5.10) performed quite similar, a significant difference is found between the single layered reference and the three multilayer configurations. All multilayers show higher discharge capacities than the reference. This is most obvious at C/2. Thereafter, the performance is reduced to almost zero for all investigated electrodes as the C rate approaches 2C. At C/2 though, an almost 30 % performance gain can be observed for the multilayers compared to the reference, especially for the electrodes which were dried at a drying rate of 2.2 g m^{-2} s^{-1}. This means that even though the adhesion force is hugely affected by the high area capacity in combination with the high drying rate, the electrochemical performance still profits from the multilayer setup and the slurry with reduced additive content.

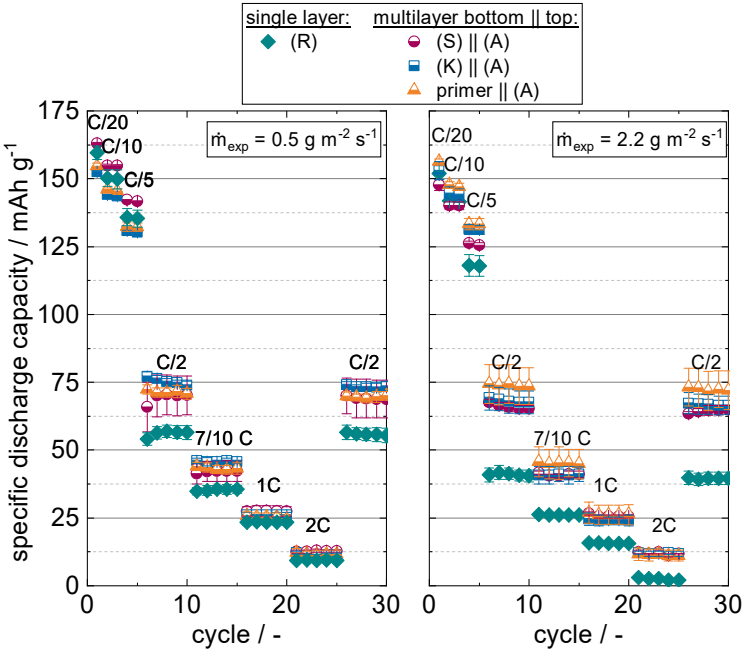

Figure 6.5: Coin cell test of simultaneously coated multilayer anodes against single layer cathodes, compared with the single-layered reference. The single layered electrode reference (R) is compared with the multilayers (S || A), (K || A), and (primer || A) - (bottom || top). (S) hereby stands for the electrode using the spherical graphite, (K) for the kneading process and (A) for the additive-reduced recipe. For anode manufacturing the experimental drying rates were 0.5 g m^{-2} s^{-1} and 2.2 g m^{-2} s^{-1}. High energy anodes were used with their exact area weights and porosities listed in Table A. 10 and Table A. 11 in the Appendix.

6.3.3 Extreme Drying Rates during Drying of Hierarchically Structured Electrodes

Based on the investigations presented here, there is a clear advantage of multi-layer over single-layer electrode coatings. This advantage could enable extreme drying rates under the assumption that a bottom layer is used which resists binder migration. The most promising candidate is the slurry based on the spherical graphite. To evaluate whether a change of the setup of the particle layers does influence the drying mechanism, the slurry based on the spherical graphite (S) was combined with the reference slurry (R). As a result, the layer configuration in terms of bottom and top layer can be changed without changing anything else

than the order of the particle layers. Slurry (R) and (S) as well as their multilayer combinations (bottom || top) layer (S || R) and (R || S) were investigated. The respective electrodes were dried at the experimentally validated drying rates of 0.5 g m^{-2} s^{-1} and 5 g m^{-2} s^{-1}. This corresponds to drying rates that are higher by more than a factor of 6 than those given as the state of the art by Kwade et al. (2018).[6]

The adhesion force of these electrodes of state-of-the-art area weight is given in Figure 6.6. Their respective area weights are listed in Table A. 12. The values of the single layers are only given for comparative reasons since they have been discussed already.

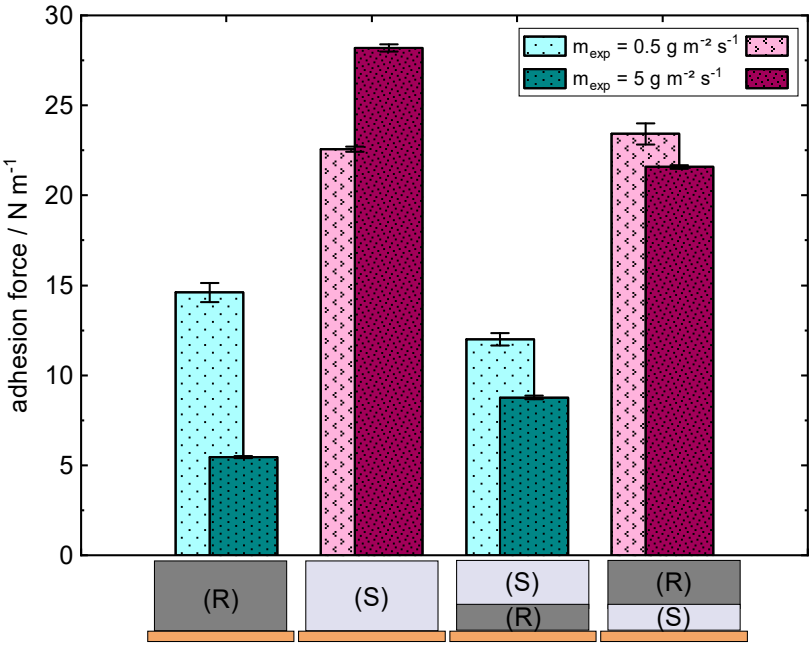

Figure 6.6: Adhesion force of the state-of-the-art single layer reference (R) and spherical (S) electrodes compared with the multilayers (R || S) and (S || R), (bottom || top). They were dried at a low drying rate of 0.5 g m^{-2} s^{-1} and an extreme drying rate of 5 g m^{-2} s^{-1}. Figure taken from Kumberg et al., 2021.[56]

In case of the multilayer (R || S), the adhesion force is reduced from single to multilayer for the low drying rate, while it is increased from single to multilayer

for high drying rates. The opposite behavior is found for the multilayer (S || R). In both cases, a distortion of the capillary pore emptying can be suspected by the two layers of different pore radii distributions on top of each other. More details on multilayer drying will be given in the appendix E.

The higher value of the absolute adhesion force of the multilayer (S || R) is in line with expectations, since more stable ester bonds increasing the adhesion force were expected. Still, the adhesion force of the single layer consisting of slurry (S) alone is highest at both drying rates. The disadvantage of single layer (S) though, is the worse electrochemical performance, as shown earlier (cf. Figure 5.9). Although the reference layer on top of slurry (S) has some negative effect on the adhesion force of the multilayer compared to the single layer (S), it still exceeds that of single layer electrode (R) by far.

Whether the advantageous behavior of multilayer (S || R) is also evident in the electrochemical performance was verified in a cell test. The discharge capacities at different C rates of the single and multilayers dried at the extreme drying rate of 5 g m^{-2} s^{-1} and a resulting drying time of 14 s are shown in Figure 6.7. The drying rate was experimentally validated (see Figure 2.5) and the drying time was determined based on the theoretical capacities of the electrodes (see Table A. 12, Appendix for theoretical capacities and porosities).

In the cell test, especially in the first few cycles at low C rates up to C/2, the slowly dried reference stands out. This might be caused by a lower performance of the spherical graphite due to its higher surface area and higher irreversible lithium loss or an intrinsically lower capacity as explained earlier. Since the fast dried slurry (R) also shows a slightly lesser performance, an influence of the inhomogeneous binder distribution already at very low C rates is concluded. The poorer performance of the fast dried electrode (R) continues over all C rates and is most severe at the highest C rate of 3C. At this C rate it performs even worse than the fast dried electrode (S), which shows lower discharge capacities than (R) for a low drying rate (see Figure 5.9). At the extreme drying rate its capability of fixating more binder seems to be advantageous, though the discharge capacity of electrode (S) in Figure 6.7 is somewhat lower than that of the slowly dried reference, as would be expected. The performance of the multilayer with the reference as bottom layer (R || S) is very similar to the one of electrode (S), which

means it is higher than that of the fast dried electrode (R), but lower than the slowly dried electrode (R).

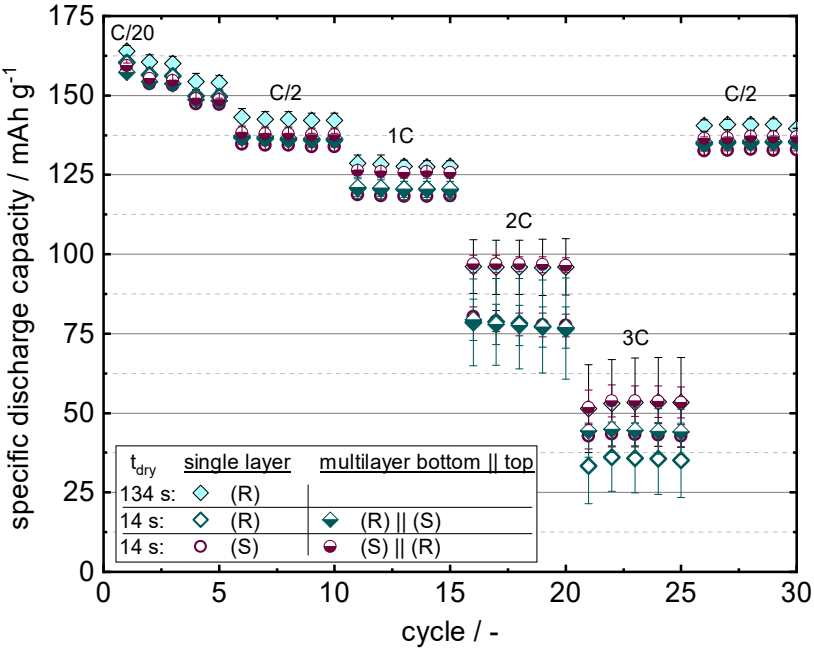

Figure 6.7: Coin cell test of simultaneously coated and high-speed dried multilayer anodes built against single layer cathodes, compared with the single layered reference. The single layered electrodes reference (R) and spherical (S) are compared with the multilayers (R || S) and (S || R), (bottom || top). For anode manufacturing the experimental drying rates were 0.5 g m^{-2} s^{-1} and 5 g m^{-2} s^{-1}. State-of-the-art anodes were used with their exact area weights and porosities listed in Table A. 12 in the Appendix. Figure taken from Kumberg et al., 2021.[56]

A quite positive effect of the multilayer setup is observed for the combination (S || R): It performs identical to the slowly dried reference cell (R) at a C rate of 3C even though the drying time was only 14 s as compared to 134 s of the reference and therefore only 10 % of its drying time.

In this section, it was shown that by the chosen multilayer setup (S || R) an almost tenfold acceleration of the drying time was realized without a performance loss, which becomes especially relevant at high C rates of 3C. Since the adhesion force

also had a value above the slowly dried reference, and well above 9 N m^{-1} no problems in roll-2-roll handling would be expected as well.

7. Summary and Outlook

The growing importance of lithium-ion-batteries for stationary energy storage and in the mobility sector requires research to focus on improving the energy density, reduce prices, increase material utilization or enhance manufacturing speed. This work addresses both energy density and increased manufacturing speeds by giving insights into the complex mechanism during drying and its influence on mechanical stability and electrochemical performance. Processing and especially drying of battery electrodes remains a challenge due to the complex mechanisms during drying which directly affect battery performance. On the way to accelerated process speeds in industrial dryers, an extensive knowledge about the drying process in relation to battery performance is needed.

In this work, the drying mechanism, experimental challenges regarding especially high energy electrodes, correlations to device performance and predictive simulations of drying of thin and thick lithium-ion battery anodes were investigated in detail. It was experimentally shown that problems such as binder migration, which directly affect cell performance, are dependent on the drying conditions (section 3). Experimental and simulated drying curves are able to predict the drying course of thin and thick electrodes and help to understand drying behavior (section 4). Based on these findings, the simulation was used to propose advantageous drying routes, which can be transferred to industrial production lines. Since different processing routes during drying enable only a limited number of improvements, a broader variety of process changes was considered in the next step. This is accomplished by conducting a closer investigation of the importance of slurry properties. Slurries with improved mechanical or electrochemical performance were found (section 5). To combine both, improved mechanical and electrochemical properties, drying of simultaneously coated multilayers with advantageous property gradients was accomplished (section 6). The goal was to minimize drying times while maintaining good electrochemical properties and simultaneously guarantee good mechanical stability to meet industrial processing and handling requirements. The scientific challenge was summarized in the beginning of this work in form of four hypotheses, which relate to the respective

section. They will again be separately addressed and summarized in the four following sections.

7.1 Drying of Thicker Electrodes

The relationship between drying parameters like drying rate and temperature to the properties of the developing dry electrode were investigated in section 3, with an emphasis on thicker electrodes. The capillary transport of solvent to the surface of the electrode is ultimately connected to the properties of the dry electrode. This is due to the fact that not only the solvent, but also the smaller additives within the solvent, like carbon black or binders, are transported to the electrode surface. This leads on the one hand to a loss in adhesion since binder, which is needed especially at the electrode-substrate interface, is transported away from there. On the other hand, it results in a deterioration of the electrochemical performance of the electrode compared to one with a more homogenous binder distribution. Binder at the top of the electrode blocks surface pores as well as the surface of the active material particles, thus hindering lithium diffusion into the depth of the electrode and into the depth of the active material particles itself.

The influence of the drying conditions on the binder distribution was investigated for thin and thick single-layer electrodes. The hypothesis was that new challenges arise in relation with drying due to binder migration when the electrode thickness is increased compared to the state of the art. To that end, a broad variety of electrodes of differing area weights were dried at different drying rates. The results show a clear trend of an increasing loss in adhesion force with an increasing drying rate. It was also found that the adhesion force of thick electrodes is always beneath that of thin electrodes. This was attributed to the early onset of capillary pore emptying, the longer drying time and the longer pathways for diffusional balancing processes.

A positive effect on the adhesion was found when drying at a higher temperature instead of a higher heat transfer coefficient when an identical drying rate was set. This can either be caused by a higher binder back diffusion, which compensates the concentration gradient developing during drying to some extent. It could also be caused by a small amount of ester bonds, which increase the adhesion force by chemical bonding of CMC to the graphite particle surface. Higher binder

gradients at higher drying rates were proven by measurements of the CMC binder content at the top of two differently dried electrodes as well as by LIBS measurements over the complete electrode thickness. Both techniques verify the CMC-binder distribution dependence on the drying rate.

The influence of the drying rate on cell performance was also analyzed in a coin cell test. In contrast to findings of Jaiser et al. (2016), the increase of the drying rate by a factor of about four did not deteriorate the discharge capacity of the cell over any C rate up to 3C. This was attributed to the water-based binder system compared to the PVDF-NMP system investigated by Jaiser et al. (2016), and to the fact that the drying rate was increased by adjusting the drying temperature rather than the heat transfer coefficient.[10]

In conclusion, binder migration poses an increased challenge when drying thick electrodes, and thus the hypothesis that new challenges arise when drying thicker electrodes was found to be true. Since binder migration and the drying mechanism are closely interlinked, an experimental and theoretical approach to better understand the drying process was focused on in the next part.

7.2 Drying Behavior of Thicker Electrodes

The drying process, being the transport of solvent within the wet electrode as well as the evaporation of solvent from the electrode, was investigated in section 4 for electrodes of increasing thickness. The drying behavior of electrodes used in lithium-ion batteries was simulated and experimentally validated. The experimental setup consisted of a stationary dryer hood, called the comb nozzle dryer, which allows industrial drying rates. The dryer was combined with a novel gravimetric setup to measure film mass and temperature during drying. Thus, electrode films of different thicknesses or area weights were examined with a special focus on limitations for solvent transport within the film. The hypothesis here was that the drying process of thin electrodes is governed by the gas phase, whereas thicker electrodes dry under a growing influence of film resistances.

A simulation of the drying of electrodes in terms of the film temperature and the solvent loading over time was developed. It is comprised of mass and energy balances around the drying film, which consider heat and mass transfer. The

simulation model was first validated for thin electrode films, where the importance of local effects of heat and mass transfer became apparent. For state-of-the-art electrode area weights, it was shown that no film resistances hinder solvent transport, and the drying itself is governed by gas phase kinetics, as assumed. A simulation considering the actual heat transfer coefficient distribution of the used dryer was shown to be able to correctly represent the solvent loading and the temperature course of a drying electrode film. In an additional experiment, using a light microscope in combination with the comb nozzle dryer, it was confirmed that capillary pore emptying determines the drying of electrode coatings, as was also suggested in literature.[26] Therefore, a fast solvent transport to the electrode surface is guaranteed for low area weight electrodes.

As the electrode thickness is increased, film resistances gain in importance. The simulation model was adapted accordingly to consider these changes in the drying kinetics. To avoid complex computational efforts, the moving drying front model proposed by Krischer was implemented into the code.[25] This model assumes a water front homogeneously receding into the film and the case of no capillary transport taking place. It was experimentally shown though, with the experimental setup using the light microscope, that capillary transport still takes place for thick electrodes. Clusterwise pore emptying was observed, increasing along with the film thickness. This means during drying of thick electrodes more solvent filled capillaries are separated from the bulk than is the case for thin electrodes. As a consequence evaporation partly does not take place at the electrode surface anymore, but within the microstructure, thereby reducing the drying rate. It was also found that the first pores breaking through to the bottom of the substrate occur at the end of film shrinkage for thin electrodes for the investigated material and the drying parameters used. At higher area weights though, first pores breaking through to the bottom of the electrode were found up to 25 % before the theoretical end of film shrinkage.

The complex mechanism behind electrode drying therefore depends on the knowledge of the exact pore size distribution and the interconnection of all capillaries with one another. This is not considered in the moving drying front model, which is a simplification of the actual drying process. However, it was shown in this work that the moving drying front model approach is still able to predict the solvent loading curve and the end of drying with an accuracy of 94 % even for the thickest electrode investigated here.

In summary, the presented simulation model is able to predict the drying of electrode films. This also applies to thick electrodes as long as film resistances are considered when drying curves of thicker electrodes are targeted, thereby validating hypothesis (2). The model can be extended to describe the drying curve in dryers comprised of different drying zones, thus leading to improved process control.

Since the problem of binder migration is still related to drying and cannot be completely prevented even by improved process control, strategies to improve microstructures were investigated and are summarized in the following section.

7.3 Influence of Slurry Properties

The wet electrode consists not only of individual components mixed together, but also of the network formed by these components and their interactions with each other. To establish whether there is a link between this interlinked network and drying, different slurry properties were adjusted in section 5. The problem of binder migration at accelerated drying rates was addressed by investigating four different slurries in detail. These are based on the reference slurry which was used and characterized in the previous sections 3 and 4. The reference slurry was modified as follows: The active material was replaced from a non-spherical to a spherical graphite as a first alternative. For the second modification, the mixing method was changed from a dissolver to a kneader. In the third and final variant, the formulation was transformed into an additive-reduced one. The intention was to modify the interconnecting network of active material, carbon black and the binder system CMC/SBR within the slurry in different ways by the three chosen cases. The hypothesis was that drying has different effects on the developing electrode microstructure in dependency of the physicochemical properties of the slurry and the interaction between binder and active material and the formed network.

The effect of modifying the slurry was evaluated by Cryo SEM micrographs. These allowed a detailed evaluation of the surface of the active materials as well as the binder network within the pores of the slurry in a quasi-wet state. Due to the experimental procedure, which allows the sublimation of the solvent at the surface pores of the cross section, an observation of the inner pore volume was

enabled. A clear difference between all four investigated slurries could be observed. The CMC network connecting the active material particles was found to form in varying complexity. The most intricate network was found in the slurry derived from the kneading process, where a higher adhesion compared to the reference was found. This was mainly attributed to the strong network, resulting from the intensity of the kneading process which sheared off smaller graphite particles, providing more open surface for the CMC binder to attach to. The additive-reduced slurry on the other hand showed the less developed binder network and the lowest adhesion force compared to the other slurries. This was justified with the low binder content which led to a network not fully formed and less surface covered with binder.

For the slurry based on the spherical graphite a close attachment of the CMC-binder on the active material particles surface could be observed. These stronger bonds seemed to correlate with a better adsorption of binder on the active material, which manifested itself also in the highest adhesion force between all four investigated slurries. Even at higher drying temperatures and correspondingly higher drying rates, the adhesion strength remained at a high level or even increased. In literature different adsorption behaviors of CMC on graphite particles in dependency of the graphite's surface order were reported.[87] It was further concluded there, that a certain adsorption on the disordered graphite surfaces leads to the formation of strong ester bonds between CMC and OH groups on its surface.[87] Raman spectroscopy confirmed the presence of a disordered graphite surface with a higher probability of binding OH groups in the spherical graphite powder used for the experiments in this work. Smaller amounts of disorder were also found for grinded graphite as well as for the pure non-spherical graphite powder. These findings can explain an increase of the adhesion force when drying at higher temperatures at a constant drying rate. Thus a connection between the interaction of the binder- particle-system and the tendency for binder migration was found, validating hypothesis (3).

Another important observation concerns the SBR-binder: Since measurement methods showing its distribution are still missing, an important clue can be gained from the Cryo-SEM-micrographs. In all four slurries the SBR binder appeared to be mainly attached to the CMC. This was also observed for the carbon black. It was therefore concluded that results regarding CMC-binder migration could also be transferred to the SBR-binder to some extent. This is in accordance

with results shown in section 3, where adhesion loss, which is mainly attributed to SBR-binder migration, and the binder distribution measured with LIBS correlate.

In contrast to the improved adhesion force, the electrochemical performance was not enhanced by the slurries with better adhesion. The best electrochemical performance was observed for the additive-reduced slurry, which performed worst in terms of adhesion due to the binder-reduced formulation. While this is not an issue in coin cell preparation, this would not be transferable to roll-2-roll processes where mechanical forces would detach the electrode from the substrate easily. Using only one layer, fast-dried electrodes with good mechanical as well as electrochemical properties could not be realized. To move one step further, slurries which resulted in advantageous adhesion and electrochemical properties were combined in a multilayer electrode, which is summarized in the following.

7.4 Simultaneously Coated and Hierarchically Structured Multilayers

With the aim of combining good mechanical with beneficial electrochemical properties slurries were chosen from the investigated ones in section 5 and combined in simultaneously coated multilayers in section 6. The hypothesis was that by multilayer coating and drying and a targeted combination of two layers, optimized electrodes can be produced at high drying rates.

The most promising multilayers for state-of-the-art (SoA) as well as high energy (HE) electrodes are compared to the single layer reference. The main results are summarized in Figure 7.1. Three different experimentally validated drying rates of 0.5 g m^{-2} s^{-1}, 2.2 g m^{-2} s^{-1} and 5 g m^{-2} s^{-1} were investigated. The adhesion force as well as the discharge capacity at 3C is given in relation to that of the reference. For the state-of-the art electrodes, the multilayers outperform the reference at all drying rates regarding the adhesion force as well as the electrochemical performance. This is also true for the high energy electrodes, though the effect is less pronounced there, due to their overall worse performance.

At a drying rate of 2.2 g m^{-2} s^{-1}, the multilayer of spherical graphite combined with the additive-reduced slurry (S || A) surpasses the reference (R) by about

25 % in adhesion and electrochemical performance. For the highest drying rate of 5 g m^{-2} s^{-1}, the reference (R) and the multilayer consisting of the spherical graphite and the reference on top (S || R) were investigated. For this setup, a discharge capacity identical to the one of the slowly dried reference, as well as a higher adhesion force than the reference can be observed.

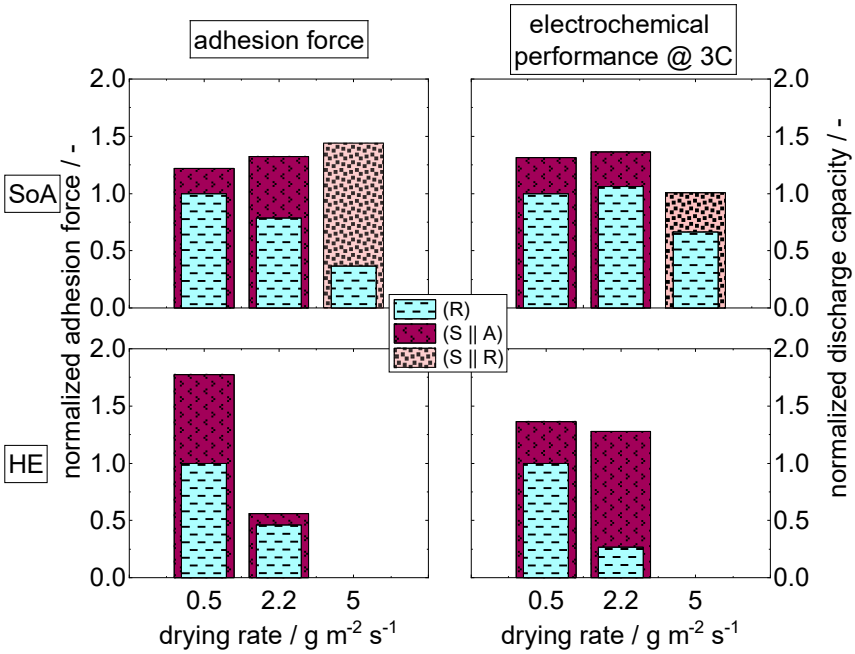

Figure 7.1: Comparison of the adhesion force and the discharge capacity at 3C of state-of-the-art (SoA) and High Energy (HE) electrodes at different drying rates. The values are normalized with the respective values of the slowly dried reference (R). The single layer electrode (R) is compared to a multilayer (S || A) consisting of a bottom layer with a spherical graphite (S) combined with an additive-reduced (A) top layer, and to a multilayer (S || R) consisting of the spherical graphite as bottom layer combined with the reference as top layer.

In this work the drying rate was successfully increased by a factor of almost ten, resulting in a drying time of only 14 s for a state-of-the-art electrode compared to 134 s of the reference, while maintaining good electrochemical performance and realizing an improved adhesion force. This validates hypothesis (4).

7.5 Outlook

The simulation models proposed in this work significantly facilitate identifying beneficial drying conditions in industrial scale processes while being computationally significantly less demanding than rigorous pore-network modelling. Defined drying profiles can be specified to improve the drying process. This is only possible though, if heat and mass transfer coefficients in production plants are known which is not the case most of the time. These would have to be determined. In the future, industrial scale dryers in research and industry should in a first step be thoroughly analyzed to get the defined relation between heat transfer coefficient, volume flow rate and gas temperature to establish full process control.

The inclusion of sensors for dew point, film temperature, film thickness or film reflection measurements along the drying chambers to measure the drying profile in-situ would be an additional measure on the way to improve drying profiles. Industrial dryers also suffer from long start-up times until stationary conditions are present within the chamber. An equilibrium solvent content in the gas phase within the dryer chambers is reached along with solvent evaporating from the film which might be additionally circulated with the air. A pretreatment of the air could reduce the time until stationary drying conditions are reached and further improve drying control.

Drying profiles within the dryer should consist of a first zone where high drying rates can be applied. The beginning of pore emptying must be considered and should be reached in a zone of moderate drying conditions. For thin electrodes an approximation with the end of film shrinkage could be a starting point. For thicker electrodes though, the beginning of pore emptying should be considered more conservatively since first empty pores were observed before the end of film shrinkage. Closer to the end of the dry electrode when capillary drag from the electrode bottom has almost ceased, higher drying rates could possibly again be applied. This should be investigated more thoroughly based on research reported from Jaiser et al. (2017) with the aim of distinguishing the relevant points during drying being the first empty pore or the end of film shrinkage and their influence not only on adhesion but also on cell performance.

As was also shown in this work, elevated drying temperatures in combination with lower heat transfer coefficients should be preferred over low temperatures and high heat transfer coefficient. Since heat transfer by contact is no option in industrial processes, IR or laser drying should be investigated thoroughly, as they pose the opportunity to increase the film temperature by an additional energy input exceeding convective methods.

Since binder migration is still likely to be a problem, the approach of using simultaneously coated multilayers with specially tuned properties in the individual layers should be pursued. A reduction of the binder content in the top layer in combination with a bottom layer resisting binder migration to some extent is very promising. The increase of the drying rate to levels far exceeding industrial state-of-the-art should be investigated and integrated to improve process times. A closer look should thereby be given on the influence of different pore radii distributions in the respective layers on the drying mechanism. By using narrower pore size distributions with small pores in the bottom layer and bigger pores in the top layer, a positive effect on binder migration could be gained. Simultaneous multilayer coating also opens a broad range of further possibilities. The electrochemical performance especially of thick electrodes should profit from broader pore sizes in the top layer, since this would enhance diffusional pathways for lithium ions. By expanding simultaneously coated multilayers to more than just two layers, layers could be tuned to meet certain demands exceeding the control of binder migration. Thus, a coating could consist of a small binder fixating layer at the bottom, followed by a layer which could be supplemented by silicon to improve the energy density and a layer to implement pathways for lithium ions with a high porosity at the top.

A problem which remains for the water-based binder system SBR and CMC is the necessity of characterization methods which give a clear evidence of the binder distribution within the dry electrode. While this is simple in the NMP-PVDF system, it is more complicated for the water-based system. Being able to track the SBR binder would enable a more explicit correlation between process conditions and cell performance. Laser-induced breakdown spectroscopy (LIBS) is a promising method to detect the CMC-binder distribution and seems to give results which could be well correlated to the experiments presented here. An additional method for detecting the SBR binder though is absolutely necessary.

References

[1] European Commission, "Paris Agreement", can be found under https://ec.europa.eu/clima/policies/international/negotiations/paris_en, **2015**.

[2] European Commission, "A European Green Deal", can be found under https://ec.europa.eu/info/strategy/priorities-2019-2024/european-green-deal_en, **2019**.

[3] Bundesministerium für Umwelt, Naturschutz und nukleare Sicherheit (BMU), www.bmu.de.

[4] Presse- und Informationsamt der Bundesregierung, "Klimaschutz", can be found under https://www.bundesregierung.de/breg-de/themen/klimaschutz/verkehr-1672896, **2021**.

[5] Daniel Kuepper, Kristian Kuhlmann, Sebastian Wolf, Cornelius Pieper, Gang Xu, and Justin Ahmad.

[6] A. Kwade, W. Haselrieder, R. Leithoff, A. Modlinger, F. Dietrich, K. Droeder, *Nat Energy* **2018**, *3*, 290–300.

[7] J.-H. Schunemann, H. Dreger, H. Bockholt, A. Kwade, *ECS Transactions* **2016**, *73*, 153–159.

[8] L. Mauler, F. Duffner, J. Leker, *Applied Energy* **2021**, *286*, 116499.

[9] R. Diehm, *Dissertation* **2021**.

[10] S. Jaiser, M. Müller, M. Baunach, W. Bauer, P. Scharfer, W. Schabel, *Journal of Power Sources* **2016**, *318*, 210–219.

[11] M. Müller, L. Pfaffmann, S. Jaiser, M. Baunach, V. Trouillet, F. Scheiba, P. Scharfer, W. Schabel, W. Bauer, *Journal of Power Sources* **2017**, *340*, 1–5.

[12] L. Pfaffmann, S. Jaiser, M. Müller, P. Scharfer, W. Schabel, W. Bauer, F. Scheiba, H. Ehrenberg, *Journal of Power Sources* **2017**, *363*, 460–469.

[13] B. Westphal, H. Bockholt, T. Gunther, W. Haselrieder, A. Kwade, *ECS Transactions* **2015**, *64*, 57–68.

[14] W. B. Hawley, J. Li, *Journal of Energy Storage* **2019**, *25*, 100862.

[15] Reiner Korthauer **2013**.

[16] R. Schmuch, R. Wagner, G. Hörpel, T. Placke, M. Winter, *Nat Energy* **2018**, *3*, 267–278.

[17] P. Kurzweil, O. K. Dietlmeier **2018**.

[18] B. G. Westphal, A. Kwade, *Journal of Energy Storage* **2018**, *18*, 509–517.

[19] H. Bockholt, W. Haselrieder, A. Kwade, *Powder Technology* **2016**, *297*, 266–274.

[20] R. Diehm, H. Weinmann, J. Kumberg, M. Schmitt, J. Fleischer, P. Scharfer, W. Schabel, *Energy Technol.* **2019**, *5*, 1900137.

[21] R. Diehm, M. Müller, D. Burger, J. Kumberg, S. Spiegel, W. Bauer, P. Scharfer, W. Schabel, *Energy Technol.* **2020**, *8*, 2000259.

[22] C.-C. Li, Y.-W. Wang, *J. Electrochem. Soc.* **2011**, *158*, A1361.

[23] S. Jaiser, L. Funk, M. Baunach, P. Scharfer, W. Schabel, *Journal of colloid and interface science* **2017**, *494*, 22–31.

[24] J. Kumberg, M. Müller, R. Diehm, S. Spiegel, C. Wachsmann, W. Bauer, P. Scharfer, W. Schabel, *Energy Technol.* **2019**, *3*, 1900722.

[25] O. Krischer, *Springer* **1956**.

[26] S. Jaiser, J. Kumberg, J. Klaver, J. L. Urai, W. Schabel, J. Schmatz, P. Scharfer, *Journal of Power Sources* **2017**, *345*, 97–107.

[27] F. Font, B. Protas, G. Richardson, J. M. Foster, *Journal of Power Sources* **2018**, *393*, 177–185.

[28] V. K. Surasani, T. Metzger, E. Tsotsas, *International Journal of Heat and Mass Transfer* **2008**, *51*, 2506–2518.

[29] M. Prat, *Int. J. Multiphase Flows*, *1993*, pp. 691-704.

[30] T. Metzger, *Drying Technology* **2018**, *37*, 497–512.

[31] T. Metzger, E. Tsotsas, *Chemie Ingenieur Technik* **2010**, *82*, 869–879.

[32] A. Kharaghani, T. Metzger, E. Tsotsas, *Chemical Engineering Science* **2012**, *75*, 267–278.

[33] E. W. Comings, T. K. Sherwood, *industrial and engineering chemistry* **1934**.

[34] M. Yamamura, K. Ohara, Y. Mawatari, H. Kage, *Drying Technology* **2009**, *27*, 817–820.

[35] E.-U. Schlünder, *Chemie Ingenieur Technik* **1988**, *60*, 117–120.

[36] D. L. Wood, J. D. Quass, J. Li, S. Ahmed, D. Ventola, C. Daniel, *Drying Technology* **2017**, *36*, 234–244.

[37] N. Susarla, S. Ahmed, D. W. Dees, *Journal of Power Sources* **2018**, *378*, 660–670.

[38] M. Stein, A. Mistry, P. P. Mukherjee, *J. Electrochem. Soc.* **2017**, *164*, A1616-A1627.

[39] H. Buqa, M. Holzapfel, F. Krumeich, C. Veit, P. Novák, *Journal of Power Sources* **2006**, *161*, 617–622.

[40] S. Lim, S. Kim, K. H. Ahn, S. J. Lee, *Journal of Power Sources* **2015**, *299*, 221–230.

[41] H. Hagiwara, W. J. Suszynski, L. F. Francis, *J Coat Technol Res* **2014**, *11*, 11–17.

[42] C.-C. Li, Y.-S. Lin, *Journal of Power Sources* **2012**, *220*, 413–421.

[43] R. Diehm, J. Kumberg, C. Dörrer, M. Müller, W. Bauer, P. Scharfer, W. Schabel, *Energy Technol.* **2020**.

[44] L.-C. Chen, D. Liu, T.-J. Liu, C. Tiu, C.-R. Yang, W.-B. Chu, C.-C. Wan, *Journal of Energy Storage* **2016**, *5*, 156–162.

[45] D. Liu, L.-C. Chen, T.-J. Liu, W.-B. Chu, C. Tiu, *Energy Technol.* **2017**, *5*, 1235–1241.

[46] H. Bockholt, *Dissertationsschrift* **2016**.

[47] M. Cerbelaud, B. Lestriez, R. Ferrando, A. Videcoq, M. Richard-Plouet, M. T. Caldes, D. Guyomard, *Langmuir : the ACS journal of surfaces and colloids* **2014**, *30*, 2660–2669.

[48] M. E. Spahr, D. Goers, A. Leone, S. Stallone, E. Grivei, *Journal of Power Sources* **2011**, *196*, 3404–3413.

[49] R. Dominko, M. Gaberscek, J. Drofenik, M. Bele, S. Pejovnik, J. Jamnik, *Journal of Power Sources* **2003**, *119-121*, 770–773.

[50] VMA-Getzmann GmbH, "Dissolver Dispermat CN10", can be found under http://www.vma-getzmann.de/know-how/dispergieren_mit_dissolvern/dispergieren_mit_dissolvern_0_921_1803.html.

[51] INOUE MFG., Inc., "Trimix TX-15", can be found under https://www.inouemfg.com/en/products/?id=1573629834-290717&ca=16.

[52] M. Baunach, S. Jaiser, S. Schmelzle, H. Nirschl, P. Scharfer, W. Schabel, *Drying Technology* **2015**, *34*, 462–473.

[53] M. Baunach, S. Jaiser, P. Cavadini, P. Scharfer, W. Schabel, *J Coat Technol Res* **2015**, *12*, 915–920.

[54] S. Jaiser, *Dissertation* **2017**.

[55] *VDI-Buch*, Springer Vieweg, Berlin, **2013**.

[56] J. Kumberg, W. Bauer, J. Schmatz, R. Diehm, M. Tönsmann, M. Müller, K. Ly, P. Scharfer, W. Schabel, *Energy Technol.* **2021**, 2100367.

[57] P. Cavadini, P. Scharfer, W. Schabel in *The 15th International Heat Transfer Conference*.

[58] N. Willenbacher and K. Georgieva, U. Bröckel., W. Meier, G. Wagner, *Wiley VCH* **2013**, 7–49.

[59] Thomas G. Mezger **2016**.

[60] M. Singh, J. Kaiser, H. Hahn, *Journal of the Electrochemical Society* **2015**, *162*, A1196-A1201.

[61] M. Singh, J. Kaiser, H. Hahn, *Journal of Electroanalytical Chemistry* **2016**, *782*, 245–249.

[62] Z. Du, D. L. Wood, C. Daniel, S. Kalnaus, J. Li, *J Appl Electrochem* **2017**, *47*, 405–415.

[63] T. Danner, M. Singh, S. Hein, J. Kaiser, H. Hahn, A. Latz, *Journal of Power Sources* **2016**, *334*, 191–201.

[64] P. Smyrek, J. Pröll, H. J. Seifert, W. Pfleging, *J. Electrochem. Soc.* **2015**, *163*, A19-A26.

[65] W. Pfleging, *Nanophotonics* **2018**, *7*, 549–573.

[66] M. A. Ghadkolai, S. Creager, J. Nanda, R. K. Bordia, *J. Electrochem. Soc.* **2017**, *164*, A2603-A2610.

[67] J. S. Sander, R. M. Erb, L. Li, A. Gurijala, Y.-M. Chiang, *Nat Energy* **2016**, *1*, 3828.

[68] S. Jaiser, A. Friske, M. Baunach, P. Scharfer, W. Schabel, *Drying Technology* **2016**, *35*, 1266–1275.

[69] L. S. Kremer, A. Hoffmann, T. Danner, S. Hein, B. Prifling, D. Westhoff, C. Dreer, A. Latz, V. Schmidt, M. Wohlfahrt-Mehrens, *Energy Technol.* **2020**, *8*, 1900167.

[70] A. Hu, *Laser Micro-Nano-Manufacturing and 3D Microprinting*, Springer International Publishing, Cham, **2020**.

[71] Y. Zheng, L. Pfäffl, H. J. Seifert, W. Pfleging, *Applied Sciences* **2019**, *9*, 4218.

[72] W. Pfleging, *Int. J. Extrem. Manuf.* **2021**, *3*, 12002.

[73] M. Baunach, M. Müller, S. Jaiser, W. Bauer, P. Scharfer, W. Schabel.

[74] J. Kumberg, M. Baunach, J. C. Eser, A. Altvater, P. Scharfer, W. Schabel, *Energy Technol.* **2020**, *3*, 2000889.

[75] J. Kumberg, M. Baunach, J. C. Eser, A. Altvater, P. Scharfer, W. Schabel, *Energy Technol.* **2021**, 2100013.

[76] A. Gören, D. Cíntora-Juárez, P. Martins, S. Ferdov, M. M. Silva, J. L. Tirado, C. M. Costa, S. Lanceros-Méndez, *Energy Technol.* **2016**, *4*, 573–582.

[77] J. C. Eser, T. Wirsching, P. G. Weidler, A. Altvater, T. Börnhorst, J. Kumberg, G. Schöne, M. Müller, P. Scharfer, W. Schabel, *Energy Technol.* **2019**, *73*, 1801162.

[78] B. Schmidt-Hansberg, M. Baunach, J. Krenn, S. Walheim, U. Lemmer, P. Scharfer, W. Schabel, *Chemical Engineering and Processing: Process Intensification* **2011**, *50*, 509–515.

[79] Edward N. Fuller/Paul D. Schettler/J. Calvin. Giddings.

[80] D. Oehler, P. Seegert, T. Wetzel, *Energy Technol.* **2020**.

[81] A. Loges, S. Herberger, P. Seegert, T. Wetzel, *Journal of Power Sources* **2016**, *336*, 341–350.

[82] YAWS **1999**.

[83] W. Schabel.

[84] C. M. Cardinal, Y. D. Jung, K. H. Ahn, L. F. Francis, *AIChE J.* **2010**, *56*, 2769–2780.

[85] S. Baesch, P. Scharfer, W. Schabel, L. Francis, *Journal of Composite Materials* **2017**, *51*, 3391–3403.

[86] V. C.-A. Gracia-Medrano-Bravo, J. Gröne, S. Baesch, P. Scharfer, W. Schabel, *Langmuir : the ACS journal of surfaces and colloids* **2020**, *36*, 6245–6253.

[87] W. J. Chang, G. H. Lee, Y. J. Cheon, J. T. Kim, S. I. Lee, J. Kim, M. Kim, W. I. Park, Y. J. Lee, *ACS applied materials & interfaces* **2019**, *11*, 41330–41337.

[88] S. Lim, K. H. Ahn, M. Yamamura, *Langmuir : the ACS journal of surfaces and colloids* **2013**, *29*, 8233–8244.

[89] R. Gordon, M. Kassar, N. Willenbacher, *ACS omega* **2020**, *5*, 11455–11465.

[90] R. Gordon, R. Orias, N. Willenbacher, *J Mater Sci* **2020**, *257*, 421.

[91] J. Drofenik, M. Gaberscek, R. Dominko, F. W. Poulsen, M. Mogensen, S. Pejovnik, J. Jamnik, *Electrochimica Acta* **2003**, *48*, 883–889.

[92] W. Schabel, *Chemie Ingenieur Technik* **2005**, *77*, 1915–1926.

[93] U. Garbe, *Bachelorarbeit; KIT-Fakultät für Chemieingenieurwesen und Verfahrenstechnik - Thin Film Technology; Gutachter: Prof. Dr.-Ing. Wilhelm Schabel; Betreuer: Jana Kumberg M.Sc. and Dr.-Ing. Philip Scharfer*, *2020*.

[94] W. Bauer, D. Nötzel, *Ceramics International* **2014**, *40*, 4591–4598.

[95] M. Cerbelaud, B. Lestriez, D. Guyomard, A. Videcoq, R. Ferrando, *Langmuir : the ACS journal of surfaces and colloids* **2012**, *28*, 10713–10724.

[96] S. H. Sung, S. Kim, J. H. Park, J. D. Park, K. H. Ahn, *Materials (Basel, Switzerland)* **2020**, *13*.

[97] M. W. Murray, Hall, D., S., J. R. Dahn, *Journal of the Electrochemical Society* **2019**, A329-A333.

[98] Daniel Westhoff, Timo Danner, Simon Hein, Rares Scurtu, Lea Kremer, Alice Hoffmann, André Hilger, Ingo Manke, Margret Wohlfahrt-Mehrens, Arnulf Latz, Volker Schmidt.

[99] J. Kramer, *Diplomarbeit; KIT-Fakultät für Chemieingenieurwesen und Verfahrenstechnik - Thin Film Technology; Gutachter: Prof. Dr.-Ing.*

Wilhelm Schabel; Betreuer: Jana Kumberg M.Sc.; Dipl.-Ing. Ralf Diehm and Dr.-Ing. Philip Scharfer **2018**.

[100] A. Benchabane, K. Bekkour, *Colloid Polym Sci* **2008**, *286*, 1173–1180.

[101] Jin-Hyon Lee,a Ungyu Paik,a,z Vincent A. Hackley,b and Young-Min Choic,*, *ECS Transactions* **2004**.

[102] Abdelrahim, K., A., Ramaswamy, H., S., G. Doyon, C. Toupin, *International Journal of Food Science and Technology* **1994**, 243–253.

[103] Ghannam, M.,T., Esmail, M., N., *John Wiley & Sons, Inc.* **1997**.

[104] X. H. Yang, W. L. Zhu, *Cellulose* **2007**, *14*, 409–417.

[105] S. Mizera, *Masterarbeit; KIT-Fakultät für Chemieingenieurwesen und Verfahrenstechnik - Thin Film Technology; Gutachter: Prof. Dr.-Ing. Wilhelm Schabel; Betreuer: Jana Kumberg M.Sc. and Dr.-Ing. Philip Scharfer*, *2020*.

[106] W. Haselrieder, B. Westphal, H. Bockholt, A. Diener, S. Höft, A. Kwade, *International Journal of Adhesion and Adhesives* **2015**, *60*, 1–8.

[107] B. Bitsch, J. Dittmann, M. Schmitt, P. Scharfer, W. Schabel, N. Willenbacher, *Journal of Power Sources* **2014**, *265*, 81–90.

[108] S. Stoltz, *Masterarbeit; KIT-Fakultät für Chemieingenieurwesen und Verfahrenstechnik - Thin Film Technology; Gutachter: Prof. Dr.-Ing. Wilhelm Schabel; Betreuer: Jana Kumberg M.Sc.; Jochen Eser, M.Sc. and Dr.-Ing. Philip Scharfer* **2018**.

[109] K. Adams, *Bachelorarbeit; KIT-Fakultät für Chemieingenieurwesen und Verfahrenstechnik - Thin Film Technology; Gutachter: Prof. Dr.-Ing. Wilhelm Schabel; Betreuer: Jochen Eser, M.Sc.; Jana Kumberg M.Sc. and Dr.-Ing. Philip Scharfer* **2018**.

[110] H. N. Yow, M. Goikoetxea, L. Goehring, A. F. Routh, *Journal of colloid and interface science* **2010**, *352*, 542–548.

[111] E. Santanach Carreras, F. Chabert, D. E. Dunstan, G. V. Franks, *Journal of colloid and interface science* **2007**, *313*, 160–168.

[112] W. P. Lee, A. F. Routh, *Langmuir : the ACS journal of surfaces and colloids* **2004**, *20*, 9885–9888.

[113] M. S. Tirumkudulu, W. B. Russel, *Langmuir : the ACS journal of surfaces and colloids* **2005**, *21*, 4938–4948.

[114] K. B. Singh, M. S. Tirumkudulu, *Physical review letters* **2007**, *98*, 218302.

[115] Z. Du, K. M. Rollag, J. Li, S. J. An, M. Wood, Y. Sheng, P. P. Mukherjee, C. Daniel, D. L. Wood, *Journal of Power Sources* **2017**.

[116] J. R. Cost, K. R. Janowski, R. C. Rossi, *The Philosophical Magazine: A Journal of Theoretical Experimental and Applied Physics* **1968**, *17*, 851–854.

[117] J. van de Lagemaat, K. D. Benkstein, A. J. Frank, *J. Phys. Chem. B* **2001**, *105*, 12433–12436.

[118] S. Lim, S. Kim, K. H. Ahn, S. J. Lee, *Ind. Eng. Chem. Res.* **2015**, *54*, 6146–6155.

[119] C. Dörrer, *Masterarbeit; KIT-Fakultät für Chemieingenieurwesen und Verfahrenstechnik - Thin Film Technology; Gutachter: Prof. Dr.-Ing. Wilhelm Schabel; Betreuer: Dipl-Ing. Ralf Diehm; Jana Kumberg M.Sc. and Dr.-Ing. Philip Scharfer* **2018**.

[120] M. S. Carvalho, H. S. Kheshgi, *AIChE J.* **2000**, *46*, 1907–1917.

[121] X. Ding, J. Liu, T. A. L. Harris, *AIChE J.* **2016**, *62*, 2508–2524.

[122] B. G. Higgins, L. E. Scriven, *Chemical Engineering Science* **1980**, *35*, 673–682.

[123] K. J. Ruschak, *Chemical Engineering Science* **1976**, *31*, 1057–1060.

[124] J. Nam, M. S. Carvalho, *J. Fluid Mech.* **2009**, *631*, 397–417.

List of Figures

Figure 1.1: Schematic picture of a typical liquid-electrolyte-based lithium-ion battery. During discharge, the lithium ions diffuse in the electrolyte from anode to cathode, inducing an external electron flow. For charging, the process is reversed.....3

Figure 1.2: Process chain for coin cell fabrication starting with a dry mixing step, followed by wet mixing, coating and drying of the slurry and calendering of the dry electrode. Electrodes are then cut, post dried and assembled to a coin cell together with casing, separator, electrolyte, spring and spacer. The final step consists of formation and cell testing. 5

Figure 1.3: Drying time (left) and dryer length (right) in dependency of the drying rate at a typical web speed of 50 m min^{-1}. Both values are calculated for a typical electrode of dry area weight of 74 g m^{-2} (2.5 mAh cm^{-2}) with an initial solid content of 43 %. The red area marks the published state of the art with 1-2 min drying time after Kwade et al. (2018) and therefore the reference drying rate of this work.[6] The orange and yellow areas mark 3 to 7 times higher drying rate ranges, which are aimed to reach in this work and which form an upper limit of drying rates applied in industry in electrode drying. The influence of up to 7 times higher drying rates than the documented state of the art on electrode properties will therefore be investigated.....7

Figure 1.4: Adhesion force in dependency of the drying rate and the transition time chosen to change between the drying rates. The adhesion force is correlated with the fluor content at the electrode bottom and thus the binder content. (Reproduced from Jaiser et al. (2016), predecessor in the authors working group at KIT-TFT, with permission from Elsevier.)[10] 9

Figure 1.5: Model presentation of the drying behavior of an electrode for lithium-ion batteries. The solvent of the wet film (a)

evaporates at the film surface until the EOF, where all capillaries are filled within the network (b). Capillary transport moves the solvent to the electrode surface where it evaporates (c). If remaining liquid clusters exist, solvent evaporates within the particle network and diffuses to the surface (d). The dry electrode film results (e). Figure taken from Kumberg et al., 2019.[24] 10

Figure 1.6: SEM micrographs showing the comparison of the cross sections of a thinner state-of-the-art electrode (a, left) and a thicker electrode (b, right). Figure taken from Kumberg et al., 2019.[24] 13

Figure 2.1: Schematic of the flow fields of a dissolver a) and picture of the dissolver disc b) after VMA Getzmann GmbH.[50] 20

Figure 2.2: Mixing tool of the kneader Inoue Trimix TX-15 (MVT-VM, KIT) 20

Figure 2.3: Picture of the Batch Coater (BC) used for defined drying of electrode films. The dryer hood has an array of 20 slot nozzles where heat transfer coefficients between 35 W m^{-2} K^{-1} and 80 W m^{-2} K^{-1} can be adjusted. A periodic movement of the film which is fixed on a heating plate enables homogenous drying conditions under the nozzle array. Spherical-shaped suction nozzles for exhaust air removal are positioned at both sides in between the supply air slot nozzles. 22

Figure 2.4: Interdependency between the drying conditions of an industrial convection dryer and its temperature $Tdryer$ and the drying conditions in the Batch Coater at wet bulb temperature $Tsteady\ state$ (derived from the relative humidity of air), as well as the resulting drying rate. The drying rate was 0.75 g m^{-2} s^{-1}, the heat transfer coefficient varied between 80 and 35 W m^{-2} K^{-1} and the dew point temperature of the drying air between 15 and 30 °C. For the industrial dryer an identical air flow from the top and the bottom was assumed. Figure taken from Kumberg et al., 2019. [24] 24

Figure 2.5: Experimental drying curves at different drying rates in the Batch Coater. The solvent loading as a function of drying time was determined by interrupting the experiment and measuring the residual moisture content of the electrodes. The heat transfer coefficient during all experiments was 35 W m^{-2} K^{-1} at a dew point of 10 °C. The reference slurry with the composition presented in Table 2.1 was used. Figure taken from Kumberg et al., 2021.[56] 25

Figure 2.6: Comb Nozzle field with marked supply and exhaust air nozzles. Comb Nozzle field from CN Drying Technology. 26

Figure 2.7: Density distribution as a function of the particle size of the reference slurry and the pure graphite powder in water. The pure graphite powder has a $d50$ of 17.1 µm. The reference slurry has a $d50$ of 17.2 µm and shows a second peak at around 0.17 µm, which can be attributed to fractured carbon black aggregates 28

Figure 2.8: Newton's law of shear stress with a fixed plate at the bottom, a moving plate at the top and a linear velocity profile known as "Couette flow". 29

Figure 2.9: Dynamic viscosity of the reference slurry as a function of increasing (upward) and decreasing (downward) shear rate with the composition given in Table 2.1 30

Figure 2.10: Phase difference angle of the reference slurry in dependency of the angular frequency with the composition of the slurry given in Table 2.1. 32

Figure 2.11: 90° peel test to measure the adhesion force of the dry electrode coatings on a substrate. 33

Figure 2.12: Pore size distribution of the dry reference electrode with the composition given in Table 2.1. It shows the main peak at a pore diameter of around 5 µm and the second smaller peak at 12 µm 35

Figure 2.13: SEM micrograph of the dry reference electrode with the composition given in Table 2.1 showing its microstructure and pore size distribution. The d_{50} of the particle size distribution is 18.4 µm (Figure 2.7). The pore size distribution

has a main peak at ~5 µm and a smaller peak at ~12 µm (Figure 2.12). Based on this SEM micrograph, pore sizes above 20 µm and especially two more small peaks in the pore size distribution at 36 µm and 64 µm are neglected since it is assumed that surface pores appeared in the measurement. 36

Figure 2.14: Measurement setup for the electrical conductivity. A current was applied by an E3633A power supply (Agilent Technologies) and the voltage difference UR measured with a multimeter (2700, Keyence) using a four-wire setup. The electrical conductivity was derived from the voltage drop $U23$ between the two cylinders with a diameter of 40 mm and an area of $Acylinder$= 12.6 cm², with the intrinsic resistance R of the setup being 11 kΩ..... 37

Figure 3.1: Normalized adhesion force of electrodes of differing theoretical capacities dried with a theoretical drying rate of 0.75 g m^{-2} s^{-1} and a heat transfer coefficient of 35 W m^{-2} K^{-1}. The area weight corresponding to a theoretical capacity is given as top x-axis. The absolute adhesion force is given as right y-axis. Normalization is conducted to guarantee comparability throughout this work, since absolute values depend on the copper foil used. The adhesion force of the reference electrode dried at a drying rate of 0.75 g m^{-2} s^{-1} and a heat transfer coefficient of 35 W m^{-2} K^{-1} at a capacity of 2.5 mAh cm^{-2} is used for normalization. Figure taken from Kumberg et al., 2019.[24]..... 42

Figure 3.2: Normalized adhesion force of electrodes with two different theoretical capacities of 2.5 mAh cm^{-2} (m = 74 g m^{-2}) and 12.5 mAh cm^{-2} (m = 371 g m^{-2}) which were dried under variation of the drying rate, according to an experiment after Baunach et al.[73] The drying rate was adjusted either by variation of the temperature or the heat transfer coefficient, corresponding to the settings (1) to (4), also summarized in Table 3.3. The adhesion force of the reference electrode dried at a drying rate of 0.75 g m^{-2} s^{-1} and a heat transfer coefficient of 35 W m^{-2} K^{-1} at a capacity of 2.5 mAh cm^{-2} is used for normalization. Figure taken from Kumberg et al., 2019. [24]47

Figure 3.3: Influence of an annealing temperature on the adhesion force of the reference electrode. The electrode was dried prior to annealing at a drying rate 0.75 g m^{-2} s^{-1} a heat transfer coefficient of 35 W m^{-2} K^{-1} and an isothermal drying temperature of 31 °C and had an area capacity of 2.5 mAh cm^{-2}. The definite impact of annealing starts well after relevant isothermal drying temperatures used for drying in this work (see appendix Table A. 2), thereby allowing to separate the effect annealing has on adhesion from the one of drying temperature. The adhesion force of the reference electrode dried at a drying rate of 0.75 g m^{-2} s^{-1} and a heat transfer coefficient of 35 W m^{-2} K^{-1} at a capacity of 2.5 mAh cm^{-2} is used for normalization. Figure taken from Kumberg et al., 2019.[24] 49

Figure 3.4: Normalized adhesion force in dependency of the drying rate for two different area capacities of 2.5 mAh cm^{-2} (m = 74 g m^{-2}) and 12.5 mAh cm^{-2} (m = 371 g m^{-2}). The heat transfer coefficient was varied between 35 W m^{-2} K^{-1} and 80 W m^{-2} K^{-1} to distinguish between the influence of increasing the heat transfer coefficient and the isothermal drying temperature to increase the drying rate. An upper boundary for the adhesion force is found for electrodes dried under free convection and a lower boundary when electrode are dried without any SBR binder. Two different substrates (f1) and (f2) were used. The adhesion force of the reference electrode dried at a drying rate of 0.75 g m^{-2} s^{-1} and a heat transfer coefficient of 35 W m^{-2} K^{-1} at a capacity of 2.5 mAh cm^{-2} is used for normalization. Figure taken from Kumberg et al., 2019. [24] 51

Figure 3.5: LIBS measurements which were made by Y. Zheng and W. Pfleging at IAM-AWP, KIT. The Na-CMC distribution of two thick electrodes of an area capacity of 12 mAh cm^{-2} (356 g m^{-2}), left and 13.5 mAh cm^{-2} (401 g m^{-2}), right is given from the top of the electrode into the depth of the electrode reaching to the bottom. The measurement was conducted over an area of 5 x 5 mm. On the x-axis a width of 4 mm is shown to avoid edge effects with the averaged Na-content for the

respective position. The electrodes were dried at a low drying rate of 0.75 g m^{-2} s^{-1} (left) and a four times higher drying rate of 3 g m^{-2} s^{-1} (right), with the respective values of their thickness, porosity and area capacity summarized in Table 3.1. The CMC-binder distribution over their height is compared. 54

Figure 3.6: Influence of different drying rates on cell performance of thin electrodes with an area capacity between 2.1 mAh cm^{-2} and 2.2 mAh cm^{-2} built into coin cells (see respective area capacities in Table 3.5). Drying was conducted at three different experimentally validated drying rates and at a heat transfer coefficient of 35 W m^{-2} K^{-1}. 56

Figure 3.7: Influence of different drying rates on cell performance of thick electrodes with an area capacity of 8.5 mAh cm^{-2} and 8.8 mAh cm^{-2} built into coin cells (see respective area capacities in Table 3.5). Drying was conducted at two different experimentally validated drying rates and at a heat transfer coefficient of 35 W m^{-2} K^{-1}. 58

Figure 4.1: Experimental procedure of coating (a, left) and drying (b, right) in the Comb Nozzle dryer. The substrate is fixed in a stenter frame which stands on a precision balance, separated from the setup by spaces through a tabletop. During coating in a), the coating knife is placed on the substrate and moved by an automated coating arm to coat a precise film. A PET-foil with a rectangular cut-out was used as mask during coating and removed directly afterwards. For the drying step in b), the scale along with the tensioned frame and the substrate are moved upwards and the dryer hood downwards. The intermediate plate is removed, resulting in a free hanging copper foil substrate with the electrode slurry film. Figure taken from Kumberg et al., 2020.[74] 63

Figure 4.2: Coating procedure. For the coating step, the coating knife was placed on the substrate and moved by an automated coating arm at a velocity of 6 m min^{-1} to coat a precise film. Since a defined coating area along with a homogenous film thickness is mandatory for the interpretation of the drying

curve, a polyethylene terephthalate (PET) foil with a rectangular cut-out of 9x9 cm was used as mask during coating and removed directly afterwards, thus defining the size of the coating Ael. Figure taken from Kumberg et al., 2020 [74] 64

Figure 4.3: Experimental setup to investigate drying patterns using an infrared (IR) camera during electrode drying with the comb nozzle dryer. The electrode film is coated on top of a transparent PET substrate. The choice of substrate allows the investigation of the film temperature without interferences due to reflections. 67

Figure 4.4: Experimental setup to investigate the pore emptying behavior during drying with the comb nozzle dryer. The electrode film is coated by the automated coating arm on top of a transparent glass substrate. The choice of substrate allows the visualization of pore emptying and is also necessary to prevent the movement of the substrate in and out of focus. Figure taken from Kumberg et al., 2021.[75] 68

Figure 4.5: Schematic of relevant in- and outgoing heat flows and mass fluxes during electrode drying in the comb nozzle dryer. An ingoing heat flux from the dryer at the top as well as an ingoing heat flux from the heating plate at the bottom can be seen. There is no contact between heating plate and electrode film. An outgoing enthalpy flux into the surrounding at the top of the film is caused by solvent evaporation. Figure taken from Kumberg et al., 2020.[74] 73

Figure 4.6: Heat transfer distribution for different values of a median heat transfer coefficient and the respective relative surface area. The distributions of the heat transfer coefficient for five different values of a median value for the heat transfer coefficient (α-median) are given. To each value of a heat transfer coefficient its relative surface fraction $A = A\alpha/Afilm$ is assigned. The shown distribution was determined by TLC measurements prior to this work. Figure taken from Kumberg et al., 2020.[74] 81

Figure 4.7: Parameters w and xc of the gaussian fit function in dependency of the experimentally determined heat transfer coefficients α-median. They clearly show a linear relation. Based on this, the linear fit functions in equation (4.34) and (4.35) can be used to describe their dependency on the heat transfer coefficient. Figure taken from Kumberg et al., 2021.[74] 82

Figure 4.8: Model of the moving drying front after Krischer and Schlünder.[25],[75] It assumes that the solvent retreats into the porous film as a homogenous drying front and that transport resistances grow in dependency of the distance of the retreating solvent front to the porous surface. Figure taken from Kumberg et al., 2021. 84

Figure 4.9: Experimentally obtained drying curve of a thin electrode film, with the solvent loading and the film temperature over time. The area weight was 72 g m^{-2}, with further properties listed in Table 4.2. The solvent loading linearly decreases until it reaches a constant value around zero. This is illuminated by a linear regression of the gravimetric data. The constant drying rate prevails well after the end of film shrinkage at a solvent loading of 0.658 $g_{solvent}\ g_{dry\ mass}^{-1}$ which is marked by a dashed line. Figure taken from Kumberg et al., 2020.[74] 87

Figure 4.10: IR images which were derived from a recording of the film temperature of an electrode during drying using an IR camera recording from below through a PET substrate. Different times during electrode drying are shown with a) showing the film after 0 s and therefore at the beginning of drying. In b) the same film is shown after a drying time of 136 s and in c) after 145 s. In d) the film is dry within the marked area after a drying time of 250 s. The white circle marks the area which was used for averaging. The obtained values are plotted in Figure 4.11 against the drying time. Figure taken from Kumberg et al., 2020.[74] 89

Figure 4.11: Temperature curve of the electrode film recorded with the IR camera. The averaged film temperature taken with the IR camera is compared to that logged by the thermocouple. The

course of the temperature is identical within the first 100 s and both converge towards the same value at the stationary temperature. Figure after Kumberg et al., 2021. [74] 91

Figure 4.12: Bottom view of an electrode filmed during drying with a digital microscope through a glass substrate. a) shows the wet film at 0 s, the beginning of drying. In b) the first empty pore can be observed after 45 s. c) shows the film after 54 s, d) after 60 s and e) after 70 s with the propagation of empty pores. The film changes no more in f) after 120 s of drying time. The drying course in terms of solvent loading and film temperature will be discussed along with Figure 4.19. Figure taken from Kumberg et al., 2021.[75].....92

Figure 4.13: Simulated drying curve of a thin electrode film using the constant rate model. The simulation using the heat transfer coefficient derived from TLC measurements (α-median$_{TLC}$) is compared to that based on the determination of the heat transfer coefficient by linear regression (α-median$_{linreg}$). Figure taken from Kumberg et al., 2020.[74] 93

Figure 4.14: Calculated distribution of the heat transfer coefficient derived for α-median$_{linreg}$ = 39.3 W m^{-2} K^{-1}. The turquoise legend assigns a grade of shading to the relative surface fraction of a respective heat transfer coefficient within the distribution. Figure taken from Kumberg et al., 2020.[74] 95

Figure 4.15: Experimental and simulated drying curve of thin electrode. The constant rate model (α-median) is compared to the lateral model (accum. α-distribution). Both calculations are based on α-median$_{linreg}$ = 39.3 W m^{-2} K^{-1}. The courses of solvent loading and temperature are shown. Since the lateral model simulates an array of area-weighted drying curves for each heat transfer coefficient, the contributing curves are depicted as well. The intensity of the shading reflects the relative surface area of the respective heat transfer coefficient (see Figure 4.14). The array of curves of solvent loading and temperature add up to the curve of the accumulated α-distribution under consideration of their respective relative

surface fractions. Figure taken from Kumberg et al., 2020.[74] 96

Figure 4.16: Heat flux densities of radiation at the top and bottom, convection and free convection as well as the sum of all contributions during drying of a thin electrode are given, left y-axis. The corresponding course of the solvent loading is given on the right y-axis. After roughly 100 s once the film temperature rises above the temperature of the heating plate, the heat flux caused by free convection changes from ingoing to outgoing. Averaged values of the heat flux densities during the steady-state phase and at the end of drying are summarized in Table 4.4. Figure after Kumberg et al., 2021.[74] 98

Figure 4.17: Experimental drying curves of thick electrodes with different area weights $m1$-$m4$, listed in Table 4.2. At the top, the (wet) area weight of the four electrodes over drying time is given. At the bottom, the solvent loading over drying time is plotted. Figure taken from Kumberg et al., 2021.[75] 101

Figure 4.18: Drying patterns of electrodes of different area weights at three different times during drying. In an experiment to further illuminate capillary transport in drying of thick electrodes, the digital microscope was used to observe pores breaking through to the bottom of the electrodes. An increased clusterwise drying with an increasing area weight can be observed. Figure taken from Kumberg et al., 2021.[75].... 102

Figure 4.19: Simulation of the solvent loading curve of the experiment with the digital microscope, based on the heat transfer coefficient found by fitting experimental and simulated temperature curves to one another. The heat transfer coefficient was 36 W m^{-2} K^{-1}. The slow temperature increase is caused by the use of the glass substrate in the experiment compared to copper or PET foil in the other two experiments. The glass plate contributes a large amount of additional weight which has to be warmed up, which was also considered in the simulation. Different times of the

experimental procedure to observe capillary pore emptying as shown in Figure 4.12b-f are marked. 104

Figure 4.20: Comparison between experimentally determined time when first pores are visible $tfirst\ pore, exp$ using the setup with the digital microscope and theoretically determined end of film shrinkage $tEOF, theo$ for electrodes with four different area weights. The absolute times are given on the left y-axis and compared to the appearance of the first pore appearing in relation to the theoretical end of film shrinkage shown on the right y-axis. Figure taken from Kumberg et al., 2021.[75] 105

Figure 4.21: Experimental and simulated gravimetric drying curves and film temperatures for four different area weights $m1$ – $m4$.with a single graph for each film. The constant rate model (α-median) is compared to the lateral model (accum. α-distribution). Both calculations are based on the values of α-median$_{linreg}$ given in Table 4.6. The courses of solvent loading and temperature are shown. Since the lateral model simulates an array of area-weighted drying curves for each heat transfer coefficient, the contributing curves are depicted as well. The intensity of the shading reflects the relative surface area of the respective heat transfer coefficient (see Figure 4.14). The array of curves of solvent loading and temperature add up to the curve of the accumulated α-distribution under consideration of their respective relative surface fractions. Figure taken from Kumberg et al., 2021.[75] 110

Figure 4.22: Comparison of the drying models MDF with accum. α-distribution, MDF with α-median, and constant rate drying in dependency of the area weight. The simulated drying times are compared with the experimental data at the time the solvent loading reaches 1 % in relation to the equilibrium solvent loading. Absolute times are given in Table 4.7. Figure taken from Kumberg et al., 2021.[75] 112

Figure 4.23: Exemplary drying curve of a state-of-the-art electrode in a three-zone dryer with an exemplary length of 9 m divided into zones of 3 m each. Web speed was assumed to be 10 m min^{-1}. The drying is assumed to be realized by an array of slot

nozzles at the top and the bottom of the film with identical heat transfer coefficients, with their specific values as well as drying temperatures given in the top of the figure. One-sided coating and drying is assumed, though double-sided coating could easily be implemented. The end of film shrinkage is reached at the beginning of the second dryer zone. In zone three a higher dryer temperature and heat transfer coefficient are applied. 115

Figure 5.1: Cryo-BIB-SEM preparation and measuring protocol to obtain micrographs of anode slurries showing the internal pore volume after solvent sublimation. The wet slurries were coated and immediately frozen in nitrogen slush without any drying taking place. The cross sections were prepared in a first step by cutting the immersed film with a diamond saw before being transferred to the Cryo-Broad Ion Beam. The surface was ablated by three argon ion guns. First all capillaries of the cross section are filled by frozen water at a specified temperature of -140 °C. To sublimate the solvent and obtain a clear view into the internal pore volume, the chamber was heated to -80 °C. Figure taken from Kumberg et al., 2021.[56] 121

Figure 5.2: Cryo-BIB-SEM micrographs of the four wet slurries denoted in Table 5.1. In a) the reference (R) is shown in overview and with two detailed images. b) shows slurry (S) based on the spherical graphite in overview and detail, c) the kneader-based slurry (K) in overview and detail and d) the additive-reduced slurry (A). The graphite particles are visible while being surrounded by a network formed by the CMC binder. For better visualization, exemplary shapes formed by the CMC are highlighted by a red rectangle in each overview picture but the additive-reduced one. More SEM images are given in the Appendix. Cryo-BIB-SEM measurements were done by J. Schmatz, from Microstructures and Pores (MaP) Aachen. Figure taken from Kumberg et al., 2021.[56]..... 123

Figure 5.3: Raman spectrum of the pure graphite powders of the non-spherical and the spherical graphite as well as the grinded

non-spherical graphite powder. All spectra are normalized on the maximum intensity of the respective spectrum. Figure taken from Kumberg et al., 2021.[56] 125

Figure 5.4: Density distribution as a function of the particle size of the reference slurry (R), slurry (K) and the pristine non-spherical graphite. Figure taken from Kumberg et al., 2021.[56] 126

Figure 5.5: Phase shift angle as a function of the angular frequency ω for the four slurries (R), (S), (K) and (A)investigated in this section. (R) hereby stands for the slurry using the reference recipe, (S) for the spherical graphite, (K) for the kneading process and (A) for the additive-reduced recipe. Figure taken from Kumberg et al., 2021.[56] 127

Figure 5.6: Adhesion force as a function of the area capacity of electrodes derived from the four slurries (R), (S), (K) and (A). (R) hereby stands for the electrode using the reference recipe, (S) for the spherical graphite, (K) for the kneading process and (A) for the additive-reduced recipe. The theoretical drying rate was 0.75 g m^{-2} s^{-1} ,the isothermal drying temperature about 30 °C and the heat transfer coefficient 35 W m^{-2} K^{-1}. All slurries were coated on substrate foil (f3)..... 129

Figure 5.7: Normalized adhesion force as a function of the drying rate of electrodes derived from the four slurries (R), (S), (K) and (A). (R) hereby stands for the electrode using the reference recipe, (S) for the spherical graphite, (K) for the kneading process and (A) for the additive-reduced recipe. The heat transfer coefficient was 35 W m^{-2} K^{-1}. Slurry (R) was coated on substrate foil (f1) or (f2), as detailed in Figure 3.4. Slurry (K) was coated on foil (f1) and slurry (S) and (A) were coated on (f3). The absolute adhesion force in dependency of the substrate used for normalizing is given in Figure A. 7-22, Appendix. The adhesion force of the reference electrode dried at a drying rate of 0.75 g m^{-2} s^{-1} and a heat transfer coefficient of 35 W m^{-2} K^{-1} at a capacity of 2.5 mAh cm^{-2} is used for normalization. 131

Figure 5.8: Top: Electrical conductivity of electrodes (R), (S), (K) and (A) of state-of-the-art area capacity of about 2.2 mAh cm^{-2} dried at the two different experimentally validated drying rates of 0.5 and 2.2 g m^{-2} s^{-1}. Bottom: The electrical conductivity of high energy electrodes with an averaged area capacity of 6.6 mAh cm^{-2} dried at the same two drying rates in comparison. (R) hereby stands for the electrode using the reference recipe, (S) for the spherical graphite, (K) for the kneading process and (A) for the additive-reduced recipe.134

Figure 5.9: Coin cell test of cells (R), (S), (K) and (A), derived from the respective slurries. (R) hereby stands for the electrode using the reference recipe, (S) for the spherical graphite, (K) for the kneading process and (A) for the additive-reduced recipe. For anode manufacturing the experimental drying rates were 0.5 g m^{-2} s^{-1} and 2.2 g m^{-2} s^{-1}. State-of-the-art anodes were used with their exact area weights and porosities listed in Table A. 4 and Table A. 5 in the Appendix. Figure taken from Kumberg et al., 2021.[56] 137

Figure 5.10: Coin cell test of cells (R), (S), (K) and (A), derived from the respective slurries. (R) hereby stands for the electrode using the reference recipe, (S) for the spherical graphite, (K) for the kneading process and (A) for the additive-reduced recipe. For anode manufacturing the experimental drying rates were 0.5 g m^{-2} s^{-1} and 2.2 g m^{-2} s^{-1}. High capacity anodes were used with their exact area weights and porosities listed in Table A. 6 and Table A. 7 in the appendix. Figure taken from Kumberg et al., 2021.[56] 139

Figure 6.1: SEM cross section of a dry multilayer with the spherical slurry (S) at the bottom and the reference slurry (R) at the top. The layer thickness ratio is 1/3 bottom layer and 2/3 top layer. Figure taken from Kumberg et al., 2021.[56] 145

Figure 6.2: Adhesion force of multilayered electrodes as a function of the area capacity compared to the single layered reference (R) and electrode (A) as a line, which was used as top layer. The single layered electrode reference (R) is compared with the multilayers (S || A), (K || A), and (primer || A) - (bottom ||

top). (S) hereby stands for the electrode using the spherical graphite, (K) for the kneading process and (A) for the additive-reduced recipe. The adhesion force of the electrodes dried at the two experimental drying rates 0.5 g m^{-2} s^{-1} and 2.2 g m^{-2} s^{-1} is compared. For all electrodes substrate (f3) was used. Detailed experimentally validated drying conditions are given in Figure 2.5. 147

Figure 6.3: Top: Electrical conductivity of multilayer electrodes of state-of-the-art (SoA) area capacity of about 2.6 mAh cm^{-2} dried at the two different experimentally validated drying rates of 0.5 and 2.2 g m^{-2} s^{-1}. Bottom: The electrical conductivity of high energy (HE) electrodes with an averaged area capacity of 7.0 mAh cm^{-2} dried at the same two drying rates in comparison. Electrical conductivity of the three multilayer setups compared to the single layered reference (R) and electrode (A) as a line which was used as top layer. The single layered electrode reference (R) is compared with the multilayers (S || A), (K || A), and (primer || A) - (bottom || top). (S) hereby stands for the electrode using the spherical graphite, (K) for the kneading process and (A) for the additive-reduced recipe. The conductivity of the electrodes dried at the two experimental drying rates 0.5 g m^{-2} s^{-1} and 2.2 g m^{-2} s^{-1} (left and right column) as well as the electrical conductivity of state-of-the-art (cA = 2.6 mAh cm^{-2}) and high energy (cA = 7.0 mAh cm^{-2}) electrodes is compared. 149

Figure 6.4: Coin cell test of simultaneously coated multilayer anodes against single layer cathodes, compared with the single-layered reference. The single layered electrode reference (R) is compared with the multilayers (S || A), (K || A), and (primer || A) - (bottom || top). (S) hereby stands for the electrode using the spherical graphite, (K) for the kneading process and (A) for the additive-reduced recipe. For anode manufacturing the experimental drying rates were 0.5 g m^{-2} s^{-1} and 2.2 g m^{-2} s^{-1}. State-of-the-art anodes were used with their exact area weights and porosities listed in Table A. 8 and Table A. 9 in the Appendix. Figure taken from Kumberg et al., 2021.[56] 151

Figure 6.5: Coin cell test of simultaneously coated multilayer anodes against single layer cathodes, compared with the single-layered reference. The single layered electrode reference (R) is compared with the multilayers (S || A), (K || A), and (primer || A) - (bottom || top). (S) hereby stands for the electrode using the spherical graphite, (K) for the kneading process and (A) for the additive-reduced recipe. For anode manufacturing the experimental drying rates were 0.5 g m^{-2} s^{-1} and 2.2 g m^{-2} s^{-1}. High energy anodes were used with their exact area weights and porosities listed in Table A. 10 and Table A. 11 in the Appendix. 153

Figure 6.6: Adhesion force of the state-of-the-art single layer reference (R) and spherical (S) electrodes compared with the multilayers (R || S) and (S || R), (bottom || top). They were dried at a low drying rate of 0.5 g m^{-2} s^{-1} and an extreme drying rate of 5 g m^{-2} s^{-1}. Figure taken from Kumberg et al., 2021.[56] 154

Figure 6.7: Coin cell test of simultaneously coated and high-speed dried multilayer anodes built against single layer cathodes, compared with the single layered reference. The single layered electrodes reference (R) and spherical (S) are compared with the multilayers (R || S) and (S || R), (bottom || top). For anode manufacturing the experimental drying rates were 0.5 g m^{-2} s^{-1} and 5 g m^{-2} s^{-1}. State-of-the-art anodes were used with their exact area weights and porosities listed in Table A. 12 in the Appendix. Figure taken from Kumberg et al., 2021.[56] 156

Figure 7.1: Comparison of the adhesion force and the discharge capacity at 3C of state-of-the-art (SoA) and High Energy (HE) electrodes at different drying rates. The values are normalized with the respective values of the slowly dried reference (R). The single layer electrode (R) is compared to a multilayer (S || A) consisting of a bottom layer with a spherical graphite (S) combined with an additive-reduced (A) top layer, and to a multilayer (S || R) consisting of the spherical graphite as bottom layer combined with the reference as top layer... 165

Figure A. 7-1: Mixing procedure in the dissolver for a battery reference slurry in the dissolver (Figure 2.1). 206
Figure A. 7-2: Mixing procedure for a battery reference slurry in the kneader Inoue Trimix TX-15 (Figure 2.2). 207
Figure A. 7-3: Dynamic viscosity as a function of the shear rate with downward and upward curve. The CMC content in respect to the content within the dry electrode is varied between 3.74 and 0.94 wt-% CMC.[99] 209
Figure A. 7-4: Zero shear viscosity as a function of the CMC concentration for anode slurries containing different amounts of CMC and for pure CMC solutions. 210
Figure A. 7-5: Sedimentation of anode slurries containing different amounts of CMC.[99] 212
Figure A. 7-6: Dynamic viscosity of slurry (R), (S), (K) and (A) with upward and downward curve as well as the dynamic viscosity of the CMC solutions the slurries are based on. 0.8 wt % CMC was used for slurries (R), (S) and (K) and 0.6 wt% for slurry (A). 213
Figure A. 7-7: Density distribution q3 and accumulated distribution Q3 of the SBR.[105] (Zetasizer from MVT-VM, KIT) 214
Figure A. 7-8: Cryo-BIB-SEM micrograph of slurry (R): reference.[56] . 215
Figure A. 7-9: Cryo-BIB-SEM micrograph of slurry (S): spherical.[56] .. 216
Figure A. 7-10: Cryo-BIB-SEM micrograph of slurry (K): kneader.[56] ... 217
Figure A. 7-11: Cryo-BIB-SEM micrograph of slurry (A): additive-reduced.[56] 218
Figure A. 7-12: Simplified drying profiles of electrodes dried under a) non-isothermal and b) isothermal drying conditions. 220
Figure A. 7-13: Adhesion force measured by an area peel-off test for electrodes with different area capacities which were dried under isothermal and non-isothermal conditions. 221
Figure A. 7-14: Estimation of the Biot numbers of heat and mass transfer in dependency of the electrode thickness. Below Biot numbers

of 1 the resistance outside the film dominates, whereas the resistance inside the film dominates above 1. 223

Figure A. 7-15: Pictures of drying patterns of two electrode films of slurry (R) of SoA area weight, which were dried at a drying rate of a) 0.75 g m^{-2} s^{-1} and b) 2.5 g m^{-2} s^{-1} compared to c) an HE electrode of slurry (K). 224

Figure A. 7-16: Nozzle position and adhesion force.[108] 225

Figure A. 7-17: Exemplary dew point measurement during drying of an electrode with increased area weight. 227

Figure A. 7-18: Area fraction which dries by solvent vapor diffusion over drying time derived from fitting experimental and simulated solvent loading curves to one another. Two approaches are compared with the first being based on the input parameters presented in the previous sections resulting in a total area of 0.0192 m² and the second one with adjusted values for λdry and $\delta s, eff$ ending in a total area of 0.0081 m². 229

Figure A. 7-19: Simulated temperature curve resulting from an adjustment of the area fraction which dries by solvent vapor diffusion which is derived from fitting experimental and simulated solvent loading curves to one another. Two approaches are compared with the first being based on the input parameters presented in the previous sections resulting in a total area of 0.0192 m² and the second one with adjusted values for λdry and $\delta s, eff$ ending in a total area of 0.0081 m². 231

Figure A. 7-20: Gravimetric drying curves which are composed of single residual moisture measurements at different times of drying. The drying curves of electrode films of four different film thicknesses are compared. 232

Figure A. 7-21: Measurement of the wet film thickness during drying, using a chromatic confocal sensor. Different original wet film thicknesses as well as drying temperatures of the heating plate used for drying are compared.[109] 233

Figure A. 7-22: Comparison of the adhesion force of electrodes on the three different copper foils f1, f2 and f3 used as substrate in this work. The drying rate was varied by changing the isothermal

drying temperature, while the heat transfer coefficient was kept at 35 W m^{-2} K^{-1}. When the adhesion force of different substrates is being compared, the adhesion force was normalized on the adhesion force measured at a drying rate of 0.75g m^{-2} s^{-1}, a heat transfer coefficient of 35 W m^{-2} K^{-1} with electrodes of an area weight of 60 g m^{-2}. 236

Figure A. 7-23: Porosity of electrode (R) in dependency of the area weight and the linear fit function to correlate area weight and porosity as measured and implemented in the drying curve simulation in section 4 Drying Behavior of Thicker Electrodes. 237

Figure A. 7-24: Porosity of electrode (R), (S), (K) and (A) in dependency of the area capacity. 238

Figure A. 7-25: Adhesion force as a function of the porosity of (R), (S), (K) and (A). 239

Figure A. 7-26: Comparison of the adhesion force of uncalendered electrode (R) and (K) with calendered electrode (R) and (K) on substrate foil (f2). 240

Figure A. 7-27: Tendency for electrodes to crack dependent on coating thickness and drying rate. The electrodes in the top row feature an inclined thickness from 89 µm to 512 µm and were dried at a drying rate of a) 3 g m^{-2} s^{-1} and b) 15 g m^{-2} s^{-1}. In the bottom row flat electrode layers are shown, with c) 490 µm thickness, dried at 3 g m^{-2} s^{-1} and d) 70 µm thickness, dried at 15 g m^{-2} s^{-1}. The heat transfer coefficient was 80 W m^{-2} s^{-1}. Figure after Kumberg et al., 2019. [24] 242

Figure A. 7-28: Critical cracking thickness derived from electrodes coated with an inclined coating knife as a function of the drying rate under variation of the heat transfer coefficient and the isothermal drying temperature. Cracks started at a thickness of about 350 µm under consideration of the error bars. All electrodes dried at a drying rate of 3 g m^{-2} s^{-1} or lower showed no sign of cracking. Figure after Kumberg et al., 2019. [24] 244

Figure A. 7-29: Crack area in relation to the total area as a function of the drying rate for different heat transfer coefficients. As can be

seen in the images, the crack area increases with an increase of the drying rate. Since no cracks were visible at drying rates below 3 g m^{-2} s^{-1}, the respective cracking area is zero. Figure taken from Kumberg et al., 2019.[24] 245

Figure A. 7-30: Experiment using the inclined coating knife gap, to evaluate the crack formation of electrode (S) and (K) in the batch coater under isothermal drying conditions with a theoretical drying rate of 0.75 g m^{-2} s^{-1}. 246

Figure A. 7-31: Crack formation during the gravimetric experiment of electrode (R), (S), (K) and (A) when dried at a theoretical drying rate of 0.75 g m^{-2} s^{-1}. Four different electrode thicknesses were investigated..... 248

Figure A. 7-32: Variation of the drying rate for electrode (K) at SoA thickness by drying under two different heat transfer coefficients of 35 W m^{-2} K^{-1} and 80 W m^{-2} K^{-1}. Electrodes were coated onto substrate (f1). 249

Figure A. 7-33: SEM picture of the top of a) the reference electrode (R) dried at a drying rate of 0.75 g m^{-2} $s^{-1}$and b) electrode (R) dried at a drying rate of 3 g m^{-2} s^{-1}. C) shows the top of electrode (K) dried at a drying rate of 0.75 g m^{-2} s^{-1} and d) shows electrode (K) dried at a drying rate of 3 g m^{-2} s^{-1}..... 250

Figure A. 7-34: LIBS measurements which were made by Y. Zheng and W. Pfleging at IAM-AWP, KIT. The Na-CMC distribution of two thick electrodes, derived from slurry (K) which were dried at a low drying rate of 0.75 g m^{-2} s^{-1} (left) and a high drying rate of 3 g m^{-2} s^{-1} (right), is compared..... 251

Figure A. 7-35: Complete adhesion force measurement with the 90° peel test of a flat layer compared to an inclined layer as shown in section 3. 252

Figure A. 7-36: The setup of the pull-off test consists of two metallic cylinders which are pressed together with a certain pressure in the first step. Adhesive tapes on the bottom and top of both cylinders fix the coating and the substrate to the cylinders. In the second step both cylinders are moved apart and the force

is measured, which then is a force in relation to the coating area adhering to the cylinder. 253

Figure A. 7-37: Electrical conductivity of single layered electrodes in dependency of the area capacity. 254

Figure A. 7-38: Comparison of Pouch and Coin cell test. Data of the pouch cell test of the reference electrode against NMC 622 are also shown by Diehm et al.[21] 257

Figure A. 7-39: Side view of the coating of simultaneous multilayers using a) a slot die and b) using two doctor blades as well as 259

Figure A. 7-40: Coating stability of simultaneously coated multilayers a) without intermixing and b) with intermixing of both layers shown in the dry state.[99] 260

Figure A. 7-41: Relative pore volume as a function of the pore size of electrodes (R), (K) and (S). The relative pore volume as a function of the pore diameter was measured with mercury intrusion porosemitry. Pore sizes above 20 µm are cropped since these are above the particle size and can therefore assumed to be surface pores. 262

Figure A. 7-42: Adhesion force of simultaneously coated multilayer (S || R) when dried at a high drying rate (of 1.5 g m^{-2} s^{-1} at 80 W m^{-2} K^{-1}) until the transition time and then at a low drying rate (of 0.5 g m^{-2} s^{-1} at 35 W m^{-2} K^{-1}). 263

Figure A. 7-43: EDS Cryo-BIB-SEM pictures of the multilayer (S || R) with the elements Cu, O and C dried at a drying rate of 0.5 g m^{-2} s^{-1} 264

Figure A. 7-44: Amount of solvent (wt-% of O) detected in the layers within the multilayer electrode which is given as the normalized film thickness. 266

Figure A. 7-45: Adhesion force as a function of the area capacity for the single layered electrodes (S) and (R) compared to the multilayers consisting or slurry ® at the bottom and slurry (S) at the top and vice versa. The multilayers had a layer ratio of 1/3 bottom and 2/3 top layer. All electrodes were coated on substrate (f3) and dried at an experimental drying rate of

0.5 g m-2 s-1 at a heat transfer coefficient of 35 W m-2 K-1. 267

Figure A. 7-46: Pouch cell test of SoA multilayers (S || R) and (R || S) compared to the reference (R). The theoretical drying rate was 0.75 g m^{-2} s^{-1}. The cathode was NMC622. 268

Figure A. 7-47: Adhesion force as a function of the area capacity for multilayered electrodes with two different top layers combined with slurries (S) and (K) as bottom layers. In the first configuration the reference (R) is used as top layer, thus no binder concentration gradient would be expected directly after coating within the wet electrode. In the second setup the additive-reduced slurry is used as top layer, as such leading to a concentration gradient of the binder in the wet electrode. The experimental drying rate was 0.5 g m^{-2} s^{-1} at a heat transfer coefficient of 35 W m^{-2} K^{-1}. 269

Figure A. 7-48: Electrical conductivity of multilayer electrodes compared to the reference as a function of the area capacity..... 270

List of Tables

Table 2.1: Overview of the composition of the slurry and the dry electrode of the **reference** recipe consisting of graphite (SMGA), carbon black, the binders CMC and SBR and distilled water in case of the wet slurry. 18

Table 3.1: Properties of the electrodes analyzed by LIBS. Electrodes with a theoretical capacity of 12 mAh cm^{-2} (356 g m^{-2}) and 13.5 mAh cm^{-2} (401 g m^{-2}) were calendered to a thickness of about 260 µm and a porosity of 0.36 and 0.39 respectively. In each step 4.8 µm or 5.1 µm were ablated and analyzed by LIBS. 41

Table 3.2: Summary of the different driving forces the SBR binder is exposed to during drying in dependency of the electrode thickness hel and its effect on the consolidation factor Kc which sets diffusion, sedimentation and evaporation into relation, after Baunach et al. (2015).[52] 45

Table 3.3: Settings (1) to (4) of the heat transfer coefficient and the corresponding isothermal drying temperature to adjust a certain drying rate corresponding to those in Figure 3.2. .. 48

Table 3.4: Comparison of the CMC-binder content at the top and the bottom of two electrodes dried at a low state of the art drying rate[6] of 0.75 g m^{-2} s^{-1} and a higher drying rate of 6 g m^{-2} s^{-1} by measuring the sodium content, which is only present in the (Na-)CMC-binder. The content is given in atomic percent (at.-%). 52

Table 3.5: Area weight and porosity for different thinner and thicker electrodes dried at 2 and 3 different drying rates which were built into coin cells. 55

Table 4.1: Parameters for the three different experimental setups combined with the comb nozzle dryer to investigate the drying behavior of battery electrodes. The setups consisted of (1) a gravimetric installation, (2) an IR camera inserted beneath the dryer and (3) a digital microscope used to

investigate capillary pore emptying. The specific settings used in each setup during drying are summarized. All three setups were developed and built within this work, whereas the comb nozzle dryer itself was built prior to this work.[57] 65

Table 4.2: Overview of the film properties of the gravimetric experiments for the four electrodes, sorted by their dry area weight m. The measured dry area weight m, film thickness hel and theoretical capacity cA, porosity ε and solvent loading at the end of film shrinkage Xs, EOF are given. The solvent loading of the film can be derived from the total mass of the wet film under knowledge of the dry mass of the film. The dry mass was measured for each film after the drying experiment. The standard deviation within a single electrode film is given under standard deviation[b]. It grows with increasing averaged film thickness and lies between 6 % to 8 % of the total film thickness. 66

Table 4.3: Calculated Biot numbers of heat (Bi) and mass transfer (Bi')and the effective diffusion coefficient δs, eff within the porous electrode at different electrode thicknesses. 71

Table 4.4: Parameters for the three different experimental setups used to investigate the drying behavior of battery electrodes. 99

Table 4.5: Summary of the different driving forces a graphite particle is exposed to during drying in dependency of the area weight m and its effect on the consolidation factor Kc which sets diffusion, sedimentation and evaporation into relation, after Baunach et al. (2015).[52] 108

Table 4.6: Overview of the experimentally determined drying conditions of the electrodes with the four area weights m1 - m4. The heat transfer coefficients were determined by linear regression of the experimental data. 109

Table 4.7: Comparison of the drying models in dependency of the area weight. The simulated drying times are compared with the experimental data at the time the solvent loading reaches 1 % in relation to the equilibrium solvent loading..... 113

Table 5.1: Overview of the denotation and differentiation of the slurries which are investigated in this section. The first slurry is the reference (R), for slurry (S) a spherical-shaped graphite was used. A change of the mixing process to a kneader, resulted in slurry (K) and an additive-reduced recipe in slurry (A). Exact recipes are given in Table 5.2. 119

Table 5.2: Overview of the composition of the dry electrodes derived from the four different slurries as presented in Table 5.1. The recipes are given for the dry electrode in wt-% for the respective material. Each wet slurry had a dry mass fraction of 43 wt-%. 120

Table 5.3: Percentage change in adhesive force when increasing the area capacity from the minimum (≈ 2.5 mAh cm^{-2}) to the maximum area capacity (≈ 9 mAh cm^{-2}) given in Figure 5.6 for the respective electrode. This is compared to the change of the adhesion force when increasing the drying rate from 0.75 g m^{-2} s^{-1} to 3 g m^{-2} s^{-1} as shown in Figure 5.7. (R) hereby stands for the electrode using the reference recipe, (S) for the spherical graphite, (K) for the kneading process and (A) for the additive-reduced recipe. Values above 100 % mean, that adhesion values of the electrodes dried at 3 g m^{-2} s^{-1} lie above the ones gained at the lower reference drying rate of 0.75 g m^{-2} s^{-1}. 130

Table 6.1: Overview of the composition of the dry multilayer electrodes derived from combination of the four different slurries in wt-%. The multilayers (S || A), (K || A), (primer || A) and (S || R) - (bottom || top) are shown. (R) hereby stands for the electrode using the reference recipe, (S) for the spherical graphite, (K) for the kneading process and (A) for the additive-reduced recipe..... 144

Table A. 1: CMC content in the dry electrode and in the slurry..... 211

Table A. 2: Settings (1) to (4) of the heat transfer coefficient and the corresponding isothermal drying temperature to adjust a certain drying rate corresponding to those in Figure 3.2. The

settings to achieve the drying rates depicted in Figure 3.4 are also given. 234

Table A. 3: Absolute values of the adhesion force of the identical slurry on three different copper foils f1-f3 dried at a drying rate of 0.75g m^{-2} s^{-1}, a heat transfer coefficient of 35 W m^{-2} K^{-1} with an area weight of 60 g m^{-2}. 236

Table A. 4: Area capacities in mAh cm^{-2} of single layer SoA electrodes that were dried at different drying rates. Area capacities are calculated based on the respective area weights..... 255

Table A. 5: Porosity of single layer SoA electrodes that were dried at different drying rates. 255

Table A. 6: Area capacities in mAh cm^{-2} of thick single layer electrodes that were dried at different drying rates. Area capacities are calculated based on the respective area weights..... 256

Table A. 7: Porosity of thick single layer electrodes that were dried at different drying rates. 256

Table A. 8: Area capacities in mAh cm^{-2} of multilayer SoA electrodes that were dried at different drying rates. Area capacities are calculated based on the respective area weights..... 271

Table A. 9: Porosity of multilayer SoA electrodes that were dried at different drying rates. 271

Table A. 10: Area capacities in mAh cm^{-2} of thick multilayer electrodes that were dried at different drying rates. Area capacities are calculated based on the respective area weights..... 271

Table A. 11: Porosity of thick multilayer electrodes that were dried at different drying rates. 272

Table A. 12: Area capacity and porosity of single and multilayer electrodes that were dried at the extreme drying rate of 5 g m^{-2} s^{-1}.. 272

Appendix

Additional information and results exceeding the ones presented in the main section are given in the following. These reach from details on slurry properties, to information on the single layered dry electrodes to simultaneously coated multilayers. Some aspects regarding the influence of the CMC content will be presented as well.

A Further Detailed Results of the Mixing Process

In this section the exact mixing procedure in the two mixers used in this work, the dissolver and the kneader are presented.

A.1 Dissolver

The mixing procedure itself is summarized in Figure A. 7-1. Slurry preparation started with the dissolving of the CMC in distilled water. For the reference recipe the binder matrix had a CMC content of 2 wt.-%. The graphite and carbon black were dry mixed in the dissolver for 15 min at 300 rpm. 40 wt.-% of the powder mixture were temporarily removed before the CMC solution was added to enable a stepwise increase of the solid content. The solid content was then stepwise increased to the final solid content of 43 wt.-%, followed by the main mixing step which lasted 45 min at 1500 rpm. The double jacket was cooled during all wet mixing steps, vacuum was applied only for the main mixing step as well as during the last step, where SBR was added under moderate mixing conditions with 500 rpm for 10 min.

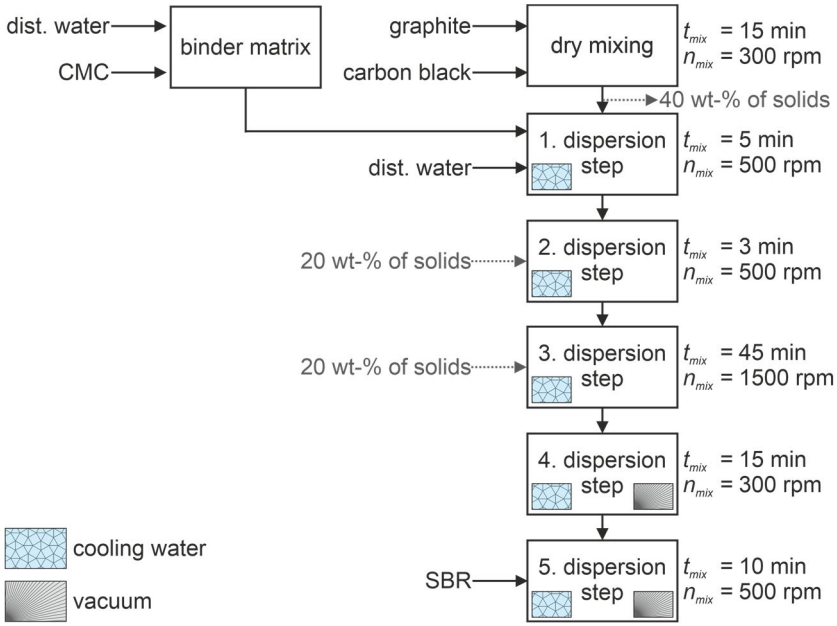

Figure A. 7-1: Mixing procedure in the dissolver for a battery reference slurry in the dissolver (Figure 2.1).

A.2 Kneader

The mixing procedure in the kneader is summarized in Figure A. 7-2. As for the dissolver, a CMC solution of 2 wt.-% CMC is prepared beforehand. A dry mixing step of graphite and carbon black is realized in the kneader at 25 rpm for 10 min. The solid content is stepwise decreased by adding the CMC solution and distilled water. The vessel is cooled during all wet mixing steps and vacuum is used starting with the main mixing step. The SBR binder dispersion is added last and mixed in for 15 min at 25 rpm.

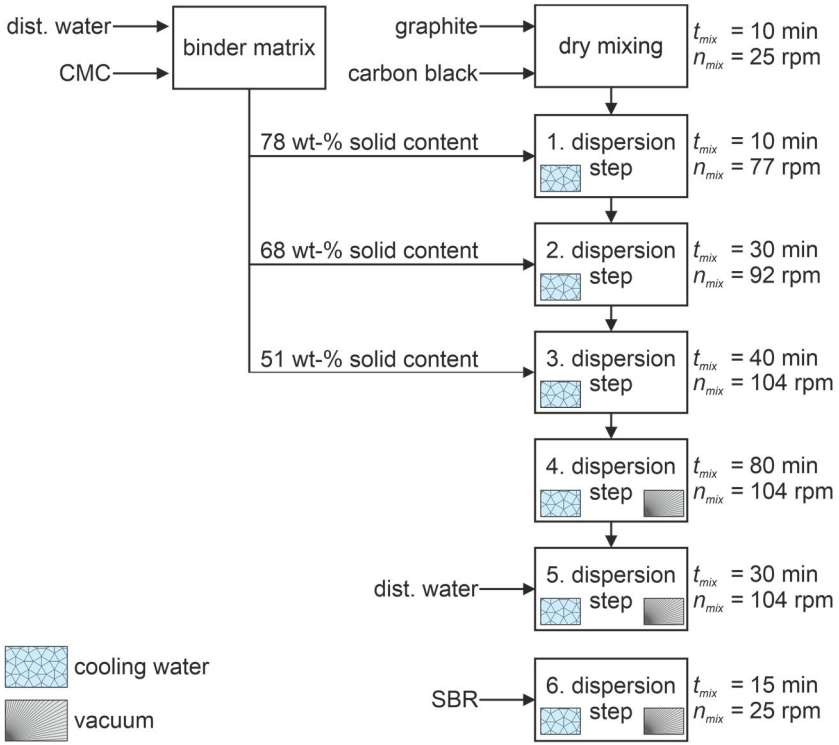

Figure A. 7-2: Mixing procedure for a battery reference slurry in the kneader Inoue Trimix TX-15 (Figure 2.2).

B Further Detailed Results of Slurry Properties

Dynamic viscosity measurements under variation of the CMC content, and its influence on sedimentation of the graphite particles during slurry storage will be shown, as well as dynamic viscosity curves as a function of the shear rate for Slurry (R), (S), (K) and (A). This is supplemented by some more detailed micrographs of the four slurries.

B.1 Dynamic viscosity under CMC variation

In Figure A. 7-3 the dynamic viscosity of slurry (R) is compared to four slurries containing different CMC-contents. The respective slurries result in the CMC-content within the dry electrodes of 3.74, 2.8, 1.87, 1.4 and 0.94 wt-% in the respective dry electrodes. The variations were chosen so they build pairs with different CMC gradients which add up to the overall CMC content of 1.87 wt-% of the reference recipe if they are combined in a multilayer with 1/3 bottom to 2/3 top layer. 3.73 wt-% CMC in the bottom layer is combined with 0.94 wt-% CMC in the top layer and 2.8 wt-% CMC in the bottom layer is combined with 1.4 wt-% CMC in the top layer.

The dynamic viscosity increases with the increase of the CMC content as would be expected. This can be attributed to the alignment of the polymer chains and particles as well as a deagglomeration of agglomerates. Almost all slurries show clear shear-thinning behavior. One exception from this is the slurry with 0.94 wt-% CMC. It has a very low viscosity at lower shear rates, due to the low amount of CMC contained in the slurry. The polymer chains are aligned with an increase of the shear rate and the viscosity decreases. With a further increase of the shear rate, particle contacts start to play a more dominant role and a slight increase of the viscosity results until the viscosity at 1000 s^{-1} reaches a value similar to the one of the other curves.

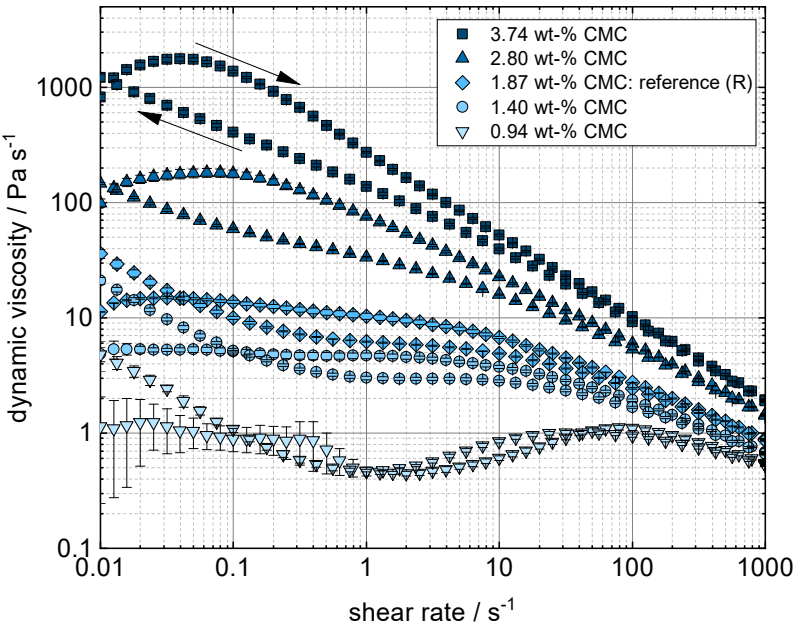

Figure A. 7-3: Dynamic viscosity as a function of the shear rate with downward and upward curve. The CMC content in respect to the content within the dry electrode is varied between 3.74 and 0.94 wt-% CMC.[99]

The entanglement of the CMC polymer chains in solution and within the slurry was observed in some more detail. Therefore, the zero-shear viscosity was determined for the anode slurries containing different amounts of CMC. It was compared to pure CMC solutions with differing concentrations of CMC. This comparison is given in Figure A. 7-4. From the experimental data, a critical entanglement concentration of 0.75 wt-% could be assumed, above which CMC polymer chains are in closer contact to one another. The CMC concentration within the anode slurry is shown in comparison. In the reference system, the CMC concentration is 0.8 wt-%. In the additive-reduced slurry the CMC concentration is 0.62 wt-%. CMC has been extensively investigated in literature, though results are not easily transferable, due to the broad variety of molecular weights and substitution degrees, which both influence the rheological behavior[40,89,90,100–104]. Two examples for a better classification of the results given here are:

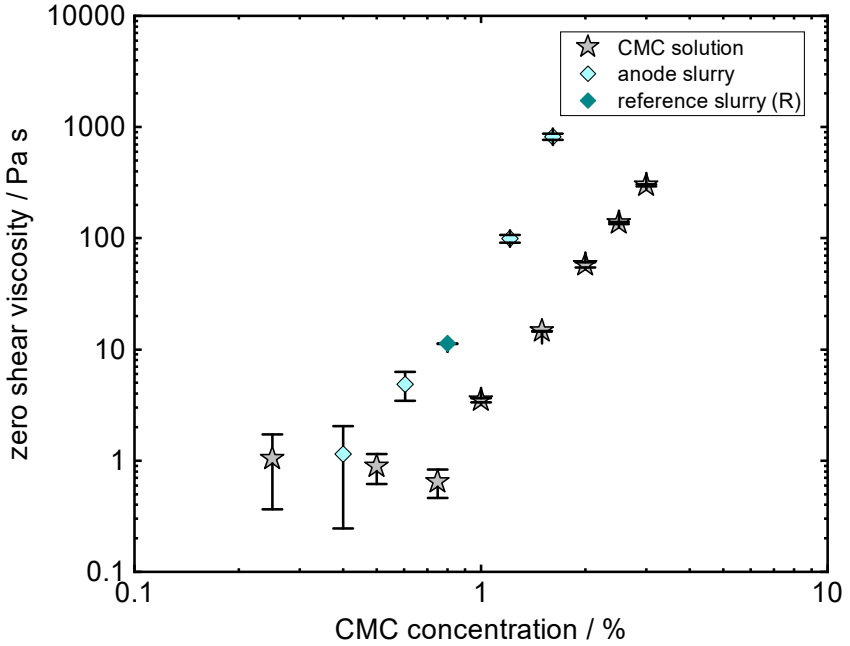

Figure A. 7-4: Zero shear viscosity as a function of the CMC concentration for anode slurries containing different amounts of CMC and for pure CMC solutions.

Benchabane et al. found a critical overlap concentration for the CMC around 1% CMC. They investigated a CMC with a substitution degree (DS) of 0.65-0.85 with a molecular weight of 700.000 g mol^{-1}. [100] The CMC in this work had a DS of 0.67 and a molecular weight of 349 000 g mol^{-1} in comparison.

Lim et al. analyzed the entanglement behavior of CMC. They used a CMC with a DS of 0.7 and a molecular weight of 330.000 g mol^{-1}. They found three critical CMC concentrations c_{CMC} at 0.1 wt%, 0.4 wt-% and 1.6 wt-% CMC: Below 0.1 wt-% CMC they defined a semidilute regime with unentangled CMC chains. A CMC solution with a CMC concentration 0.1 wt%< c_{CMC} < 0.4 wt-% was found to be in a semidilute state, containing entangled CMC chains. For 0.4 wt%< c_{CMC} < 1.6 wt-% a concentrated CMC solution was found. Above 1.6 wt% of CMC they found gel-behavior of the solution. These results can be compared to the ones in this work, though only two regimes were found from the data gained in

this work. Entanglement started at a concentration above 0.75 wt-% of CMC to take a dominant role, which lies in the area of the given examples from literature.

The exact values of the CMC concentrations in the dry electrode and the slurries which were investigated are summarized in Table A. 1.

Table A. 1: CMC content in the dry electrode and in the slurry.

CMC content dry electrode	CMC concentration in slurry
wt-%	wt-%
3.74	1.61
2.8	1.21
1.87	0.8
1.4	0.6
0.94	0.4

B.2 Sedimentation under CMC variation

With only a loose or even no entanglement present in the slurry, sedimentation of particles might turn into a problem due to a missing network of stabilizing polymer chains. This was investigated by filling all slurries into test tubes and taking samples at the top of these test tubes at different time intervals. The results are shown in Figure A. 7-5. The solid content within the slurry as a function of the time is shown. All slurries with a CMC content above 1.4 wt-% show a constant solid content over the investigated time interval. Only the slurry with 0.94 wt-% CMC seems to sediment over time. The sedimentation seems to take place quite fast, since a change in the solid content can be observed within the first hours. This renders the application of a slurry of CMC contents (using the CMC examined in this work) below 0.94 wt-% almost impossible for industrial application, since a direct handling or continuous mixing would have to be guaranteed.

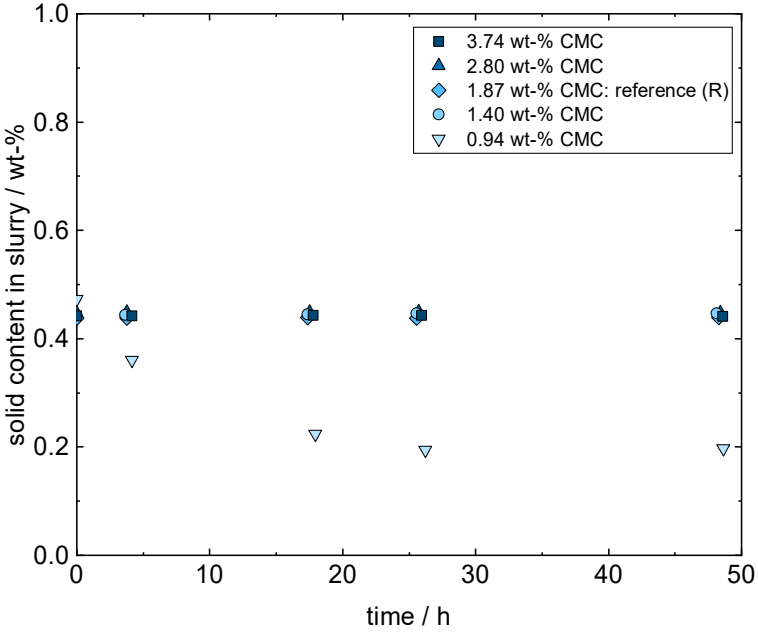

Figure A. 7-5: Sedimentation of anode slurries containing different amounts of CMC.[99]

A.1 Dynamic viscosity of slurry (R), (S), (K) and (A)

The dynamic viscosity of the slurries (R), (S), (K) and (A) investigated in section 5 (Influence of Slurry Properties) as a function of the shear rate is shown in Figure A. 7-6. It is compared to the viscosity of the CMC solutions the slurries contain. Slurries (R), (S) and (K) contain 0.8 wt-% CMC and slurry (A) 0.6 wt-% CMC.

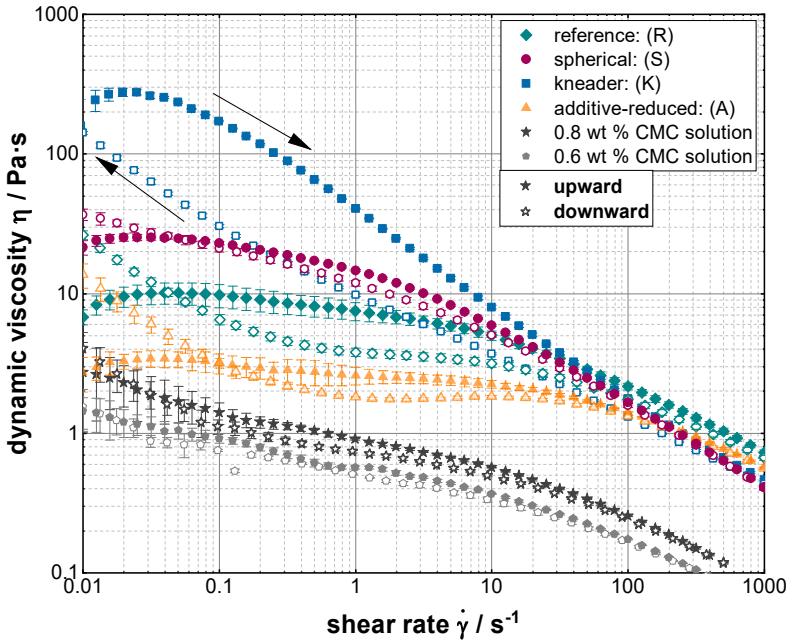

Figure A. 7-6: Dynamic viscosity of slurry (R), (S), (K) and (A) with upward and downward curve as well as the dynamic viscosity of the CMC solutions the slurries are based on. 0.8 wt % CMC was used for slurries (R), (S) and (K) and 0.6 wt% for slurry (A).

B.3 SBR particle distribution

The SBR particle distribution was measured with a Zetasizer Nano Series (NS) (Malvern Instruments Ltd. UK) using dynamic light scattering (MVT-VM, KIT). For the measurements, 5 µl of the SBR dispersion were diluted in 995 µl demineralized water and filled into a cuvette. The Attenuator Index for the measurement was 3. The cuvettes refractive index was 1.59 and the absorption index 0.01. The measurement was performed at 25 °C. Demineralized water with a refractive index of 1.33 and a viscosity of 0.8872 mPa s at a measurement temperature of 25 °C was the dispersion medium. Before each measurement, the meter equilibrated for 120 s. Three measurements were performed in total. The resulting density distribution as well as the accumulated distribution of the SBR is shown in Figure A. 7-7.

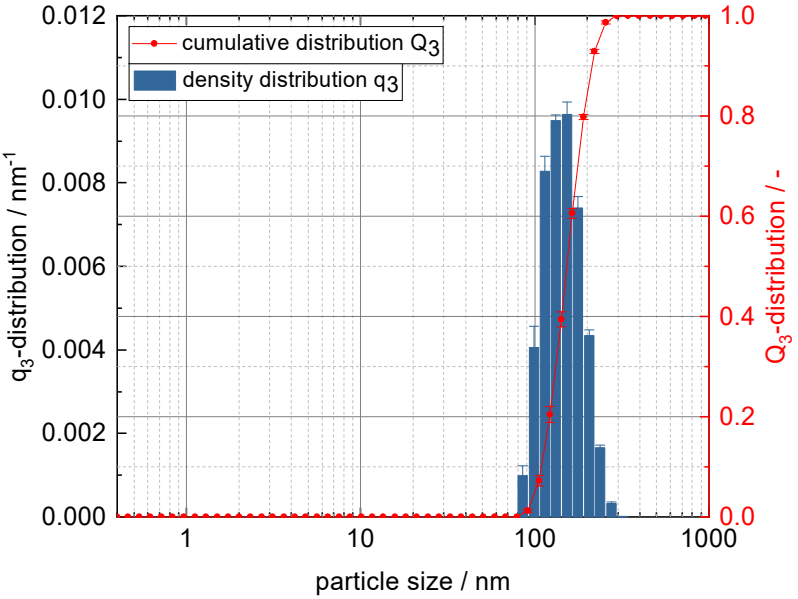

Figure A. 7-7: Density distribution q3 and accumulated distribution Q3 of the SBR.[105] (Zetasizer from MVT-VM, KIT)

The peak in the distribution is positioned at a particle size of 153 nm.

B.4 Further Cryo-BIB-SEM micrographs

Cryo-SEM micrographs of slurries (R), (S), (K) and (A) are shown in Figure A. 7-8 to Figure A. 7-11.

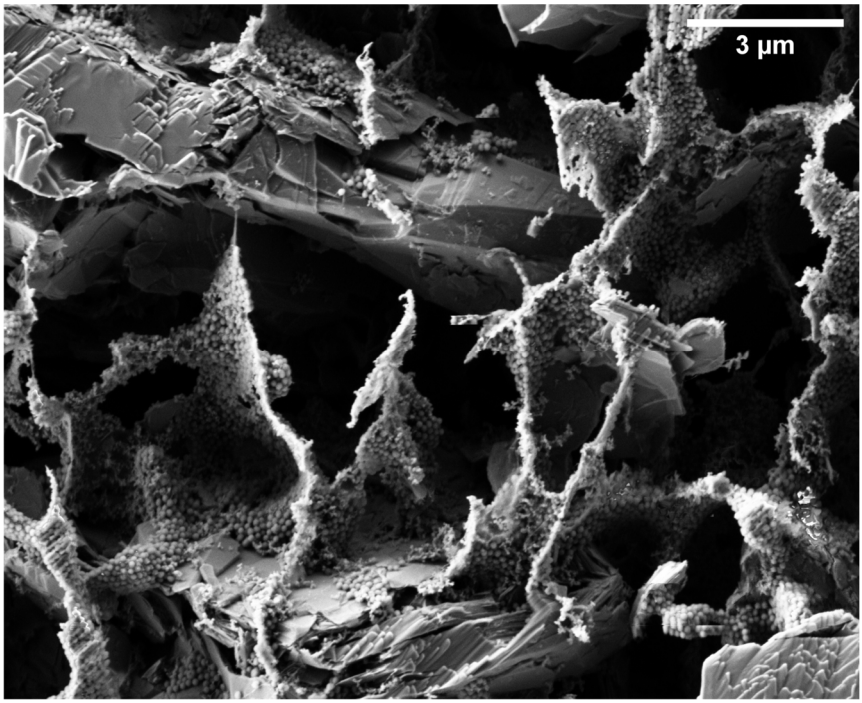

Figure A. 7-8: Cryo-BIB-SEM micrograph of slurry (R): reference.[56]

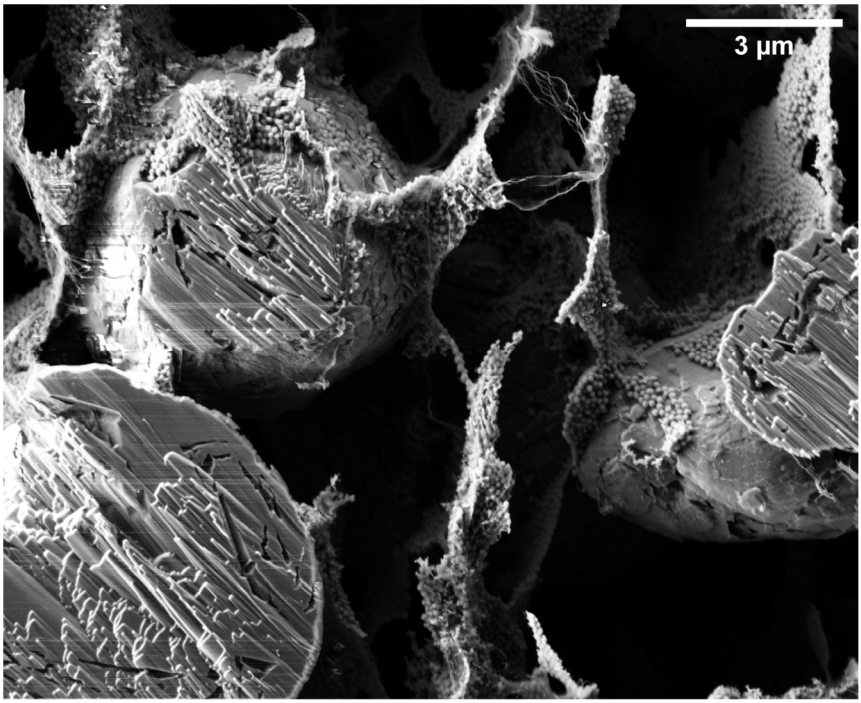

Figure A. 7-9: Cryo-BIB-SEM micrograph of slurry (S): spherical.[56]

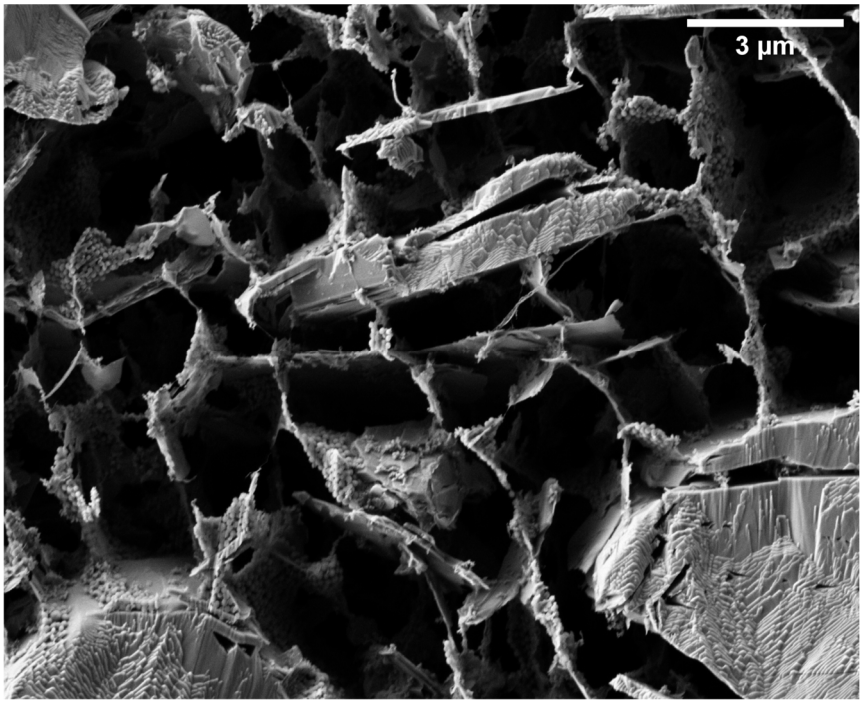

Figure A. 7-10: Cryo-BIB-SEM micrograph of slurry (K): kneader.[56]

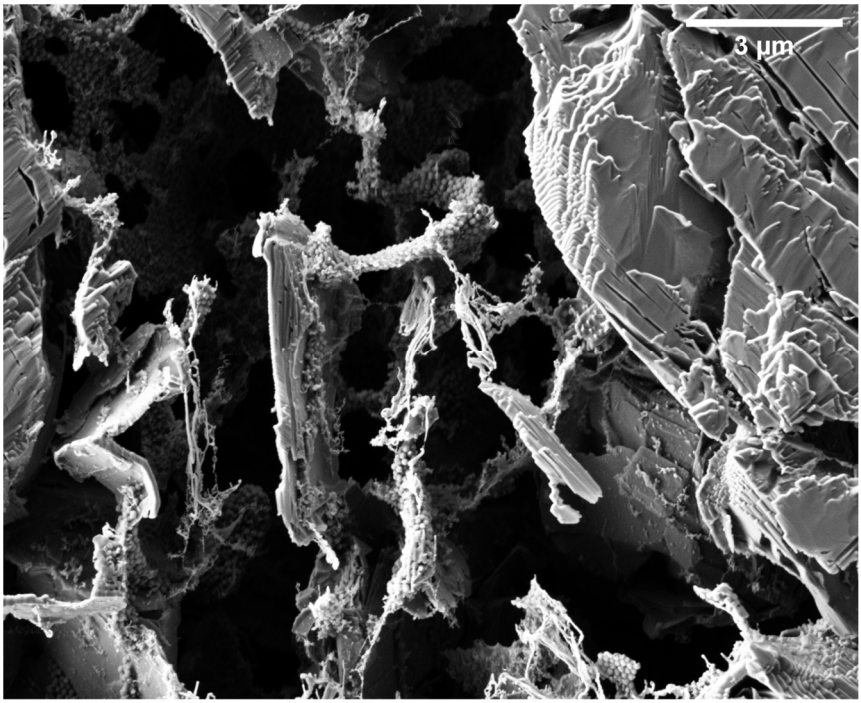

Figure A. 7-11: Cryo-BIB-SEM micrograph of slurry (A): additive-reduced.[56]

C Further Detailed Results of Electrode Drying

In this section, drying will be further illuminated. Isothermal and non-isothermal drying will be discussed in first instance. Drying patterns and adhesion force differences due to these patterns as well as an exemplary dew point measurement are further shown. Additionally, methods of drying characterization are presented.

C.1 Isothermal vs. non-isothermal drying

The experiments presented in sections 3, 5 and 6 are based on the assumption that the isothermal drying process in the batch-coater is scalable due to the time-independent experimental setup which allows scalable drying times. To evaluate, to which extent the results are comparable to these of the non-isothermal drying process in the comb nozzle dryer in section 4, isothermal and non-isothermal drying experiments were conducted.

When drying thin electrodes (m_1, see section 4.4.1), it can be assumed, that isothermal and non-isothermal drying conditions lead to identical electrode properties, since the temperature profile is identical as long as the electrode is wet. As soon as a film resistance starts to play a role this is not true anymore due to reduced evaporative cooling, as is the case for thicker electrodes (m_4) which was discussed in section 4.4.3 (Experimental Drying of Thick Electrodes). The comparison is shown as a simplified version in Figure A. 7-12. The gravimetric experiment under non-isothermal drying conditions is the equivalent to industrial dryers. The electrodes temperature increases after the end of the first drying stage. Isothermal drying conditions so far are realized by contact heating in the batch coater. By changing the gravimetric setup to a heating plate identical drying conditions can also be adjusted in the Comb Nozzle dryer (Figure A. 7-12b). Electrodes of an elevated area weight experience different drying profiles in dependency of the drying setup: Isothermal drying conditions force the film to stay on the equivalent wet bulb temperature. In non-isothermal drying conditions, the film heats up after leaving the first drying stage.

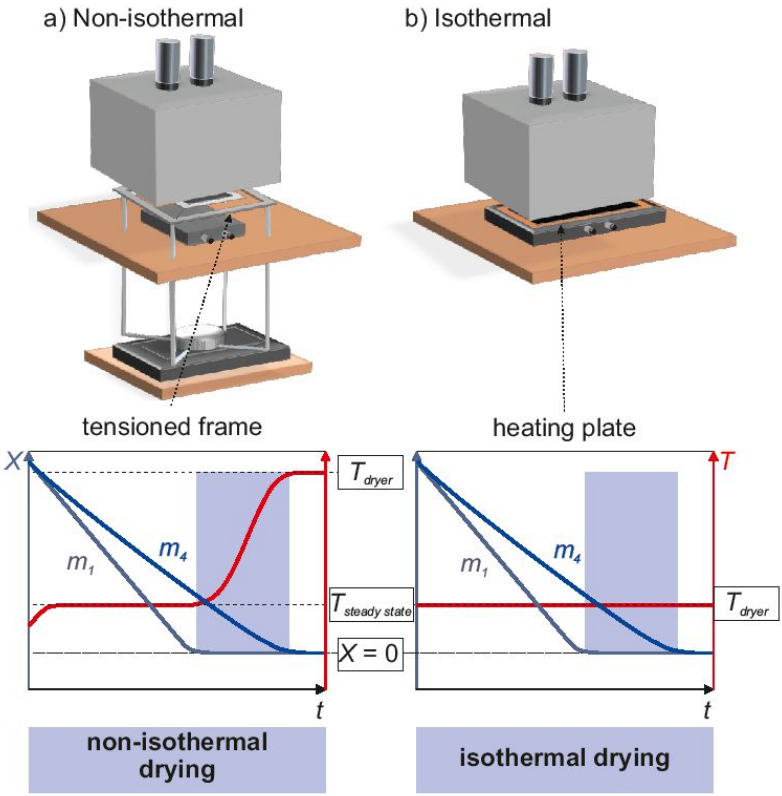

Figure A. 7-12: Simplified drying profiles of electrodes dried under a) non-isothermal and b) isothermal drying conditions.

To get an impression of the transferability of both experimental setups, electrode films of different area capacities were dried in the Comb Nozzle dryer under isothermal and non-isothermal drying conditions. The results are shown in Figure A. 7-13. The adhesion force was in this case measured with an area pull-off test and can therefore be compared to values reported in literature.[18,106] At the SoA area capacity, the adhesion force of isothermal and non-isothermal dried electrodes are identical, as would be expected due to the identical drying profiles. All electrodes of a higher area capacity show a deviation between isothermal and non-isothermal drying conditions though. The adhesion force of the isothermally dried electrodes lies beneath that of the non-isothermally dried one. This fits well

in the reasoning, that the temperature profile does influence the electrodes microstructure, although the elevated temperature only concerns later stages of drying. As was shown in this section, increased temperatures positively affect the adhesion force. Therefore, the shown deviation between isothermal and non-isothermal drying is in accordance with the expectance. Since the influence of isothermal or non-isothermal drying conditions on the adhesion force is smaller than the influence of the area weight, the comparison of both processes is justified. Especially since the dependency on process conditions is the same for both and only the absolute values of adhesion differ.

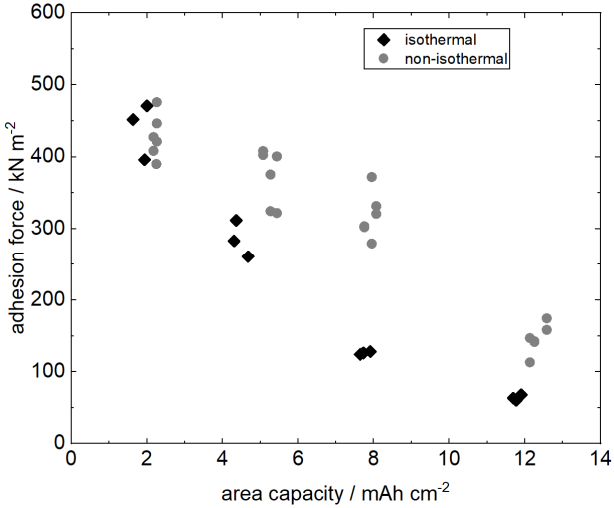

Figure A. 7-13: Adhesion force measured by an area peel-off test for electrodes with different area capacities which were dried under isothermal and non-isothermal conditions.

In conclusion, the so far investigated experiments using isothermal drying conditions in the laboratory scale are transferable to industrial non-isothermal drying conditions. Increased area weights lead to slight deviations between both drying routes, though non-isothermal drying conditions are in fact beneficial due to the higher film temperature.

C.2 Estimation of the Biot Number and Capillary Drying

The Biot numbers of heat and mass transfer were estimated for different electrode thicknesses, as shown in Figure A. 7-14. While the Biot number of heat transport (*Bi*) remains at values << 1 for all electrode thicknesses considered here, the Biot number of mass transport (*Bi'*) increases to values above 1, already at an electrode thickness of 275 µm. Since the boundary conditions outside the film remain the same this means the resistances within the film starts to increase. A domination of resistances within the film starts at values above one. This is the case if no capillary solvent transport takes place. As was shown, capillary solvent transport does take place though, which is why the estimation of the Biot number can only give an idea on the importance of film resistances.

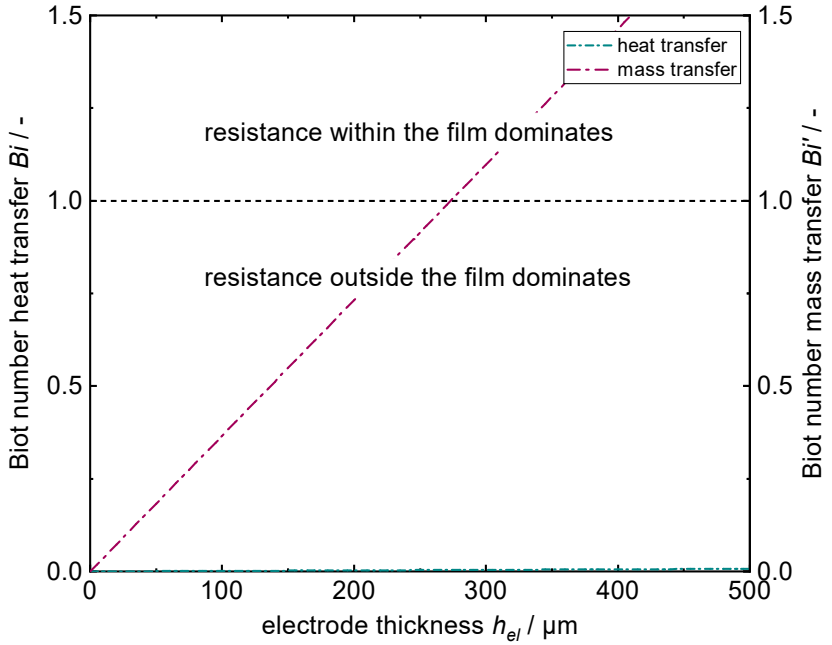

Figure A. 7-14: Estimation of the Biot numbers of heat and mass transfer in dependency of the electrode thickness. Below Biot numbers of 1 the resistance outside the film dominates, whereas the resistance inside the film dominates above 1.

An estimation if the solvent within a bundle of identical single capillaries, breaks at a higher length of these capillaries, based on the capillary pressure can be approximated after equation (A.1). The height of the water column in the capillary $h_{water\ column}$ is dependent on the surface tension of the solvent σ_s and the contact angle between solvent and the material θ which forms the surrounding of each capillary. The density of the solvent ρ, the acceleration due to gravity g and the radius of the capillary r have also to be taken into account.

$$h_{water\ column} = \frac{2\,\sigma_s \cos\theta}{\rho\, g\, r} \tag{A.1}$$

Transferred to electrode drying, the solvent would be the CMC-solution and the surrounding material of each capillary would be graphite. The contact angle of the CMC-solution on graphite was estimated with 74° with the surface tension being 72.4 mN m^{-1}.[107] The density of the CMC-solution was calculated to be

1002 kg m^{-3}, and for the pore radius the peak of the pore size distribution (see Figure 2.12) with 4.8 µm was chosen. This results in a capillary height of 0.53 m. For the larger pore radius of 12.1 µm the capillary height would be 0.21 m. This means, that capillary transport would not be a limitation if the microstructure consisted of a bundle of homogenous capillaries. Since the real microstructure is built from a broad pore and particle size distribution (see Figure 2.13), more complex interactions in capillary transport can be expected.

C.3 Drying Patterns at the Comb Nozzle Dryer

As was discussed in section 4 (Drying Behavior), drying patterns result from drying under a stationary dryer. These drying patterns are more pronounced the higher the drying rate and the higher the film thickness. This is shown exemplarily for two electrode films of SoA area weight in Figure A. 7-15. On the left (Figure A. 7-15a) an electrode film which was dried at a theoretical drying rate of 0.75 g m^{-2} s^{-1} and on the right (Figure A. 7-15b) one dried at 2.5 g m^{-2} s^{-1} is shown. The comb nozzle pattern is clearly visible especially at the faster dried film. A HE electrode film of slurry (K) (Figure A. 7-15c) shows cracks with a similarity to the comb nozzle pattern.

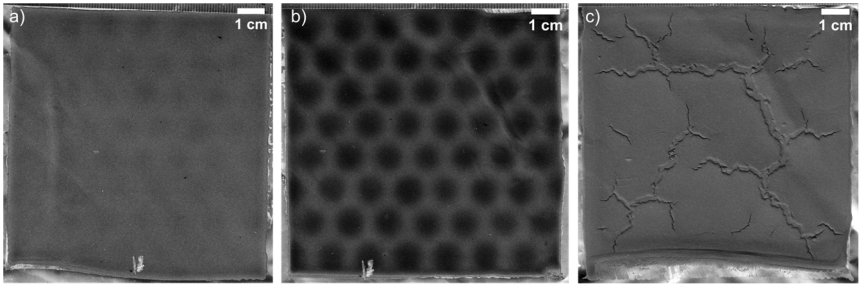

Figure A. 7-15: Pictures of drying patterns of two electrode films of slurry (R) of SoA area weight, which were dried at a drying rate of a) 0.75 g m^{-2} s^{-1} and b) 2.5 g m^{-2} s^{-1} compared to c) an HE electrode of slurry (K).

The different coloring can be attributed to different amounts of binder on the surface of these electrodes. A darker shading thereby hints on a higher amount of binder at the surface, which also correlates to the position directly beneath the nozzles.[99] This can be also found in adhesion force measurements which are shown in Figure A. 7-16. The adhesion force was measured along the nozzle-

shaped area and is compared to the position of the nozzle field. A minimum of the adhesion force can clearly be observed at the center of the nozzles. The adhesion force between minimum and peak thereby varies by more than 5 N m^{-1}. This emphasizes the need for a dryer hood movement to further homogenize the heat transfer coefficient, especially when drying at high drying rates.

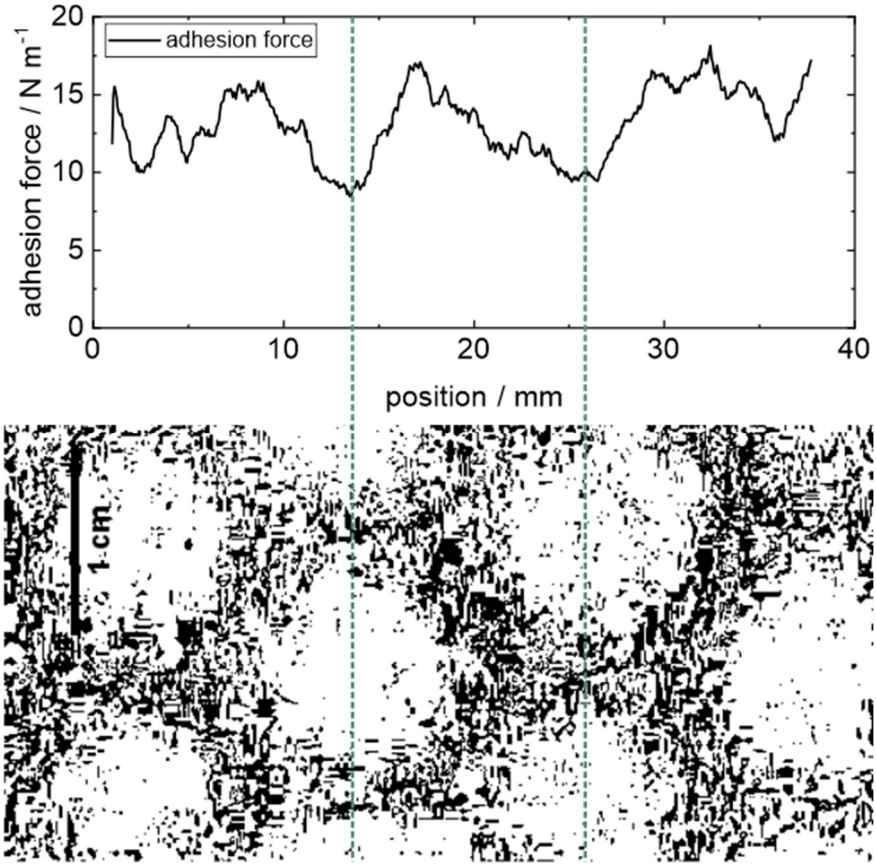

Figure A. 7-16: Nozzle position and adhesion force.[108]

C.4 Dew Point Measurement

Knowledge about the dew point during drying is necessary for simulating drying curves. The dew point as a function of the drying time is given in Figure A. 7-17. While in the shown example, the dew point has a value of about -3 °C before the measurement starts, it rises to a value of about 8 °C as soon as solvent evaporation starts. The dew point stays at this level until the film is almost dry and then reaches a level below 0 °C again. The relevant dew point for simulation therefore is the plateau it reaches during solvent evaporation. Since the dew point sensor has to be placed on top of the film reaching within the relevant area of drying, the dew point was determined in a separate measurement and then removed when the gravimetric measurement started, as to not disturb the drying conditions on top of the drying film. If the drying conditions in term of the volume flow rate, ambient temperature and ambient humidity were not changed, it was assumed that the dew point would remain the same.

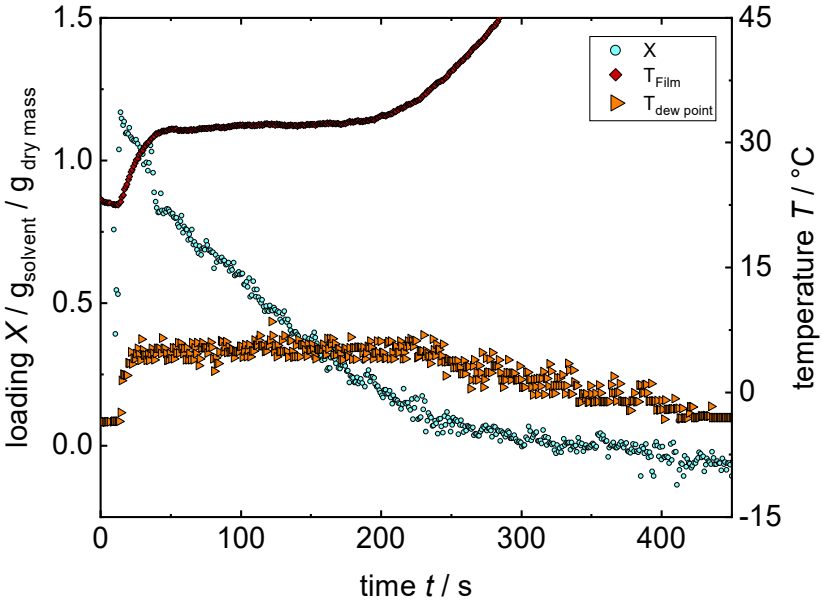

Figure A. 7-17: Exemplary dew point measurement during drying of an electrode with increased area weight.

C.5 Simulation Model Optimization

The MDF model can predict the solvent loading curve for drying of electrodes with elevated area weights. This is true even though it was shown that the actual drying process is more complex than the model considers. On the way to improve the model and to extend the knowledge about the drying process, the model was adapted in a last step: From the drying experiments in section 4 it can be assumed, that a mixture of capillary transport and solvent vapor diffusion from the inner pore volume takes place. In the model this could be implemented by allocating different area fractions of the total area to the two mechanisms. One area fraction would still dry with a high drying rate due to capillary transport of solvent, while the drying rate of the other area fraction would be slowed down due to diffusion of solvent vapor through the porous electrode. The question remains which area

fraction applies to which mechanism, with the further difficulty that the respective area fraction is presumably time dependent.

As a means to determine a realistic area fraction, an optimization function has been included in the python script: The simulated solvent loading was fitted to the experimental solvent loading in each time step by variating the proportion of the area which dries with the MDF model. The experimental data was described with a polynomial function of 9th degree. The temperature course was meanwhile calculated as presented before. The relevant distance for vapor diffusion within the porous electrode was not implemented with a moving drying front, but instead with an averaged value of the distance between the water column and the surface of the electrode of $h_{el}/2$. Therefore, the possibility is included that solvent vapor diffusion takes place in deeper regions within the microstructure from the beginning. The start of the optimization was set to the end of film shrinkage.

The resulting course of the area fraction which dries with solvent vapor pore diffusion is shown in Figure A. 7-18. The total area increases to a value of 0.0192 m² which is more than twice the coating area. Under the assumption of a 3D network with a lot of menisci within the microstructure contributing to drying this could be plausible, though the simulated temperature course in Figure A. 7-19 in the top graph still deviates from the experimental one. The discontinuity in the temperature course is caused by the assumption that the total area of the MDF model is 0.0081 m² when 1 % of the total solvent loading are reached, which results in a jump in the area curve (see in Figure A. 7-19).

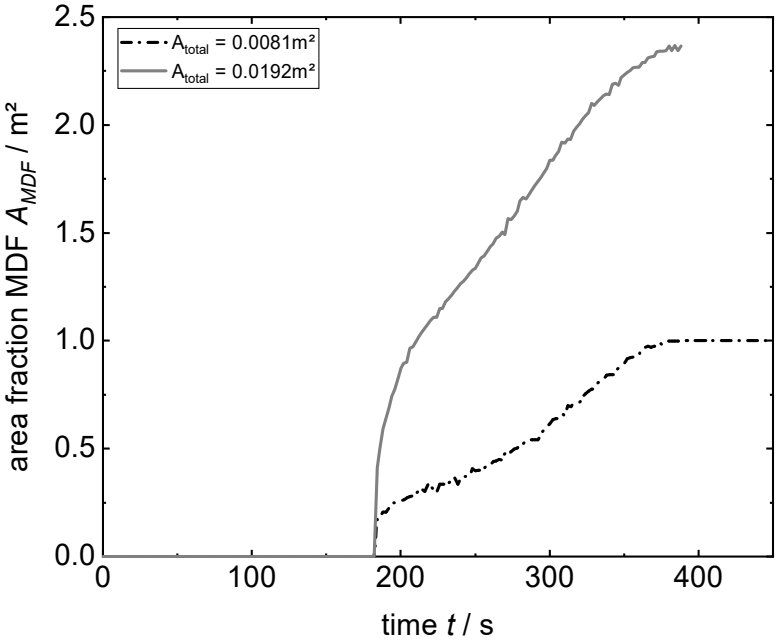

Figure A. 7-18: Area fraction which dries by solvent vapor diffusion over drying time derived from fitting experimental and simulated solvent loading curves to one another. Two approaches are compared with the first being based on the input parameters presented in the previous sections resulting in a total area of 0.0192 m² and the second one with adjusted values for λ_{dry} and $\delta_{s,eff}$ ending in a total area of 0.0081 m².

One way for the total area to result in the experimentally given value of the coating area (0.0081 m²) is to vary the values of the heat transfer coefficient of the coating λ_{dry} and of the effective diffusion coefficient $\delta_{s,eff}$ in the MDF model. In Figure A. 7-18, $\lambda_{new} = \lambda_{dry}/16$ and $\delta_{new} = \delta_{s,eff}/24$ were found to result in a total area fraction of 0.0081 m². The adjustment of both parameters leads to the temperature curve shown in Figure A. 7-19 at the bottom graph. The experimental and simulated temperature curve match perfectly. It has to be remarked that a different distance for vapor diffusion (which was assumed to be $h_{el}/2$ in both scenarios presented here), has a similar effect as increasing the heat and mass transfer resistances. A slower mass transfer diffusion than applied in the model caused by the pathways throughout the porous structure could be imaginable. A decreased heat transfer though, seems unlikely due to the high heat

conductivity of graphite. The assumption that simulated and experimentally determined temperature curves have to align is another debatable question due to the discussed influence of the single measuring spot (section 4.4.1 Experimental Drying of Thinner Electrodes). Even though, the optimizing approach can give some valuable information about the interdependency of capillary water and diffusional solvent vapor transport. Experimentally determined transport coefficients for heat and mass transfer of the material system at hand as opposed to the Zehner Bauer Schlünder approach, could be included in the future to validate the findings and improve the model and distinguish between the influence of transport coefficients and length scale. If a time-resolved area function for the actual area contributing to solvent evaporation could be found, more realistic simulations of the drying process could be derived.

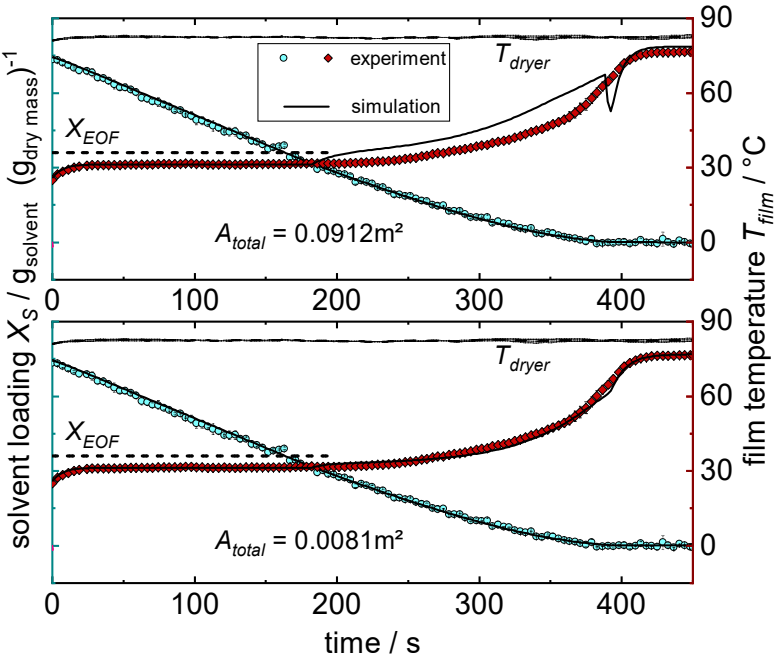

Figure A. 7-19: Simulated temperature curve resulting from an adjustment of the area fraction which dries by solvent vapor diffusion which is derived from fitting experimental and simulated solvent loading curves to one another. Two approaches are compared with the first being based on the input parameters presented in the previous sections resulting in a total area of 0.0192 m² and the second one with adjusted values for λ_{dry} and $\delta_{s,eff}$ ending in a total area of 0.0081 m².

C.6 Further Methods to Determine Drying Curves

Methods to characterize drying and get valuable information about dryers are mandatory for full process control. The heat transfer coefficient of a dryer can thereby be determined if a film dries at a constant drying rate and the drying curve can be obtained. Two ways to obtain drying curves in an industrial dryer are shown in the following.

One way to determine the heat transfer coefficient is a gravimetric drying curve which consists not of a continuous measurement but is composed of single measurements. In an industrial dryer, samples would be taken at different positions

within the dryer and the residual moisture within the film would have to be measured. Such drying curves are shown in Figure A. 7-20.

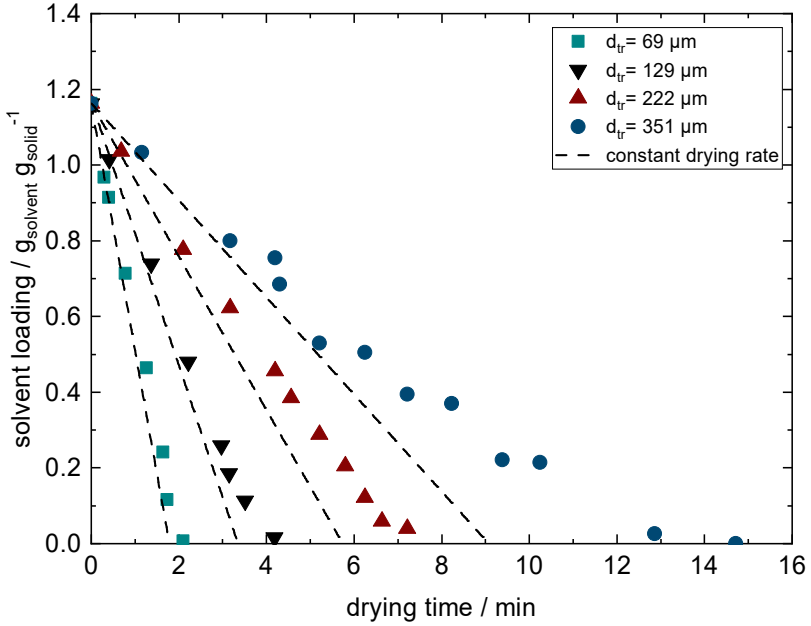

Figure A. 7-20: Gravimetric drying curves which are composed of single residual moisture measurements at different times of drying. The drying curves of electrode films of four different film thicknesses are compared.

Another method to determine the drying rate is the measurement of the film thickness. In this example it is shown for a stationary film placed on a heating plate for drying. No defined gas conditions were present since the goal was to establish whether the change in film thickness could be measured with sufficient accuracy. The measurement was conducted by a chromatic confocal sensor CHRocodile SE (Precitec GmbH & Co. KG, Germany), with an optical probe having a measurement range of 8 mm and a measurement distance of 36.3 mm. Films of different wet film thicknesses which were dried at two different heating plate temperatures are compared in Figure A. 7-21. The measurements are compared to the dry film thickness determined by a measuring probe. While the measurement is limited by the end of film shrinkage it can still give important

insights into drying curves until that point of drying is reached, since the drying rate during the constant rate period can be determined. From the drying rate the heat transfer coefficient could be derived Measurement probes could be implemented at different positions in industrial dryers and a dryer characterization as well as improved process control be realized.

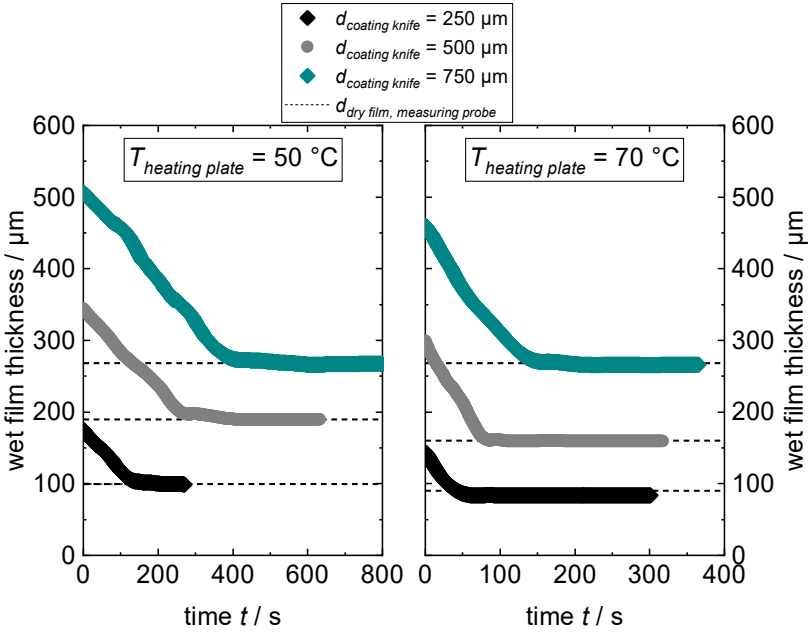

Figure A. 7-21: Measurement of the wet film thickness during drying, using a chromatic confocal sensor. Different original wet film thicknesses as well as drying temperatures of the heating plate used for drying are compared.[109]

D Further Detailed Results of Single Layer Electrodes

Information on single layer electrodes exceeding the one given in the main section is summarized here. A summary of the settings used in section 3 to apply a certain drying rate are given in Table A. 2.

Table A. 2: Settings (1) to (4) of the heat transfer coefficient and the corresponding isothermal drying temperature to adjust a certain drying rate corresponding to those in Figure 3.2. The settings to achieve the drying rates depicted in Figure 3.4 are also given.

Setting	Drying rate$_{theo}$	Heat transfer coefficient	Isothermal drying temperature
	g m^{-2} s^{-1}	W m^{-2} K^{-1}	°C
-	0.75	35	31
-	0.75	80	24
Figure 3.2 (1)	1.5	35	41
Figure 3.2 (2)	1.5	80	31
Figure 3.2 (3)	2.5	35	49
Figure 3.2 (4)	2.5	80	41
-	0.75	80	24
-	3.5	35	54
-	3.5	80	40
-	6	35	63
-	6	80	48

-	10	35	72
-	10	80	57
-	15.5	35	80
-	15.5	80	65

D.1 Comparison of Different Substrate Foils

The choice of copper foil influences the absolute values of adhesion, which is shown in Figure A. 7-22. The three different copper foils used in this work are summarized here, showing their absolute values of adhesion force and the decrease of adhesion when increasing the drying rate.

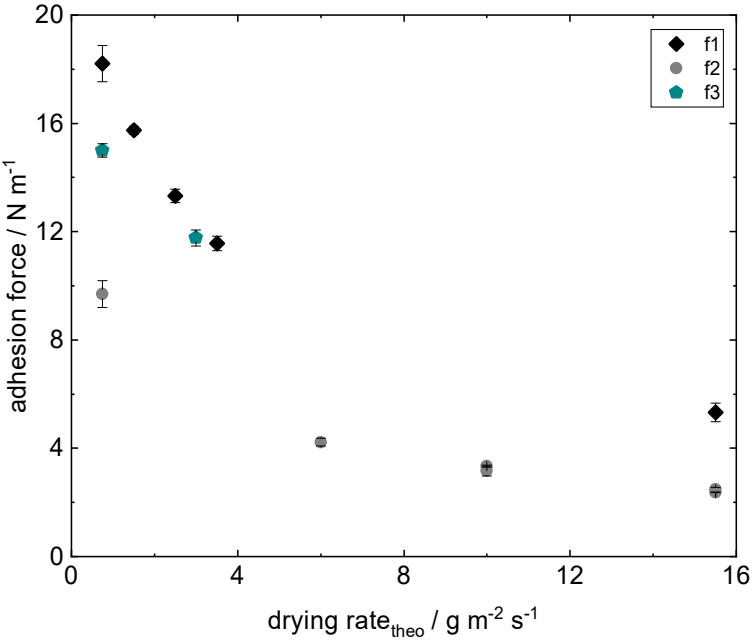

Figure A. 7-22: Comparison of the adhesion force of electrodes on the three different copper foils f1, f2 and f3 used as substrate in this work. The drying rate was varied by changing the isothermal drying temperature, while the heat transfer coefficient was kept at 35 W m^{-2} K^{-1}. When the adhesion force of different substrates is being compared, the adhesion force was normalized on the adhesion force measured at a drying rate of 0.75g m^{-2} s^{-1}, a heat transfer coefficient of 35 W m^{-2} K^{-1} with electrodes of an area weight of 60 g m^{-2}.

The adhesion force values used for normalization are summarized in Table A. 3.

Table A. 3: Absolute values of the adhesion force of the identical slurry on three different copper foils f1-f3 dried at a drying rate of 0.75g m^{-2} s^{-1}, a heat transfer coefficient of 35 W m^{-2} K^{-1} with an area weight of 60 g m^{-2}.

	f1	f2	f3
Adhesion force N m^{-1}	18.2	9.7	15.0

D.2 Porosity of dry electrode layers

The porosity of electrode (R) in dependency of the area weight and the linear fit function to correlate area weight and porosity are given in Figure A. 7-23.

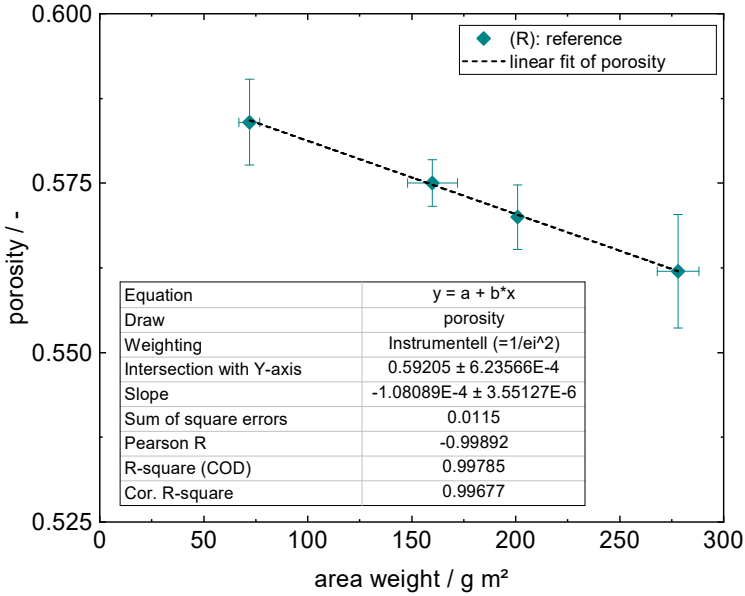

Figure A. 7-23: Porosity of electrode (R) in dependency of the area weight and the linear fit function to correlate area weight and porosity as measured and implemented in the drying curve simulation in section 4 Drying Behavior of Thicker Electrodes.

The porosity of electrodes (R), (S), (K) and (A) in dependency of the area capacity are shown in Figure A. 7-24. The porosity decreases with an increasing area weight.

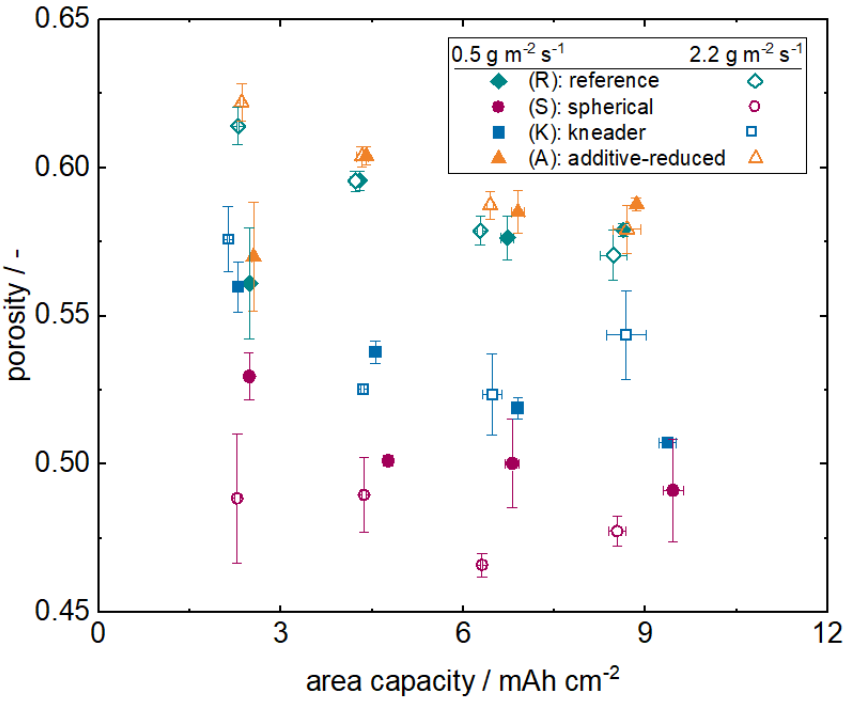

Figure A. 7-24: Porosity of electrode (R), (S), (K) and (A) in dependency of the area capacity.

The porosity as a function of the adhesion force is shown in Figure A. 7-25. While it was discussed in detail, that the porosity itself cannot be assumed to be the main factor determining the adhesion force, it might still contribute to some extent by increasing the contact between particles and substrate foil.

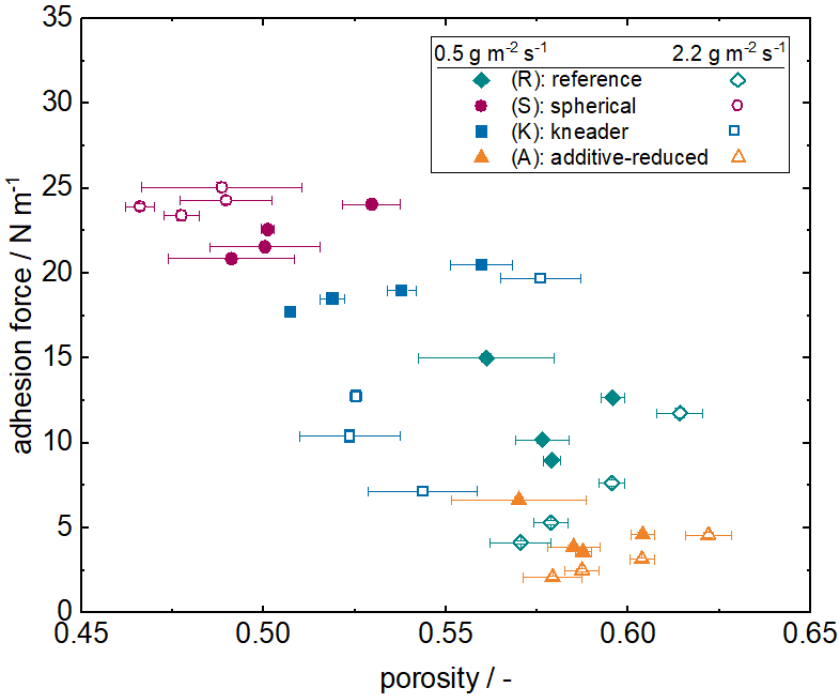

Figure A. 7-25: Adhesion force as a function of the porosity of (R), (S), (K) and (A).

To evaluate whether a calendering to the same porosity leads to the same adhesion force, electrode (R) and electrode (K) were calendered. The uncalendared and the calendered adhesion force of both electrodes is compared in Figure A. 7-26. While the adhesion force is increased by the calendaring step, the difference of the adhesion force between both electrodes remains.

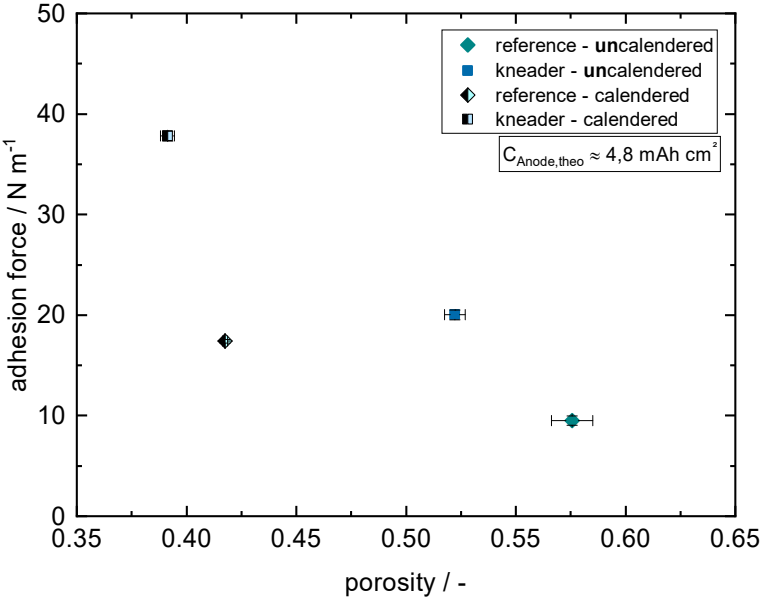

Figure A. 7-26: Comparison of the adhesion force of uncalendered electrode (R) and (K) with calendered electrode (R) and (K) on substrate foil (f2).

D.3 Cracking of the Reference Electrode during Drying

Another problem which arises when electrodes are dried is crack formation in the film. The probability for the occurrence of cracks increases along with the thickness of the electrode.[110–114] These develop during drying, when capillary stresses grow with particles moving closer together and capillary pressure building up. They can also manifest in the dry electrode if the current collector foil is deformed during drying in pilot plants.

After equation (7.2), the critical cracking thickness depends on the shear modulus of the graphite particles G, their coordination number N, the volume density of the electrode layer at the random closest packing ϕ_{rcp}, the particle radius $r_{particle}$ and the interfacial tension between solvent and air γ.[114,115] Based on literature, the shear modulus was approximated with 5.05 GPa.[116]

$$h_{max} = 0.41 \left[\frac{GN\,\phi_{\mathrm{rcp}}\,r_{particle}^{3}}{2\,\gamma}\right]^{\frac{1}{2}} \rightarrow h \sim r^{1.5} \tag{7.2}$$

The coordination number was calculated to be 3.92 after the empirical formula $N = \frac{3.08}{\varepsilon} - 1.13$.[117] The d_{50} was used for an estimation of $r_{particle} = 9\ \mu m$ and the surface tension of water was assumed to be 0.072 N m^{-1}. This results in a theoretical critical cracking thickness of 2.6 mm at a porosity of 0.61. This is a highly simplified calculation though, since no monomodal particle distribution is present but a broad particle size distribution. For example, a particle radius of $r_{particle} = 5\ \mu m$ would reduce the critical cracking thickness to 1058 µm. Furthermore, only the graphite particles are considered. The coating additionally contains CMC and SBR binder as well as carbon black, which also affects the critical cracking thickness and further complicates prediction.[118] Therefore an experimental approach to access critical process conditions for crack formation is chosen.

Cracking Experiments: To determine a critical cracking thickness for electrodes dried at different drying rates, a non-uniform gap was adjusted in the coating knife with a width of 100 mm. The lower gap was 160 µm and the larger one was 1000 µm. This resulted in a wedge-shaped coating of the electrode. For crack area determination, all layers were scanned with a flat-bed scanner and processed using "ImageJ". All analyzed images had an area of 40270 ± 497 mm². For crack area determination, all areas smaller than 0.3 mm² were excluded.

Critical cracking thickness

Electrodes with an inclined coating knife gap were coated and dried at different drying rates. The heat transfer coefficient was 80 W m^{-2} K^{-1} in each case. The inclined wet coating resulted in a wedge-shaped cross section perpendicular to the coating direction. A continuously decreasing adhesion force can be measured along with the increasing electrode thickness (see appendix, Figure A. 7-35). Two inclined layers and two flat layers dried at two different drying rates are shown in Figure A. 7-27.

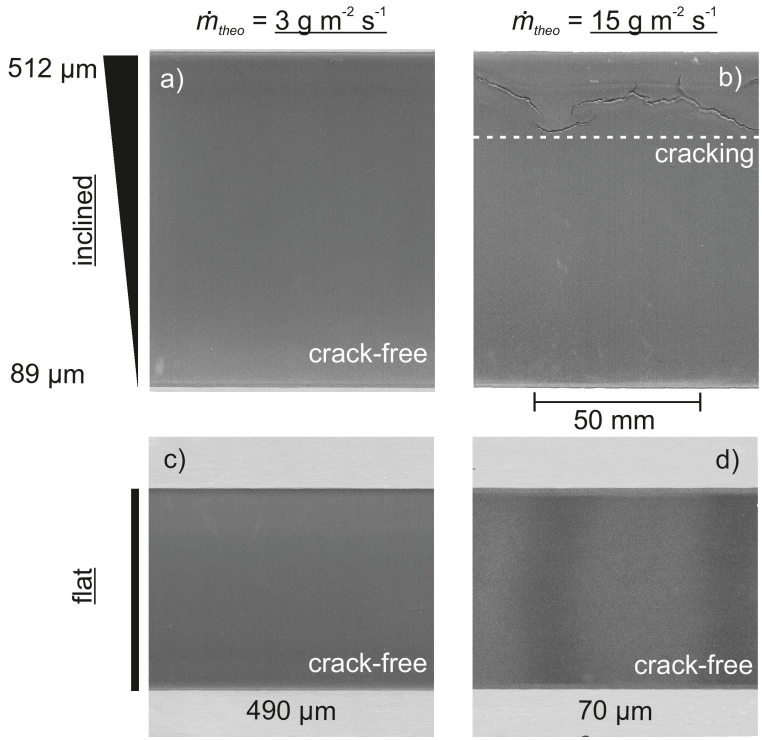

Figure A. 7-27: Tendency for electrodes to crack dependent on coating thickness and drying rate. The electrodes in the top row feature an inclined thickness from 89 µm to 512 µm and were dried at a drying rate of a) 3 g m^{-2} s^{-1} and b) 15 g m^{-2} s^{-1}. In the bottom row flat electrode layers are shown, with c) 490 µm thickness, dried at 3 g m^{-2} s^{-1} and d) 70 µm thickness, dried at 15 g m^{-2} s^{-1}. The heat transfer coefficient was 80 W m^{-2} s^{-1}. Figure after Kumberg et al., 2019. [24]

Both inclined layers have a minimum film thickness of 89 µm and a maximum film thickness of 512 µm (Figure A. 7-27a Figure A. 7-27b). The inclined electrode dried at 3 g m^{-2} s^{-1} and 37 °C shows no sign of cracking, while the electrode dried at 15 g m^{-2} s^{-1} and 64 °C shows cracking starting at a thickness of around 400 µm. The flat layer with a thickness of 490 µm dried at 3 g m^{-2} s^{-1} is crack-free which is also true for the thin flat layer of 70 µm thickness dried at 15 g m^{-2} s^{-1} (Figure A. 7-27c) and d) respectively). The flat layer dried at the extreme drying rate shows a coloring going from darker to brighter grey. Since the experiments were conducted in the batch coater (see Figure 2.3), this is caused by the extreme drying rate, where the plate movement is not able to homogenize the

drying conditions anymore. The brighter coloring can be associated with less binder at the surface caused by the electrode being positioned directly underneath a slot nozzle and the darker color with more binder at the surface was positioned in between the nozzles. This was found by comparing the shade of electrodes processed with different binder contents.[99,119]

For a more complete conception of the dependency between cracking and drying rate, more drying rates were investigated with the set-up using the inclined coating knife. The drying rate was adjusted by either varying the temperature or the heat transfer coefficient. Four heat transfer coefficients (35, 52, 67 and 80 W m^{-2} K^{-1}) were investigated. In Figure A. 7-28 the critical cracking thickness as a function of the drying rate is presented. For the theoretical drying rates of 0.75, 1.5 and 3 g m^{-2} s^{-1} no cracking was observed, independent of the heat transfer coefficient. Only when the drying rate is increased above values of 6 g m^{-2} s^{-1} cracks do appear for all heat transfer coefficients. Cracks started at a thickness of about 350 µm under consideration of the error bars at all higher drying rates. The temperature for the shown heat transfer coefficients was between 57 °C and 64 °C. Cracks were observed at a drying rate of 6 g m^{-2} s^{-1} also for combinations of lower temperature and higher heat transfer coefficients as well as the other way around. No distinction between the heat transfer coefficients in relation to the critical cracking thickness was detected when further increasing the drying rate.

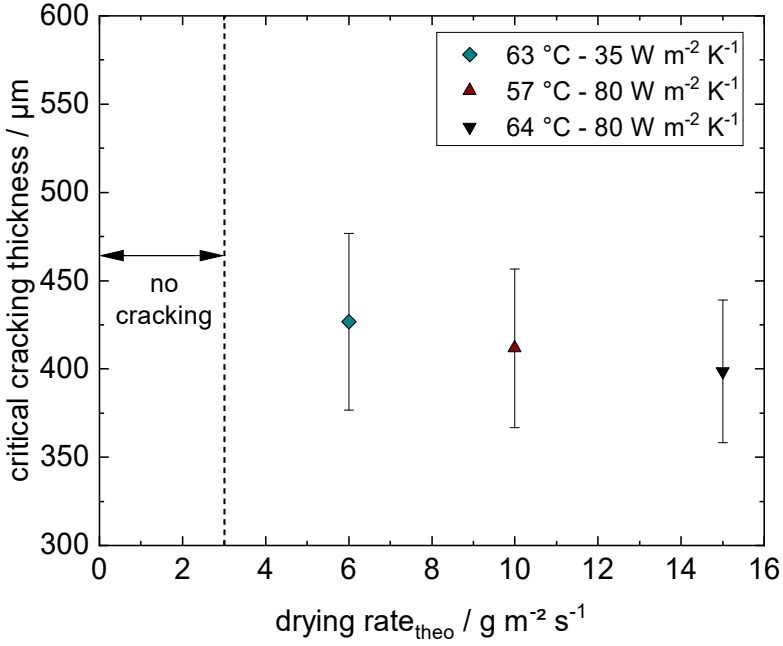

Figure A. 7-28: Critical cracking thickness derived from electrodes coated with an inclined coating knife as a function of the drying rate under variation of the heat transfer coefficient and the isothermal drying temperature. Cracks started at a thickness of about 350 µm under consideration of the error bars. All electrodes dried at a drying rate of 3 g m^{-2} s^{-1} or lower showed no sign of cracking. Figure after Kumberg et al., 2019. [24]

Crack area

For quantification of crack formation and to correlate crack development with the drying rate, the crack area was analyzed by means of image evaluation. The crack area in relation to the total coating area as a function of the drying rate is given in Figure A. 7-30. The heat transfer coefficient was varied to adjust a certain drying rate by setting the heat transfer coefficient and the corresponding isothermal drying temperature. Between all coatings the temperature was varied between 28 °C for the lowest drying rate at the highest heat transfer coefficient and 79 °C for the highest drying rate at the lowest heat transfer coefficient.

Their influence on the crack area was investigated. Since no cracks were visible at drying rates below 3 g m^{-2} s^{-1}, the respective cracking area is zero. When the drying rate is increased, the crack area increases as well.

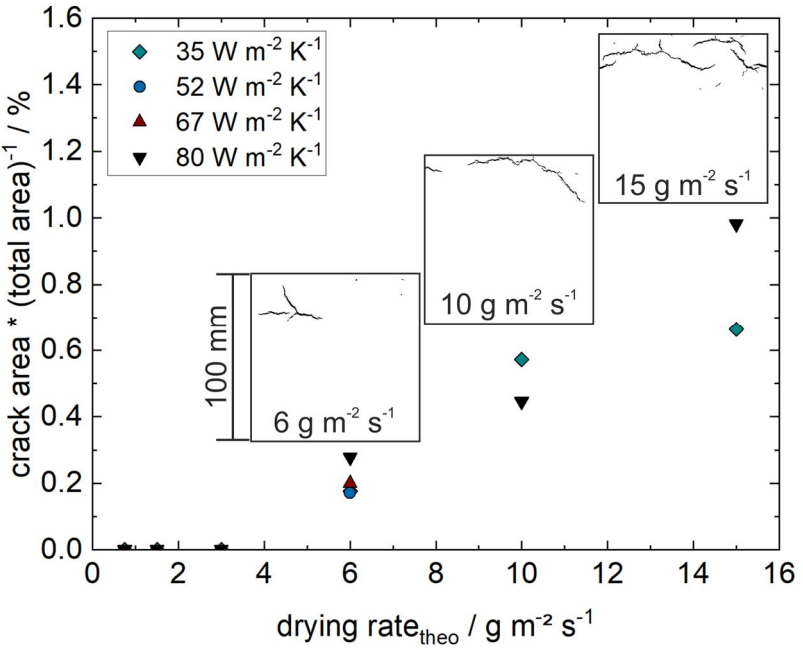

Figure A. 7-29: Crack area in relation to the total area as a function of the drying rate for different heat transfer coefficients. As can be seen in the images, the crack area increases with an increase of the drying rate. Since no cracks were visible at drying rates below 3 g m^{-2} s^{-1}, the respective cracking area is zero. Figure taken from Kumberg et al., 2019.[24]

It can be summarized that electrodes are more likely to crack at elevated thicknesses and higher drying rates. Thick electrodes could be processed without cracks developing up to a theoretical drying rate of 3 g m^{-2} s^{-1}. These findings are restricted to the slurry with the given particle size distribution and composition investigated here but can still give insights into relevant parameters which can be adjusted to avoid cracking.

In summary, electrodes with a thickness up to 350 µm, which corresponds to an area capacity of about 10.9 mAh cm^{-2}, could be dried even at extreme drying rates of 15 g m^{-2} s^{-1} without cracking.

This is true for the given slurry composition and particle size distribution and can be expected to deviate from the values shown here if any of the material parameters are changed.

If slurry properties are changed, a higher or reduced tendency for cracking might result as will be addressed in the following.

D.4 Cracking of slurry (R), (S), (K) and (A) in comparison

In contrast to reference electrode (R) which did not show any sign of cracking at the investigated electrode thicknesses when dried at a theoretical drying rate below 3 g m^{-2} s^{-1}, slurry (S) and (K) showed cracks at higher thicknesses. When repeating the experiment using the inclined coating knife gap, electrode (S) and (K) both showed signs of cracking at a dry electrode thickness exceeding 325 µm even though the drying rate was only 0.75 g m^{-2} s^{-1} (see Figure A. 7-30).

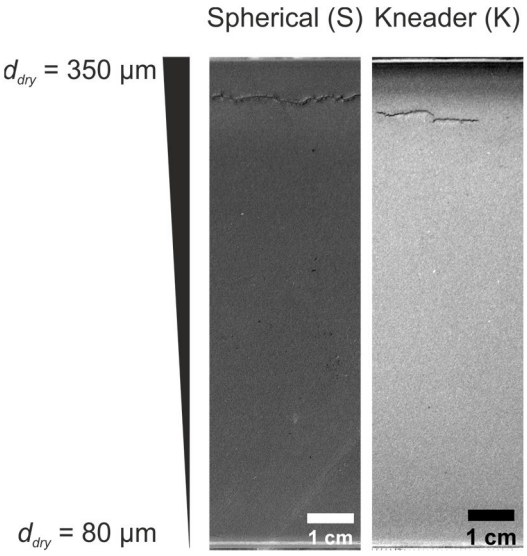

Figure A. 7-30: Experiment using the inclined coating knife gap, to evaluate the crack formation of electrode (S) and (K) in the batch coater under isothermal drying conditions with a theoretical drying rate of 0.75 g m^{-2} s^{-1}.

A higher tendency for crack formation to occur was found in the gravimetric setup as well, as is depicted in Figure A. 7-31. All four slurries were coated at four different film thicknesses and dried in the comb nozzle dryer at a theoretical drying rate of 0.75 g m^{-2} s^{-1}. Even electrode (R) shows some cracks at the highest electrode thickness of about 300 µm. For electrode (S) cracks were found starting at a thickness of 225 µm and for electrode (K) even starting at 125 µm. Only electrode (A) was crack-free over all electrode thicknesses. The inhomogeneous temperature and heat transfer distribution might be the reason for the earlier onset of crack formation since all cracks follow the comb nozzle field in form and size. Another factor that should be considered is the loose substrate in the gravimetric experiment in contrast to the fixed substrate in the experiments conducted within the batch coater. The higher tendency for slurry (K) and slurry (S) to crack, could be reasoned with the tighter network formed by polymer and particles. Stresses cannot be released as easily since the network does not allow for particle movement to release these stresses during drying. This explains also why no cracks were found in slurry (A) with the not fully developed binder-particle network. This could be another advantage of multilayer coatings with slurry (A) as the top layer, since cracks developing during drying could be compensated by slurry (A).

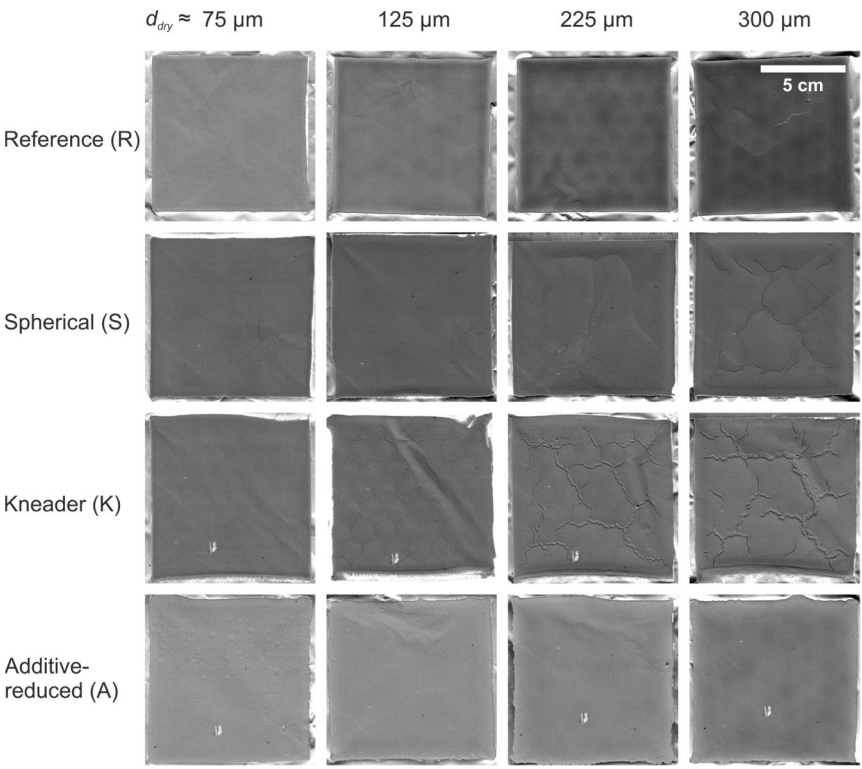

Figure A. 7-31: Crack formation during the gravimetric experiment of electrode (R), (S), (K) and (A) when dried at a theoretical drying rate of 0.75 g m^{-2} s^{-1}. Four different electrode thicknesses were investigated.

D.5 Variation of heat transfer coefficient during drying of slurry (K)

With the assumption of ester bonds being responsible for an adhesion force increase at higher drying rates when the drying rate is adjusted by an increase of the drying temperature, an adhesion force loss would be expected when the drying rate is adjusted by an increase of the heat transfer coefficient while the drying temperature remains constant. This thesis is evaluated for slurry (K). In Figure A. 7-32, the drying rate of 3 g m^{-2} s^{-1} was adjusted by an increase of the drying temperature with a constant heat transfer coefficient of 35 W m^{-2} K^{-1} on the one hand. The drying rate of 1.5 g m^{-2} s^{-1} was on the other hand reached by increasing

the heat transfer coefficient to 80 W m^{-2} K^{-1} and keeping the temperature identical to the one which was used to adjust the drying rate of 0.75 g m^{-2} s^{-1} at a heat transfer coefficient of 35 W m^{-2} K^{-1}. The adhesion force of the electrode dried at the higher heat transfer coefficient is reduced to a value below the one of the electrode dried at of 0.75 g m^{-2} s^{-1}. This would be expected, since at the identical temperature, less time remains for ester bond formation, due to the elevated drying rate and the faster capillary pore emptying.

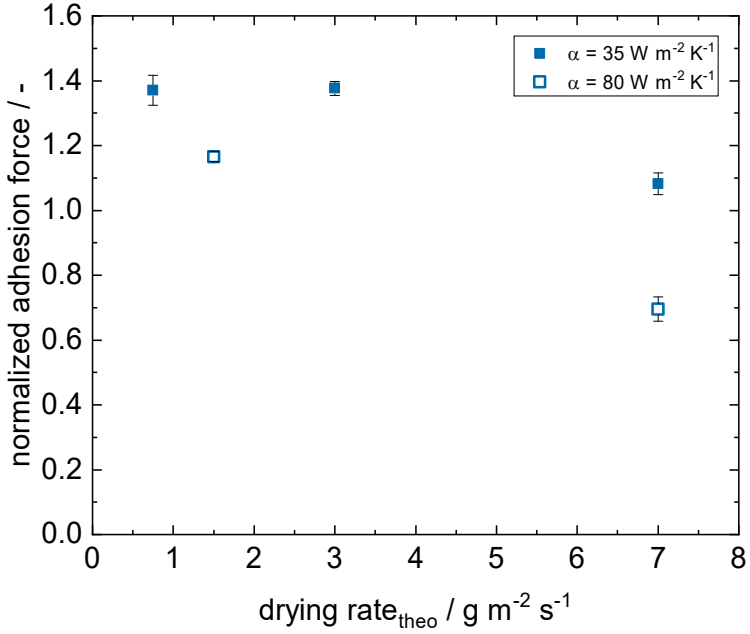

Figure A. 7-32: Variation of the drying rate for electrode (K) at SoA thickness by drying under two different heat transfer coefficients of 35 W m^{-2} K^{-1} and 80 W m^{-2} K^{-1}. Electrodes were coated onto substrate (f1).

D.6 Binder migration of slurry (K)

The electrode surfaces of electrode (R) and electrode (K) when dried at two different theoretical drying rates are compared in Figure A. 7-33 in two SEM pictures. The reference shows a quite open pore space especially at the lower drying rate of 0.75 g m^{-2} s^{-1} (Figure A. 7-33a and Figure A. 7-33b). The pores of

electrode (K) seem to be clogged, which seems to be more pronounced at the higher drying rate of 3 g m^{-2} s^{-1} (Figure A. 7-33d).

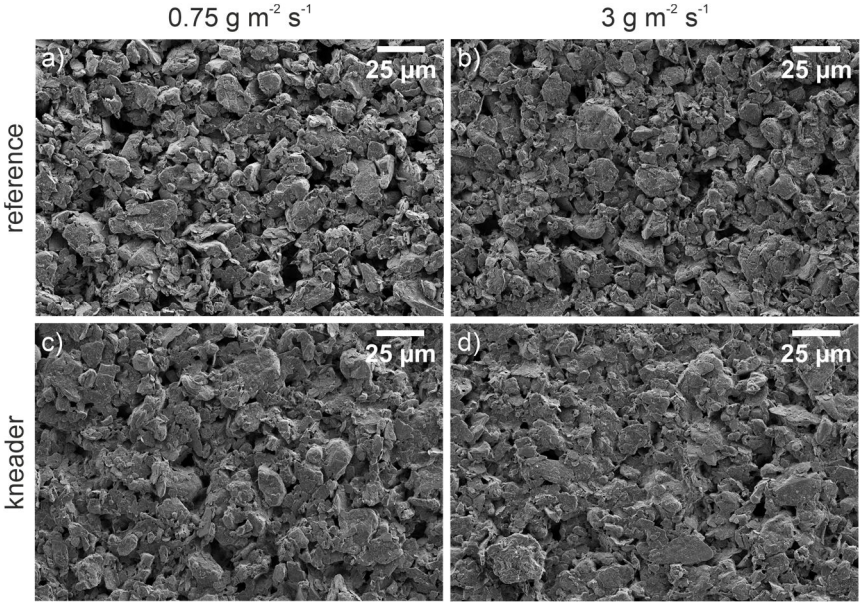

Figure A. 7-33: SEM picture of the top of a) the reference electrode (R) dried at a drying rate of 0.75 g m^{-2} $s^{-1}$and b) electrode (R) dried at a drying rate of 3 g m^{-2} s^{-1}. C) shows the top of electrode (K) dried at a drying rate of 0.75 g m^{-2} s^{-1} and d) shows electrode (K) dried at a drying rate of 3 g m^{-2} s^{-1}.

The finding of a dense binder layer at the top of electrode (K) is confirmed by LIBS measurements of electrode (K) dried at the two different drying rates. The comparison of the lower and the higher drying rate is shown in Figure A. 7-34. Both LIBS measurements show a dense layer of binder at the top of the electrode which is more pronounced at the theoretical drying rate of 3 g m^{-2} s^{-1}.

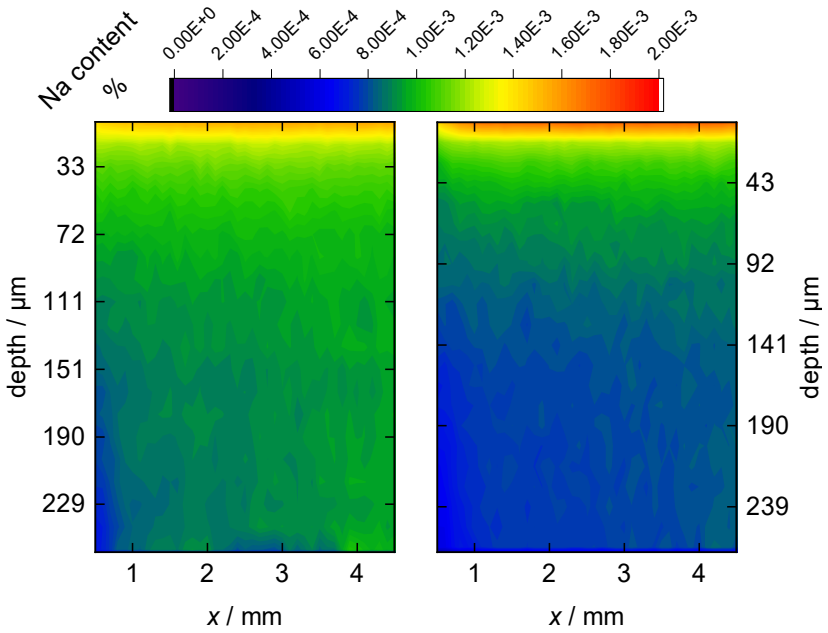

Figure A. 7-34: LIBS measurements which were made by Y. Zheng and W. Pfleging at IAM-AWP, KIT. The Na-CMC distribution of two thick electrodes, derived from slurry (K) which were dried at a low drying rate of 0.75 g m^{-2} s^{-1} (left) and a high drying rate of 3 g m^{-2} s^{-1} (right), is compared.

D.7 90° Peeltest of a flat and an inclined layer

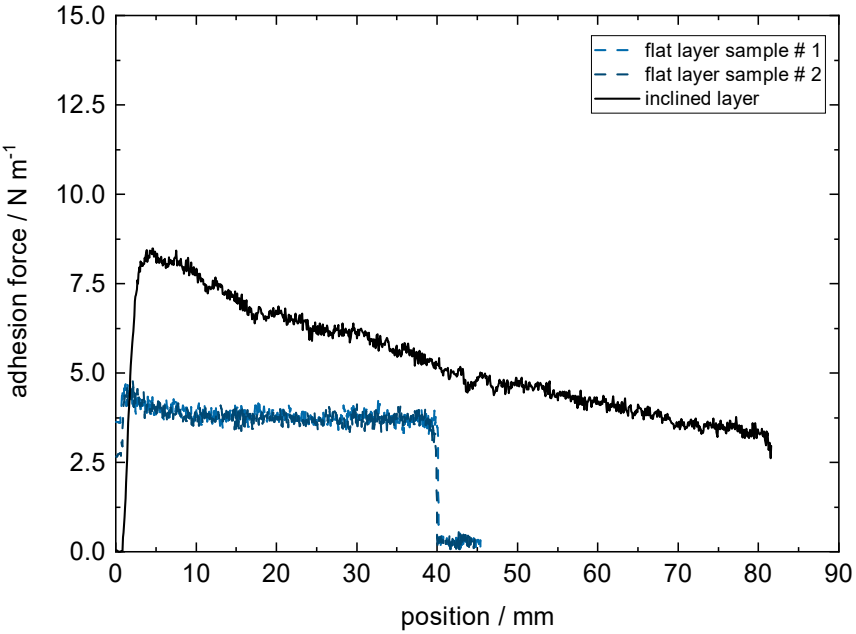

Figure A. 7-35: Complete adhesion force measurement with the 90° peel test of a flat layer compared to an inclined layer as shown in section 3.

D.8 Setup for pull-off test

In case of the pull-off test, used to measure the area related adhesion force, other test parameters apply than for the 90° peel test. The pull-off test was conducted with a round head with a diameter of 2 cm (see Figure A. 7-36). Two heads with the sample in between were pressed together with a force of 17.46 N for 30 s before the test.

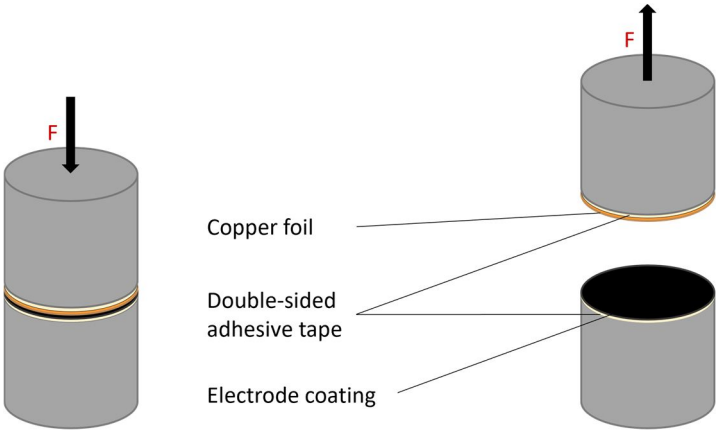

Figure A. 7-36: The setup of the pull-off test consists of two metallic cylinders which are pressed together with a certain pressure in the first step. Adhesive tapes on the bottom and top of both cylinders fix the coating and the substrate to the cylinders. In the second step both cylinders are moved apart and the force is measured, which then is a force in relation to the coating area adhering to the cylinder.

D.9 Electrical conductivity

The electrical conductivity of the single layered electrodes (R), (S), (K) and (A) which were dried at the two different experimental drying rates of 0.75 g m^{-2} s^{-1} and 3 g m^{-2} s^{-1} are given in Figure A. 7-37 as a function of the area capacity.

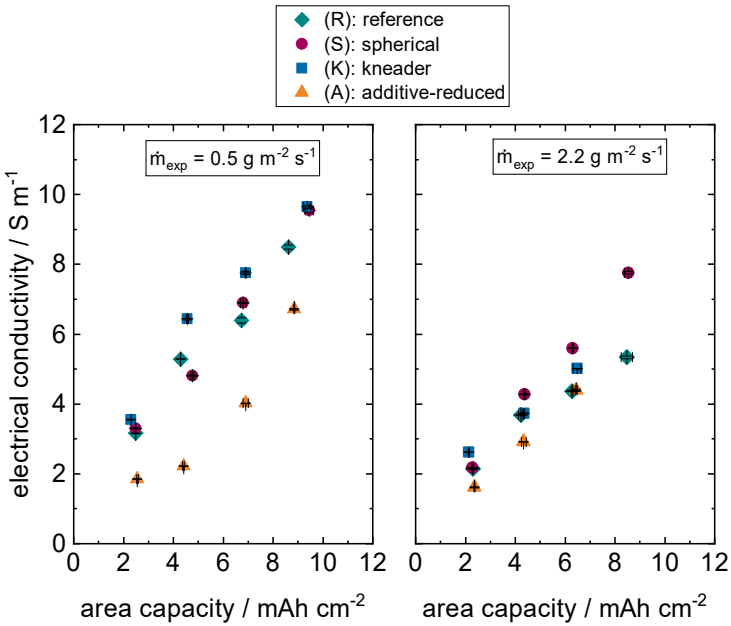

Figure A. 7-37: Electrical conductivity of single layered electrodes in dependency of the area capacity.

D.10 Properties for electrochemical tests

The exact values of the anodes which were used for the coin cell tests which are discussed in the main sections are given in Table A. 4 to Table A. 7.

Table A. 4: Area capacities in mAh cm^{-2} of single layer SoA electrodes that were dried at different drying rates. Area capacities are calculated based on the respective area weights.

Experimental drying rate g m^{-2} s^{-1}	0.5	2.2
(R): Reference	2.1	2.2
(S): Spherical	2.1	2.2
(K): Kneader	2.4	2.0
(A): Additive-reduced	2.3	2.2

Table A. 5: Porosity of single layer SoA electrodes that were dried at different drying rates.

Experimental drying rate g m^{-2} s^{-1}	0.5	2.2
(R): Reference	0.5	0.54
(S): Spherical	0.47	0.45
(K): Kneader	0.47	0.42
(A): Additive-reduced	0.47	0.48

Table A. 6: Area capacities in mAh cm^{-2} of thick single layer electrodes that were dried at different drying rates. Area capacities are calculated based on the respective area weights.

Experimental drying rate g m^{-2} s^{-1}	0.5	2.2
(R): Reference	8.8	8.5
(S): Spherical	9.2	8.5
(K): Kneader	9.1	9.2
(A): Additive-reduced	8.7	8.4

Table A. 7: Porosity of thick single layer electrodes that were dried at different drying rates.

Experimental drying rate g m^{-2} s^{-1}	0.5	2.2
(R): Reference	0.43	0.47
(S): Spherical	0.43	0.47
(K): Kneader	0.50	0.50
(A): Additive-reduced	0.45	0.44

D.11 Comparison of pouch and coin cells

For better evaluation of the coin cell tests which are presented in the main sections, a comparison with pouch cell tests was conducted. The electrochemical performance of coin and pouch cells of electrode (R) and (K) are shown in Figure A. 7-38. The reference was built against a cathode comprised of NMC 622 and cycled for 100 cycles. The reference shows a performance loss at 3C in that case. When the same electrode (R) as well as electrode (K) are combined with a cathode of NMC111, the performance is constant at 3C. It can therefore be assumed,

that the performance loss at 3C of the pouch cell with NMC622 is caused by the cathode side. The discharge rates of the pouch cells exceed that of the coin cells at all C rates, which was expected based on literature. [97,99]

The trend of a better performance of electrode (R) compared to electrode (K) over all C rates with the difference being the highest at 3C is clearly identical in both coin and pouch cell test. It can be assumed therefore, that the coin cell tests used in this work are a valid method for examining process influences.

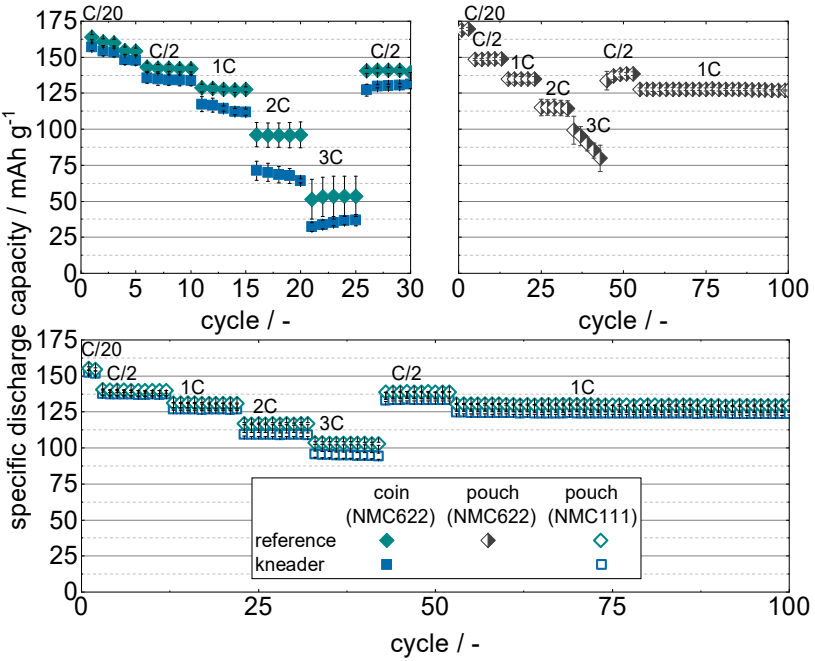

Figure A. 7-38: Comparison of Pouch and Coin cell test. Data of the pouch cell test of the reference electrode against NMC 622 are also shown by Diehm et al.[21]

E Further Detailed Results of Multilayer Electrodes

Since multilayer electrodes could not be extensively addressed in the main sections, some additional information is summarized here. This includes details on coating of simultaneous multilayers. Further information is also given on drying of multilayers with a viscosity or a porosity gradient.

E.1 Simultaneous Coating of Multilayers

In slot-die coating the wet film thickness is adjusted by the volume flow of slurry pumped into the slot die in relation to the web speed and coating width. In a thin single-layered film, two failure mechanisms can occur which lead to film defects: Air Entrainment and reaching the low flow limit. During Air Entrainment, air enters the film due to an instable dynamic contact line between slurry and substrate on the upstream side of the slot die, leading to stripes or bubbles in the film. The low flow limit is reached when instabilities occur in the downstream meniscus between coating and slot die lip. This can also lead to stripes in the coating. Both failure mechanisms can be described by the Visco Capillary Model and a process window can be derived.[120–123]

During slot-die coating of multilayers, the failure mechanisms which can occur in single layer films are supplemented by Swelling and Intermixing of the two layers. Swelling can be observed when the coating liquid moves out of the slot die against the web direction. Intermixing is caused by vortexes due to flow-induced refluxes.[124] Diehm et al. have shown, that coating of multilayered LIB anodes is possible, though the coating window is smaller than for single layer electrodes due to the different flow fields in single and multilayer electrodes. It was also shown, that intermixing does not occur for multilayer electrodes of a thickness ratio of 1:1 and similar viscosities in both layers as long as the web speed exceeds 1 m min^{-1}.[43]

In this work, the recipes of the slurries used for simultaneously coated multilayers were adapted, as such influencing the viscosities. Furthermore, a thickness ratio of bottom to top layer of 1:3 was applied. Consequently, the stability criteria

of Diehm et al. had to be validated for the parameter settings used in this work.[43] For coating, the slot nozzle was mounted on a carriage and the gap between slot nozzle and substrate was adjusted with shims. Pastes were fed by two automated syringe pumps.

The appearance of defects was visualized using 0.4 wt.-% of the UV marker Disodium 4,4‘-bis(2-sulfonatostyryl)-biphenyl (DSBB) in the bottom layer of the multilayer system (Figure A. 7-39a). The multilayer film was coated on top of a PET substrate and recorded from above and from below while illuminating the flow behavior of the films with an UV lamp as described by Diehm et al.[43]. These experiments were also repeated with a knife-coating system consisting of two coating knifes fixed to each other and two different coating gaps to coat multilayers (Figure A. 7-39b). Pastes were manually fed by two syringes. All multilayer films which were dried and fabricated to coin cells were coated by the double doctor-blade system.

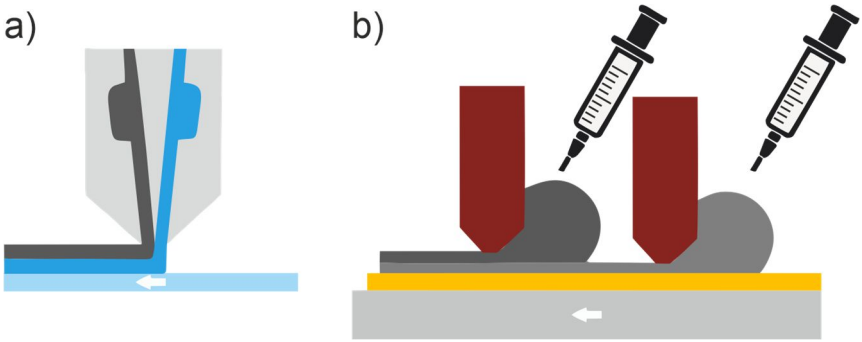

Figure A. 7-39: Side view of the coating of simultaneous multilayers using a) a slot die and b) using two doctor blades as well as

Coating Stability

The coating stability of the simultaneously coated multilayers presented in this work were investigated regarding the intermixing of these layers. In Figure A. 7-40 an example of a stabile coating (Figure A. 7-40a) is shown in the wet state. A dry film which showed intermixing of the layers is shown in Figure A. 7-40b. An intermixing of both layers was only observed when the extreme CMC-contents (3.74 wt-% CMC bottom layer and 0.94 wt-% CMC top layer) with the rheology shown in Figure A. 7-3 were combined in a multilayer using a slot die

with an internal merging of both layers within the slot die. When a slot die with a separating wedge as depictured in Figure A. 7-39a) was used, no intermixing even of the multilayers with the extreme CMC gradients was observed. For all multilayers which were simultaneously coated with the two doctor blades, no intermixing was found.

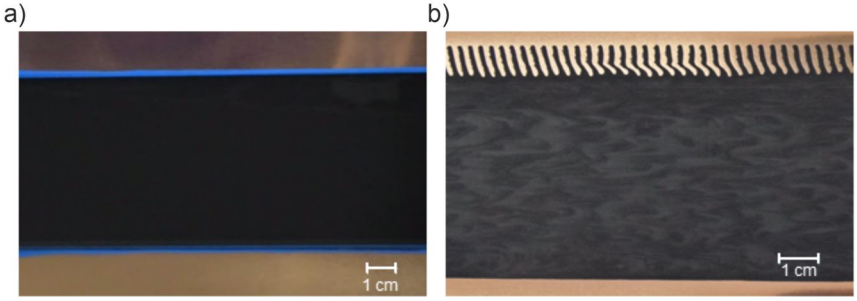

Figure A. 7-40: Coating stability of simultaneously coated multilayers a) without intermixing and b) with intermixing of both layers shown in the dry state.[99]

E.2 Drying of Simultaneous Multilayers

Some more details concerning the drying mechanism of multilayer electrodes is presented in the follow, providing some additional information in relation to section 6 (Simultaneously Coated and Hierarchically Structured Multilayers). The adhesion force of multilayer electrodes was shown there for drying at two different drying rates. The adhesion force decreased more than expected when either drying rate or film thickness was increased, especially when compared to single-layered electrodes. The most unexpected result was the performance of the multilayer (S || A) compared to the single layer (S).

By using the additive-reduced slurry (A) with the non-spherical graphite with a larger and broader particle size distribution on top of slurry (S) with the spherical graphite with a smaller and narrower particle size distribution (see Figure A. 7-41), capillary pore emptying might by affected. If the smaller pores at the bottom were emptied earlier binder could be dragged away from its original positions before strong ester bonds are formed. If binder is dragged away before the

reaction takes place less ester bonds would result. This would manifest in a loss in adhesion if CMC and SBR binder were associated with one another.

In the case of the simultaneously coated multilayers (S || A) and (K || A), a binder gradient directly after coating within the wet electrode is present. Resulting from this, a diffusion of binder to the top layer could also take place during film shrinkage. The binder content of the top layer appears to influence the adhesion which was aimed to be defined by the bottom layer at least to some extent: Multilayers with the reference on top instead of slurry (A) possess a slightly higher adhesion force (see Appendix, Figure A. 7-45). The severe adhesion loss of the multilayer (S || A) dried at the high drying rate cannot be solely explained by the concentration gradient within the multilayer, since this should manifest itself also at the low drying rate. Therefore, a negative effect on capillary pore emptying caused by the multilayer setup could be the explanation.

Again, besides a concentration gradient which might increase the unwanted binder migration at the multilayer setup, the mechanism of capillary pore emptying could also have an impact: capillaries might transport liquid from the electrode bottom to the surface. As a hindrance, a bottom layer consisting of spherical particles with smaller pore radii was introduced. A comparison of the pore radii of the spherical particles and the ones with non-spherical graphite is given in see Figure A. 7-41. The pore size distributions of electrode (R), (S) and (K) measured by mercury intrusion porosemitry are shown. The peaks of electrode (R) and (S) are separate from one another while the peaks of electrode (R) and (K) overlap. The main peak of the electrode comprised of the spherical graphite lies at 2.5 µm, the main peak of electrode (K) at 4 µm and the one of electrode (R) at 4.8 µm. Introducing a hindrance layer was only partly realized here. The peaks of the pore size distributions are separate from each other, meaning that the most common pore sizes are different in electrode (R) and (S). They still share a smaller amount of identically sized pores though, which could mean that capillaries still reach from the top to the bottom of the electrode. Hence, an earlier onset of capillary pore emptying, which was observed to especially take place at higher electrode thicknesses, in combination with the increased drying rate, could reduce the available time for the ester reaction to take place.

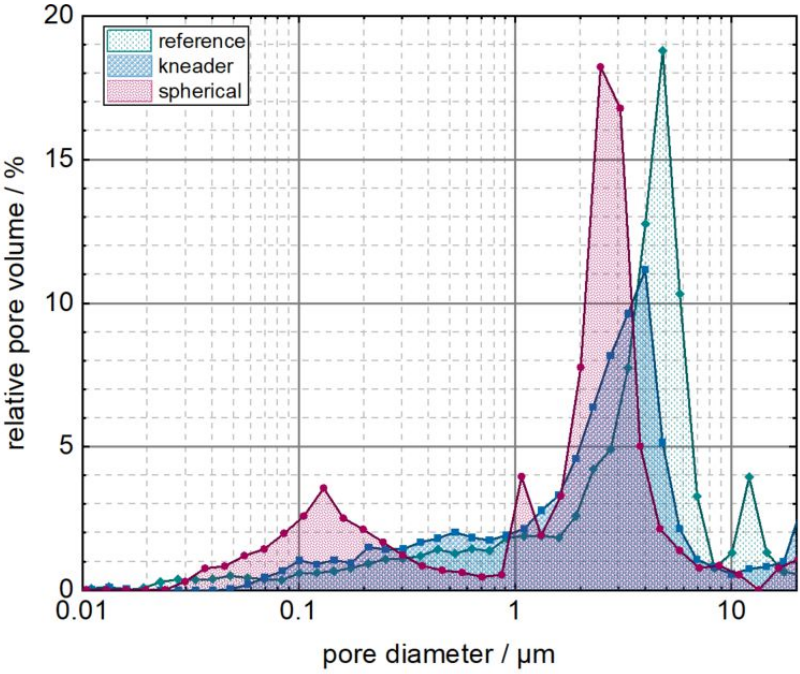

Figure A. 7-41: Relative pore volume as a function of the pore size of electrodes (R), (K) and (S). The relative pore volume as a function of the pore diameter was measured with mercury intrusion porosemitry. Pore sizes above 20 µm are cropped since these are above the particle size and can therefore assumed to be surface pores.

The drying of the simultaneously coated multilayer of slurry (S) as bottom and slurry (R) as top layer was investigated in some more detail. Electrodes of twice the area capacity of a state-of-the-art-electrode were dried at the experimental procedure described by Jaiser et al.[68] The heat transfer coefficient was changed from a high one (here 80 W m^{-2} K^{-1}) to a low one (35 W m^{-2} K^{-1}) during drying. Characteristic points during drying were thereby determined. The respective drying rates were 1.5 g m^{-2} s^{-1} for the high drying rate and 0.5 g m^{-2} s^{-1} for the low drying rate. The electrodes in Figure A. 7-42 show the same behavior the single layered electrodes described in literature did.[68] An initial drying at the high drying rate does not influence the adhesion force. Only if the high drying rate is applied until after the end of film shrinkage has been reached does the high drying rate negatively affect the adhesion force. Based on these findings, one can assume, that a higher drying rate, if applied by means of a higher heat transfer

coefficient negatively influences the adhesion force of the spherical graphite. This is in accordance with the assumption, that the higher adhesion force at higher drying rates is solely caused by the increased temperature and the ester reaction. One can further assume, that capillary drag still takes place, since otherwise an influence of the transition between both drying rates would not be expected.

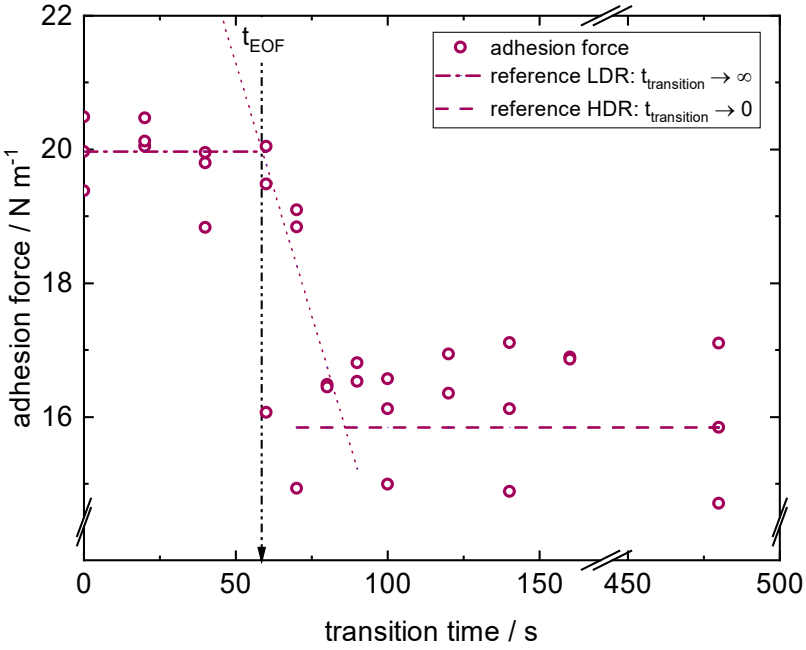

Figure A. 7-42: Adhesion force of simultaneously coated multilayer (S || R) when dried at a high drying rate (of 1.5 g m^{-2} s^{-1} at 80 W m^{-2} K^{-1}) until the transition time and then at a low drying rate (of 0.5 g m^{-2} s^{-1} at 35 W m^{-2} K^{-1}).

The drying of this multilayer setup was investigated some more. The drying mechanism was illuminated by means of Cryo-BIB-SEM cross sections of electrode films during drying. The detailed experimental procedure is described elsewhere.[26] Multilayered electrode films were coated and dried at 0.5 g m^{-2} s^{-1} in the batch coater (see section 2.2.3) for different time intervals and then rapidly removed from the dryer and transferred to nitrogen slush as to directly freeze

them. These samples were stored in liquid nitrogen until preparation in the Cyro-SEM. The respective electrode cross sections are shown in Figure A. 7-43.

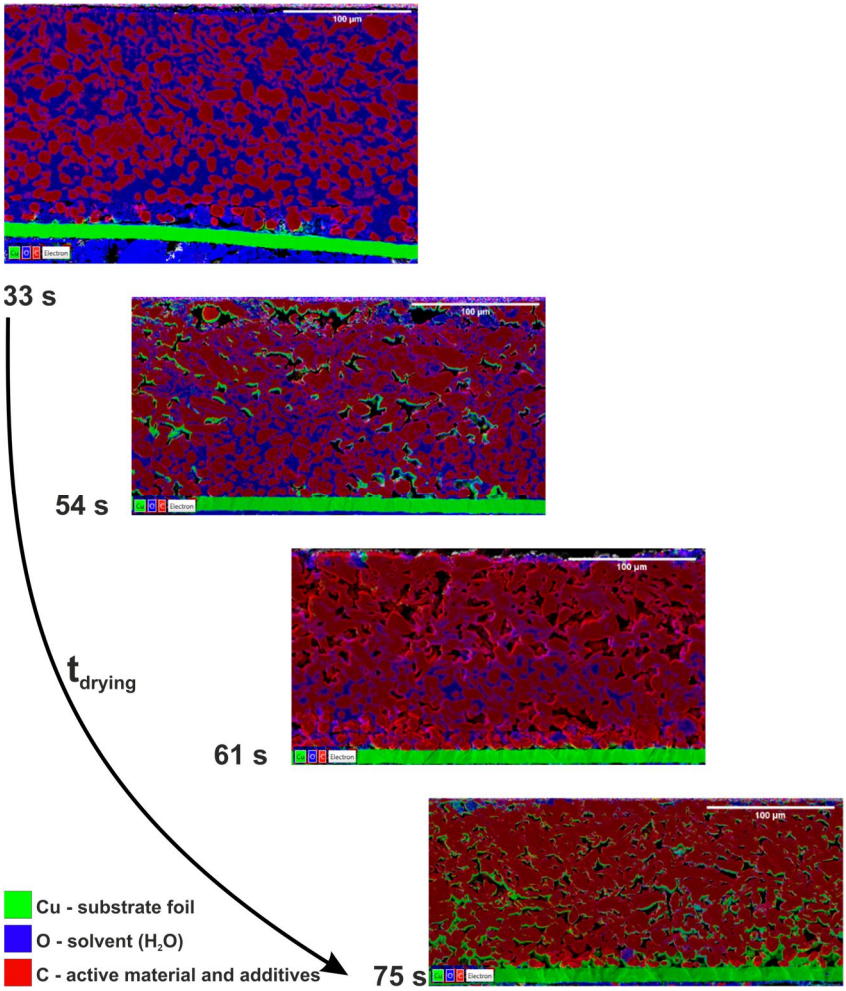

Figure A. 7-43: EDS Cryo-BIB-SEM pictures of the multilayer (S || R) with the elements Cu, O and C dried at a drying rate of 0.5 g m^{-2} s^{-1}.

Different times during drying are shown. After 33 s of drying time, the film has shrinked due to solvent evaporation, but all pores are still water-filled. This is recognizable by the blue color, which stands for O-atoms detected in the EDS

(Xmax 150, Oxford Instruments, UK) measurement. The green color can be attributed to the copper substrate. This becomes especially visible in some pores where the electrode is already dry since copper redeposited there during BIB cross section preparation. The red color is mainly attributed to the graphite particles, though binder and carbon black also contain C-atoms, which is why they cannot be distinguished. After 54 s of drying time the theoretical end of film shrinkage should be reached (Figure A. 7-43). The Cryo-SEM micrographs though, shows empty pores throughout the microstructure. This could either be caused by the single film which might slightly deviate in their film thickness, or by an earlier onset of capillary pore emptying, as described earlier. After 61 s of drying, the pores in the top section of the electrode seem to be empty, while a solvent-filled belt remains in the bottom region of the electrode. After 75 s of drying time, the whole electrode seems to be dry based on the observed cross section.

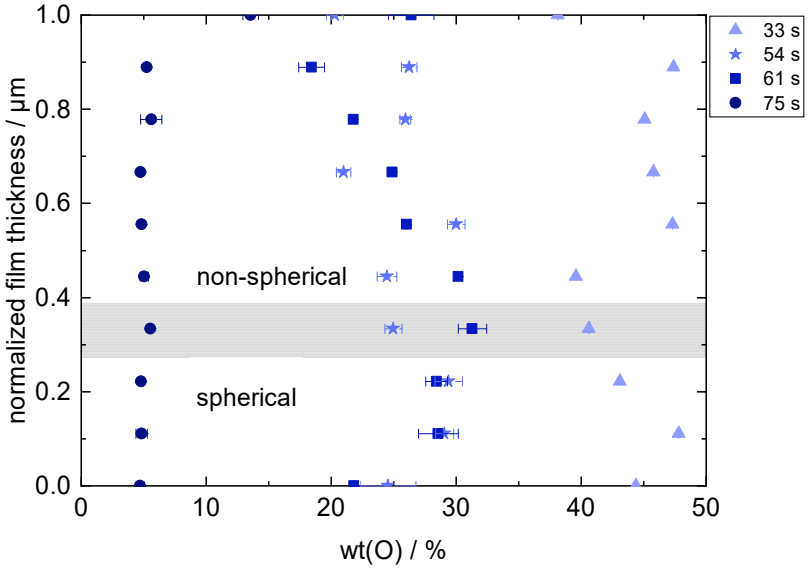

Figure A. 7-44: Amount of solvent (wt-% of O) detected in the layers within the multilayer electrode which is given as the normalized film thickness.

To get an idea of the solvent content over the electrode thickness, the oxygen-content over the film thickness was evaluated. Each film was therefore segmented into 10 layers and the oxygen content was determined (see Figure A. 7-44). The impression that a higher O-content can be found in the bottom region of the film with the spherical graphite seems to be confirmed. More oxygen in the part of the spherical graphite is detected especially after 54 s and 61 s of drying. The content is only constant over the electrode height after 75 s of drying time. From these findings one could indeed assume, that the change of the pore radius at the boundary layer does indeed slow down capillary transport. Even though, empty capillaries can still be found at the bottom of the electrode in the Cryo-Bib-Sem micrographs. This agrees with the other results, which show no clear trend of preventing capillary transport in the bottom layer.

Properties of dry simultaneously coated multilayers

The adhesion force of the simultaneously coated multilayers (S || R) and (R || S) is shown in Figure A. 7-45 as a function of the area capacity and compared to the respective single layers.

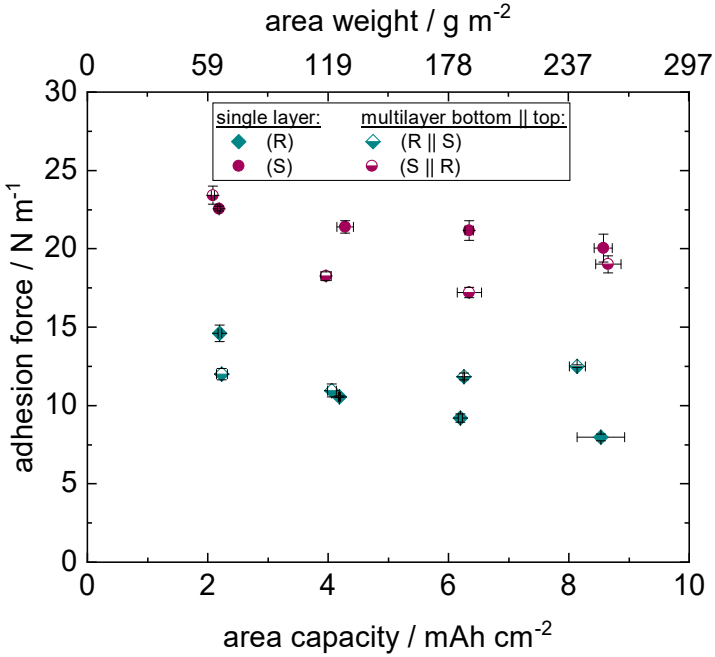

Figure A. 7-45: Adhesion force as a function of the area capacity for the single layered electrodes (S) and (R) compared to the multilayers consisting or slurry ® at the bottom and slurry (S) at the top and vice versa. The multilayers had a layer ratio of 1/3 bottom and 2/3 top layer. All electrodes were coated on substrate (f3) and dried at an experimental drying rate of 0.5 g m-2 s-1 at a heat transfer coefficient of 35 W m-2 K-1.

The specific discharge capacities of the multilayers (S || R) and (R || S) at different C rates determined in a pouch cell test are given in Figure A. 7-46. The lower specific capacity of the multilayer anodes containing the spherical graphite at the low C rate of C/20 can be observed. Even though, the specific discharge capacity of the multilayer (S || R) is identical or even exceeds that of the reference. Only the multilayer (R || S) performs worse. This could be attributed to the binder

distribution on the one hand. Since the theoretical drying rate was only 0.75 g m^{-2} s^{-1} a positive effect of the porosity gradient could also be assumed.

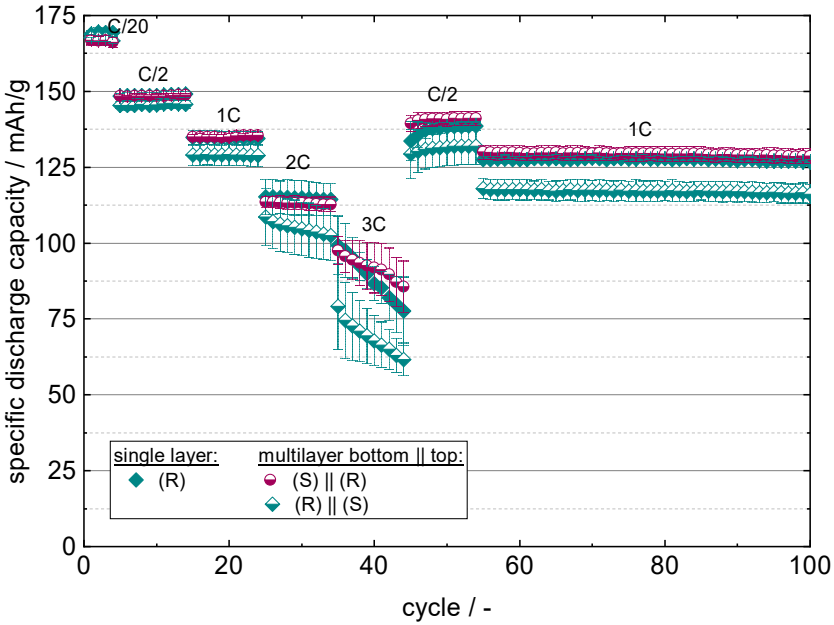

Figure A. 7-46: Pouch cell test of SoA multilayers (S || R) and (R || S) compared to the reference (R). The theoretical drying rate was 0.75 g m^{-2} s^{-1}. The cathode was NMC622.

The adhesion forces of the multilayers (S || A), (S || R) and (K || A) and (K || R) are compared to one another in Figure A. 7-47. It clearly shows that the adhesion force of the entire electrode is not solely determined by the adhesion force of the bottom layer. Both bottom layers which are combined with slurry (A) as top layer have a lower adhesion force than the ones which are combined with slurry (R) as top layer. This is especially true at the lowest area capacity since the values approximate similar values at the higher area weights.

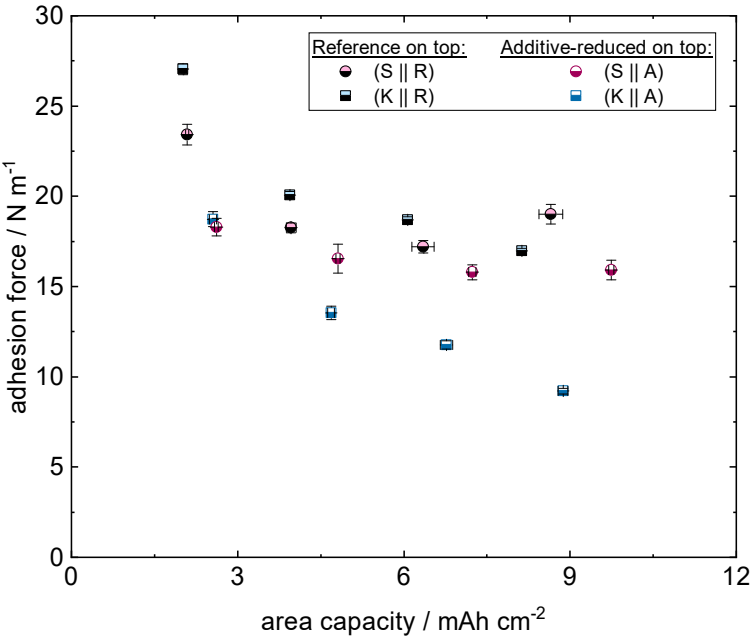

Figure A. 7-47: Adhesion force as a function of the area capacity for multilayered electrodes with two different top layers combined with slurries (S) and (K) as bottom layers. In the first configuration the reference (R) is used as top layer, thus no binder concentration gradient would be expected directly after coating within the wet electrode. In the second setup the additive-reduced slurry is used as top layer, as such leading to a concentration gradient of the binder in the wet electrode. The experimental drying rate was 0.5 g m^{-2} s^{-1} at a heat transfer coefficient of 35 W m^{-2} K^{-1}.

The electrical conductivity of the multilayers (S || A), (K || A) and (primer || A) are given as a function of the area capacity and for two different experimental drying rates in Figure A. 7-48.

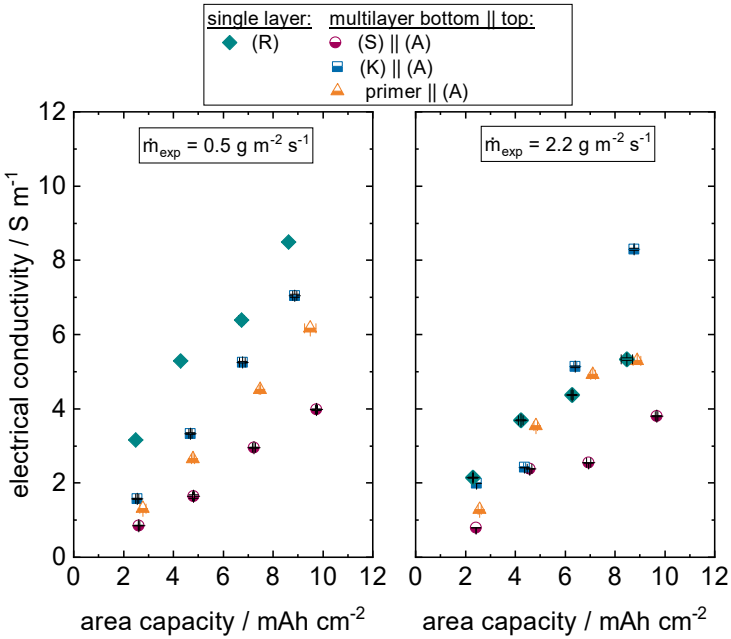

Figure A. 7-48: Electrical conductivity of multilayer electrodes compared to the reference as a function of the area capacity.

Properties for electrochemical tests

Measured area capacities and porosities of the multilayer electrodes built into coin cells are summarized in Table A. 8 to Table A. 12.

Table A. 8: Area capacities in mAh cm^{-2} of multilayer SoA electrodes that were dried at different drying rates. Area capacities are calculated based on the respective area weights.

Experimental drying rate	0.5 / g m^{-2} s^{-1}	2.2 / g m^{-2} s^{-1}
(S) || (A)	2.6	2.3
(K) || (A)	2.5	2.4
Primer || (A)	2.5	2.5

Table A. 9: Porosity of multilayer SoA electrodes that were dried at different drying rates.

Experimental drying rate	0.5 / g m^{-2} s^{-1}	2.2 / g m^{-2} s^{-1}
(S) || (A)	0.47	0.48
(K) || (A)	0.42	0.47
Primer || (A)	0.45	0.46

Table A. 10: Area capacities in mAh cm^{-2} of thick multilayer electrodes that were dried at different drying rates. Area capacities are calculated based on the respective area weights.

Experimental drying rate	0.5 / g m^{-2} s^{-1}	2.2 / g m^{-2} s^{-1}
(S) || (A)	9.4	9.3
(K) || (A)	8.7	8.5
Primer || (A)	9.1	8.6

Table A. 11: Porosity of thick multilayer electrodes that were dried at different drying rates.

Experimental drying rate	0.5 / g m^{-2} s^{-1}	2.2 / g m^{-2} s^{-1}
(S) || (A)	0.47	0.52
(K) || (A)	0.49	0.50
Primer || (A)	0.48	0.49

Table A. 12: Area capacity and porosity of single and multilayer electrodes that were dried at the extreme drying rate of 5 g m^{-2} s^{-1}.

Layer configuration	Area capacity / mAh cm^{-2}	Porosity / -
(R)	2.1	0.54
(S)	2.1	0.50
(S) || (R)	2.5	0.52

Publications

As first author

- **Kumberg, Jana;** Bauer, Werner; Schmatz, Joyce; Diehm, Ralf; Tönsmann, Max; Müller, Marcus; Ly, Kevin; Scharfer, Philip; Schabel, Wilhelm (2021): *Reduced Drying Time of Anodes for Lithium-Ion Batteries through Simultaneous Multilayer Coating.* In: Energy Technol., S. 2100367. DOI: 10.1002/ente.202100367.

- **Kumberg, Jana**; Baunach, Michael; Eser, Jochen C.; Altvater, Andreas; Scharfer, Philip; Schabel, Wilhelm (2021): *Influence of Layer Thickness on the Drying of Lithium-Ion Battery Electrodes—Simulation and Experimental Validation*. In: Energy Technol., S. 2100013. DOI: 10.1002/ente.202100013.

- **Kumberg, Jana**; Baunach, Michael; Eser, Jochen C.; Altvater, Andreas; Scharfer, Philip; Schabel, Wilhelm (2020): *Investigation of Drying Curves of Lithium-Ion Battery Electrodes with a New Gravimetrical Double-Side Batch Dryer Concept Including Setup Characterization and Model Simulations.* In: Energy Technol. 3, S. 2000889. DOI: 10.1002/ente.202000889.

- **Kumberg, Jana**; Müller, Marcus; Diehm, Ralf; Spiegel, Sandro; Wachsmann, Christian; Bauer, Werner; Scharfer, Philip; Schabel, Wilhelm (2019): *Drying of Lithium-Ion Battery Anodes for Use in High-Energy Cells. Influence of Electrode Thickness on Drying Time, Adhesion, and Crack Formation.* In: Energy Technol. 3, S. 1900722. DOI: 10.1002/ente.201900722.

As Co-Author

- Diehm, Ralf; **Kumberg, Jana**; Dörrer, Christopher; Müller, Marcus; Bauer, Werner; Scharfer, Philip; Schabel, Wilhelm (2020): *In-situ Investigations of Simultaneous Two-Layer Slot Die Coating of Component Graded Anodes for improved High Energy Li-Ion Batteries.* In: Energy Technol. DOI: 10.1002/ente.201901251.

- Diehm, Ralf; Müller, Marcus; Burger, David; **Kumberg, Jana**; Spiegel, Sandro; Bauer, Werner; Scharfer, Philip; Schabel, Wilhelm (2020): *High-Speed Coating of Primer Layer for Li-Ion Battery Electrodes by Using Slot-Die Coating*. In: Energy Technol. 8 (9), S. 2000259. DOI: 10.1002/ente.202000259.

- Diehm, Ralf; Weinmann, Hannes; **Kumberg, Jana**; Schmitt, Marcel; Fleischer, Jürgen; Scharfer, Philip; Schabel, Wilhelm (2019): *Edge Formation in High-Speed Intermittent Slot-Die Coating of Disruptively Stacked Thick Battery Electrodes*. In: Energy Technol. 5, S. 1900137. DOI: 10.1002/ente.201900137.

- Eser, Jochen C.; Wirsching, Tobias; Weidler, Peter G.; Altvater, Andreas; Börnhorst, Tobias; **Kumberg, Jana**, Schöne, Gerrit; Müller, Marcus; Scharfer, Philip; Schabel, Wilhelm (2019): *Moisture Adsorption Behavior in Anodes for Li-Ion Batteries.* In: Energy Technol. 73, S. 1801162. DOI: 10.1002/ente.201801162.

- Jaiser, Stefan; **Kumberg, Jana**; Klaver, Jop; Urai, Janos L.; Schabel, Wilhelm; Schmatz, Joyce; Scharfer, Philip (2017): *Microstructure formation of lithium-ion battery electrodes during drying – An ex-situ study using cryogenic broad ion beam slope-cutting and scanning electron microscopy (Cryo-BIB-SEM).* In: Journal of Power Sources 345, S. 97–107. DOI: 10.1016/j.jpowsour.2017.01.117.

- Zeiger, Claudia; **Kumberg, Jana**; Vüllers, Felix; Worgull, Matthias; Hölscher, Hendrik; Kavalenka, Maryna N. (2017): *Selective filtration of oil/water mixtures with bioinspired porous membranes.* In: RSC Adv. 7 (52), S. 32806–32811. DOI: 10.1039/C7RA05385A.

- Kavalenka, Maryna N.; Vüllers, Felix; **Kumberg, Jana**; Zeiger, Claudia; Trouillet, Vanessa; Stein, Sebastian et al. (2017): *Adaptable bioinspired special wetting surface for multifunctional oil/water separation.* In: Scientific reports 7, S. 39970. DOI: 10.1038/srep39970.

Conference contributions

- **J. Kumberg;** L. Eymann; J. Schmatz; M. Müller; W. Bauer; P. Scharfer; W. Schabel: *Drying two-layered electrodes of different particle sizes for use in lithium-ion batteries* (**Talk**), 20th International Coating Science and Technology Symposium (ISCST), Online Venue, September 20th – 23rd 2020

- **J. Kumberg;** R. Diehm; M. Müller; W. Bauer; P. Scharfer; W. Schabel: *Processing of Thick Electrodes for Li-Ion Batteries with increased Microstructure Homogeneity* (**Talk**), European Coating Symposium (ECS), September 09th – 11th 2019, Heidelberg

- R. Diehm; **J. Kumberg;** P. Scharfer; W. Schabel: *Multilayered Coating and Drying of Thick Electrodes for Li-Ion Batteries to increase Microstructure Homogeneity* (**Tandem Talk**), International Coating Science and Technology Symposium (ISCST), September 16th – 19th 2018, Long Beach, CA, USA

- **J. Kumberg;** R. Diehm; M. Müller; W. Bauer; P. Scharfer; W. Schabel: *Processing of Thick Electrodes for Li-Ion Batteries with increased Microstructure Homogeneity* (**Talk**), International Coating Science and Technology Symposium (ISCST), September 16th – 19th 2018, Long Beach, CA, USA

- **J. Kumberg;** R. Diehm; P. Scharfer; W. Schabel: *Multilayered Coating and Drying of Thick Electrodes for Li-Ion Batteries to increase Microstructure Homogeneity* (**Awarded Poster**), International Coating Science and Technology Symposium (ISCST), September, 16th – 19th 2018, Long Beach, CA, USA

- **J. Kumberg**; S. Jaiser; J. Klaver; J. L. Urai; W. Schabel; J. Schmatz; P. Scharfer: *Cryo SEM morphology characterization and drying research on Li-ion battery electrodes* (**Talk**), Euopean Coating Symposium (ECS), November 7-10, 2017, Fribourg, Switzerland

- R. Diehm; **J. Kumberg**; W. Haselrieder; A. Hoffmann; S. Haag; F. Röder; D. Westhoff; S. Hein; T. Danner; M. Wohlfahrt-Mehrens; J. Fleischer; A. Kwade; P. Scharfer; W. Schabel: *ProZell HighEnergy - Production and Simulation of High Capacity and Structured Electrodes* (**Poster**),

Euopean Coating Symposium (ECS), November 7-10, 2017, Fribourg, Switzerland

- **J. Kumberg**; R. Diehm; J. Knack; C. Dörrer; P. Scharfer; W. Schabel, *Going the next step: Coating and Drying of Multilayer Electrodes for Li-Ion Batteries* (**Poster**), Euopean Coating Symposium (ECS), November 7-10, 2017, Fribourg, Switzerland

- **J. Kumberg;** S. Jaiser; J. Klaver; J. L. Urai; W. Schabel; J. Schmatz; P. Scharfer: *Cryo SEM morphology characterization and drying research on Li-ion battery electrodes* (**Talk**), Formula IX, October 15th – 18th 2017, Peking, China

National

- **J. Kumberg;** K. Ly; M. Baunach; J.C. Eser; A. Altvater; P. Scharfer; W. Schabel: *Investigation of the drying mechanism of electrodes of different thicknesses for lithium-ion batteries* (**Talk**), Annual meeting of the ProcessNet specialist group "Hochdruckverfahrenstechnik und Trocknungstechnik zusammen mit Phytoextrakte", March, 15th – 17th 2021, online venue

- **J. Kumberg;** K. Ly; M. Baunach; J.C. Eser; A. Altvater; P. Scharfer; W. Schabel: *Experimentelle und simulative Untersuchung des Trocknungsverlaufs von Lithium-Ionen-Batterie-Elektroden unterschiedlicher Dicke im stationären Trockner* (**Poster**), Annual meeting of the ProcessNet specialist group " Fluidverfahrenstechnik und Wärme- und Stoffübertragung", February, 24th – 25th 2021, online venue

- W. Schabel; R. Diehm; **J. Kumberg**, S. Spiegel; P. Scharfer: *Multilayer Coating and Drying of Component Graded Anodes for improved High Energy Li-Ion Batteries* (**Poster**), Batterieforum Berlin, January, 22nd – 24th 2020, Berlin

- **J. Kumberg;** R. Diehm; P. Scharfer; W. Schabel: *Trocknung mehrlagiger Elektroden für Lithium-Ionen-Batterien* (**Talk**), Annual meeting of the ProcessNet specialist group "Wärme- und Stoffübertragung, Trocknungstechnik und Mischvorgänge", March, 18th – 20th 2019, Essen

- H. W. Weinmann; R. Diehm; **J. Kumberg**; P. Scharfer; W. Schabel; J. Fleischer: *Prozessierbarkeit dickschichtiger Anoden* (**Poster**), Batterieforum Berlin, January, 23rd – 25th 2019, Berlin
- **J. Kumberg**; S. Jaiser; J. Klaver; J. L. Urai; W. Schabel; J. Schmatz; P. Scharfer: *Cryo SEM morphology characterization and drying research on Li-ion battery electrodes* (**Talk**), ProcessNet Jahrestagung, September 13, 2018, Aachen, Germany

- **J. Kumberg;** R. Diehm; P. Scharfer; W. Schabel: *New insights into drying of Li-Ion battery electrodes* (**Talk**), Thin Film Technology Forum, June, 06th – 07th 2018, Karlsruhe

- **J. Kumberg;** P. Scharfer; W. Schabel: *Untersuchung des Einflusses der Schichtdicke auf das Trocknungsverhalten von Lithium-Ionen-Batterie-Anoden* (**Talk**), Annual meeting of the ProcessNet specialist group "Trocknungstechnik", February, 26th 2018, Merseburg

- **J. Kumberg;** R. Diehm; C. Dörrer; J. Knack; P. Scharfer; W. Schabel: *Multilayered Electrodes for Li-Ion Batteries to reduce Drying Time* (**Poster**), AABC Europe, January, 31st 2018, Mainz

- **J. Kumberg;** S. Jaiser; M. Baunach; P. Scharfer; W. Schabel: *Drying characterization of battery electrodes* (**Talk**), Short Course of Coating and Drying of Thin Films, May, 29th – 31st 2017, Karlsruhe

- **J. Kumberg**; S. Jaiser; J. Klaver; J. L. Urai; J. Schmatz; W. Schabel; P. Scharfer: *Untersuchung der Strukturausbildungsmechanismen während der Trocknung von Lithium-Ionen-Batterie-Anoden mit Kryo-REM-Messungen* (**Talk**), Jahrestreffen der ProcessNet-Fachgruppen Trocknungstechnik, February 02, 2017, Bruchsal, Germany

- **J. Kumberg**; S. Jaiser; J. Klaver; J. L. Urai; J. Schmatz; P. Scharfer; W. Schabel: *Drying of Li-Ion Battery Anodes and its Impact on Film Morphology* (**Poster**), AABC Europe, January 31, 2017, Mainz, Germany

- W. Schabel; S. Jaiser; R. Diehm; **J. Kumberg;** P. Scharfer: *Current Limitations in Coating and Drying of Lithium-Ion Battery Electrodes* (**Poster**), Annual meeting ProcessNet, September, 12th – 15th 2016, Aachen

Supervised student work in the context of this work

Principal Supervisor:

- Alimohammad Eghbalpoor: *Optimierung von Multilagen-Konzepten zur Verbesserung der Lade- und Entladeraten von dicken Anoden für Lithium-Ionenbatterien* (2020, Masterarbeit)
- Ulf Garbe: *Prozessierung von Elektroden mit reduziertem Bindergehalt durch simultane Multilagen-Beschichtung* (2020, Bachelorarbeit)
- Luisa Eymann: *Aufklärung des Porenentleerungsmechanismus bei der Trocknung von Doppellagen unterschiedlicher Porenradienverteilungen* (2020, Bachelorarbeit)
- Sabine Mizera: *Untersuchung des Einflusses der Komponenten-und Phasenverteilung im Nassfilm auf das Trocknungsverhalten und die sich ausbildende Mikrostruktur von Elektroden für Lithium-Ionen-Batterien* (2020, Masterarbeit)
- Thomas Renaldy: *Produktqualität bei der Trocknung zweiseitiger Elektrodenbeschichtungen für die Anwendung in Lithium-Ionen-Batterien* (2019, Bachelorarbeit)
- Johannes Fladerer: *Untersuchung des Einflusses des Aktivmaterials auf die Trocknungsmechanismen und die resultierenden Eigenschaften von Elektroden für Lithium-Ionen-Batterien* (2018, Bachelorarbeit)
- Jella Kramer: *Gradierte und simultan prozessierte Elektrodendoppellagen für Lithium-Ionen-Batterien* (2018, Diplomarbeit)
- Sarah Stolz: *Gegenüberstellung des Trocknungseinflusses zweier Energiespeichersysteme zur Optimierung ihrer Mikrostruktur* (2018, Masterarbeit)
- Oliver Dobler: *Einfluss des Feststoffgehaltes auf die Mikrostrukturausbildung von Elektroden für Lithium-Ionen-Batterien* (2018, Bachelorarbeit)
- Cedric Großelindemann: *Untersuchung des Trocknungseinflusses bei der einlagigen Herstellung hochkapazitiver Batterieelektroden*

gegenüber der sequentiellen und simultanen Prozessierung mehrlagiger Elektroden (2018, Bachelorarbeit)

- Andreas Altvater: *Optimierung eines Trockners zur gravimetrischen Aufnahme von Trocknungsverlaufskurven zur gezielten Untersuchung der Trocknungskinetik funktionaler Schichten zur Anwendung in der Energiespeicherung* (2018, Masterarbeit)
- Christian Wachsmann: *Aufklärung charakteristischer Stadien der Morphologieausbildung bei der Trocknung hochkapazitiver Batterieelektroden* (2017, Bachelorarbeit)
- Jaroslav Knack: *Untersuchung des Trocknungseinflusses bei der Herstellung mehrlagiger, hochkapazitiver Batterieelektroden* (2017, Bachelorarbeit)

Second Supervisor:

- Narigul Khamzaeva: *Untersuchung des Trocknungsverhaltens von Batterieelektroden mit Hilfe von optischen Messmethoden* (2019, Bachelorarbeit)
- David Burger: *Forschung und Entwicklung von Prozesstechnik zur Herstellung von dünnen Primärschichten für Lithium-Ionen Batterieelektroden* (2018, Bachelorarbeit)
- Andreas Albrecht: *Ermittlung von Prozess-Eigenschaftsbeziehungen der intermittierten Schlitzdüsenbe-schichtungen sowie Rolle-zu-Rolle Trocknung von Li-Ion Batterieelektroden* (2018, Masterarbeit)
- Florian Karg: *Untersuchung und Optimierung der intermittierten Schlitzdüsenbeschichtungen für Li-Ion Batterieslurries mit erhöhter Viskosität* (2018, Masterarbeit)
- Kilian Adams: *Inbetriebnahme eines Weißlichtinterferometers zur Aufnahme von Trocknungsverlaufskurven von funktionellen Schichten für Energiespeicher* (2018, Bachelorarbeit)
- Christopher Dörrer: *Untersuchung der simultanen Mehrlagenbeschichtung von Lithium-Ionen-Batterieelektroden und das Potential zur Verbesserung der Zelleigenschaften* (2018, Masterarbeit)

- Sandro Spiegel: *Untersuchung der Anforderungen an die Eigenschaften hochkapazitiver Elektroden für Lithium-Ionen Batterien für den Herstellungsprozess im industriellen Rolle-zu-Rolle Verfahren* (2017, Masterarbeit)

- Simone Knaus: *Untersuchung der Trocknungskinetik von Schlickern für funktionale Schichten zur Anwendung in der Energiespeicherung* (2017, Bachelorarbeit)